

# Low Background Techniques and Experimental Challenges for Borexino and its Nylon Vessels

Andrea Pocar

A dissertation  
presented to the faculty  
of Princeton University  
in candidacy for the degree  
of Doctor of Philosophy

Recommended for acceptance  
by the department of Physics

November 2003

© Copyright by Andrea Pocar, 2003. All rights reserved.

# Abstract

Neutrino physics has seen exciting developments over the past five years, following the experimental evidence of their oscillations in the atmospheric and solar sectors; precise measurements of neutrino properties play a crucial role in understanding fundamental interactions and physics at the cosmological scale.

Borexino is an experiment for low energy ( $< 1$  MeV) solar neutrino spectroscopy approaching completion at the underground Gran Sasso laboratories in Italy. It is specifically designed to measure in real time the flux of mono-energetic  ${}^7\text{Be}$  neutrinos produced by fusion reactions in the Sun. Its 300-ton liquid scintillator target is contained in an 8.5 meter diameter nylon inner vessel (IV) and is surrounded by 1000 tons of buffer fluid. A second, 11.5 meter diameter concentric nylon outer vessel (OV) around the IV serves as a barrier for radon emanated at the periphery of the detector.

Borexino requires unprecedented low levels of radioactive impurities to be a success ( $\sim 1$  background event/day in the central 100-tons of scintillator). The IV, which is in direct contact with the scintillator, also has to meet extremely stringent radioactive and cleanliness requirements. Intrinsic levels  $\sim 10^{-12}$  g/g for U and Th and  $\sim 10^{-8}$  g/g for K are needed. A maximum  $\sim 5$  mg of “dust” and  $\sim 5 \times 10^{-5}$  Bq  ${}^{210}\text{Pb}$  activity deposited (from radon in the air) on its surface can be tolerated.

The vessels, assembled in a clean room in Princeton, made of a 125 micron-thick membrane, need to be leak tight at the  $10^{-2}$  cc/s and 1 cc/s level for the IV and OV respectively, and have to withstand mechanical stresses due to density differences and temperature gradients between the fluids they contain. Their requirements and assembly process are presented in detail. An upper limit on the inner vessel leak rate of  $10^{-3}$  cc/s was measured. The performance of a matrix of light sources, placed on both vessels for monitoring its shape with digital cameras, is demonstrated. A measurement of the relative densities of the scintillator and buffer solutions to better than 1 part in  $10^4$  is also discussed.

The problem of surface contamination by radon in the air is extensively addressed,

strategies for minimizing it are analysed, and the effectiveness of their application evaluated. In particular, an original radon filter based on vacuum swing adsorption on activated charcoal has been developed for use in connection with the clean room. Such a technique yielded radon abatement factors in excess of  $10^4$  in a small-scale prototype, and  $\sim 100$  in the final system. The device ran continuously for one year and contributed significantly in controlling the radon contamination of the IV during its assembly. Similar filters could be valuable for other low-background experiments.

Finally, trace scintillator radioactivity data are reported from CTF3, a counting test facility for Borexino now in its third data-taking phase. An intrinsic  $^{14}\text{C}$  isotopic contamination of the scintillator  $\sim 5 \times 10^{-18}$  has been measured. Upper limits of  $\sim 3.5 \times 10^{-16}$  g/g on  $^{238}\text{U}$  contamination and of  $\sim 10^{-4}$  Bq/ton for the  $^{85}\text{Kr}$  residual activity have also been set.

# Acknowledgements and Credits

The work presented in this thesis was carried out within a collaboration of approximately 100 people; it could not have taken place without the participation of many colleagues. I wish to thank them all for their help. I am grateful to the members of the Borexino group in Princeton and, in particular, to Frank Calaprice and Tom Shutt for their guidance and support during my graduate studies.

Many people ought to be individually given credit for work that has directly contributed to the results that are being presented. Particular recognition is due to the core of the “Vessel Construction Team”: Beth Harding, Allan Nelson, Charles Sule, and Brian Kennedy. A fundamental role in the development and realization of the nylon vessels was played by Frank Calaprice, Bruce Vogelaar, Fred Loeser, Laura Cadonati, Richard Fernholz, Tom Shutt, Allan Nelson, Beth Harding, Cristian Galbiati, Kevin McCarty, and Ernst deHaas. Invaluable support for the vessel effort was provided by the Physics Department machine shop: Laszlo Vargas, Glen Atkinson, Ted Lewis, and Mike Peloso, thank you.

The idea of using vacuum swing adsorption for radon removal was originally suggested by Tom Shutt, who also enthusiastically supported its development. Essential contributions to the successful realization of such system were also made by: Ernst deHaas and Charles Sule for technical help and initiative; Beth Harding for performing crucial measurements on the prototype in my absence; and Costin Bontas for programming the control system for the full-scale device. My work benefited from previous work by Nick Darnton and from useful discussions with Frank Calaprice and Jay Benziger. I also wish to thank all those who kept up with the noise levels produced by the full-scale filter. In my defense is the fact of having supplied the clean room personnel with healthier, radon-suppressed air!

The development of the light sources on the vessels was carried out together with Davide Gaiotto, following discussions with Frank Calaprice. I wish to thank Bob Austin, Lisa Olsen, and Steve Smith for useful discussions and for letting us use their lab equipment.

The analysis on CTF3 data presented here was performed together with Aldo Ianni

and Kevin McCarty. Discussions with Cristian Galbiati, Laura Cadonati, Frank Calaprice, Davide D'Angelo, Davide Franco, and Maria Elena Monzani were useful in addressing some of the questions.

My work has undoubtedly been made easier by the help offered by the Department's personnel. I particularly thank Susan Oberlander, Helen Ju, Kathy Patterson, Laurel Lerner, Kathy Warren, John Washington, and Claude Champagne.

I am also grateful to the many people that made my stay at the Gran Sasso laboratories a pleasant one. Among them I specially wish to thank Andrea and Aldo Ianni, Augusto Goretti, and Stefano Gazzana: the labs wouldn't be the same without you!

Finally, I wish to thank Kevin McCarty and Beth Harding for proof-reading the manuscript, and my cat Pennie for her purring affection during the past five years.

# Foreword

This thesis reports on work carried out in Princeton in the past five years for developing, designing, and assembling the nylon vessel system for Borexino.

In chapter 1, the current situation of neutrino oscillations and solar neutrino physics is presented, along with an outline of how the so-called “solar neutrino problems” arose and were recently solved. The importance of performing precision measurements of low energy solar neutrinos with experiments such as Borexino is also discussed.

Chapter 2 summarizes Borexino’s physics goals, its design, detection principle, and requirements. The unprecedented low background requirements of the detector are emphasized. The CTF test facility is briefly described.

The stringent cleanliness, radioactivity, and mechanical requirements of the nylon vessel system are summarized in chapter 3. A measurement of the relative densities of the scintillator and buffer solutions is presented. A thorough description of the radon contamination problem during vessel assembly in the clean room is given.

The following two chapters are dedicated to the description of an original vacuum swing adsorption radon filter. Chapter 4 reports on the results obtained with a small-scale prototype, after providing an extensive overview of the basic operational principles. Results from tests of radon adsorption on activated charcoal, essential for designing the system, are also shown. Chapter 5 describes the full-scale radon filter and its performance. Conclusions on the radon contamination of the Borexino inner vessel are drawn. A discussion of the filter performance along with suggestions based upon our experience are given.

The vessel assembly process and leak checking are detailed in chapter 6 with the aid of sketches and pictures. The original assembly technique of the light sources on the vessels’ surfaces is described in chapter 7, together with pictures that demonstrate their performance.

Chapter 8 presents data from the counting test facility (CTF) for Borexino. Results

from measurements of the contamination levels of trace impurities are shown. The analysis of the krypton residual levels were measured using statistical tools specifically developed for very low counting rates.

Every effort was made to write each chapter so that it could be read (and understood) individually. Cross-references to sections from different chapters are given for better comprehension of specific topics.

*“The life of the spirit may be fairly represented in diagram form as a large acute-angle triangle divided horizontally into equal parts with the narrowest segment uppermost. The lower the segment the greater it is in breadth, depth, and area.*

*The whole triangle is moving slowly, almost invisibly forwards and upwards. Where the apex was today the second segment is tomorrow; what today can be understood only by the apex and to the rest of the triangle is an uncomprehensible gibberish, forms tomorrow the true thought and feeling of the second segment.”*

W. Kandinski, 1910 [1]

# Contents

<b>Abstract</b>	<b>iii</b>
<b>Acknowledgements and Credits</b>	<b>v</b>
<b>Foreword</b>	<b>vii</b>
<b>1 The Physics of Low Energy Solar Neutrinos</b>	<b>1</b>
1.1 Neutrinos . . . . .	2
1.2 Neutrino oscillations . . . . .	4
1.2.1 Vacuum oscillations . . . . .	5
1.2.2 Matter-enhanced oscillations . . . . .	6
1.3 Solar neutrinos . . . . .	8
1.3.1 The Standard Solar Model . . . . .	8
1.3.2 Solar Neutrino Experiments . . . . .	10
1.4 A 30-year-long pursuit . . . . .	16
1.5 What next? . . . . .	23
<b>2 The Borexino Detector and its Counting Test Facility</b>	<b>26</b>
2.1 Detection mechanism and physics potential . . . . .	27
2.1.1 Solar neutrinos . . . . .	27
2.1.2 Antineutrinos . . . . .	31
2.1.3 Neutrino physics with sources . . . . .	33
2.2 Design of the Borexino detector . . . . .	33

2.3	Radioactivity requirements and background rejection . . . . .	40
2.4	The Counting Test Facility (CTF) . . . . .	43
<b>3</b>	<b>The Borexino Nylon Vessels</b>	<b>47</b>
3.1	Why nylon for the scintillator containment vessel? . . . . .	48
3.2	Design and specifications of the nylon vessel system . . . . .	50
3.2.1	Film strength and handling . . . . .	50
3.2.2	Cleanliness and radioactivity . . . . .	51
3.2.3	The mechanical support structure . . . . .	54
3.2.4	Leak tightness requirements . . . . .	55
3.2.5	The hold-down ropes . . . . .	56
3.2.6	Monitoring instrumentation . . . . .	57
3.2.7	The CTF inner vessel . . . . .	59
3.3	Scintillator solution density . . . . .	59
3.3.1	Experimental apparatus and procedure . . . . .	60
3.3.2	Measurement and results . . . . .	60
3.4	Radon contamination and requirements for the nylon vessels . . . . .	65
3.5	The Princeton clean room . . . . .	69
3.5.1	Clean room specifications . . . . .	73
3.5.2	The clean room water supply . . . . .	74
<b>4</b>	<b>A Prototype Radon Filter for Air</b>	<b>78</b>
4.1	Air filtering technique . . . . .	79
4.1.1	Adsorption principles . . . . .	82
4.1.2	Adsorption constant . . . . .	83
4.1.3	Dynamic adsorption . . . . .	84
4.1.4	Pressure Swing Adsorption (PSA) . . . . .	86
4.1.5	Early attempts . . . . .	88
4.1.6	Vacuum Swing Adsorption (VSA) . . . . .	89
4.2	The chromatographic plate model . . . . .	90

4.2.1	Special cases . . . . .	92
4.2.2	PSA system modeling . . . . .	93
4.3	Single column tests . . . . .	95
4.3.1	Charcoal selection . . . . .	95
4.3.2	Experimental setup . . . . .	95
4.3.3	Measurement procedure . . . . .	98
4.3.4	Measurements and results . . . . .	100
4.4	Nitrogen adsorption . . . . .	103
4.5	The VSA prototype . . . . .	107
4.5.1	Experimental setup . . . . .	107
4.5.2	The VSA cycle . . . . .	110
4.5.3	Measurements and results . . . . .	112
4.5.4	Comments on the prototype VSA results . . . . .	119
4.5.5	Implications for the full-scale VSA . . . . .	120
<b>5</b>	<b>The Full-Scale Radon Filter</b>	<b>123</b>
5.1	Radon mitigation requirements . . . . .	123
5.2	Scale-up parameters and requirements . . . . .	124
5.3	Experimental setup . . . . .	127
5.3.1	Cost of the VSA filter . . . . .	135
5.3.2	The filter cycle . . . . .	135
5.4	Preliminary tests . . . . .	138
5.5	Stand-alone radon tests . . . . .	143
5.6	Charcoal radioactivity and radon emanation . . . . .	144
5.7	Performance and results . . . . .	144
5.8	Comments on the radon levels achieved in the clean room . . . . .	150
5.8.1	Implications for vessels exposure . . . . .	151
5.9	Comments on the VSA filter performance . . . . .	152
5.10	Ideas for VSA improvement . . . . .	153

<b>6</b>	<b>Aspects of Vessel Assembly</b>	<b>156</b>
6.1	Preliminary operations . . . . .	157
6.2	Chronology and details of vessel construction . . . . .	158
6.3	End region design . . . . .	169
6.4	Vessel leak checking . . . . .	174
6.4.1	Leak checking procedure . . . . .	177
6.4.2	Leak checking results . . . . .	180
6.5	Inner Vessel contamination from air exposure and handling . . . . .	182
<b>7</b>	<b>Light Sources on the Nylon Vessels' Surfaces</b>	<b>184</b>
7.1	The Borexino CCD cameras . . . . .	185
7.2	The light diffusers . . . . .	186
7.2.1	The Teflon diffusers . . . . .	188
7.3	Light sources for scintillator stability monitoring . . . . .	192
7.4	Placing the light sources on the vessels . . . . .	195
7.5	Radiopurity screening . . . . .	201
7.6	External connection to LEDs and lasers . . . . .	201
<b>8</b>	<b>Results from CTF3</b>	<b>204</b>
8.1	CTF3 operations . . . . .	204
8.2	$^{14}\text{C}$ contamination of the scintillator . . . . .	205
8.3	Detector monitoring using radon . . . . .	208
8.3.1	$^{214}\text{Bi}$ - $^{214}\text{Po}$ coincidence sequence . . . . .	211
8.3.2	$^{214}\text{Bi}$ - $^{214}\text{Po}$ event selection . . . . .	211
8.4	Radium (Uranium) contamination . . . . .	215
8.5	Krypton contamination . . . . .	218
8.5.1	$^{85}\text{Kr}$ decay channels . . . . .	218
8.5.2	$^{85}\text{Kr}$ event selection . . . . .	219
8.5.3	$^{85}\text{Kr}$ analysis method . . . . .	222
8.5.4	Results . . . . .	224

8.5.5	Possible krypton contamination paths . . . . .	226
8.5.6	Spurious krypton activity from surface contamination . . . . .	232
	<b>Bibliography</b>	<b>235</b>
	<b>Afterword</b>	<b>253</b>

# The Physics of Low Energy Solar Neutrinos

*“Today neutrinos have a larger and larger place in the study of elementary particles and astrophysical phenomena; they might become the most important elementary particles in physics.”*

(G. Gamow, 1966 [2])

The last few years have witnessed enormous successes in the field of experimental neutrino physics. In 1998, the results from the Japan-based experiment Super-Kamiokande gave the first uncontroversial evidence that neutrinos oscillate [3]. In other words, they transform from one type to another, changing their so-called *leptonic flavour*. The neutrinos under investigation were those commonly known as *atmospheric neutrinos*, produced as decay products of particles generated in the upper layers of the atmosphere by high energy cosmic rays (energetic charged particles coming from all directions in space). Just a few years later, the results from the Sudbury Neutrino Observatory in Canada provided beautiful experimental evidence of neutrino oscillations using *solar neutrinos* [4, 5] emitted in the nuclear fusion reactions by which the Sun burns.

Neutrinos were widely believed to be massless since postulated by Pauli in 1930 [6]; they were not believed to oscillate since they must have mass in order for the phenomenon to occur. From the particle physics point of view neutrino oscillations could naïvely be

accommodated simply by adding a few more parameters (namely the masses of the three known types of neutrinos) to the Standard Model (SM), the current successful theory of particles and interactions. Nonetheless, the details of neutrino masses and interactions have a very significant impact on the development of both grand unified theories of fundamental interactions and cosmological models of the origin of the universe: only theories that are able to precisely account for them will survive. It is fair to say that particle physics and cosmology have never been so closely linked.

Solar (and atmospheric) neutrino physics is a good example of how particle physics can still be on the cutting edge even when accelerators seem to be reaching technological and budgetary limits. The newly recognized subfield of *astroparticle physics* uses celestial bodies as accelerators. They can be near and familiar like the Sun, or far away and little known such as Active Galactic Nuclei and Gamma Ray Bursts. The objects under study range from neutrinos,  $\gamma$ -rays and other known particles to more exotic ones, such as those that could make up the sought-for *dark matter*. Detector technologies developed in the past 70 years for physics at accelerators are now used to build particle “telescopes” placed on satellites, in the ocean, in the desert, at the South Pole, or deep underground.

While the potential for discovery in this field is very high, there is no control on the initial state of the phenomena being observed as there is for accelerator-generated events. The increased understanding of fundamental particles and interactions has to go hand in hand with that of the objects and phenomena which generate them. In this respect, the study of solar neutrinos has been an alternate succession of advances in the comprehension of neutrinos and of the Sun. Almost four decades after Ray Davis’ pioneering experiment in 1967 [7], solar neutrinos provide now a unique tool with which to perform precision neutrino and solar physics.

## 1.1 Neutrinos

Introduced to explain the missing energy and the continuous electron energy spectrum in  $\beta$ -decays, neutrinos (“little neutral ones”, as Enrico Fermi dubbed them in 1934 [8]) were

first directly detected more than two decades later in 1953. Reines and Cowan's organic liquid scintillator apparatus [9] detected electron antineutrinos from a nuclear reactor via the inverse  $\beta$ -decay reaction

$$p + \bar{\nu}_e \rightarrow n + e^+ \quad (1.1)$$

and the subsequent detection of positron annihilation and delayed neutron capture. It is interesting to note that the clear signature of this reaction made it possible to move away from the initial idea of using a nuclear explosion as neutrino source and use the weaker neutrino flux from a reactor instead. A very nice review of this and related experiments is given in Reines' Nobel lecture [10].

In the Standard Model there are three types of neutrinos, associated with the three charged leptons  $e, \mu$ , and  $\tau$ , with which they form weak doublets. Massless and chargeless (according to the SM), neutrinos are subject to the weak force alone and the model allows for the existence of left-handed ones only. For this reason, they are in principle the ideal tool to study the weak force. In practice though, they present a big challenge for experimentalists because their cross section with matter is very small. Their interactions are mediated by the carriers of the weak interaction, the massive bosons  $Z_0$  and  $W^\pm$ . It is only at interaction energies comparable to these bosons' masses (80-90 GeV) that the neutrino cross section becomes comparable to that of electrons.

In order to appreciate how invisible neutrinos are and how hard it is to detect them at low energy, it's worth estimating the neutrino-electron elastic scattering cross section  $\sigma_{\nu e}$ , where the reaction is schematically shown in fig. 1.2. The cross section has dimensions  $(\text{energy})^{-2}$  (natural units) and is proportional to Fermi's constant squared,  $G_F^2$  (dimensions of  $(\text{energy})^{-4}$ ). The only invariant quantity with dimensions  $(\text{energy})^2$  is the center of mass energy squared  $s = (k + p)^2$  ( $k$  and  $p$  are the momenta of the incoming particles) which can be written as  $s = 2m_e E_\nu + m_e^2$  in the rest frame of the electron and with a massless neutrino. For a 1 MeV neutrino,

$$\sigma_{\nu e} \sim G_F^2 s \sim 1.7 \cdot 10^{-22} \text{ MeV}^{-2} \longrightarrow 7 \cdot 10^{-44} \text{ cm}^2 \quad (1.2)$$

Otherwise stated, its mean path in water would be approximately 100 light years!

## 1.2 Neutrino oscillations

Neutrino oscillations are the first sign of physics beyond the Standard Model (SM). Since its formulation in the 70's, the SM has been thoroughly tested. Not only had it never been contradicted, measurements have often agreed with the theoretical expectations with unprecedented accuracy. All the predicted fundamental particles have been detected [11] with the exception of the Higgs boson, whose discovery is the main objective of the Large Hadron Collider (LHC) under construction at CERN in Geneva.

In 1958 Bruno Pontecorvo discussed possible neutrino-antineutrino oscillations [12]. Maki (1962) [13] and Pontecorvo (1967) [14] proposed oscillations between weak (flavour) eigenstates: neutrino oscillations can be thought of as the analog for leptons of quark mixing. If at least one neutrino has mass, there is no fundamental reason why energy (mass) eigenstates should coincide with the weak ones and mixing could occur in the the lepton sector as well (if all the neutrinos are massless, the mass eigenstates would be degenerate and the weak eigenstates alone would define the three neutrino types). Without loss of generality it is possible to think of lepton mixing as being carried out entirely by the neutrinos.

In general, neutrinos produced as weak eigenstates are linear combinations of energy eigenstates, thereby evolving differently while they propagate in free space. They can then be detected as neutrinos of a different flavour (weak eigenstate) away from the source. Oscillations could be enhanced when neutrinos travel through a region with a non-zero electron density (such as regular matter) according to the so-called MSW effect [15, 16]. In matter, electron neutrinos will have a larger forward scattering amplitude. In this case, the phase of the time-evolved neutrino wave function contains a flavour dependent index of refraction, as explained below. Alberico and Bilenky give a clear historic overview of neutrino oscillations [17].

### 1.2.1 Vacuum oscillations

For three flavour mixing, every weak eigenstate  $|\nu_\lambda\rangle$  ( $\lambda = e, \mu, \tau$ ) is a superposition of energy eigenstates,  $|\nu_\lambda\rangle = \sum_j \langle \nu_j | \nu_\lambda \rangle |\nu_j\rangle$  ( $j = 1, 2, 3$ ). The simplest possible oscillation pattern among neutrinos is one which involves mixing of two lepton flavours. In this case the parameters of the problem are the mixing angle  $\theta$  and the difference of the square of neutrino masses  $\delta m^2$ . Defining the two neutrino weak flavours as  $|\nu_e\rangle$  and  $|\nu_x\rangle$  and the two mass states as  $|\nu_1\rangle$  and  $|\nu_2\rangle$ , their mixing is expressed by

$$\begin{cases} |\nu_e\rangle = \cos\theta |\nu_1\rangle + \sin\theta |\nu_2\rangle \\ |\nu_x\rangle = -\sin\theta |\nu_1\rangle + \cos\theta |\nu_2\rangle \end{cases} \quad (1.3)$$

An electron neutrino  $|\nu_e\rangle$  produced at time  $t = 0$  with momentum  $p$  will propagate as the superposition of the two mass (energy) eigenstates,

$$|\nu_e(\vec{x}, t)\rangle = \cos\theta |\nu_1\rangle e^{-i(E_1 t - \vec{p} \cdot \vec{x})} + \sin\theta |\nu_2\rangle e^{-i(E_2 t - \vec{p} \cdot \vec{x})} \quad (1.4)$$

Under the assumption that their masses are small, neutrinos can be assumed relativistic and the energy of the mass states can then be rewritten as  $E_j = \sqrt{\vec{p}^2 + m_j^2} \simeq p + \frac{m_j^2}{2p}$  ( $|\vec{p}| \equiv p$ ) for mass states with momentum  $p \simeq E$  ( $\hbar = c = 1$ ). Defining  $\delta m^2 \equiv m_1^2 - m_2^2$  and using the above approximation, eq. 1.4 becomes

$$|\nu_e(\vec{x}, t)\rangle = \left[ \cos\theta |\nu_1\rangle + \sin\theta |\nu_2\rangle e^{-i\delta m^2 t / 2E} \right] e^{-i(E_1 t - \vec{p} \cdot \vec{x})} \quad (1.5)$$

The probabilities to observe a transformed or an electron neutrino at time  $t$  are given by

$$\begin{cases} P(\nu_e \rightarrow \nu_x; E, t) = |\langle \nu_x | \nu_e(t) \rangle|^2 = \sin^2 2\theta \sin^2 \left( \frac{\delta m^2 t}{4E} \right) \\ P(\nu_e \rightarrow \nu_e; E, t) = |\langle \nu_e | \nu_e(t) \rangle|^2 = 1 - \sin^2 2\theta \sin^2 \left( \frac{\delta m^2 t}{4E} \right) \end{cases} \quad (1.6)$$

In the relativistic limit,  $t \simeq |\vec{x}|$  and an oscillation length can be defined as

$$\Lambda_v = \frac{4\pi E}{\delta m^2} = \frac{E [\text{GeV}]}{1.27 \delta m^2 [\text{eV}^2]} \text{ km} \quad (1.7)$$

By varying the energy of the neutrinos and the distance  $L$  of the detector (so that  $L \equiv \lambda_{osc}$ ), the mass-squared difference parameter space can be tested. Figure 1.1 shows the value of  $L/E$  for neutrino experiments around the world. An interesting quantum-mechanical treatment of neutrino oscillations that supports the derivation above is found in [18].

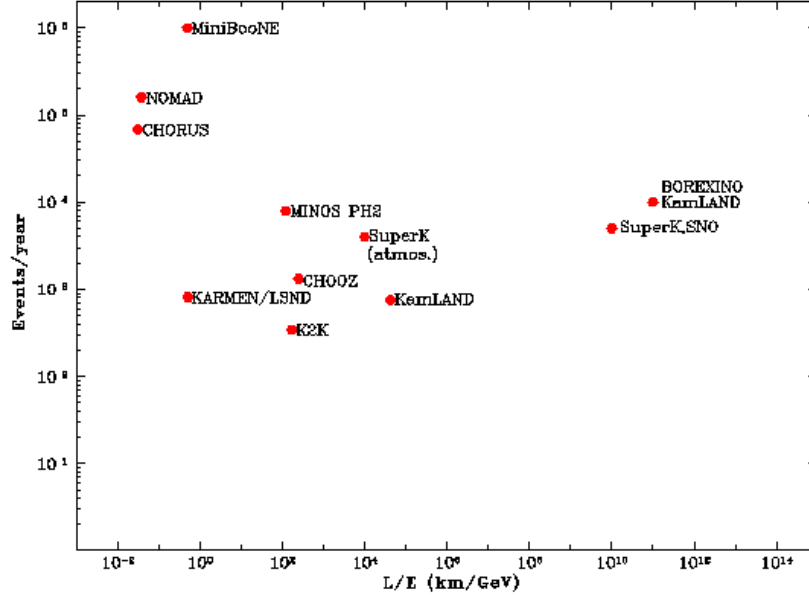


Figure 1.1: The ratio of the source-to-detector distance and the neutrino energy ( $L/E$ ) and neutrino event rate for many experiments around the world. Solar neutrino experiments, on the far right, combine very long baselines with relatively low neutrino energies and can probe regions with very small  $\delta m^2$ .

### 1.2.2 Matter-enhanced oscillations

The interaction of  $\nu_e$ 's with matter (non-zero electron density  $N_e$ ), is stronger than that of  $\nu_\mu$ 's or  $\nu_\tau$ 's. All neutrinos scatter off electrons through neutral current weak interactions, but electron neutrinos also interact via charged current exchanges (see fig. 1.2).

An effective way to describe the phenomenon is to introduce in the neutrino propagated wave function an index of refraction  $n_\lambda$  ( $\lambda = e, \mu, \tau$ ), which depends on the electron density  $N_e$  and the forward scattering amplitude  $f_\lambda(0)$  as follows:

$$\begin{cases} |\nu_\lambda\rangle = \sum_j \langle \nu_j | \nu_\lambda \rangle |\nu_j\rangle e^{E_j - n_\lambda \vec{p} \cdot \vec{x}} & (j = 1, 2, 3) \\ n_\lambda = 1 + \frac{2\pi N_e}{p^2} f_\lambda(0) \end{cases} \quad (1.8)$$

The contribution to  $n_\lambda$  from neutral current components is diagonal (i.e. the same for

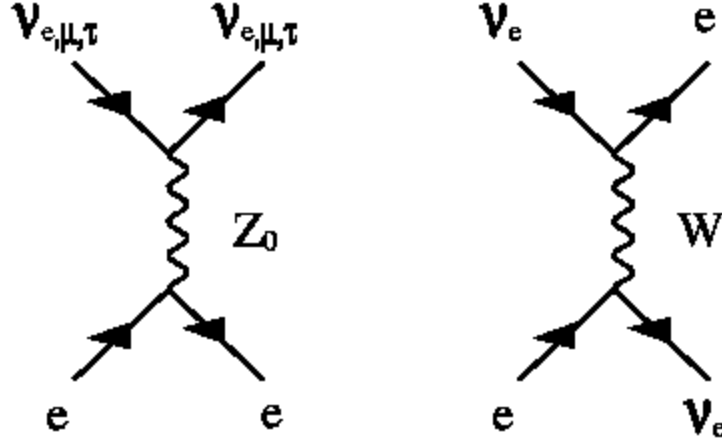


Figure 1.2: First order Feynman diagrams for  $\nu - e$  elastic scattering. All neutrino flavours interact via neutral current exchange, while only  $\nu_e$  undergoes charged current exchange reactions. For 0.5 MeV neutrinos, the cross section for  $\nu_e$  elastic scattering off electrons is  $\sim 4.5$  times bigger than for  $\nu_{\mu,\tau}$ .

all neutrino flavours) and is just a global phase factor. What's important is the non-diagonal contribution (in the energy eigenstate basis) of the charged current interaction of the electron neutrino. In other words, the energy eigenstates propagating in matter are different from those propagating in vacuum and they are very strongly dependent on  $N_e$ . The basic quantity of the problem is the phase difference  $\Delta\phi$  that appears in the propagation of  $\nu_e$  only, that depends on the different forward scattering amplitude [19]

$$\begin{cases} \Delta f(0) \equiv f_e(0) - f_{\mu,\tau}(0) = -\frac{G_F p}{\sqrt{2}\pi} \\ |\nu_e\rangle \propto e^{\Delta\phi} = e^{-i\sqrt{2}N_e G_F x} \end{cases} \quad (1.9)$$

The periodicity of the the phase  $\Delta\phi$  defines the  $\nu - e$  interaction length in matter as

$$\Lambda_{e\nu} = \frac{2\pi}{\sqrt{2}N_e G_F} \sim \frac{1.7 \times 10^7 [\text{m}]}{\rho [\text{g}/\text{m}^3] \langle Z/A \rangle} \quad (1.10)$$

This length only depends on the electron density  $N_e$  and corresponds to roughly 200 km in the Sun's core and to  $\sim 10^4$  km in the Earth. A mixing angle in matter  $\theta_m$ , also affected by the non-diagonal contribution, can be defined as the angle associated with the rotation

matrix that diagonalizes the hamiltonian and is related to the mixing angle in vacuum  $\theta$  by the following relation:

$$\sin^2 2\theta_m = \frac{\sin^2 2\theta}{(\cos 2\theta - \Lambda_\nu/\Lambda_{e\nu})^2 + \sin^2 2\theta} \quad (1.11)$$

It is worthwhile pointing out that because of the resonant nature of equation (1.11), if  $\frac{\Lambda_\nu}{\Lambda_{e\nu}} = \cos 2\theta$  there is maximal mixing ( $\sin^2 2\theta_m = 1$ ) for any non-zero mixing angle in vacuum. In practical terms, even if  $\theta$  is very small, neutrinos which cross a dense enough region can have a very high probability of converting into other flavours. On the other hand, non-zero mixing in vacuum is needed for oscillations in matter to occur. The resonant condition depends on the neutrino mixing parameters according to the relation

$$\delta m^2 \cos 2\theta = 2\sqrt{2} G_F N_e E_\nu \quad (1.12)$$

where  $E_\nu$  is the energy of the neutrino.

### 1.3 Solar neutrinos

We owe the idea that the Sun's energy is produced by nuclear fusion reactions to Hans Bethe [20], who in 1939 laid out the foundations of the theory of how stars burn. In his work he points out that the basic reaction that occurs in the Sun's core is the combination of four protons and two electrons to produce an  $\alpha$  particle and excess energy. In detail this can be written as



Worthy of notice is the emission of two neutrinos as a product of the reaction. An elaborate model of the Sun has been developed since, known as the Standard Solar Model (SSM). Nice (and personal) overviews of the subject have been given on more than one occasion by John Bahcall [21].

#### 1.3.1 The Standard Solar Model

The basic, although simple assumption of the model is that gravitational contraction and radiative pressure from the thermonuclear reaction exactly counterbalance each other in

Reaction	Termination (%)	Q [MeV]	$E_{\nu_e}$ [MeV]	$\langle q_{\nu_e} \rangle$ [MeV]
1a) $p + p \rightarrow {}^2\text{H} + e^+ + \nu_e$	(pp) 99.77	1.442	$\leq 0.420$	0.265
or				
1b) $p + e^- + p \rightarrow {}^2\text{H} + \nu_e$	(pep) 0.23	1.442	1.442	1.442
2) ${}^2\text{H} + p \rightarrow {}^3\text{He} + \gamma$	100	5.494		
3a) ${}^3\text{He} + {}^3\text{He} \rightarrow \alpha + 2p$	84.92	12.860		
or				
3b) ${}^3\text{He} + {}^4\text{He} \rightarrow {}^7\text{Be} + \gamma$	15.08	1.586		
${}^7\text{Be} + e^- \rightarrow {}^7\text{Li} + \nu_e$	( ${}^7\text{Be}$ ) 15.07	0.862 (90%)	0.862	0.862
		0.383 (10%)	0.383	0.383
${}^7\text{Li} + p \rightarrow 2\alpha$	15.07	17.347		
or				
${}^7\text{Be} + p \rightarrow {}^8\text{B} + \gamma$	0.01	0.137		
${}^8\text{B} \rightarrow {}^8\text{Be}^* + e^+ + \nu_e$	( ${}^8\text{B}$ ) 0.01	17.980	$\leq 15$	6.71
or				
3c) ${}^3\text{He} + p \rightarrow {}^4\text{He} + e^+ + \nu_e$	(hep) $10^{-5}$	19.795	$\leq 18.8$	9.27

Table 1.1: The  $pp$  thermonuclear cycle which produces in excess of 98% of the Sun's energy, as predicted by the SSM. The third column lists the percentage of terminations that include the reaction in question. There are five  $\nu$ -emitting reactions in this cycle: the names of neutrinos from each source are listed in the second column.

the Sun. The boundary conditions are the luminosity, radius, age, and mass of the Sun. Input is also provided by the cross sections and energies of the nuclear reactions involved, the opacity of the Sun, and its isotopic abundances. The evolution equation then outputs (among other quantities) the energy spectrum and fluxes of the emitted neutrinos. The most recent revision of such a model is the one suggested by Bahcall, Basu and Pinsonneault in 2000 (BP00, [22]).

The details of the nuclear reactions believed to power the Sun are summarized in tables 1.1 and 1.2. They describe two cycles by which the SSM allows the reaction (1.13) to occur. The first one is known as the  $pp$  chain while the second is the CNO cycle, where carbon, nitrogen and oxygen are catalysts of the fusion processes. It is believed that only

Reaction		Q [MeV]	$E_{\nu_e}$ [MeV]	$\langle q_{\nu_e} \rangle$ [MeV]
$^{12}\text{C} + p \rightarrow ^{13}\text{N} + \gamma$		1.943		
$^{13}\text{N} \rightarrow ^{13}\text{C} + e^+ + \nu_e$	( $^{13}\text{N}$ )	2.221	$\leq 1.199$	0.7067
$^{13}\text{C} + p \rightarrow ^{14}\text{N} + \gamma$		7.551		
$^{14}\text{N} + p \rightarrow ^{15}\text{O} + \gamma$		7.297		
$^{15}\text{O} \rightarrow ^{15}\text{N} + e^+ + \nu_e$	( $^{15}\text{O}$ )	2.754	$\leq 1.732$	0.9965
$^{15}\text{N} + p \rightarrow ^{12}\text{C} + \alpha$		4.966		
or				
$^{15}\text{N} + p \rightarrow ^{16}\text{O} + \gamma$		12.128		
$^{16}\text{O} + p \rightarrow ^{17}\text{F} + \gamma$		0.600		
$^{17}\text{F} \rightarrow ^{17}\text{O} + e^+ + \nu_e$	( $^{17}\text{F}$ )	2.762	$\leq 1.740$	0.9994
$^{17}\text{O} + p \rightarrow ^{14}\text{N} + \alpha$				

Table 1.2: The CNO cycle. The SSM predicts that only 1.5% of the energy comes from this source. There are three  $\nu$ -emitting reactions in this cycle.

1.5% of the energy comes from the CNO cycle, although experimentally only an upper limit of about 7% can be set [23].

Most of the energy produced by the Sun is released as photons, while approximately 3% is believed to be carried out by neutrinos, all with energies  $< 20$  MeV [22] (see table 1.3 and fig. 1.3). Neutrinos, given their tiny cross section, emerge from the Sun mostly unperturbed and give us a “snapshot” of the Sun’s interior. Photons, on the other hand, interact very strongly with solar matter and are essentially in equilibrium with Sun’s surface once we are able to detect them. Neutrinos are hence one of the best ways to study what goes on in the star’s core.

### 1.3.2 Solar Neutrino Experiments

To date, only six experiments have detected solar neutrinos. This section will briefly review these experiments and try to give a taste of how the field has developed and questions that have risen over time.

With the goal of directly detecting solar neutrinos and thus proving that the Sun burns

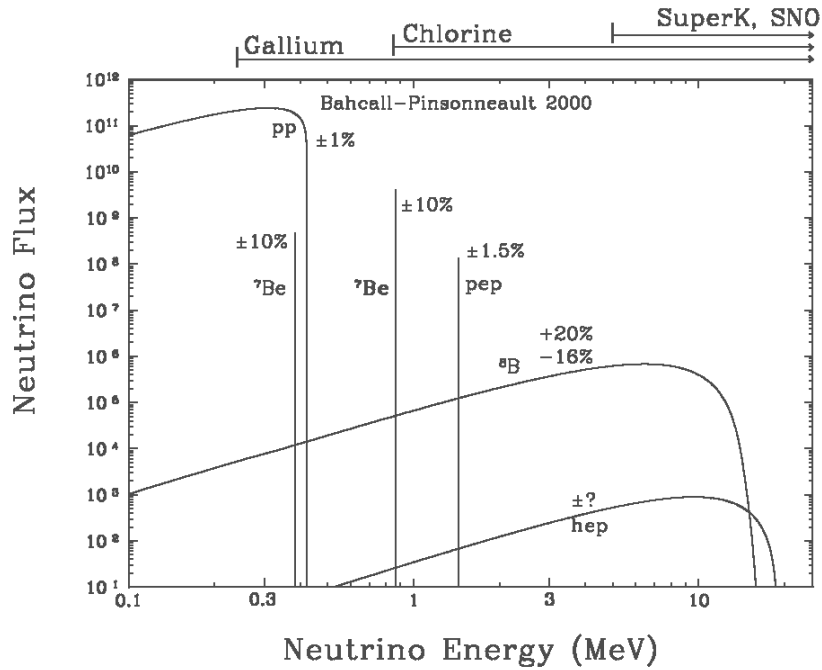


Figure 1.3: A pictorial view of the solar neutrino fluxes predicted by the SSM (BP2000, [22]). The plot shows the neutrinos from the  $pp$  chain only 1.1.

by thermonuclear reactions, in 1967 a 390 m<sup>3</sup> tank full of liquid tetrachloroethylene (C<sub>2</sub>Cl<sub>4</sub>) was placed underground in the Homestake gold mine in South Dakota to look for the reaction [7]



where the net reaction is  $n + \nu_e \rightarrow p + e^-$ . Until recently, <sup>37</sup>Ar atoms were extracted every couple of months and were counted with proportional counters which look for the 2-3 keV Auger electrons that follow the conversion of <sup>37</sup>Ar back into <sup>37</sup>Cl by electron capture (it is interesting to notice how the detected reaction is in fact the inverse of the reaction under study!). This radiochemical detection technique is sensitive only to  $\nu_e$  with energy above the 814 keV threshold of the charged current reaction (1.14). The experiment successfully detected solar neutrinos (mainly <sup>7</sup>Be, <sup>8</sup>B and CNO ones, see tables 1.1 and 1.2); the average

Source	Flux [ $10^{10} \text{ cm}^{-2} \text{ s}^{-1}$ ]	Cl [SNU]	Ga [SNU]	Li [SNU]
<i>pp</i>	5.95	0.0	69.6	0.0
<i>pep</i>	$1.40 \times 10^{-2}$	0.22	2.8	9.2
<i>hep</i>	$9.3 \times 10^{-7}$	0.04	0.1	0.1
${}^7\text{Be}$	$4.77 \times 10^{-1}$	1.15	34.2	9.1
${}^8\text{B}$	$5.05 \times 10^{-4}$	5.76	12.1	19.7
${}^{13}\text{N}$	$5.48 \times 10^{-2}$	0.09	3.4	2.3
${}^{15}\text{O}$	$4.80 \times 10^{-2}$	0.33	5.5	11.8
${}^{17}\text{F}$	$5.63 \times 10^{-2}$	0.0	0.1	0.1
Total		$7.6^{+1.3}_{-1.1}$	$129^{+8}_{-6}$	$52^{+7}_{-6}$

Table 1.3: Solar neutrino fluxes predicted by the SSM (BP2000) with corresponding predicted capture rates for the Chlorine (Cl), Gallium (Ga) and Lithium (Li) experiments [22]. One SNU is defined as  $10^{-36}$  captures per target atom per second.

neutrino capture rate after 25 years of data taking is [25]

$$R_{\text{Homestake}} = 2.56 \pm 0.16 \text{ (stat.)} \pm 0.16 \text{ (syst.) SNU} \quad (1.15)$$

where 1 SNU (Standard Neutrino Unit) is defined as  $10^{-36}$  captures per target atom per second (i.e. one argon atom every few days!). Solar neutrino fluxes predicted by the SSM are presented in table 1.3. According to this table, the Homestake result (a Chlorine experiment) is only one-third of the predicted value. This discrepancy was noted (with much bigger uncertainties) from the early days of the Homestake experiment and represented the so-called *solar neutrino problem* [26].

In 1983 the Kamioka Nucleon Decay Experiment (Kamiokande) was built in a mine in Japan to look for proton instability. It was soon clear that it made a wonderful neutrino detector (the acronym could also be interpreted as Kamioka Neutrino Detector!). With one kton of ultra pure water (fiducial volume) in a 16 m diameter cylindrical tank instrumented with approximately 11000 photomultiplier tubes, the experiment could detect Čerenkov radiation from the electrons elastically scattered off of solar neutrinos at the higher end of

the energy spectrum, via the reaction [27]

$$\nu_{e,\mu,\tau} + e^- \rightarrow \nu_{e,\mu,\tau} + e^- \quad (1.16)$$

With this technique all neutrino flavours are detected (with different sensitivities for charged and neutral current reactions respectively, see fig. 1.2) on an event-by-event basis with directional information (crucial for studying atmospheric neutrinos). Short time dependencies of the neutrino flux and its energy spectrum can be measured (only integrated above-threshold information was accessible to the chlorine experiment). In almost a decade of data taking (1985-1994), Kamiokande observed a solar neutrino flux [28]

$$\Phi_{\text{Kamiokande}} = 2.80 \pm 0.16 \text{ (stat.)} \pm 0.16 \text{ (syst.)} \times 10^6 \text{ cm}^{-2} \text{ s}^{-1} \quad (1.17)$$

above a 7.5 MeV threshold (only  $^8\text{B}$  and *hep* neutrinos). This value, approximately half that predicted by the SSM, not only confirmed the solar neutrino deficit observed by the Homestake experiment, but added a second element to the puzzle. The capture rate observed by the chlorine experiment (which also detects  $^7\text{Be}$  and CNO neutrinos) didn't account for all the neutrinos observed by Kamiokande. This neutrino deficit, completely independent of the solar model, became known as the *second solar neutrino problem* [26] and has been a strong argument for non-standard properties of neutrinos. A new and improved version of the detector, Super-Kamiokande or SuperK, was built in 1996. In 4 years and with a neutrino threshold lowered to 5 MeV it measured a  $^8\text{B}$  neutrino flux equal to [29]

$$\Phi_{\text{SuperK}} = 2.32 \pm 0.03 \text{ (stat.)} {}^{+0.08}_{-0.07} \text{ (syst.)} \times 10^6 \text{ cm}^{-2} \text{ s}^{-1} \quad (1.18)$$

and is 45% of the BP2000 expectation. Incredibly massive (22.5 ktons of ultra pure water in a 39 m diameter cylindrical tank and  $\sim 11,000$  photomultipliers), it successfully increased the statistics and the precision of solar neutrino observations (more than 100 events/day, 20-36 degrees angular resolution). Measurements of the solar neutrino energy spectrum and of the day-to-night neutrino scattering event rate asymmetry were performed with unprecedented precision. SuperK also made ground breaking discoveries measuring atmospheric neutrino fluxes [3].

Two other radiochemical experiments, the Soviet American Gallium Experiment (SAGE) and the Gallium Experiment (GALLEX), had gone online in the meantime (1990 in the Caucasus mountains in Russia and 1991 at the Gran Sasso underground laboratory in Italy, respectively). Each used a gallium target (50 tons of solid gallium for SAGE, 30 tons of gallium in liquid  $\text{GaCl}_3$  solution for GALLEX) to look for solar neutrino interactions with the reaction



where the net reaction is  $n + \nu_e \rightarrow p + e^-$  as for the chlorine experiment. The radioactive Ge atoms were then counted in very low background proportional counters by looking at the electron capture process of  ${}^{71}\text{Ge}$  into  ${}^{71}\text{Ga}$ . The unique characteristic of these experiments is that they can detect solar neutrinos down to 233 keV: they are the first and only ones to have detected  $pp$  neutrinos to date, which make up most of the solar neutrino flux (see table 1.3). GALLEX underwent an upgrade in 1998 and is currently running as the Gallium Neutrino Observatory (GNO). The measured capture rates after approximately 10 years of running are [30, 31]

$$\begin{cases} R_{GALLEX+GNO} = 70.8 \pm 4.5 \text{ (stat.)} \pm 3.0 \text{ (syst.) SNU} \\ R_{SAGE} = 70.8 \begin{smallmatrix} +5.3 \\ -5.2 \end{smallmatrix} \text{ (stat.)} \begin{smallmatrix} +3.7 \\ -3.2 \end{smallmatrix} \text{ (syst.) SNU} \end{cases} \quad (1.20)$$

significantly below the BP2000 predictions (see table 1.3). It is notable that the  $pp$  neutrino flux predicted by the SSM alone would account for the capture rate observed in the gallium detectors. No room seems to be left for the  ${}^7\text{Be}$  neutrinos. Hence, the *third solar neutrino problem*.

In 1999 the Sudbury Neutrino Observatory (SNO) started taking data, deep underground in a nickel mine in Sudbury, Canada. SNO has an active 1 kton heavy water ( $\text{D}_2\text{O}$ ) target contained in a 12 m diameter spherical acrylic vessel. It detects the following neutrino-induced interactions:

$$\begin{cases} \nu_e + d \rightarrow p + p + e^- & \text{(CC)} \\ \nu_{e,\mu,\tau} + d \rightarrow p + n + \nu_{e,\mu,\tau} & \text{(NC)} \\ \nu_{e,\mu,\tau} + e^- \rightarrow \nu_{e,\mu,\tau} + e^- & \text{(ES)} \end{cases} \quad (1.21)$$

The neutral current reaction's threshold is 2.2 MeV, and is tagged by detecting  $\gamma$  rays from neutron capture on deuterium. Čerenkov light generated by electrons and  $\gamma$  rays is detected by almost 9600 photomultiplier tubes. To enhance sensitivity to the neutral current reaction,  $\text{MgCl}_2$  (8.6 MeV  $\gamma$  rays follow neutron capture on this salt) has been added to the deuterium and data are currently being collected. The latest results from SNO, for neutrinos above 5 MeV are [5]

$$\begin{cases} \Phi_{SNO}^{CC} = 1.76 \pm 0.06 \text{ (stat.)} \pm 0.09 \text{ (syst.)} \times 10^6 \text{ cm}^{-2} \text{ s}^{-1} \\ \Phi_{SNO}^{NC} = 5.09 \begin{smallmatrix} +0.44 \\ -0.45 \end{smallmatrix} \text{ (stat.)} \begin{smallmatrix} +0.46 \\ -0.43 \end{smallmatrix} \text{ (syst.)} \times 10^6 \text{ cm}^{-2} \text{ s}^{-1} \\ \Phi_{SNO}^{ES} = 2.39 \begin{smallmatrix} +0.24 \\ -0.23 \end{smallmatrix} \text{ (stat.)} \pm 0.12 \text{ (syst.)} \times 10^6 \text{ cm}^{-2} \text{ s}^{-1} \end{cases} \quad (1.22)$$

The charged current result is a measurement of the  $\nu_e$  component of the  $^8\text{B}$  solar neutrino flux. The neutral current result is a measurement of the total  $^8\text{B}$  solar neutrino flux, independent of leptonic flavour (the cross section for deuterium disintegration is the same for all flavours). The electron scattering result is sensitive to all flavours, but with reduced sensitivity for  $\mu$  and  $\tau$  neutrinos. Electron-neutrino scattering can be used to measure the total solar neutrino flux, taking into account the difference in cross section for various neutrino types, but only if the flavour composition is known. Above 5 MeV, the cross section is  $\sim 6.5$  times smaller for  $\nu_{\mu,\tau}$  than for  $\nu_e$ .

It appears clear from (1.22) that only one third of the solar neutrino flux above 5 MeV has electronic flavour. Recall that in the case of no neutrino oscillations, the non-electronic neutrino flux from the Sun should be zero. The electron scattering result, in agreement with SuperK even if with poorer statistics, is also compatible with having approximately two thirds of the detected solar neutrino flux is made up of non-electronic, active neutrinos. The measured  $\nu_e$  and  $\nu_{\mu,\tau}$  components of the flux, assuming that the  $^8\text{B}$  neutrino spectrum is undistorted compared to the SSM prediction, are illustrated in fig. 1.4. SNO's total measured solar  $^8\text{B}$  neutrino flux is  $\Phi_{SNO}^{total} = 5.17_{-0.65}^{+0.67} \times 10^6 \text{ cm}^{-2} \text{ s}^{-1}$ , which agrees very well with the SSM prediction  $\Phi_{SSM} = 5.05_{-0.81}^{+1.01} \times 10^6 \text{ cm}^{-2} \text{ s}^{-1}$  (compare with table 1.3).

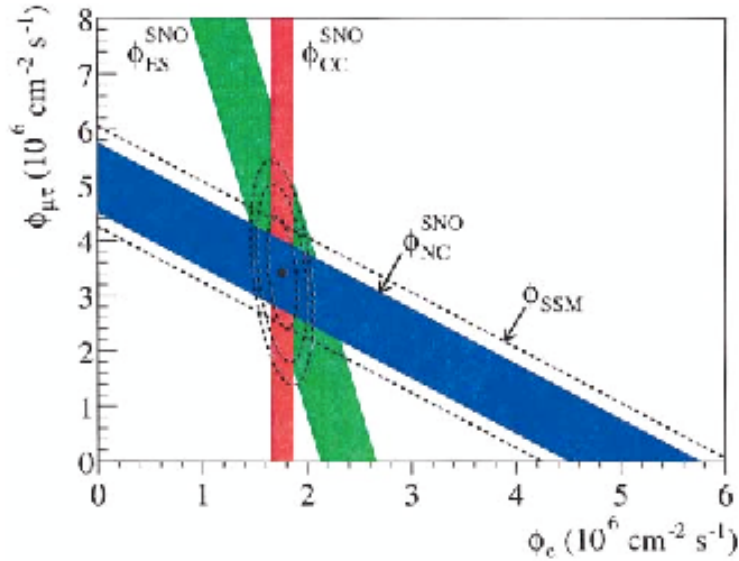


Figure 1.4: The solar  ${}^8\text{B}$   $\nu_e$  and  $\nu_{\mu,\tau}$  fluxes as measured by SNO, combined with results from SuperK [5]. The best fit results are  $\Phi_{SNO}^e = 1.76 \pm 0.05$  (stat.)  $\pm 0.09$  (syst.)  $\times 10^6 \text{ cm}^{-2} \text{ s}^{-1}$  and  $\Phi_{SNO}^{\mu,\tau} = 3.41 \pm 0.45$  (stat.)  $^{+0.48}_{-0.45}$  (syst.)  $\times 10^6 \text{ cm}^{-2} \text{ s}^{-1}$ . The results are compatible with conversion of  $\nu_e$  into other active neutrinos and agree very well with the prediction of the SSM of  $\Phi_{SSM} = 5.05^{+1.01}_{-0.81} \times 10^6 \text{ cm}^{-2} \text{ s}^{-1}$  [22].

## 1.4 A 30-year-long pursuit

SNO's milestone result gives evidence of neutrino flavour transformation without having to rely on any solar model-dependent assumptions. Systematic effects arising from comparing results of separate experiments are greatly reduced through measurement of various neutrino interaction channels within a single detector. Direct evidence of solar neutrino oscillations didn't come as a big surprise. Since the discovery of the solar neutrino problem, neutrino oscillations has been considered to be one of the most compelling solutions. This is supported by the fact that many experiments have explicitly mentioned the search for neutrino oscillations in their initial proposals (e.g. [32]).

Meanwhile, solar models have become more detailed and precise. They have had independent experimental confirmation, in particular from helioseismological studies that helped trim down uncertainties to the point where the inconsistencies between solar models and

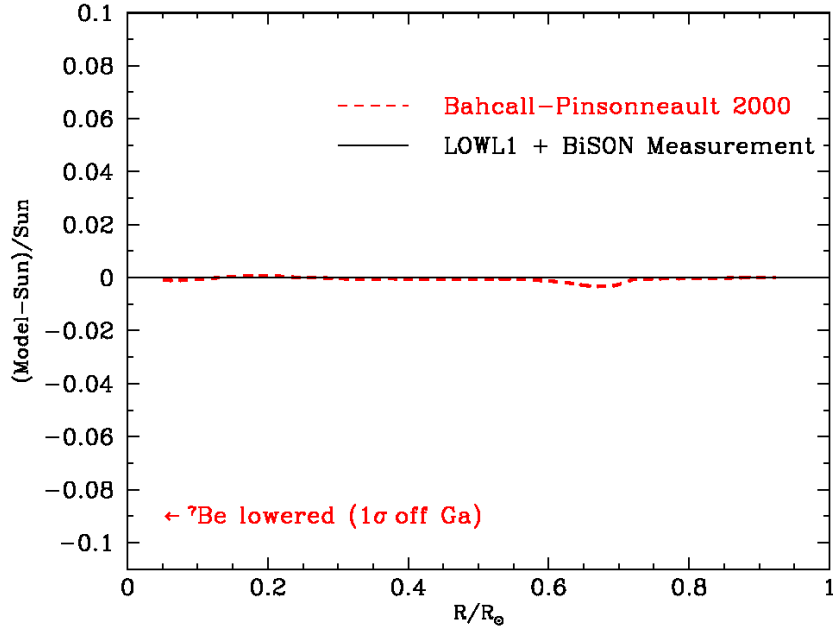


Figure 1.5: One of the most convincing tests of the validity of the SSM is the measurement of the sound speed as a function of distance from the Sun’s core. The agreement with the theoretical expectations is astonishingly good and seems to leave no room for an explanation of the *solar neutrino problem* that relies on poor understanding of the Sun [22].

solar neutrino experiments have become increasingly reduced. One such study is a comparison of the measured and calculated sound speeds in the Sun as a function of the distance from the center and is represented in fig. 1.5.

A graphical summary of the neutrino fluxes measured to date by all solar neutrino experiments against the SSM theoretical expectations is shown in fig. 1.6. Overall neutrino fluxes are not the only measured quantities. SuperK, for example, has performed an accurate analysis of the  $^8\text{B}$  solar neutrino energy spectrum. The measured spectral shape is, by the way, compatible with that predicted by BP2000 [29] (see fig. 1.7).

SuperK and SNO have also published results for the so-called *day-night effect* by measuring the difference in neutrino rate during the day and at night, when they have to cross the Earth’s dense core to reach the detectors. This effect can be expressed in terms of a

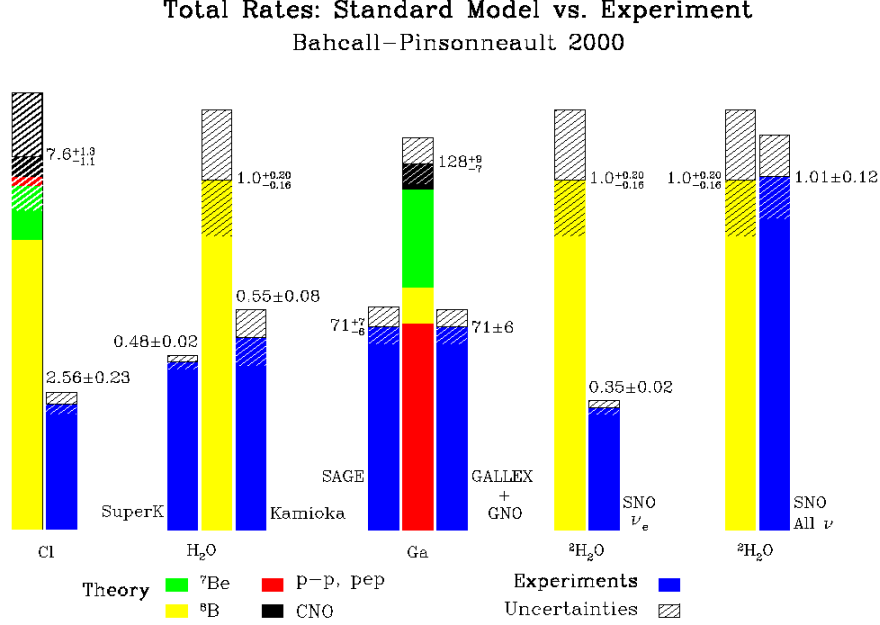


Figure 1.6: A pictorial view of the *solar neutrino problem* after the announcement of the SNO results [33]. The theoretical predictions are those of BP2000 [22]. The experimental results are compared against a normalized expected theoretical value with no neutrino oscillations. The bar on the right shows the excellent agreement between the total <sup>8</sup>B neutrino flux measured by SNO (including all neutrino flavours) and the theoretical expectations. For a detailed account of the problem, refer to paragraphs 1.3, and 1.4

dimensionless constant  $\mathcal{A}$  defined as [29, 34]

$$\mathcal{A} \equiv \frac{\Phi_{night} - \Phi_{day}}{\Phi_{average}} \quad (1.23)$$

The measured values are

$$\begin{cases} \mathcal{A}_{SuperK} = 3.3\% \pm 2.2\% \text{ (stat.) } +1.3\% \text{ (syst.)} \\ \mathcal{A}_{SNO}^{CC} = 7.0\% \pm 4.9\% \text{ (stat.) } +1.3\% \text{ (syst.)} \end{cases} \quad (1.24)$$

It is interesting to note how the  $\nu_e$  flux is greater at night; this is due to the *regeneration effect* in which some  $\nu_{\mu,\tau}$  convert back to  $\nu_e$  while passing through the Earth. The measured effect is bigger when observing a pure  $\nu_e$  flux, possible for SNO.

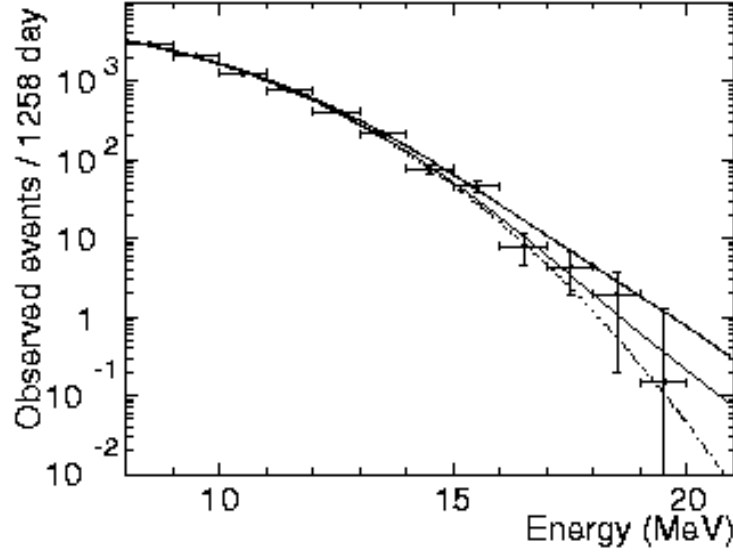


Figure 1.7: Energy spectrum of recoil electrons produced by  ${}^8\text{B}$  and  ${}_{\text{hep}}$  neutrinos in the Super-Kamiokande detector [29]. The solid line is the prediction of BP2000 [22], with which there's an excellent agreement.

Combining all experimental solar neutrino results allows computing with good accuracy the most likely set of mixing parameters among neutrinos (refer to sections 1.2.1 and 1.2.2). Assuming a two mixing scenario (i.e.  $\nu_e$  transforms into either  $\nu_\mu$  or  $\nu_\tau$ ), Bahcall et al. [35] have computed the best fit values (at  $3\sigma$  level) for the mixing angle  $\theta$  and the mass squared difference  $\delta m^2$  as

$$\begin{cases} \delta m_{\text{solar}}^2 = 5.0_{-2.7}^{+32.0} \times 10^{-5} \text{ eV}^2 \\ \tan^2 \theta_{\text{solar}} = 0.42_{-0.47}^{+0.18} \end{cases} \quad (1.25)$$

It must be noted that other authors have carried out similar analyses and obtained comparable results (see for example Fogli et al. [36]). This value corresponds to a solution known in literature as the Large Mixing Angle (LMA) solution. It can be seen from fig. 1.8 that the allowed regions in parameter space were already very limited before SNO published its results. Solutions such as vacuum oscillations, LOW (large mixing angle at small mass differences) and Small Mixing Angle (SMA), along with the likelihood of sterile neutrinos

existing have been essentially eliminated by the SNO data.

A strong confirmation of SNO's solar neutrino data came at the beginning of this year from the Kamioka Liquid scintillator Anti-Neutrino Detector (KamLAND) experiment, located at the former Kamiokande site. By looking at reactor electron anti-neutrinos produced some 180 km away via inverse  $\beta$ -decay (see eq.(1.1)), it was able to probe the LMA parameter space. For  $\bar{\nu}_e$ 's with energy greater than 3.4 MeV, KamLAND detected an antineutrino flux smaller than expected if there were no neutrino oscillations. The measured disappearance factor is  $0.611 \pm 0.085$  (stat.)  $\pm 0.041$  (syst.) [38]. As shown in fig. 1.8, the results are in basic agreement with the values in (1.25) if CPT symmetry is assumed and the allowed values of  $\delta m^2$  are further reduced (an interesting paper on experimental sensitivity to CPT symmetry using neutrinos is found in [39]). KamLAND will aim at measuring solar neutrinos too, the  ${}^7\text{Be}$  in particular.

So far, only the neutrino mixing parameters deduced from solar neutrino data have been discussed. As mentioned at the beginning of the chapter, the first evidence of neutrino oscillation was found with atmospheric neutrinos. SuperK observed a deficit of  $\nu_\mu$ 's compared to  $\nu_e$ 's (see fig. 1.9). The expected ratio is around 2, since pions produced in the upper atmosphere decay as  $\pi^+ \rightarrow \nu_\mu + \mu^+ \rightarrow \nu_\mu + e^+ + \nu_e + \bar{\nu}_\mu$  (and their charged conjugates), and the branching ratio for  $\pi^0 \rightarrow \nu\bar{\nu}$  is negligible [11]. This result has been confirmed by the KEK-to-Kamioka (K2K) experiment that observed a  $\sim 30\%$  disappearance of accelerator-generated 1.3 GeV  $\nu_\mu$ 's after they traveled 250 km to Kamioka [41]. These results are compatible with  $\nu_\mu \leftrightarrow \nu_\tau$  oscillation with the following parameters [42, 43]:

$$\begin{cases} \delta m_{atm}^2 = (2.6 \pm 0.4) \times 10^{-3} \text{ eV}^2 \\ \sin^2 2\theta_{atm} = 1.00^{+0.00}_{-0.05} \end{cases} \quad (1.26)$$

Summarizing, the picture that arises by combining atmospheric and solar neutrino data is:

- 1) almost maximal  $\nu_e \leftrightarrow \nu_\mu$  mixing with  $\delta m^2 \sim 5 \cdot 10^{-5} \text{ eV}^2$
- 2) maximal  $\nu_\mu \leftrightarrow \nu_\tau$  mixing with  $\delta m^2 \sim 3 \cdot 10^{-3} \text{ eV}^2$
- 3) very small or zero mixing between  $\nu_e$  and  $\nu_\tau$

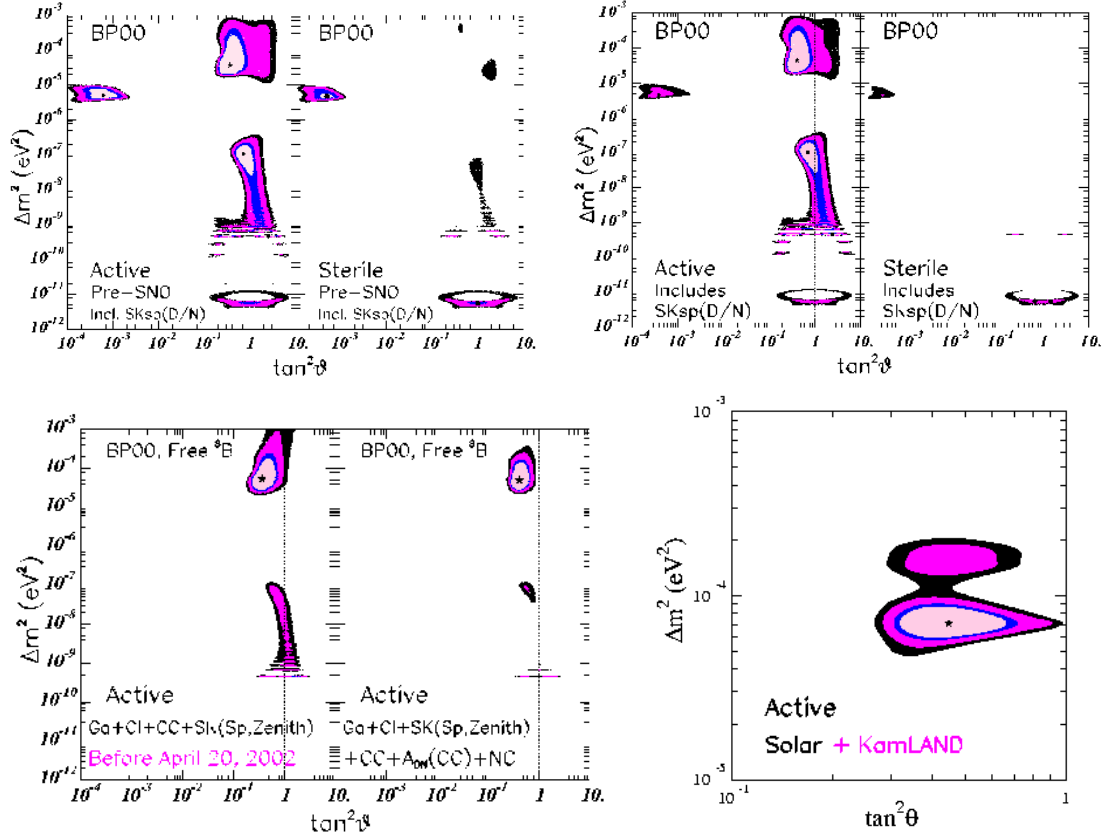


Figure 1.8: Evolution of the allowed regions in neutrino oscillation mixing parameter space with solar and reactor neutrino data.  $2\nu$  mixing is assumed. The top left sub-plots show the situation before the SNO results: LMA, LOW and SMA are all equivalently possible solutions, with room for vacuum oscillations and sterile neutrinos. The top right plot represents the allowed area in parameter space after the charged current SNO results: the sterile neutrinos are practically excluded and the likelihood of the SMA solution has significantly dropped. The two bottom left sub-plots refer to before and after the neutral current results from SNO, that essentially rule out the SMA solution. The bottom right plot is the situation after the results from KamLAND, where CPT symmetry is assumed. Only the LMA region in parameter space survives at  $3\sigma$  confidence level. The plots are taken from [37] and [40].

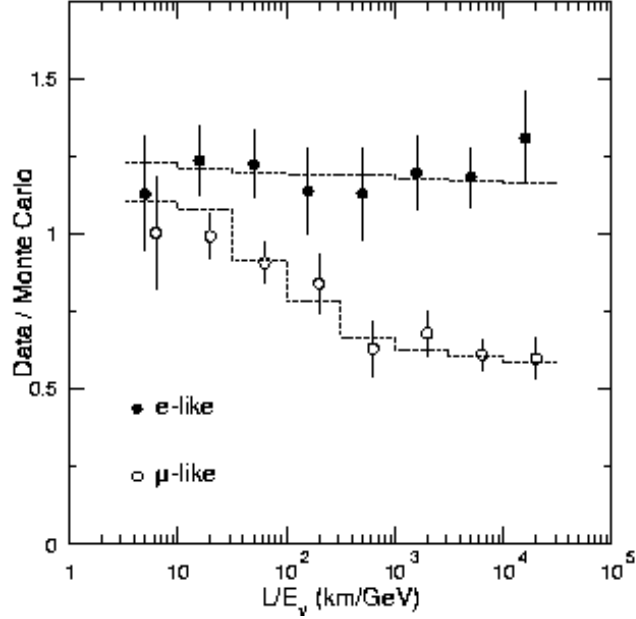


Figure 1.9: Ratio of observed versus predicted events in SuperK, as a function of the distance traveled through the atmosphere and the neutrino energy.  $\nu_e$  don't show any sign of oscillation, while the  $\nu_\mu$  deficit is quite evident [3].

In addition, the KamLAND data support excellent (if not exact) CPT symmetry in  $\nu_e \leftrightarrow \nu_\mu$  mixing.

Further published evidence for neutrino oscillations comes from the Liquid Scintillator Neutrino Detector (LSND) at Los Alamos, New Mexico [44]. The experiment looked for  $\bar{\nu}_\mu \rightarrow \bar{\nu}_e$  oscillations of antineutrinos produced with a proton beam. The data are consistent with neutrino oscillations with the following characteristics (see fig. 1.10):

$$\begin{cases} \delta m_{LSND}^2 \sim 1 \text{ eV}^2 \\ \sin^2 2\theta_{LSND} \sim 3 \times 10^{-3} \end{cases} \quad (1.27)$$

This result, partially contradicted by the Karlsruhe-Rutherford Medium Energy Neutrino experiment (KARMEN) [45], awaits direct confirmation by the MiniBooNE experiment at Fermilab [46].

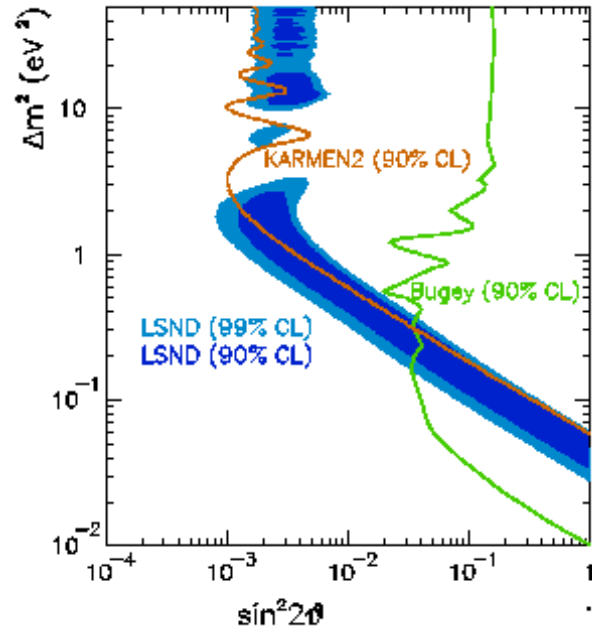


Figure 1.10: The region of  $(\delta m^2, \sin^2 2\theta)$  identified by the LSND data for possible neutrino oscillations together with exclusion regions to date. The plot is taken from [46].

## 1.5 What next?

While the solar neutrino problem appears resolved, there remain many interesting questions to address, such as:

- what is the absolute mass scale of neutrinos?
- are neutrinos Dirac or Majorana particles?
- why are neutrino masses so small?
- are there heavy neutrinos in addition to the three light ones already known?
- how much do neutrinos contribute to the dark matter in the universe and what is their role in cosmological structure formation?

- f. what can neutrinos contribute towards the theory of fundamental interactions and do they have a role in the dominance of matter over antimatter in the Universe?
- g. is there CP or CPT violation in the lepton sector?
- h. is there something more to learn from solar neutrinos about the Sun?

The answers to all these questions are intertwined at a very fundamental level. For example, whether neutrinos have a role in the dominance of matter over antimatter is connected to whether they violate CP symmetry and to the magnitude of such a phenomenon, if it exists. Moreover, the small masses of neutrinos are often explained by postulating the existence of heavy partner particles within the frame of supersymmetric theories [47].

Numerous efforts are taking place to address these questions, from studying supernovæ neutrinos to searching for neutrinoless double beta decays and Weakly Interacting Massive Particles (WIMPs). Stringent limits on neutrino properties are also set by cosmological measurements and arguments. Recent results from the Wilkinson Microwave Anisotropy Probe (WMAP) satellite experiment [48], combined with data from other experiments [49], set a limit on the contribution of relativistic neutrinos to the critical density of the universe. This translates into an upper bound on the sum of the neutrino masses [50],

$$\sum_{\nu=1}^3 m_{\nu} < 0.71 \text{ eV}, \quad (1.28)$$

in contradiction with the LSND result. The current direct experimental upper limits for neutrino masses are [11]

$$\begin{aligned} m(\nu_e) &< 3 \text{ eV} \\ m(\nu_{\mu}) &< 0.19 \text{ MeV} \\ m(\nu_{\tau}) &< 18.2 \text{ MeV} \end{aligned} \quad (1.29)$$

The current status of neutrino masses and the open questions related to them are elegantly summarized by Bilenky and Giunti [51].

Regarding the last three questions in the list, the answer will come with precision measurements of the neutrino mixing parameters. The Sun has proven to be a powerful natural

neutrino source, but most of what we have understood from solar neutrinos has been obtained from only the neutrinos at the high end of the energy spectrum, which make up about 1 part in  $10^4$  of the total solar neutrino flux. The goal then is to design experiments which are able to observe the low energy spectrum ( ${}^7\text{Be}$  and  $pp$ ) of the neutrinos emitted by the Sun [52]. John Bahcall and Carlos Peña-Garay clearly review the physics importance of performing such experiments [53]. The experimental difficulties to overcome in the design of the detectors are vast. One of the biggest problems is that the naturally occurring radioactive backgrounds one has to face are many orders of magnitude higher than the signals to detect. This is why cleanliness and radiopurity are among the greatest challenges the Borexino experiment has to face in its quest to directly measure in real-time the  ${}^7\text{Be}$  solar neutrino flux for the first time.

# The Borexino Detector and its Counting Test Facility

*“From an observational point of view the ideal object is the sun. If the oscillation length is smaller than the radius of the sun region effectively producing neutrinos, [...] direct oscillations will be smeared out and unobservable. The only effect on the earth’s surface would be that the flux of observable sun neutrinos must be two times smaller than the total (active and sterile) neutrino flux.”*

(B. Pontecorvo, 1967 [14])

First proposed more than ten years ago [54], Borexino is a real time, low energy solar neutrino detector [55]. Its assembly in Hall C of the Laboratori Nazionali del Gran Sasso (LNGS) in central Italy is close to completion. Borexino specifically aims at measuring and characterizing the flux of  ${}^7\text{Be}$  neutrinos from the Sun which are an important ingredient in understanding how neutrinos oscillate and how the Sun burns, as reviewed in chapter 1. A liquid scintillator target will emit flashes of light as a consequence of the incoming neutrinos scattering off electrons of its constituent molecules. The light is detected and measured by an array of more than 2000 photomultiplier tubes (PMTs) allowing to record energy and position of each event in real time.

Additionally, Borexino has the potential to detect neutrinos and antineutrinos from supernovæ explosions in our galaxy [56], antineutrinos emitted by naturally decaying elements in the Earth's crust and mantle [57], and those produced in nuclear reactors in nearby countries [58]. Borexino could also investigate non-standard neutrino interactions using strong sources [59].

In order to succeed in observing neutrinos, the detector has to be essentially free of other sources of scintillation. Natural radioactivity, present in trace levels in every material that surrounds us, emits charged particles that produce light signals in the detector which are essentially identical to those produced by neutrino-electron interactions. For this reason, the main overall challenge for the experiment is that of being intrinsically extremely radiopure in all its innermost components and sufficiently screened off from surrounding radioactivity ( $\gamma$  rays, muons, radon gas, etc.).

## 2.1 Detection mechanism and physics potential

### 2.1.1 Solar neutrinos

Borexino relies on neutrino-electron scattering for detecting solar neutrinos. The target electrons are those in the liquid scintillator molecules. The interaction energy of the incoming solar neutrinos (see the solar neutrino spectrum in fig. 1.3) is much higher than the typical electronic molecular binding energies (of the order of a few keV). In the scattering reaction the electron can then be considered free. The first order Feynman diagrams for  $\nu - e$  scattering are shown in fig. 1.2. All three neutrino flavours interact via neutral current reaction; electron neutrinos also interact via charged current exchange. Because of the extra term in the scattering amplitude the cross section for  $\nu_e - e$  scattering is larger than that for  $\nu_\mu -$  and  $\nu_\tau - e$  scattering. Using kinematic arguments (see, for example [60]), one can see that the charged current reactions  $\nu_{\mu(\tau)} + e \rightarrow \mu(\tau) + \nu_e$  have an energy threshold  $E_{th}$  for the incoming neutrino

$$E_{th} = \frac{m_{\mu(\tau)}^2 - m_e^2}{2m_e} \simeq 11 \text{ (3115) GeV}, \quad (2.1)$$

far above the energy of solar neutrinos. In addition, for neutrino-electron elastic scattering the kinetic energy  $T$  of the scattered electron can range between zero and a maximum value  $T_{max}$  (Compton edge) defined as

$$T_{max} = \frac{E_\nu}{1 + \frac{m_e}{2E_\nu}} \quad (2.2)$$

where  $E_\nu$  is the energy of the neutrino. The differential scattering cross section for  $\nu - e$  scattering is

$$\frac{d\sigma}{dT} = \frac{2G_F^2 m_e}{\pi} \left[ g_L^2 + g_R^2 \left(1 - \frac{T}{E_\nu}\right)^2 - g_L g_R \frac{m_e T}{E_\nu^2} \right] \quad (2.3)$$

where  $g_R = \sin^2\theta_W$  and  $g_L = \sin^2\theta_W \pm 1/2$  for  $\nu_e$  and  $\nu_{\mu,\tau}$  neutrinos respectively, and the total cross section is

$$\sigma = \int_0^{T_{max}} \left( \frac{d\sigma}{dT} \right) dT = \frac{2G_F^2 m_e T_{max}}{\pi} \left[ (g_L^2 + g_R^2) - \left( \frac{g_R^2}{E_\nu} + g_L g_R \frac{m_e}{2E_\nu^2} \right) T_{max} + g_R^2 \frac{T_{max}^2}{3E_\nu^2} \right] \quad (2.4)$$

According to equations (2.2) and (2.3), the signal from the 862 keV  ${}^7\text{Be}$  solar neutrinos will show a distinctive Compton edge of the scattered electron at 667 keV, as can be seen in fig. 2.1. Naturally, the signal that Borexino will record will not be as simple as what shown in the plot. The signal will be mixed with all the signals from radioactive background intrinsically present in the detector. The strategy is then to have as radiopure a detector as possible to begin with and to characterise the residual background in the best possible way in order to be able to identify the “shoulder” from  ${}^7\text{Be}$  neutrinos in the data. The total cross section for  ${}^7\text{Be}$  neutrinos is computed from eq. (2.4) to be

$$\sigma({}^7\text{Be}, 862 \text{ keV}) = 1.5 \times 10^{-16} \text{ GeV}^{-2} \longrightarrow 6 \cdot 10^{-44} \text{ cm}^2 \quad (2.5)$$

which is in perfect agreement with the estimate presented in chapter 1 (see eq. (1.2)).

The signature to confirm that a neutrino signal actually comes from the Sun is a seasonal variation of the total measured rate as a function of the Earth’s distance from the Sun along its orbit, expressed by

$$L(t) = L_0 \left[ 1 - \epsilon \cos\left(\frac{2\pi t}{T}\right) \right] + O(\epsilon^2) \quad (2.6)$$

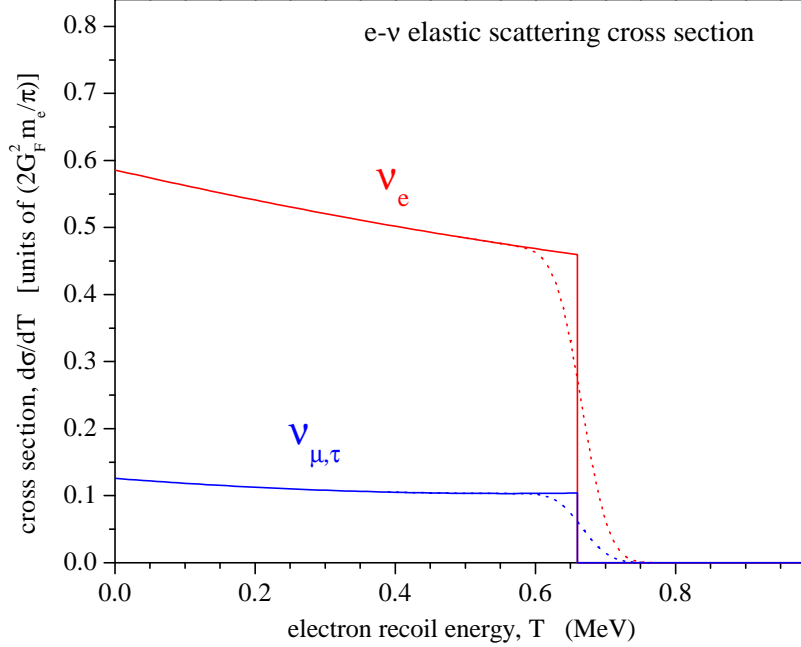


Figure 2.1: Differential cross section of electron-neutrino scattering for monochromatic, 862 keV  ${}^7\text{Be}$  solar neutrinos (from eq. 2.3), shown versus the scattered electron recoil kinetic energy  $T$ . The maximum recoil kinetic energy  $T_{max}$  of the electron is 667 keV. The cross section for muon and tau neutrinos of the same energy is also shown. The smearing effect for both cases is demonstrated for a detector resolution of 30 keV. For reference, the differential cross section for antineutrino-electron elastic scattering for antineutrinos of the same energy is shown in fig. 2.3.

where  $\epsilon = 0.0167$  is the eccentricity and terms of order  $\epsilon^2$  may be neglected in the following calculations.  $L_0 = 1.496 \times 10^8$  km is the semimajor axis and  $t = 0$  corresponds to the perihelion. The solid angle the Sun covers as seen from Earth differs by approximately 7% between aphelion and perihelion. In the case of no neutrino oscillations, the neutrino signal  $S(t)$  would be (neglecting factors of order  $\epsilon^2$ )

$$S(t) = S_0 \left( \frac{L_0}{L(t)} \right)^2 \simeq S_0 \left[ 1 + 2\epsilon \cos\left(\frac{2\pi t}{T}\right) \right] \quad (2.7)$$

where

$$S_0 \equiv N_e \Phi_0 \int dE_\nu \lambda(E_\nu) \sigma_e(E_\nu) \quad (2.8)$$

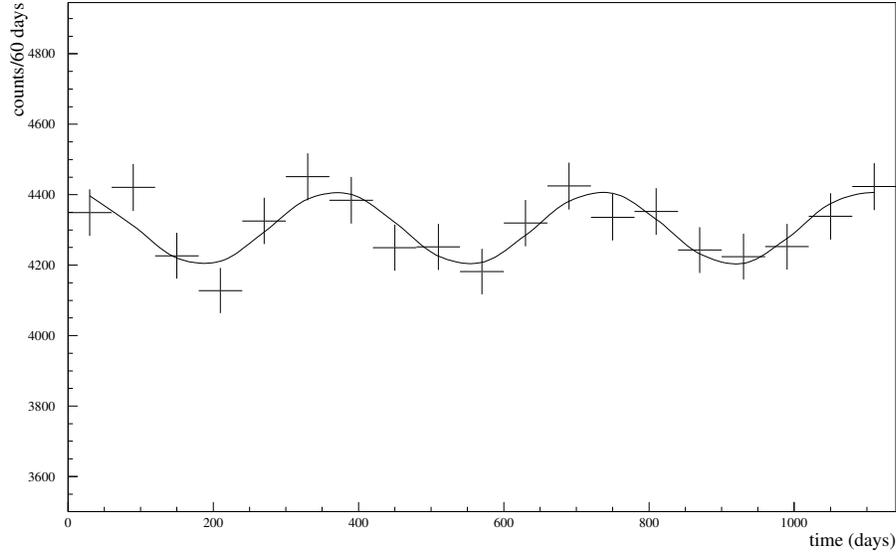


Figure 2.2: Simulated data showing the seasonal variation of the neutrino signal between 250 and 800 keV after three years of data taking in the no-oscillation scenario and with the neutrino fluxes predicted by the SSM [22]. Plot taken from [61].

in which  $N_e$  is the electron density in the target material ( $3.4 \times 10^{29}$  electrons/ton),  $\Phi_0$  the average solar neutrino flux on Earth,  $\sigma_e(E_\nu)$  the  $e - \nu_e$  cross-section (eq. 2.4) and  $\lambda(E_\nu)$  the solar neutrino spectrum (fig. 1.3). This effect as it would be seen after three years by Borexino under the assumption of no oscillations and with the neutrino fluxes predicted by the SSM ([22]) is shown in fig. 2.2. An average of approximately 70 events per day is expected under these assumptions in the neutrino energy window 250-800 keV.

For the current best fit oscillation parameters (LMA solution) listed in eq. (1.25) and assuming conversion of electron neutrinos into other active flavours, the rate in the same energy window is reduced by  $\sim 40\%$ . In this scenario, no more than 40 events/day are expected, approximately 25 of which are from  ${}^7\text{Be}$  neutrinos. Borexino also has the potential to further test (and possibly rule out) unfavoured solutions. If the SMA solution were the correct one, an even lower event rate would be expected in Borexino. Partial conversion into sterile neutrinos would also yield lower total rates in the detector (sterile neutrinos would not interact at all via the weak interaction). Seasonal distortions other than the

orbital geometrical effect illustrated above would involve oscillation distances on the order of the Earth-to-Sun distance difference at perihelion and aphelion ( $5 \times 10^{-6}$  km) and would probe the vacuum oscillations parameter space. Day/night rate fluctuations would indicate oscillations in the LOW solution; in this case the combination of oscillation parameters and neutrino energy is such that a detectable fraction of the neutrinos that had oscillated from electron to another flavour after being generated in the Sun convert back to electron type while crossing the Earth. Refer to section 1.4 and fig. 1.8 for the definition of the above mentioned neutrino oscillation solutions.

### 2.1.2 Antineutrinos

Electron antineutrinos can be detected via capture on protons in the scintillator:

$$\bar{\nu}_e + p \rightarrow n + e^+ \quad (Q = 1.8 \text{ MeV}) \quad (2.9)$$

This is the reaction used in Reines and Cowans' experiment that first directly detected neutrinos. The neutron capture on protons induces a 2.2 MeV  $\gamma$  emission with a 250  $\mu\text{s}$  delay. The energies  $E_{\bar{\nu}}$  and  $E_e$  of the incoming antineutrino and the outgoing positron are related by (see for example [47])

$$E_e = E_{\bar{\nu}} \left( 1 + \frac{E_e - p_e \cos\theta}{m_p} \right) - \frac{1}{2m_p} (m_n^2 - m_p^2 - m_e^2) \stackrel{m_e \ll m_p}{\sim} E_{\bar{\nu}} - \frac{m_n^2 - m_p^2}{2m_p} \quad (2.10)$$

where  $p_e$  is the positron momentum,  $\theta$  is the scattering angle in the laboratory frame and  $m_p$  and  $m_n$  are the proton and neutron masses. The  $e^+ - \gamma$  delayed coincidence provides a clear signal for  $\bar{\nu}_e$  capture. Possible sources of  $\bar{\nu}_e$  are the Earth, nuclear reactors, the Sun and supernovæ.

A measurement of the electron antineutrino flux from natural radioactivity (e.g.  $^{238}\text{U}$  and  $^{232}\text{Th}$ ) in the Earth's crust and mantle would provide important information on heat generation within our planet. According to the current knowledge of the radiochemical composition of Earth, several tens of  $\bar{\nu}_e$  events per year with energies up to 3 MeV are expected in Borexino [57].

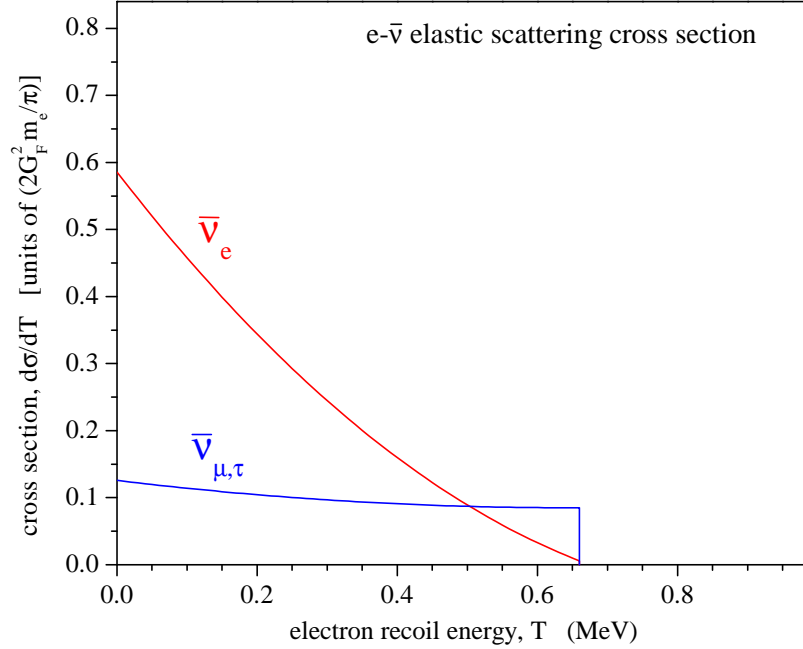


Figure 2.3: Differential cross section of electron-antineutrino scattering for monochromatic, 862 keV antineutrinos, shown versus the scattered electron recoil kinetic energy  $T$ . The different cross section for electron and muon (tau) antineutrinos are apparent. The maximum recoil kinetic energy  $T_{max}$  of the electron is 667 keV. The differences with electron-neutrino scattering can be appreciated by comparing with fig. 2.1

With no active reactor present in Italy, Borexino would be sensitive to antineutrinos in France, Switzerland and Germany. Possible  $\bar{\nu}_e$  disappearance could probe neutrino oscillation parameters with a longer baseline ( $\sim 1000$  km) than that for KamLAND [58]. Several tens of  $\bar{\nu}_e$  events per year with energies up to 8 MeV are expected in Borexino from these sources.

No antineutrino emission is expected from the Sun. Possible detection of solar  $\bar{\nu}$ s would be a smoking gun for new physics. The current upper limit on the  $\bar{\nu}_e$  flux from the Sun ( $5 \times 10^4 \text{ cm}^{-2} \text{ s}^{-1}$  [62], corresponding to approximately 100  $\bar{\nu}_e$  events per year) could be significantly improved by Borexino.

Intense neutrino and antineutrino fluxes of all flavours are emitted in supernovæ collapses, with average energies 10-30 MeV. The main detection channel in Borexino is via antineutrino capture on protons (eq. (2.9)). Approximately 80 events are expected from a supernova collapse in the center of our galaxy from this source. Detection channels for neutrinos and antineutrinos in Borexino are offered by charged- and neutral-current interactions on  $^{12}\text{C}$  [63]. Such studies could put stringent limits on the absolute masses of neutrinos [56].

Antineutrinos of all flavours also elastically scatter off electrons. The cross section for this reaction is obtained from eqs. (2.3) and (2.4) by the substitution  $g_L \leftrightarrow g_R$  and is shown in fig. 2.3 for hypothetical monoenergetic 862 keV antineutrinos.

### 2.1.3 Neutrino physics with sources

Sources of neutrinos ( $^{51}\text{Cr}$ ) or antineutrinos ( $^{90}\text{Sr}$ ) are an excellent tool to probe non-standard neutrino properties with Borexino. In particular, if neutrinos carry a magnetic moment, the electron recoil pattern in low energy  $\nu - e$  scattering would deviate from the Standard Model predictions. Sensitivities to neutrino magnetic moments  $\mu_\nu \sim 10^{-11} \mu_B$  would be in the reach of Borexino using MCi sources [59, 64].

## 2.2 Design of the Borexino detector

The design of Borexino has to satisfy two main requirements. On one hand the detector has to be massive enough to allow the interaction of a statistically significant number of elusive neutrinos inside its active volume. On the other, all its central constituents must be extremely radiopure. The first requirement is satisfied by a hundred-ton-scale unsegmented liquid volume that is expected to “capture” a few tens of  $^7\text{Be}$  solar neutrinos every day. The second is pursued via a number of different paths: careful selection and screening of the constitutive materials (scintillator liquid, mechanical structures and light-detection devices) that need to satisfy very strict radiopurity standards, minimization of the mass of the structural materials in close contact with the active core of the detector, and layered

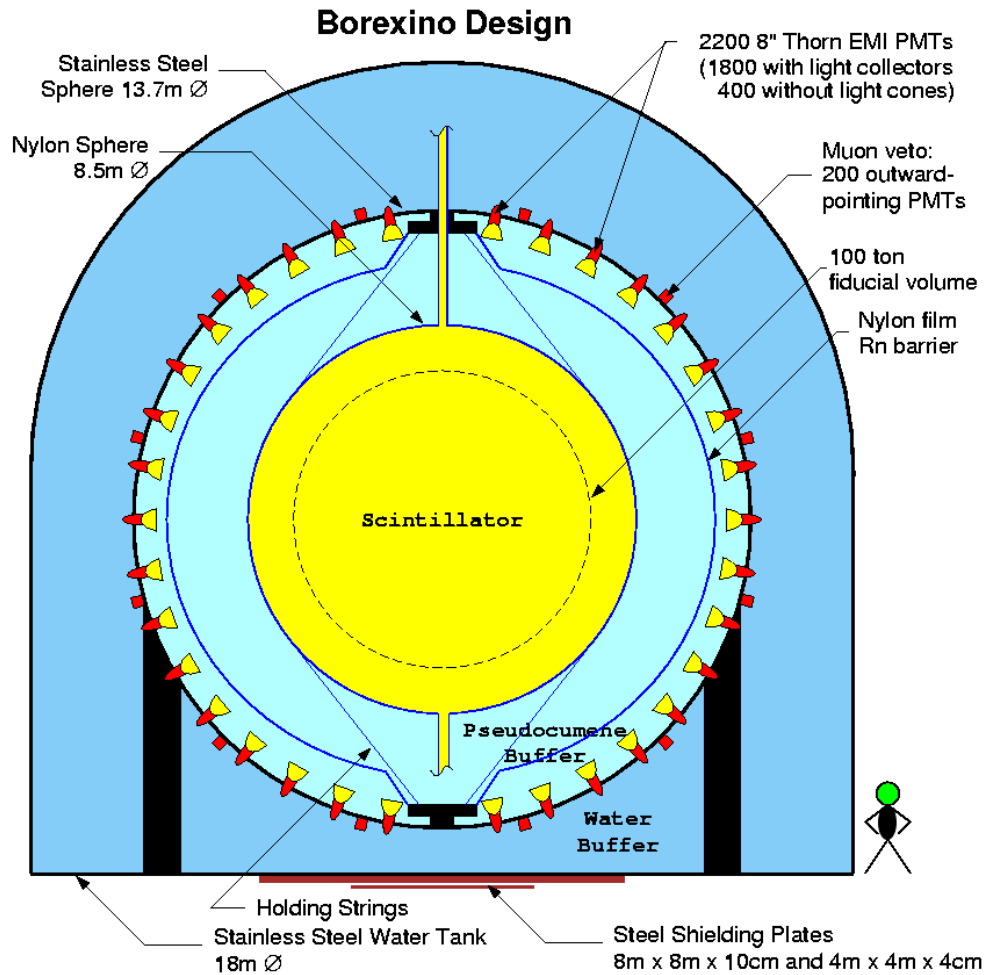


Figure 2.4: A simplified sketch of the Borexino detector.

radial screening of the target volume from the surroundings. Further purification of the scintillator and buffer fluids is also implemented. A sketch of the apparatus is shown in fig. 2.4.

The core of the detector is a spherical 300 ton volume of liquid scintillator; this is a 1.5 g/l solution of 2,5-diphenyl oxazole (PPO,  $C_{15}H_{11}NO$ ) in 1,2,4-trimethylbenzene or pseudocumene (PC) solvent ( $C_6H_3(CH_3)_3$ ). The scintillator is mechanically confined by a thin transparent, nylon spherical “balloon”, referred to as the Inner Vessel (IV). With a 8.5 m diameter, the IV is placed at the center of a bigger 13.5 m diameter Stainless Steel

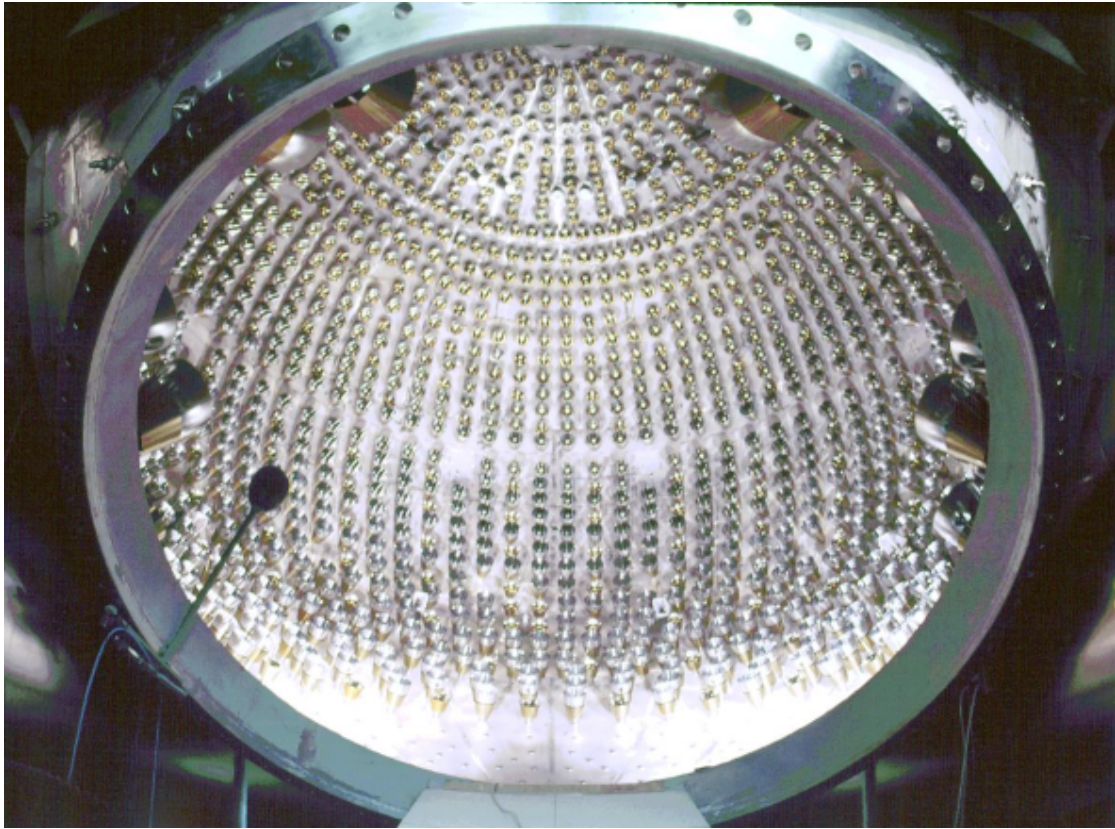


Figure 2.5: A look inside the Borexino Stainless Steel Sphere (SSS), in the final commissioning phase. Most of the 2200 photomultiplier tubes (PMTs) are visible: the bottom ones await the spherical nylon vessels to be deployed before being installed. The sphere is 13 m in diameter, the two concentric nylon “balloons” (not installed) 8.5 m and 11.5 m respectively; the diameter of the flange through which the picture has been taken is 3 meters.

Sphere (SSS) on which 2200 photomultiplier tubes (PMTs) are mounted (see fig. 2.5). The volume between the SSS and the IV is filled with a quenched pseudocumene solution, 5 g/ℓ dimethylphthalate (DMP) in PC and is used as a buffer volume. This design is meant to keep the IV+scintillator almost neutrally buoyant, reducing the mass of the IV envelope and its supports to a minimum. A second spherical nylon membrane, called the Outer Vessel (OV), is placed between the IV and the PMTs as a barrier for radon emanated mainly by the PMTs and the SSS. The vessels are connected at the two poles to the SSS with cylindrical pipes that allow fluids to fill the different volumes and provide basic mechanical support.

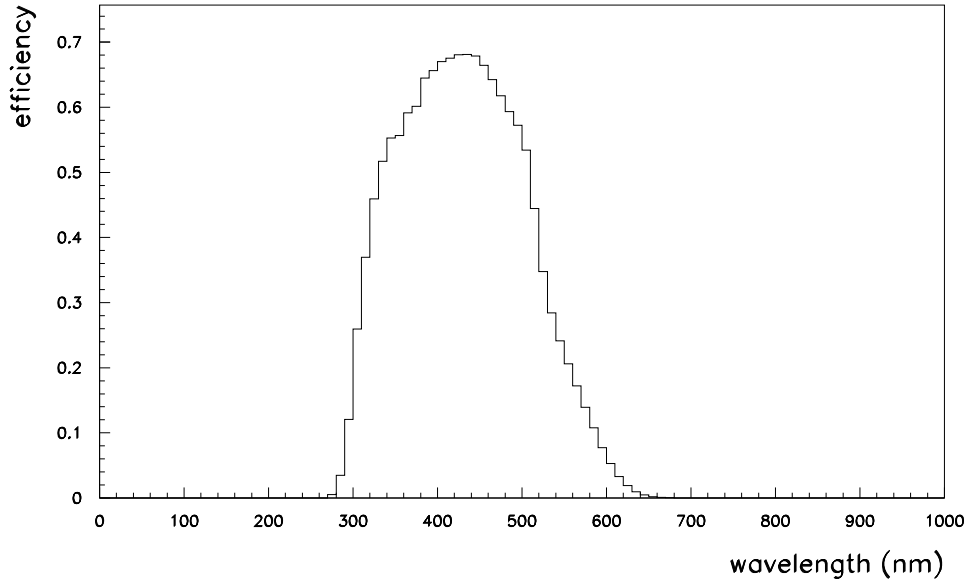


Figure 2.6: The spectral sensitivity and quantum efficiency of the Borexino ETL 9351 8'' photomultiplier tubes.

The nylon film out of which the vessels made is thin ( $125 \mu\text{m}$ ) and flexible and since absolute buoyancy cannot be relied upon, a web of strings attached to the pipes embrace the two vessels holding them in position. The vessels will be maintained in a spherical shape by keeping them at a slight overpressure.

The choice of PC for the scintillation solution is dictated by many reasons, among which are high scintillation light yield ( $\sim 10^4$  photons/MeV), high transparency (5-10 m mean free path [65]), and fast decay time of the scintillation light ( $\sim 5$  ns) essential for good spatial resolution of the detector. In addition, conventional petrochemical purification techniques can be applied to purify the hundreds of tons of fluid needed for Borexino. The PPO additive to the scintillator works as a wavelength shifter to fine tune the scintillation light to the spectral response of the PMTs (fig. 2.6). The scintillation spectrum of the PC+PPO scintillator versus that of pure PC is shown in fig. 2.7 [66].

The addition of the DMP quencher to the buffer fluid is meant to drastically reduce

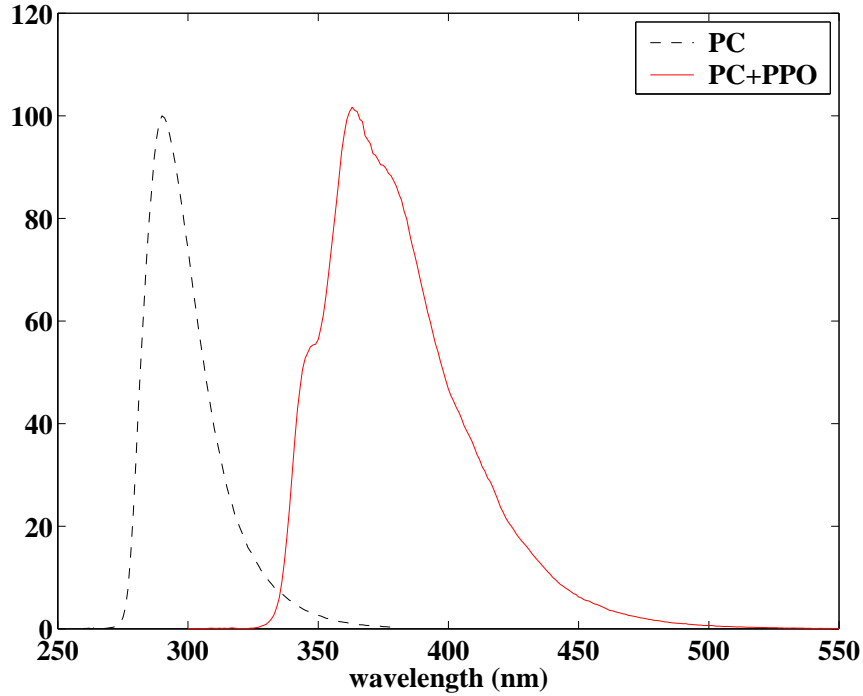


Figure 2.7: The scintillation spectrum of pure PC (dashed line) and of a 1.5 g/l PPO+PC solution (solid line) [66].

scintillation light in proximity of the PMTs which are intrinsically much less radiopure than the scintillator. An excessive amount of light on the external region would unacceptably increase the overall trigger rate and swamp the signal of events inside the IV. The light yield of PC is reduced 10 times with the addition of DMP at the design concentration [67].

The SSS is enclosed inside a bigger stainless steel Water Tank (WT). The water surrounding the sphere provides a buffer to screen the inner volume of the detector against radiation (mainly neutrons and  $\gamma$  rays) emitted by the rock of the underground cave walls. Instrumented with  $\sim 200$  PMTs mounted outwards on the SSS and on the WT floor, it also works as a Čerenkov muon detector. Muons that cross through the scintillator are easily identified by the large amount of light released, but those which pass almost tangentially to it can produce short-lived light radioactive isotopes (e.g.  ${}^7\text{Be}$ ,  ${}^{11}\text{C}$ , etc) that would be a background [68]. It is thus very important to accurately veto a time window associated to

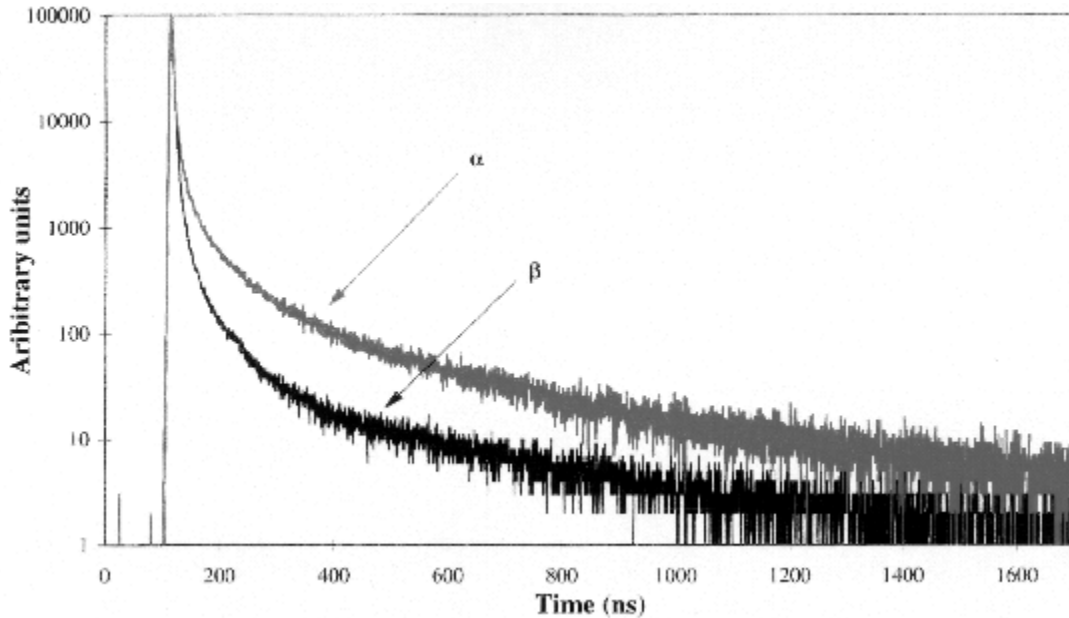


Figure 2.8: The different decay time of the scintillation light produced by  $\alpha$  and  $\beta$  particles. A pulse shape analysis of the PMT charge (light) collected in the “tail” compared to the total amount of charge (light) released allows efficient discrimination between the two types of events. The plot is taken from [73].

the passage of a muon [69].

The PMTs and read out electronics are appropriately chosen to be able to detect very small amounts of light, typical of recoil electrons below 1 MeV. The PMTs are suitable for single photoelectron count [70] and the dynamic range of the electronics is optimized for low energy counting [71]. Precise timing of the PMTs is crucial for the spatial reconstruction of each event inside the detector. The read out electronics will also provide discrimination between events with different decay times of the scintillation light. It has been verified that the time profiles of the scintillation light for  $\alpha$  particles and electrons are different, the latter typically decaying faster (fig. 2.8). A careful calibration of the properties of the scintillator, the PMTs, and the read out electronic chain will allow an  $\alpha/\beta$  separation in excess of 90% [72, 73].

The photomultipliers are 8” ETL model 9351 and have been developed together with the

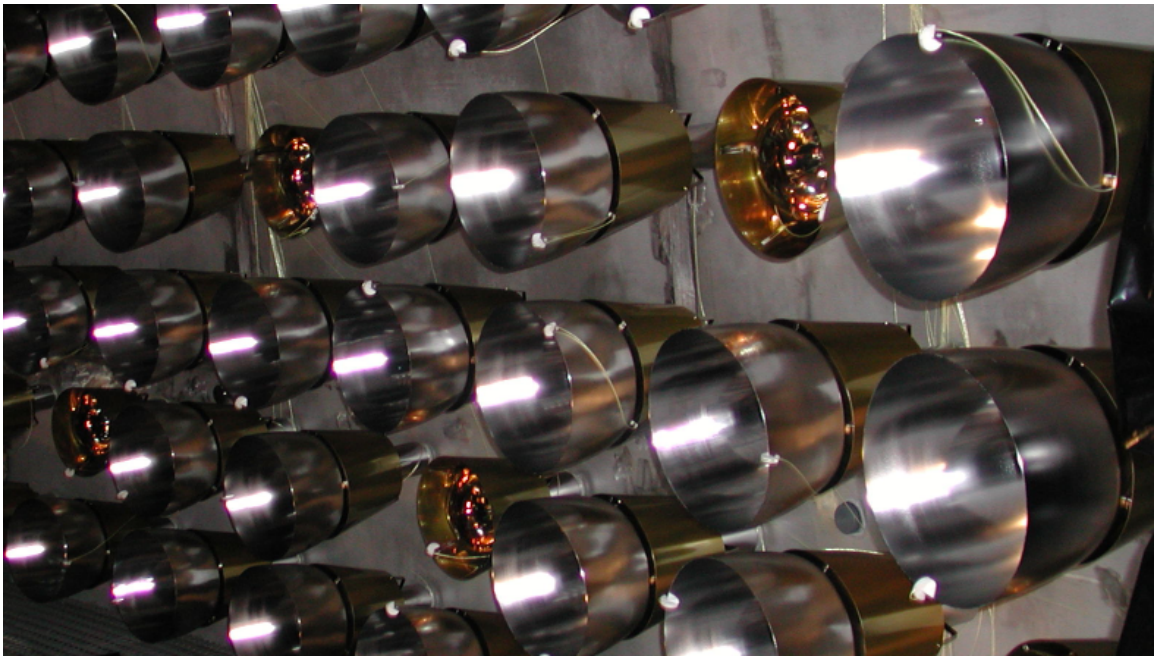


Figure 2.9: A closeup view of the Borexino photomultiplier tubes (PMTs). 80% of them are equipped with aluminum light concentrators designed to focus the field of view to the scintillator inside the IV. The others can detect light generated in the whole SSS, in particular Čerenkov radiation emitted by muons.

manufacturer to contain very low amounts of residual radioactivity in the glass. Approximately 1800 of them are equipped with aluminum light concentrators designed to capture the light of events inside the IV. The PMTs without concentrators will also capture the light from the buffer region. In addition to residual scintillation, they will detect Čerenkov light associated with the passage of a muon, and are therefore a complementary component of the Borexino muon detector. A close view of the Borexino PMTs, with and without concentrators is displayed in fig. 2.9.

The Borexino detector is equipped with numerous auxiliary plants, mainly devoted to the overall fluid handling and circulation, and the purification of scintillator, buffer solution, and water. The fluid handling plants are needed to regulate and maintain gas and liquid flows, pressures and levels during all initial filling operations as well as during the long term steady-state period of data taking; they are made up of various modules

and interconnect virtually all parts of the detector. The purification plants are needed to purify the pseudocumene and scintillator before it enters the detector. It is also possible that further online purification of the scintillator will be needed during the lifetime of the experiment. Water is purified by reverse osmosis deionization and nitrogen stripping to eliminate gaseous radioactive species and oxygen [74]. The purification processes for pseudocumene include nitrogen stripping, counter current water extraction, filtration on a silica gel adsorbing bed, and vacuum distillation. Nitrogen stripping has proven effective in removing radioactive gaseous species as well as oxygen. Water extraction and adsorption onto silica gel are designed to eliminate metallic impurities. Distillation should separate anything less volatile than PC.

An extensive description of the Borexino detector and its auxiliary plants is found in [55].

### 2.3 Radioactivity requirements and background rejection

The radioactivity specifications for Borexino are such that unambiguous identification and measurement of the  ${}^7\text{Be}$  solar neutrinos can be assumed. The primary concern is that of having an intrinsically ultra low radioactivity liquid scintillator solution. The second is to keep the radioactivity in the structural materials that are close to or in contact with the scintillator (nylon, pipes, PMTs, etc.) low enough not to “drown” the neutrino signal in the central target volume. In practical terms, based on the final radioactivity levels achieved, a central “fiducial” volume will be selected from the data for performing physics analysis. The size of this region will depend on the residual radioactivity (e.g.  $\gamma$  rays, radon, ...) leaking into the center of the detector from surrounding elements. A larger fiducial target mass implies an increased physics potential of the experiment.

Borexino has a 100-ton fiducial target mass design specification (which corresponds to the 2.9 m radius central volume). Just a few tens of solar neutrino events are expected per day in this volume (this figure will of course depend on the exact solar neutrino oscillation parameters). The residual, irreducible background events need to be at most comparable with this number in the fiducial volume in the neutrino energy window, yielding an overall

total acceptable background on the order of  $\sim 10^{-9}$  Bq/kg or better in the scintillator.

The fundamental radioactivity requirement is set on the amount of  $^{14}\text{C}$  in the scintillator. The  $^{14}\text{C}$  abundance will determine the overall trigger rate of the experiment (the exact value will also depend on the hardware energy threshold that will be chosen).  $^{14}\text{C}$  is a  $\beta$  emitter with a 156 keV endpoint energy, as shown in fig. 8.1. Because of finite detector energy resolution, events from this source could be observed at higher energy inside the detector. This carbon isotope is present in the pseudocumene molecule ( $\text{C}_9\text{H}_{12}$ ) and cannot be eliminated by purification. Borexino aims at setting an operating threshold for physics at 250 keV. To limit these  $\beta$ 's to on the order of one event per day above threshold, the  $^{14}\text{C}$  isotopic abundance in the scintillator should be  $\frac{^{14}\text{C}}{^{12}\text{C}} \sim 10^{-18}$  or better [75].

Many radioactive impurities are of concern for Borexino, including most daughters of the  $^{238}\text{U}$  and  $^{232}\text{Th}$  natural decay chains (see figures 3.7 and 4.1 respectively). For these elements, levels on the order of  $10^{-16}$  g<sub>U,Th</sub>/g<sub>PC</sub> or better in the scintillator are required. The presence of these species can be efficiently tagged by looking for short delayed consecutive decays within their radioactive chains. In the  $^{238}\text{U}$  chain, there is the  $^{214}\text{Bi}$ - $^{214}\text{Po}$   $\beta$  –  $\alpha$  sequence with a mean lifetime of 235  $\mu\text{s}$  (see section 8.3.1). Analogously, in the  $^{232}\text{Th}$  chain it is possible to search for  $^{212}\text{Bi}$ - $^{212}\text{Po}$   $\beta$  –  $\alpha$  sequence with a 432 ns mean lifetime. Knowing the rate of these decays (allowing for the appropriate branching ratios) specifies the amounts of  $^{226}\text{Ra}$  and  $^{228}\text{Th}$  respectively (along with all the daughters in the series). Their  $\alpha$  and  $\beta$  decays can then be accounted for and subtracted from the collected data set. A cross-check of these event rates may be possible using longer-lived delayed coincidences (seconds or even minutes apart), imposing a spatial constraint to their search (e.g. the  $^{222}\text{Rn}$ - $^{218}\text{Po}$   $\alpha$  –  $\alpha$  sequence in the  $^{238}\text{U}$  series). Assuming secular equilibrium in the decay chain, it is possible to extrapolate the amounts of  $^{238}\text{U}$  and  $^{232}\text{Th}$  present in the scintillator.

Other dangerous background elements are  $^{40}\text{K}$ ,  $^{85}\text{Kr}$ , and  $^{39}\text{Ar}$ , all  $\beta$  emitters. The limit required on the total potassium abundance is  $K_{\text{nat}} \sim 10^{-14}$  g/g ( $K_{\text{nat}}$  indicates the overall potassium content including all isotopes with their natural abundance).  $^{85}\text{Kr}$  can be tagged by looking for its secondary decay mode to the metastable state  $^{85m}\text{Rb}$ , generating a  $\beta$  –  $\gamma$  delayed coincidence with a 1.46  $\mu\text{s}$  mean life (see fig. 8.7); a corresponding number

of  $\beta$  events can then be subtracted. Some decays without time coincidence patterns can be identified in different ways:  $\alpha$  decays can be spotted via pulse shape discrimination (as explained in the previous section), while a careful energy spectrum analysis can identify and separate individual, known sources which may then be statistically subtracted from the total energy spectrum.

Separate specifications are set by the so-called external background, originating from the periphery of the detector. The concern is for  $\gamma$  rays emitted by radioactive impurities in the detector's materials which can penetrate into the fiducial volume.  $\gamma$  rays may originate from impurities in the nylon film of the vessels, on the surface of the materials of their mechanical support structures and hold-down ropes, and from every component inside the SSS. The  $\gamma$  activity is dominated by that coming from the PMTs. In fact, the thickness of the buffer region was determined by the need to absorb the highest energy (several MeV)  $\gamma$  rays from this source (the attenuation length in PC of photons of this energy is many tens of cm!). The radioactivity of the PMTs and the detector geometry should yield  $\sim 1$  event/day from this source in the fiducial volume. A thorough discussion of these backgrounds is found in [76].

Having met the design radioactivity specifications and using all the above-mentioned background identification techniques, the final goal is to be able to distinguish a clear signature of solar neutrino interactions. In particular, the aim is to observe the Compton-like edge from the 862 keV  ${}^7\text{Be}$  neutrinos in the recorded electron scattering energy spectrum.

The low radioactivity levels needed can be achieved only with thoroughly clean construction and purification techniques and by very carefully selecting and screening all construction materials, including the scintillator. A collection of milestone results from extremely low level radioactivity measurements performed within the Borexino collaboration can be found in [77].

## 2.4 The Counting Test Facility (CTF)

Built to test the feasibility of ton-scale purification of organic liquid scintillators at the levels required by Borexino, the Counting Test Facility (CTF) is now in its third data taking campaign since 1995. The detector, located in the same underground hall as Borexino, also shares with it most of the design concepts.

Approximately 4 tons of scintillator (1.5 g/ℓ PPO in PC solution) are contained in a transparent nylon spherical vessel (500 μm-thick membrane, 1 m radius, see fig. 2.11) immersed in ultra pure water used as screening material. Because water is denser than PC, a set of strings wrap around the vessel anchoring it to the bottom. 100 PMTs mounted on an open stainless steel structure measure the scintillation light inside the vessel. The open structure and nylon vessel can be seen in figures 2.10 and 2.11.

The first campaign (CTF1) was carried out in 1995. It supplied the proof of practice for Borexino-like detectors, and, after purification, allowed measurement of [75, 78]:

- 1)  $\frac{^{14}\text{C}}{^{12}\text{C}} \sim 2 \times 10^{-18}$  (lowest  $^{14}\text{C}$  isotopic abundance ever measured)
- 2)  $\sim 4 \times 10^{-16}$  g/g for  $^{238}\text{U}$  and  $^{232}\text{Th}$  equivalent contamination (assuming secular equilibrium in their respective decay chains)

The purification techniques adopted were water extraction, nitrogen stripping and vacuum distillation. For a more detailed description of the data analysis for CTF1, refer to [79].

A second data-taking campaign (CTF2) was performed in 2000, this time with a different scintillator: Phenyl-ortho-xylene (PXE) as a solvent with para-Terphenyl (2 g/ℓ) and bis-MSB (20 mg/ℓ) as wavelength shifters. There were two major upgrades of the detector: 20 PMTs were placed on the bottom of the water tank to detect Čerenkov light produced by muons so they could be vetoed. In addition, a second nylon membrane was interposed between the inner vessel and the PMTs, much like the Borexino design. This membrane, maintained during the third run (CTF3) and visible in fig. 2.12, functions as a radon barrier. The radiopurity results were somewhat worse than those found in CTF1 [80]. Nonetheless, CTF2 put new lower limits on the lifetime of some interesting non-standard processes [81]

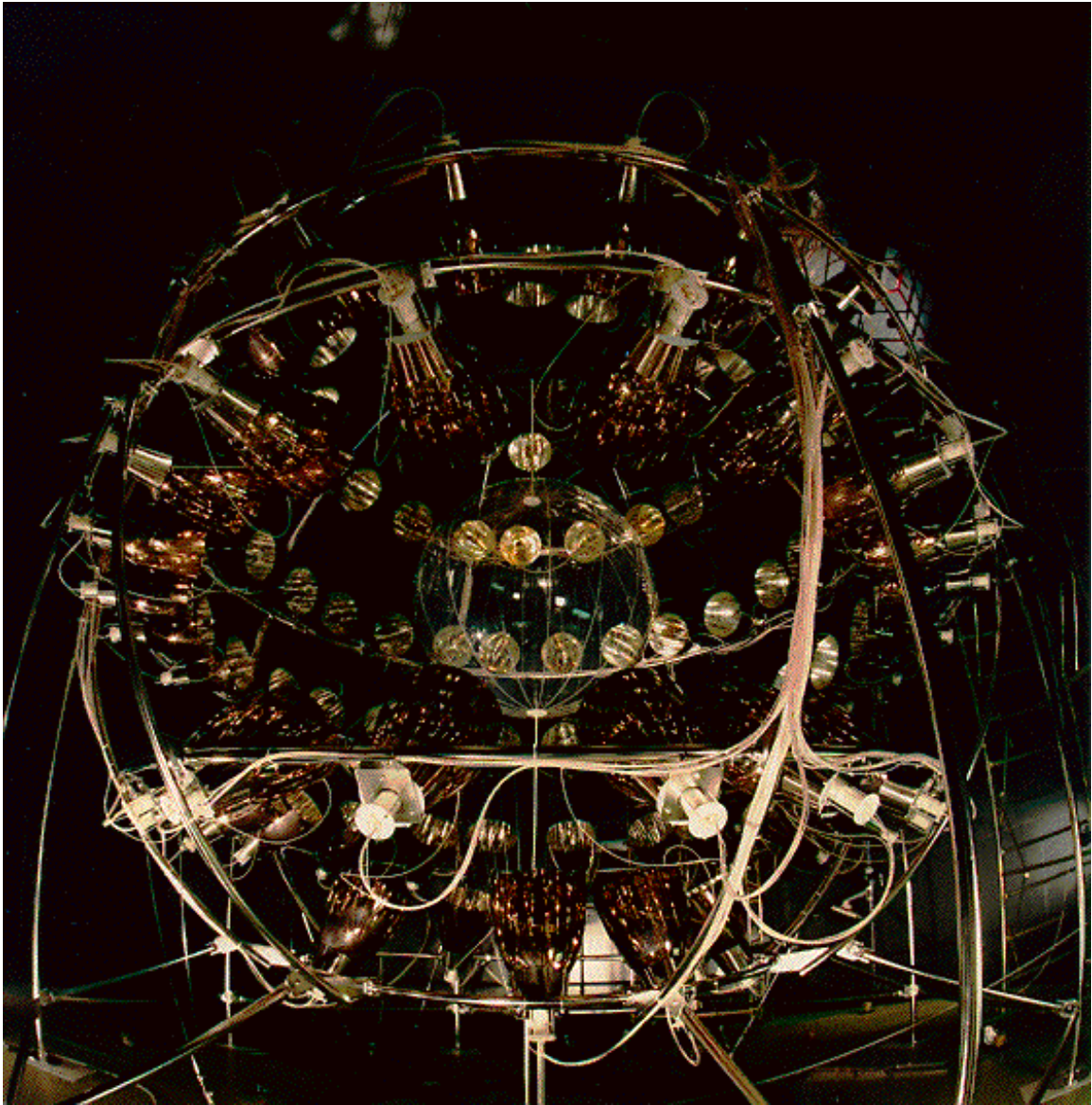


Figure 2.10: The 1 meter diameter CTF nylon vessel surrounded by 100 PMTs mounted on a stainless steel open structure. Clearly visible are the light concentrators mounted on the PMTs.

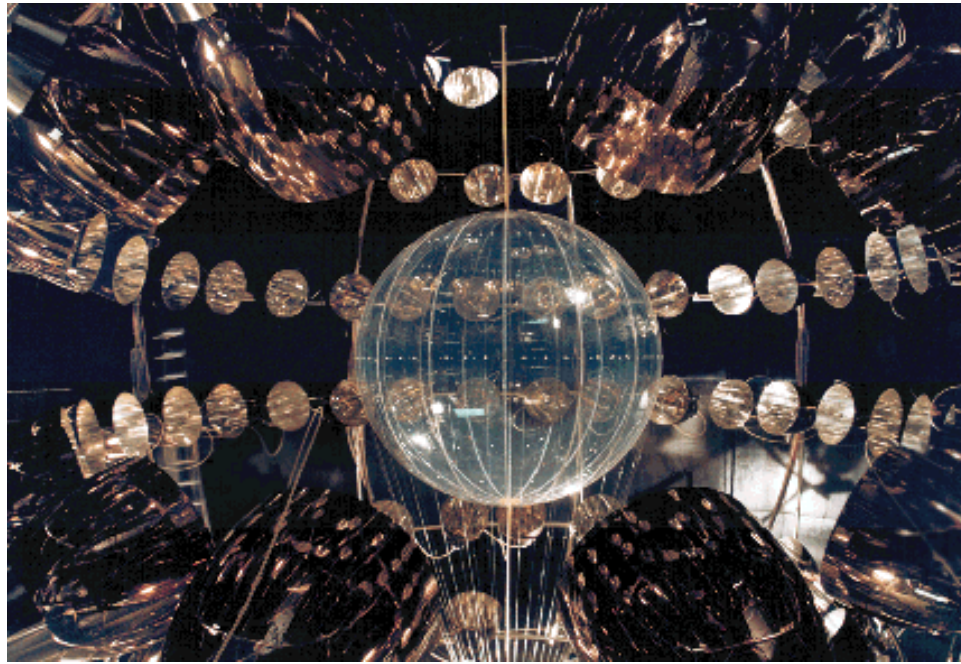


Figure 2.11: A closeup of the CTF nylon vessel. The nylon pipes at the two poles of the vessel, the nylon strings holding it in place against the upward buoyant force and the glue seams of the panels out of which it is constructed can be appreciated.

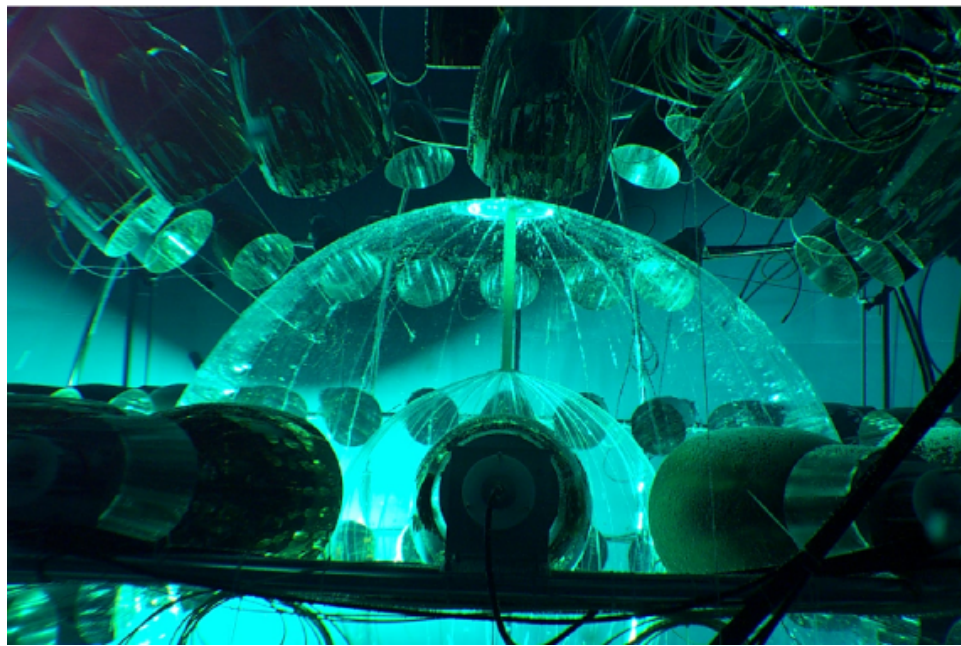


Figure 2.12: A view of the CTF3 detector, with its double nylon vessel, following its filling with ultra pure water.

and an upper limit on the neutrino magnetic moment [82].

The main goals of the third campaign (CTF3) which has been ongoing since mid-2001 are to measure the  $^{14}\text{C}$  abundance of the scintillator delivery for Borexino and to test purification methods, sequences and efficiency of the Borexino plants. During these tests, the leak tightness and overall cleanliness of many interconnecting plant sections are also tested. The outcome of the tests will be crucial to define the filling and purification strategies for Borexino. Some representative results from this run are reported in chapter 8.

# The Borexino Nylon Vessels

The Borexino liquid scintillator is contained in a nylon spherical vessel (8.5 m diameter) called the Inner Vessel (IV) which separates it from surrounding buffer fluid. A second, concentric nylon vessel (Outer Vessel, OV, 11.5 m diameter) is placed around it as a barrier for radon emanated by the PMTs and other structural elements. Both vessels must satisfy the following requirements:

- a. Transparency in the blue and near UV range (350-450 nm). This is the wavelength of the scintillation light of the PC+PPO solution that has to reach the PMTs (see spectrum in fig. 2.7).
- b. Chemical compatibility with aromatic compounds (pseudocumene) and water. These two liquids coexist in CTF. For Borexino, the filling strategy is to fill the detector (i.e. the SSS + vessel system) first with water and then with pseudocumene. In addition, the membrane has to present very low permeability towards pseudocumene and radon gas.
- c. Mechanical robustness. The vessels have to withstand the stresses and buoyant forces occurring during filling and steady-state operations (see section 3.2).
- d. Extremely low radioactivity. The radioactivity requirements of the IV are second only to those of the scintillator itself. These requirements set limits on film surface cleanliness and tolerable film intrinsic radioactivity contamination.  $\gamma$ 's from  $^{238}\text{U}$ ,

$^{232}\text{Th}$ , and  $^{40}\text{K}$  emitted at the IV radius can penetrate into the central volume of the detector. In addition, if  $^{226}\text{Ra}$  ( $^{238}\text{U}$ ) is present in the membrane, radon can emanate from the nylon film and diffuse into the scintillator. These issues are addressed more in detail in sections 3.1 and 3.2.

### 3.1 Why nylon for the scintillator containment vessel?

After initially considering a rigid acrylic scintillator containment vessel for Borexino [54] similar to the heavy water containment vessel of SNO [83], a thin nylon membrane was chosen instead [84]. This approach offers numerous advantages.

Nylon presents a very high compatibility with pseudocumene. Tests have shown that its mechanical properties (e.g. yield point, Young's modulus, creep) are essentially unchanged after immersion in dry PC, PC+PPO, and PC+DMP for many months [76]. Nylon is weakened at high humidities (immersion in water lowers the yield point by a factor of  $\sim 3$ ), but the effect has been shown to be reversible [76]. Water can indeed cause hydrolysis in nylon compromising its molecular structure, but the time scale for this process is long compared to the expected lifetime of Borexino (10 years) [85]. Thorough mechanical tests of nylon films have been performed on nylon exposed to air and PC at different relative humidities [86]. The typical behaviour of the stress as a function of strain (i.e. fractional elongation) is shown in fig. 3.1. Relevant results of these tests are reported in section 3.2.

Nylon films can be produced with excellent light transmittance and low haze properties. Such characteristics allow to minimize scattering and loss of photons along their path to the PMTs. These conditions are essential for accurate energy measurement, good energy resolution and precise position reconstruction of the events. The nylons films selected for Borexino all show good transmittance ( $> 90\%$  in PC) above 300 nm (compare with fig. 2.7) and less than 1% scattering at angles greater than  $7^\circ$  with 366 nm light [76].

A useful property of nylon is that of having an index of refraction which almost perfectly matches that of pseudocumene ( $\sim 1.5$  for both). This simplifies the optical reconstruction of the events for Borexino, where the vessels are immersed in pseudocumene. In comparison,

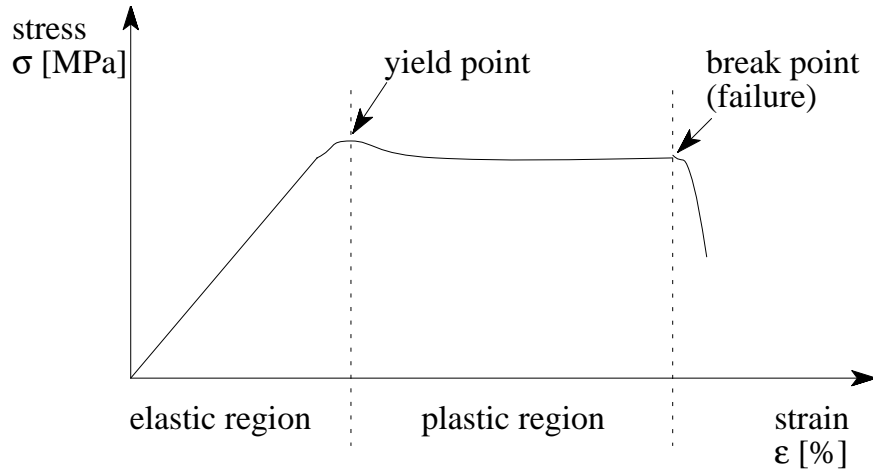


Figure 3.1: Typical stress vs strain behaviour of thin nylon film (from [76]). A reversible elastic elongation (stretch) is followed by an irreversible, plastic deformation (creep) at a particular value of the applied stress. Eventually, the film breaks.

the event reconstruction in CTF is more complicated since photons cross a pseudocumene-nylon-water interface before they reach the photomultiplier tubes.

By using a sub-millimeter thick film, one can minimize the total mass of the vessel. This implies a corresponding reduction of its intrinsic radiopurity requirements. Nonetheless, strict material selection and screening was undertaken in order to identify the cleanest possible nylon. The biggest problems are posed by  $\gamma$  rays emitted by  $^{40}\text{K}$  and by isotopes along the  $^{238}\text{U}$  and  $^{232}\text{Th}$  chains that could penetrate into the fiducial volume of the detector. The amount of  $^{222}\text{Rn}$  emanated by  $^{226}\text{Ra}$  in the material and possible wash-off of  $^{210}\text{Po}$  present on the nylon surface following  $^{222}\text{Rn}$  exposure must also be minimized. It has been found that plastics produced by extrusion can be made more radiopure than cast ones, most likely due to releasing agents (typically high in potassium) [76]. Details of the purity of nylons for Borexino are reported in section 3.2.

The radon diffusion rate through nylon films has also been carefully addressed and weighed in selecting the appropriate material for Borexino. The double nylon vessel design is specifically meant to minimize the amount of radon reaching the center of the detector. It was found that the diffusion coefficient for dry nylon is  $\sim 10^{-12} \text{ cm}^2 \text{ s}^{-1}$ , while the value

for wet nylon is two orders of magnitude higher [76, 87]. The increased diffusivity with humidity poses some constraints on the operating humidity conditions for Borexino when the  $^{226}\text{Ra}$  contamination is at the limit of specifications, as discussed in section 3.2.

The use of a thin membrane also allowed construction of the nylon vessels in a clean room environment, instead of *in situ* inside the SSS. Assembly in a clean room guarantees very low particulate contamination. In addition, a newly designed radon filter has been inserted along the makeup air line that feeds the vessel construction clean room, reducing the radon exposure of the vessel surfaces (see chapters 4 and 5). Finally, the vessels enter the sphere as deflated balloons, already nested into one another. Nesting makes vessel fabrication harder but the presence of the OV as a sealed bag around the IV combined with the use of very clean gas for inflating them further controls contamination of the surfaces of the IV during production, shipping, and installation.

For reference, a very detailed review of nylon properties and applications is found in [85].

## 3.2 Design and specifications of the nylon vessel system

The Borexino IV and OV are made, respectively, of 36 and 40 separate panels cut out and glued to one another to form a sphere (once inflated). The gluing technique uses a resorcinol solution sprayed onto the joint surfaces, followed by tight clamping for several hours (discussed further in chapter 6). The thickness of the nylon film is  $125\ \mu\text{m}$ .

### 3.2.1 Film strength and handling

The typical tensile strength for dry nylon of this thickness is 70 MPa, which drops to about 20 MPa at 50% RH (room temperature) [86]. When the viscoelastic behaviour of the membrane (or “creep”, the plastic region in fig 3.1) is considered, the maximum stresses on the nylon vessels foreseen during Borexino are approximately 3 MPa (for maximum temperature differences between the scintillator and buffer regions of  $5\ ^\circ\text{C}$  [88]). The thickness not only plays a role for mechanical tensile strength, but also for brittleness (fragility under folding). As everyone has probably experienced with shopping bags, thin films do not crack easily.

The Borexino vessels are below the so-called critical thickness [86], above which a polymer film tends to crack when folded with a radius of curvature comparable to its thickness. A third parameter considered for the design and assembly of the vessels is the glass transition temperature of nylon, at which a second order phase transition occurs in polymers [89]. The transition temperature is highly dependent on relative humidity; it separates polymer phases characterized by glassy/brittle and rubbery/supple state properties. The assembly and handling of the vessels is performed at high humidities ( $> 50\%$  RH), such that the glass transition temperature is lower than ambient temperature. Radon diffusion through nylon increases with humidity. To limit contamination, the vessels' humidity will be reduced ( $\leq 10\%$ ) once installed and inflated inside the detector. Full-scale inflated prototypes are shown in fig. 3.2.

### 3.2.2 Cleanliness and radioactivity

The limit on tolerable radioactivity contamination on the IV is determined by the number of extraneous, irreducible events in the neutrino energy window (250-800 keV) considered acceptable ( $\sim 10$  events per day in the scintillator, see section 2.3). The fact that a  $^{238}\text{U}$  and  $^{232}\text{Th}$  concentration of  $10^{-17}$  g/g in the scintillator contributes 1 decay/day for each element in the radioactive chains in the central 100 tons of the detector (the so-called “fiducial volume”) is taken as a reference for determining the cleanliness and radioactivity requirements for Borexino.

**Cleanliness levels:** Constraints on uranium and thorium levels in the scintillator can be directly translated into a cleanliness requirement for the inside surface of the IV, since all particles on the IV can potentially wash off into the liquid volume. If one assumes that all vessel contamination is from “dust” (typically 1 ppm U, Th), a limit of 3 mg of particles distributed over the nylon can be tolerated. Under conservative assumptions described in [90] a surface cleanliness specification of Level 25 Mil. Std. 1246C [91] or better must be maintained over the entire inside vessel surface.



Figure 3.2: Full scale prototypes of the Borexino Inner Vessel (top) and Inner+Outer Vessels nested set (bottom). The two vessels are respectively 8.5 and 11 m in diameter, and were inflated inside Princeton's indoor gymnasium, the only building on campus able to accommodate their size when inflated. The diameter of the final Borexino OV is 11.5 m.

**Intrinsic nylon radioactivity:** Gamma activity from impurities embedded in the nylon membrane must be limited.  $\gamma$  rays from  $^{40}\text{K}$  and from the  $^{238}\text{U}$  and  $^{232}\text{Th}$  decay chains (among which are those emitted by  $^{214}\text{Bi}$ ,  $^{208}\text{Tl}$ , and  $^{228}\text{Ac}$ ) can release some or all of their energy inside the scintillator and be a background for Borexino (the attenuation length for a 1 MeV  $\gamma$  ray in PC is 25 cm). Assuming intrinsic uranium and thorium concentrations in the nylon on the order of  $10^{-12}$  g/g and a total potassium concentration  $K_{nat} \sim 10^{-8}$  g/g,  $\sim 150$   $\gamma$  events/day above 250 keV are expected in the IV. This number drops to 0.05 events/day in the central 100 tons of scintillator, which represents a completely acceptable value for Borexino [76].  $\alpha$  and  $\beta$  decays at the IV radius do not pose the same problem since they do not reach the core of the detector (a 1 MeV electron travels  $\sim 1$  cm) and can be eliminated from the data by a volume cut. The intrinsic concentrations required for the nylon film of the IV are:

- $10^{-12}$  g/g or lower for  $^{238}\text{U}$  and  $^{232}\text{Th}$
- $10^{-8}$  g/g or lower for potassium.

**Radon emanation:**  $^{222}\text{Rn}$  produced in the  $^{238}\text{U}$  decay chain can emanate from the nylon surface and diffuse into the scintillator. Its decay and those of its daughters represent a background for detecting solar neutrino interactions. A 1 ppt ( $10^{-12}$ )  $^{238}\text{U}$  contamination in nylon will give  $\sim 13$  events/day in the central 100 tons of scintillator from emanated  $^{222}\text{Rn}$  (when secular equilibrium in the chain is assumed) [76]. The  $10^{-12}$  limit on uranium stated above thus meets radon emanation requirements as well. A  $^{238}\text{U}$  content up to 10 ppt could probably be tolerated for Borexino (this relies on  $> 90\%$  efficiency in identifying  $\alpha$  events and  $^{214}\text{Bi}$ - $^{214}\text{Po}$   $\alpha - \beta$  delayed coincidence events) [76].

**Radon contamination:** A separate source of contamination for the vessel surface is from radon daughters. When  $^{222}\text{Rn}$  decays in proximity of the vessel, its daughters can deposit on the nylon film and eventually wash off into the scintillator they come in contact with. It is important to minimize direct exposure of the vessel surface to air (that naturally contains significant amounts of radon) during construction, shipping, installation, and fluid operation

inside the SSS. The maximum allowed radon exposure and related issues are discussed in section 3.4.

Stringent limits on intrinsic radioactivity and radon emanation also apply to all components of the vessel system close to the scintillator. These include the mechanical support structure and the ropes for the hold down system.

### 3.2.3 The mechanical support structure

At each pole of the vessels is a set of concentric pipes for connection to the SSS, WT, and to the fluid handling plants. These pipes carry the scintillator and buffer fluid into the IV and OV, as well as functioning as the main mechanical support for the vessels (see fig. 3.3). Designing the transition between the vessels and the pipes has been an intense R&D effort. The problem was to have a low-mass, mechanically resistant structure that would meet the IV leak tightness specifications under design load. The basic philosophy that drove the design is to have the polar assemblies (also referred to as the “end regions” in the following chapters) stronger than the nylon membrane (i.e. the film would fail first, preserving the mechanical integrity of the supporting structure). Considering a nylon film’s Young modulus of 50 MPa, the end regions have to withstand a 300 kg (3000 N) load.

The nylon membrane of the IV is glued onto a bulk nylon ring (the so-called “end caps”). A nylon corona-shaped “bridge” film connects the ring to the bulk nylon internal pipe. An IV end region can be seen in fig. 7.8. The OV end caps have a similar design, but they have a solid nylon disk instead of the nylon bridge film (see fig. 6.11). From the OV outwards the two pipes are coaxial. The final section of such pipe is made of stainless steel, appropriately pickled and passivated to avoid long-term corrosion. The roughness of its surface was carefully minimized to avoid particulation. Metal struts connect the nylon rings of both vessels to the coaxial pipes for mechanical strength (copper for the IV, stainless steel for the OV). The particular design of the tube assemblies was driven by minimization of the total mass and utilizing the most radiopure materials (nylon and copper) close to the IV. All materials used in the “tube assemblies” (end caps + pipes) underwent strict radiopurity screening. All IV pipe sections were precision cleaned by AstroPak [92] and their surfaces

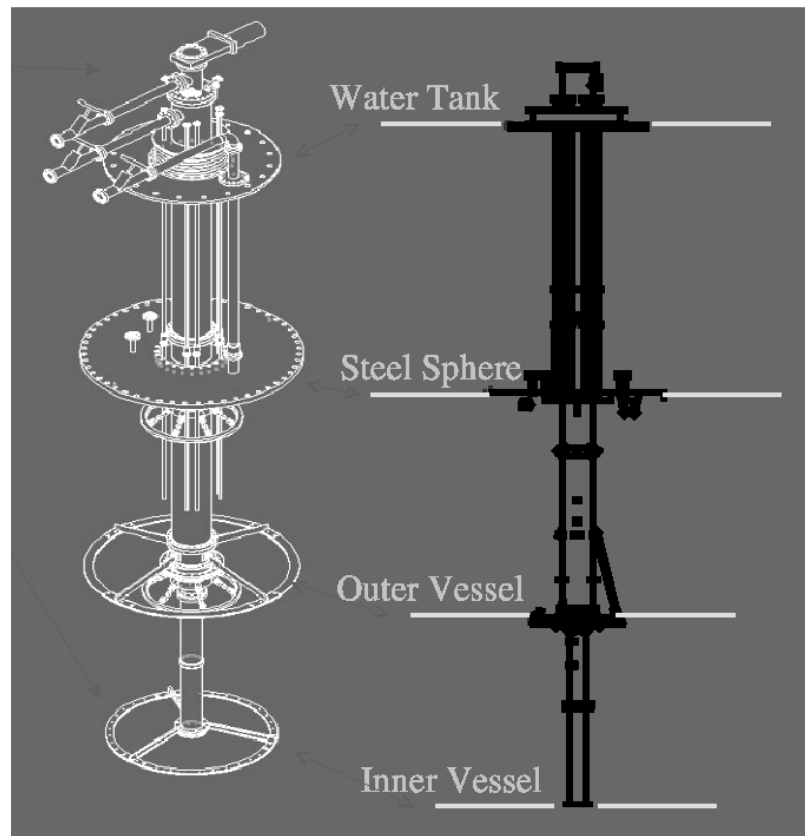


Figure 3.3: Drawing of the north pole tube assembly, with the coaxial pipe section and the two end caps connecting to the IV and OV nylon envelopes. The final OV vessel has a solid nylon disk instead of a nylon “bridge” film. The diagonal struts connecting the nylon rings and the coaxial pipes are not shown.

certified to Level 25 (Mil. Std. 1246C [91]). The radiopurity of all the components of the vessel system are analyzed in depth in [76]. Details of the design and construction of the end regions are presented in chapter 6.

### 3.2.4 Leak tightness requirements

The IV as a whole (including the end caps) must also satisfy certain leak tightness specifications. If scintillator (with PPO) leaks into the quenched buffer region, it will cause undesired scintillation outside the IV. The light yield of a PC+DMP+PPO solution as a

function of PPO concentration is what dictates the tolerable leak rate [67]. A limit of 10 ppm of PPO in the buffer has been considered acceptable in terms of event reconstruction and total event rate of the experiment. Conservatively speaking, if the detector remained in a steady-state condition for 10 years without fluid purification, a leak tightness limit on the IV can be set [96]:

$$\text{tolerable IV leak rate} \sim 10^{-2} \text{ cc/s (liquid)} \quad (3.1)$$

The specification set for the OV is based on the philosophy that its leak rate should not be more than two orders of magnitude above that of the IV, i.e:

$$\text{tolerable OV leak rate} \sim 1 \text{ cc/s (liquid)} \quad (3.2)$$

Results from bench top leak checking of the IV and its end regions are reported in chapter 6. A final and possibly more definitive leak checking is planned after the vessels are installed inside the SSS.

### 3.2.5 The hold-down ropes

Due to the density difference between the scintillator and buffer solutions, the IV will experience an upward buoyancy force of approximately 2750 N (see section 3.3). Other deviations from the neutrally buoyant conditions are due to temperature-driven density fluctuations (see section 3.3.2), on the order of

$$\frac{1}{\rho} \frac{d\rho}{dT} \sim 0.1\% (\text{°C})^{-1} \quad (3.3)$$

Temperature differences between the liquid volumes will determine a buoyancy and stress the vessels. The direction of such force can be in either direction and it applies to both vessels (given the bigger size, the OV is subject to higher stresses). The Borexino vessels are designed to withstand an averaged temperature difference between fluid volumes separated by the nylon vessels of 5 °C. Applied to the IV it translates into a 12500 N buoyant force; for the OV it could be as high as 24000 N. Realistically, during fluid operations, it is hard to imagine a sudden and abrupt temperature difference between the scintillator and the

buffer or between the two buffer regions of this magnitude; the design specifications should be considered very conservative.

In order to maintain their position, each vessel is wrapped by two sets of low radioactivity ropes that limit their upward and downward movements respectively [93]. The ropes are made of Tensylon, an ultra-high molecular weight polyethylene polymer [94]. Each rope (two sets of 18 and 20 for the IV and OV respectively) is attached at both ends to the stainless steel vessel support pipes. A set of 6 (8) strain gauges at each pole of the IV (OV) measures their tension; summing the tension for all ropes of a vessel and dividing it by  $\cos \theta_x$  ( $x = \text{IV}, \text{OV}$ ) gives the value of the buoyancy force acting on it. The nominal angle of incidence of the ropes on the support pipes is

$$\theta_{\text{IV}} = 58^\circ; \quad \theta_{\text{OV}} = 53^\circ \quad (3.4)$$

The readings from the gauges (or load cells) are logged by the online monitoring system. The ropes are designed to be stronger than the nylon membrane. In the 5 °C design limit described above the IV (OV) ropes have to withstand a 650 (1000) N tension. The effect of creep, always present with any load, no matter how small, is acceptable for the expected lifetime of the experiment ( $\sim 10$  years). A detailed discussion of the mechanical and radiopurity properties of the rope system and its compatibility with pseudocumene is given in [95]. A sketch of the rope system is shown in fig. 3.4; a picture of an installed IV load cell assembly is found in fig. 6.8.

### 3.2.6 Monitoring instrumentation

Completing the vessel system are various monitoring devices. Four load cells at each pole (in addition to those connected to the ropes) will measure elongations along the pipes (one is shown in fig. 6.8). Temperature sensors are deployed in various positions to measure the temperature of the fluids inside the SSS. The sensors will be installed on the vessel system at LNGS, before it is installed in the detector. Three sensors will be placed along the stainless steel pipe close to the OV end cap, just inside the SSS and in an intermediate position between these two. Placing a sensor just inside the OV is still under consideration.

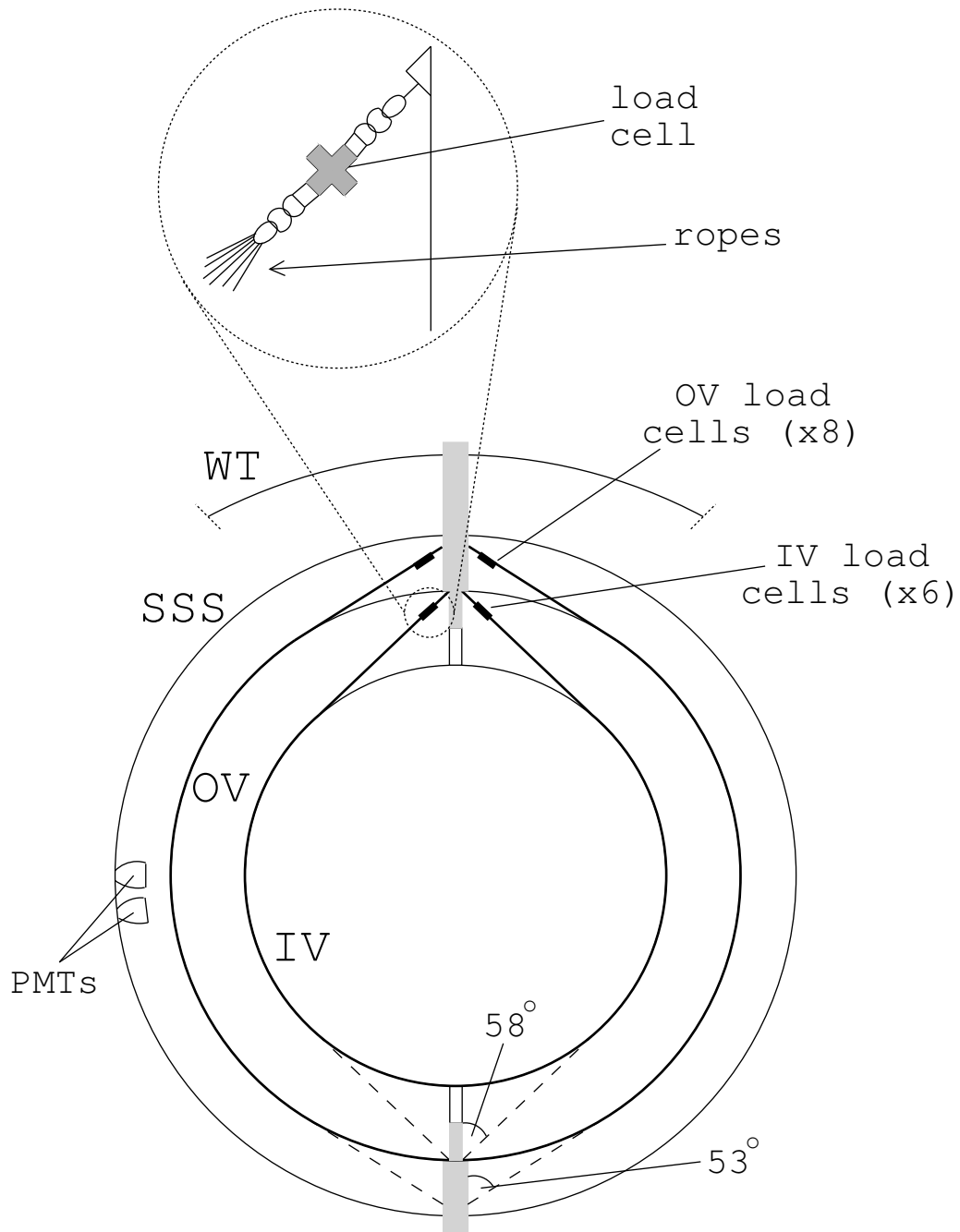


Figure 3.4: Schematic representation of the Borexino hold-down rope system. There are two sets of 18 (20) ropes on the IV (OV). The ropes attached to the north pole hold the vessels against downward buoyancy, and viceversa. Each rope wraps around the vessel and is attached at both ends to a load cell that measures its tension. Six (five) rope ends are connected to each load cell for the IV (OV). The sum of the readings from all load cells from a vessel, divided by the cosine of the angle the ropes make with the pipes (nominally  $58^\circ$  and  $53^\circ$  for the IV and OV), gives its total buoyancy force. The south pole load cells are not shown for simplicity. An IV load cell assembly is shown in fig. 6.8.

The sensors are Pt 100 (Pt resistance of 100  $\Omega$ ) in a stainless steel enclosure complemented with a welded stainless steel conduit with 4 copper wires in MgO insulation [97].

A set of light sources is placed on the surface of both vessels for scintillator and vessel monitoring purposes. They are meant to monitor the position of the vessels using red light from LEDs and the Borexino digital cameras. A subset of such light sources will be used to monitor the scintillation properties of the scintillator close to the IV. This system is extensively described in chapter 7.

### 3.2.7 The CTF inner vessel

A separate discussion applies to the CTF inner vessels. These are meant to withstand a much higher upward buoyancy force due to the density difference between PC and water ( $\sim 500$  kg for 4 m<sup>3</sup> of PC). They are made of a Durethan C38F nylon 6 copolymer by BASF [98], 500  $\mu\text{m}$  thick. This film is significantly stiffer than the film of the Borexino vessels. The CTF vessels were built in a spherical shape inside the clean room, since they could not be folded flat. Only one set of hold-down strings is needed, given the unidirectionality of the buoyancy force (see fig. 2.11).

## 3.3 Scintillator solution density

Knowing the densities of the scintillator and buffer fluids is extremely important for the design and the operation of the nylon vessels. Every part in ten thousand density difference between the inside and the outside of the IV corresponds to a net buoyancy force of approximately 300 N.

The density of PC+PPO and PC+DMP solutions relative to pure PC has been measured at room temperature for a variety of concentrations, including the ones foreseen for operating Borexino (1.5 g/ $\ell$  for PPO, 5 g/ $\ell$  for DMP). This measurement allows one to know precisely the contribution of the density differences to the overall buoyancy forces acting on the vessel. An accurate knowledge of the solution densities also allows defining, if needed, operating scenarios where a definite buoyancy is maintained between the various fluid volumes through

a careful control of the concentration of the solutions in different regions of the Borexino detector.

### 3.3.1 Experimental apparatus and procedure

The measurements have been carried out via hydrostatic methods, using a 1-liter glass jar connected to a long, removable glass graded neck with a resolution of 0.01 ml. The exact, absolute volume of the jar was not known: it was not needed for measuring relative density differences between the various solutions. The net weight of equal volumes of the different solutions were measured using a scale with 0.01 g accuracy that guarantees a  $1:10^4$  sensitivity on a 1 liter sample (a density differences of 1 part in  $10^4$  between the scintillator and the buffer fluids corresponds to 300 N of buoyancy force on the IV). The ratio of these values yields their relative densities. The measurements took place in a room with very good temperature stability for a period of weeks ( $\sim 22$  °C). The temperature variations were on the order of 0.1 °C or less. To minimize the systematic error due to these fluctuations, each solution was weighed at different times during the day and the measurements were averaged.

### 3.3.2 Measurement and results

The densities of pure PC (Pseudocumene or 1,2,4-Trimethylbenzene), DMP (Dimethylphthalate) + PC solutions at 5, 10 and 20 g/l and PPO (2,5-Diphenyloxazole) at 1.5 and 3 g/l were measured at 22 °C relative to each other. Table 3.1 shows the raw data and the errors considered for all the data points; the densities of the various solutions relative to the pure PC density are shown in fig. 3.5.

The data show that the densities of both the PC+DMP and PC+PPO solutions behave linearly as a function of solute concentration. Performing a linear fit for the relative density and constraining the point for pure PC to be strictly 1 gives:

$$\frac{\rho_{\text{DMP+PC}}}{\rho_{\text{PC}}} = 1 + (2.75 \pm 0.05) \times 10^{-4} \eta_{\text{DMP}} \quad (3.5)$$

$$\frac{\rho_{\text{PPO+PC}}}{\rho_{\text{PC}}} = 1 + (3.16 \pm 0.01) \times 10^{-4} \eta_{\text{PPO}} \quad (3.6)$$

Solute	Concentration (g/ℓ)	Error on concentration (g/ℓ)	Net weight (g)	Error net weight (g)	Temperature (°C)
none	0.000	0.000	919.16	0.081	22.1
DMP	5.000	0.250	920.44	0.081	22.1
DMP	5.116	0.009	920.51	0.081	22.1
DMP	10.109	0.013	921.88	0.081	22.1
DMP	20.269	0.021	924.19	0.081	22.1
PPO	1.500	0.075	919.60	0.081	22.1
PPO	3.006	0.076	920.03	0.081	22.2

Table 3.1: Data for the density measurements of PC+DMP (top five rows) and PC+PPO (bottom two rows) solutions. The error on the net weight is dominated by the 0.1 °C uncertainty on the temperature, which directly translates into an uncertainty in the volume by using the coefficient of thermal expansion of the solutions (assumed to be the same for all,  $\sim 8 \times 10^{-4}$  g/cm<sup>3</sup>/K).

where  $\eta_j$  ( $j = \text{PPO, DMP}$ ) is the solute concentration in g/ℓ. It is possible to estimate the density of a mixture of liquids from their individual densities and concentrations, neglecting any new interaction between the molecules of the two species. Taking 0.88 g/cm<sup>3</sup> and 1.19 g/cm<sup>3</sup> for the densities of PC and DMP at room temperature respectively (see for example [99]) one obtains

$$\frac{\rho_{\text{DMP+PC}}^{\text{th}}}{\rho_{\text{PC}}} = 1 + 3 \times 10^{-4} \eta_{\text{DMP}} \quad (3.7)$$

which is within 9% of the measured value (eq. (3.5)). With this information one can compute the relative density between any two solutions. An important number is the relative density between the 1.5 g/ℓ PPO+PC and 5 g/ℓ DMP+PC solutions, since these are the foreseen scintillator and buffer concentrations for Borexino. Equations (3.5) and (3.6) with  $\eta_{\text{PPO}} = 1, 5$  g/ℓ and  $\eta_{\text{DMP}} = 5$  g/ℓ yield

$$\frac{\rho_{\text{scintillator}}}{\rho_{\text{buffer}}} = 1 - (9.01 \pm 0.25) \times 10^{-4} \quad (3.8)$$

The coefficient of thermal expansion of pure PC, of the scintillator solution (1.5 g/ℓ PPO),

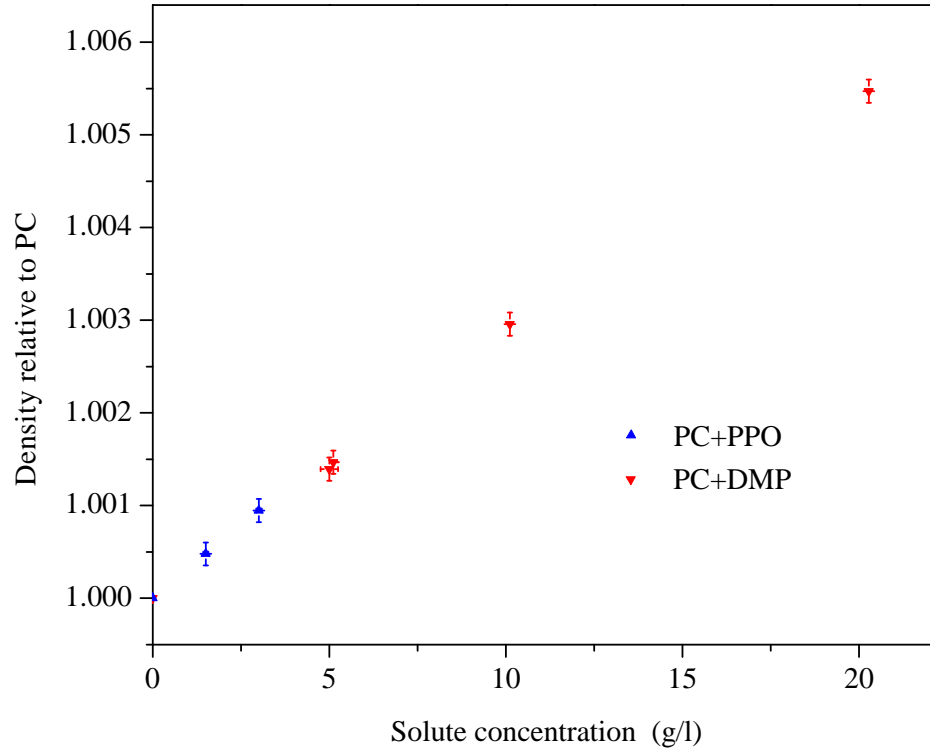


Figure 3.5: Density of PC+DMP (red, downward triangles, data points from 5 g/ℓ and above) and PC+PPO (blue, upward triangles) solutions at various concentrations relative to the density of pure PC taken at 22.1 °C.

and of the buffer solution (5 g/ℓ DMP), measured by J. Benziger, is  $\sim 8 \times 10^{-4}$  g/cm<sup>3</sup>/K for all three fluids [100]. The data do not allow to differentiate this parameter for the different solutions (see fig. 3.6). The density difference between the scintillator and the buffer fluids in eq. (3.8) corresponds to a temperature difference of approximately 1 °C.

The error bars shown in fig. 3.5 are almost completely due to the effects of the uncertainty on the temperature; they reflect a conservative error on the temperature of 0.1 °C with the reported coefficient of thermal expansion for PC (assumed essentially the same for all the solutions). The data suggest that the uncertainty on the temperature might be smaller than that assumed. The errors on the solution concentrations, on the weight and on the volume differences of the samples have a typically smaller effect.

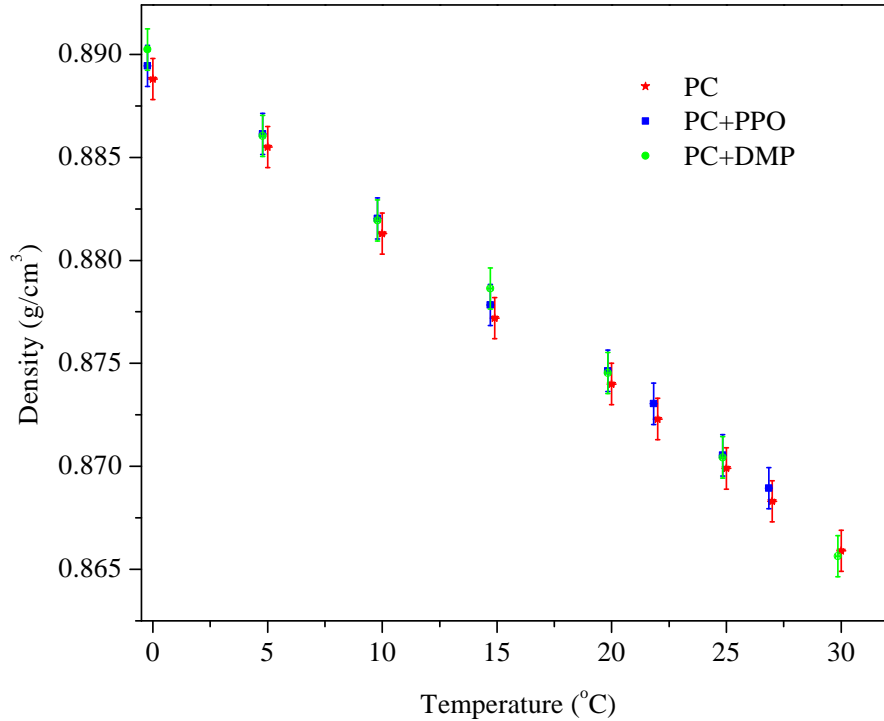


Figure 3.6: Density variations versus temperature for DMP and PPO solutions in PC [100]. The slope defines the coefficient of thermal expansion ( $\sim 8 \times 10^{-4} \text{ g/cm}^3/\text{K}$ ). The errors on each data point do not allow to distinguish between pure PC, the scintillator, and the buffer solutions.

Another potentially uncontrolled source of error could have been presented by the density variations of the PC samples used in the measurement: specifically, the PC used for the PPO solutions and for one of the 5 g/l DMP solutions came from one bottle, while that used for all the other solutions came from a different bottle of the same distillation batch. The pure PC and the DMP+PC solutions data points are the result of adding an increasing amount of DMP to the same PC sample in order to minimize errors due to possible non-uniformities in the density of pure PC. The data clearly show that the different "history" of the PC used is not an appreciable source of error (see for example the two data points for 5 g/l PC+DMP solutions).

Another factor that has been considered and checked for is the possible difference in water content of the samples, which could alter the density value. Several measurements were made with a moisture analyzer [101] and all the values were between 42 and 84 ppm, thus consistent with equilibrium with air at 20-25% RH measured in the lab (for a measurement of the moisture content in PC refer to [86]). As a reference, assuming a simple two-liquid mixing each with its density, without further interactions, a 50 ppm water content in PC would cause a density difference  $\sim 6 \times 10^{-6}$  relative to dry PC and therefore is not an appreciable source of error for these measurements. Furthermore, in the worst possible case in which no knowledge of the water content of the samples is possible, the maximum density variation to be expected between water-saturated PC ( $\sim 400$  ppm by weight) and dry PC is  $\sim 5 \times 10^{-5}$ .

### **Buoyancy force on the Inner Vessel from density differences**

From equation 3.8 the buoyant force on the Inner Vessel due to the density difference of the scintillator and buffer solutions can be computed. The nominal volume of the IV is 321 m<sup>3</sup>. At room temperature, the density of PC is 0.875 g/cm<sup>3</sup> (see fig. 3.6), which yields an upwards buoyant force of approximately 2750 N.

### **Density differences and leak rates**

Leak paths can change the buoyancy force on the Inner Vessel by allowing mixing of the scintillator and buffer solutions. The maximum tolerable liquid leak rate for the Borexino Inner Vessel is  $10^{-2}$  cc/s. This leak rate is set by the upper limit on the PPO concentration considered acceptable in the Inner Buffer Region without threatening the performance of the detector. PPO in the buffer would cause unwanted scintillation, while DMP inside the IV would quench the neutrino signal [67]. A simple model is used to estimate the effect of such a leak on the density differences between the Inner Vessel and the buffer region. The first assumption is to consider leaks from the scintillator volume into the buffer only; this means that the Inner Vessel is always filled with the nominal 1.5 g/l PC+PPO solution. The second condition is to assume that the PC+PPO volume replaces an equivalent PC+DMP

volume in the Inner Buffer region (contained between the two nylon vessels); no leaks are considered between the Inner and Outer Buffers, so that the Outer Buffer is constantly filled with the initial 5 g/ℓ PC+DMP solution. Supposing that the  $10^{-2}$  cc/s leak rate condition is allowed to evolve for 10 years with no fluid operation, 3.2 m<sup>3</sup> of PC+PPO solution will have leaked out into the Inner Buffer. The Inner Buffer volume is 285 m<sup>3</sup>, so the density change in this region after 10 years would then be [102]

$$\Delta\rho_{\text{IB}} \sim 10^{-5} \text{ g/cm}^3 \quad (3.9)$$

This has the effect of reducing the buoyant load by approximately 1% and corresponds to negligible temperature fluctuations of about 0.01 °C. If one considers more realistic two-way leaks (i.e. PC+DMP solution leaking into the Inner Vessel as well), this effect is amplified by roughly a factor of two, and remains negligible. The effect of these variations is at least 10 times smaller than any controllable temperature fluctuation and is therefore not a concern in terms of the mechanical stability of the Borexino nylon scintillator containment vessels.

### 3.4 Radon contamination and requirements for the nylon vessels

Extensively described in section 3.5, the clean room for vessel assembly was designed with the radon problem in mind. It is worth briefly and specifically examining how the presence of radon during vessel construction can be dangerous for Borexino.

The vessel construction process involves joining long, flat nylon panels together on an assembly table in the clean room (fig. 3.10). The contamination from radon exposure of the nylon surfaces is as follows: <sup>222</sup>Rn atoms in the air column above the assembly table  $\alpha$ -decay; the resulting <sup>218</sup>Po ions plate out on the surface and eventually decay into long-lived <sup>210</sup>Pb ( $\tau_{1/2} \sim 20$  years). The plate out mechanism could clearly involve the other intermediate daughters, <sup>214</sup>Pb, <sup>214</sup>Bi and <sup>214</sup>Po as well (the complete <sup>238</sup>U radioactive chain is shown in fig. 3.7). Once the detector is filled, <sup>210</sup>Pb or its daughters on the inner surface

of the Inner Vessel could then wash off into the scintillator.  $^{210}\text{Bi}$  and  $^{210}\text{Po}$  nuclides could also re-emit into the scintillator at the time of the decay that produces them. Once in the liquid medium, they could freely reach the “fiducial volume” where it would produce background events, some of truly irreducible nature. Of particular concern are the  $\beta$ -decays of  $^{210}\text{Bi}$ : with an end-point energy of 1.14 MeV, electrons from this source would easily be mistaken for  $\nu - e$  scattering events in the energy region of interest for Borexino. Hopes of tagging these events by associating them with the subsequent  $\alpha$  particle emitted by  $^{210}\text{Po}$  are shattered by the long half-life of this decay ( $> 100$  days, during which any spatial and time correlation of the two events would be lost).

Borexino is expected to detect up to  $\sim 50$   $\nu - e$  scattering events generated by solar  $^7\text{Be}$  neutrinos per day in the 100-ton scintillator central fiducial volume. A reasonable working platform is to require  $< 1$  count/day from radon contamination of the Inner Vessel in the same volume. The rest of the section is dedicated to estimating how much radon contamination can be tolerated to meet this requirement.

An estimate for the amount of radon allowed in the clean room air can be obtained with a simple calculation, as follows. All the inner surface  $S$  of the Inner Vessel will on the average be exposed to the clean room atmosphere for a time  $t$ . Suppose that a fraction  $p$  of the radon decay daughters present in the air column of height  $h$  above the vessel during this time will stick to the surface (plate out) and that a fraction  $w$  of them will later transfer from the inner surface of the IV into the scintillator (wash off). Assume that the average radon concentration in the clean room is  $A_{\text{air}}$ . It follows that  $[p(S)h](A_{\text{air}}t)$   $^{210}\text{Pb}$  atoms will deposit on the IV surface and that  $[pw(S)h](A_{\text{air}}t)$  will eventually end up in the scintillator. Substituting in the values for the IV and the clean room, ( $S = 227 \text{ m}^2$ ,  $h = 3 \text{ m}$ ) we get

$$2.5 \times 10^6 (w p A_{\text{air}} t) \quad ^{210}\text{Pb} \text{ atoms on IV surface,} \quad (3.10)$$

where  $A_{\text{air}}$  is expressed in  $\text{Bq}/\text{m}^3$  and  $t$  in hours. This translates into

$$215 (w p A_{\text{air}} t) \quad ^{210}\text{Bi}, ^{210}\text{Po} \text{ decays/day} \quad (3.11)$$

in the scintillator, where the mean lifetime of  $^{210}\text{Pb}$  (32.2 y) has been used ( $t$  expressed in

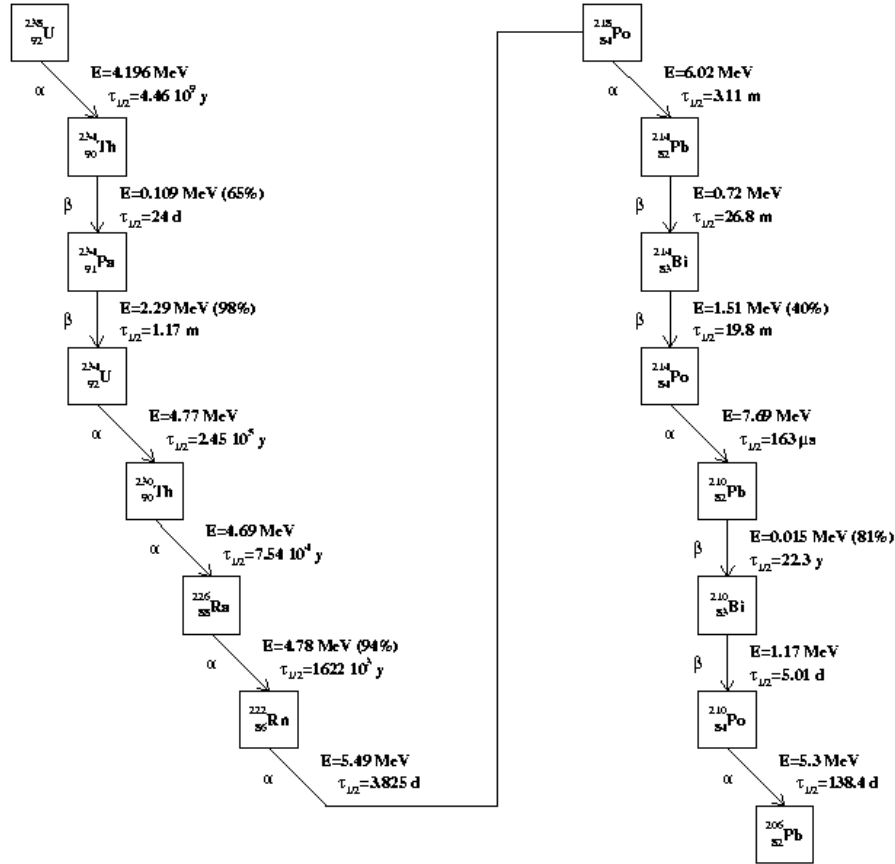


Figure 3.7: The  $^{238}\text{U}$  natural radioactive chain. The presence of the long-lived isotopes  $^{210}\text{Pb}$  and  $^{210}\text{Po}$  near the end of the chain makes radon contamination of low background detectors an enormous concern.

hours,  $A_{air}$  in  $\text{Bq}/\text{m}^3$ ).

The most conservative approach, without any knowledge of the plate out and wash off processes, is to assume  $p = w = 1$ . Considering  $30 \text{ Bq}/\text{m}^3$  to be a typical value for indoor air (see for example [103]),  $\sim 6500$   $^{210}\text{Bi}$   $\beta$  events/day (as well as  $^{210}\text{Po}$   $\alpha$  events) could occur in the scintillator, per hour of exposure of the entire IV surface (with 100% plateout and 100% wash off)!

Tests have been performed in Princeton to measure plate out and wash off fractions. Plate out rates measured using a mock clean room (essentially a box with a HEPA filter

for laminar flow) yielded a plate out fraction  $p \sim 1\%$  (deduced from the  $^{210}\text{Po}$   $\alpha$  activity alone) [104]. These measurements do not study with what efficiency individual radon daughters stick to the nylon surface. Wash off tests were also performed on nylon samples exposed to high radon levels. Only  $\sim 1\%$  of  $^{210}\text{Po}$  on the surface washes off in PC, which yields  $w \sim 0.01$  [105]. Using these values for  $p$  and  $w$ , eq. (3.11) becomes

$$0.02 (A_{\text{air}} t) \quad ^{210}\text{Bi} (^{210}\text{Po}) \text{ decays/day in the scintillator,} \quad (3.12)$$

where, as before,  $t$  is expressed in hours and  $A_{\text{air}}$  in  $\text{Bq}/\text{m}^3$ . From this estimate, for air at  $30 \text{ Bq}/\text{m}^3$ , the number of  $\beta$  decays (from  $^{210}\text{Bi}$ ) and  $\alpha$  decays (from  $^{210}\text{Po}$ ) expected in the scintillator per hour of exposure of the whole vessel surface is  $\sim 0.7$  events/day. The wash off data do not take the possibility of  $^{210}\text{Bi}$  or  $^{210}\text{Po}$  nuclides leaving the surface because of their nuclear recoil in the decay that produces them.

If one hour average exposure time is assumed for the IV during assembly, this value meets the Borexino specifications of less than 1 count/day from  $^{210}\text{Bi}$  and  $^{210}\text{Po}$  decay is the 100-ton fiducial volume.

Some care must be taken in evaluating the possible vessel contamination. The values for plate out and wash off should be taken as good indication rather than definitive measurements. For wash off in particular, there is still no unambiguous indication on long term effects in PC. Also, the effect of nuclides recoiling off the surface has not been quantified. From geometrical arguments alone, approximately half of the daughters could leave the surface at every step in the decay chain; the effect presumably also depends on the energy of the decay. This effect should be considered in quantifying the number of  $^{210}\text{Bi}$  and  $^{210}\text{Po}$  nuclides that end up in the scintillator. A conservative scenario is to assume that half of the  $^{210}\text{Bi}$  nuclides leave the surface in  $^{210}\text{Pb}$  decays and half of the  $^{210}\text{Po}$  nuclides leave the surface in  $^{214}\text{Bi}$  decays. In this case,  $w = 75\%$ . This would yield one  $^{210}\text{Bi}$  and 1.5  $^{210}\text{Po}$  decays/day in the scintillator.

Another unknown is the exposure time of the vessel. Assuming one hour as the average exposure time for the entire surface seems reasonable, but it must be confirmed by experience and relies on vessel handling and construction details. For these reasons, other

steps were taken to reduce radon exposure of the nylon film during vessel construction. One is to keep the surface covered as much as possible with thin sheets of clean nylon during most of the construction phase (see section 6). This is clearly a very effective technique, although it is difficult to quantify its efficiency. Another is to supply the clean room with radon-suppressed air, reducing the contamination source in the first place. Eliminating radon from the air around the nylon film is conceptually the most direct way to reduce the contamination. It is also the one that depends the least on operational procedures and possible human errors. The difficulty is represented by developing a device that can radon-filter the amount of air needed to operate the clean room (see chapters 4 and 5).

Finally, there is a tentative plan to spray wash the inner surface of the IV with high purity water after it is installed inside the SSS and inflated. It has been shown in laboratory tests that  $^{210}\text{Po}$  contamination can be reduced by approximately a factor of two by thorough rinsing with water [105].

A summary of the overall radon exposure of the IV surface after vessel construction is provided at the end of chapter 6; implications for Borexino are also discussed.

### 3.5 The Princeton clean room

The Princeton clean room for nylon vessel fabrication, manufactured by Control Solutions [106], is approximately  $22 \times 6.5 \times 4.5$  meters in dimension and was completed in 1999. It was built according to three main requirements which define it as a non-standard facility:

1. the recirculation blowers and ducts, as well as the air conditioning, humidification and water treatment equipment, are enclosed,
2. the room is as leak tight as possible,
3. the room is provided with an air lock vestibule along the entry path to be connected to a radon-suppressed air shower if needed.

A side view cross section is shown in fig. 3.8.

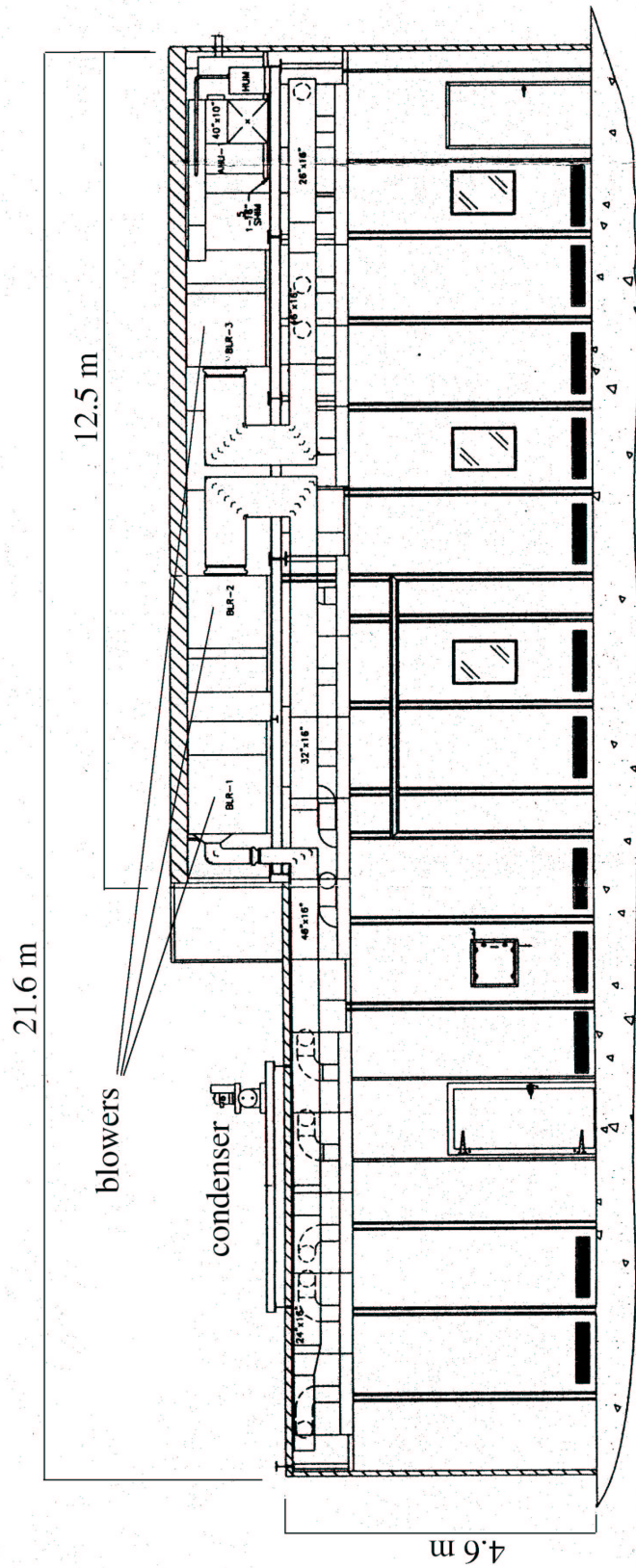


Figure 3.8: Longitudinal cross section of the Princeton clean room (as seen from inside, looking north-east). In the middle there is the big removable wall panel from which the assembled vessels exited the room. The enclosed plenum with the air handling unit and the blowers can be seen. The condenser is part of the cooling system for the air conditioning system. Drawing taken from [106].

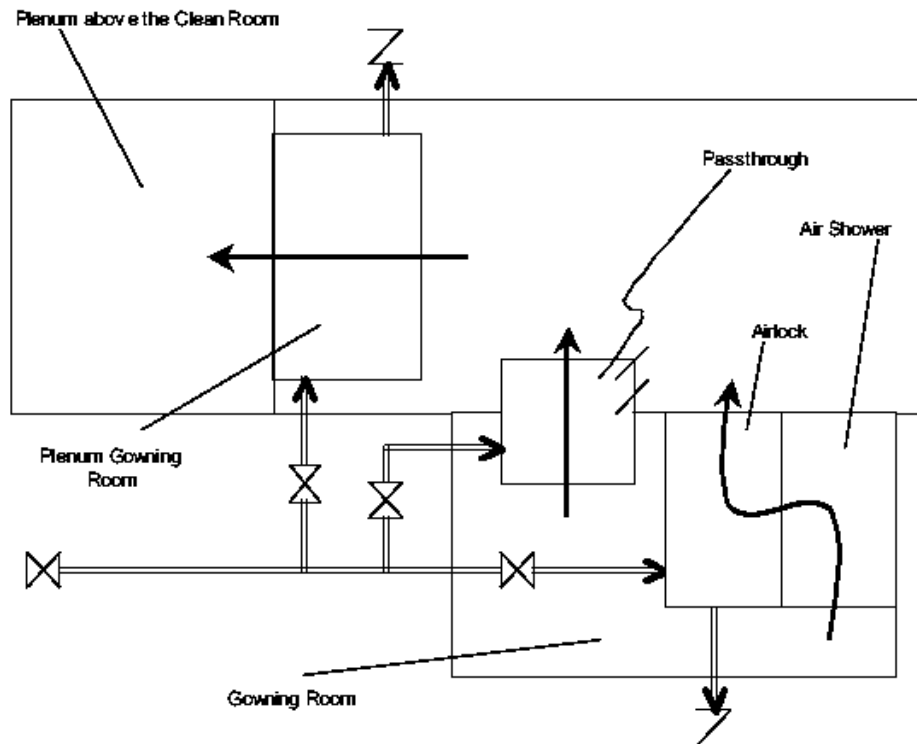


Figure 3.9: Paths (black arrows) through which ambient, radon-rich air could enter the clean room and reduce the effectiveness of radon suppression in the make up air stream. The sketch is a top view of the clean room but is not to scale; the exhaust check valves and the lines that were put in place for hook up to a radon-filtered air supply are shown. The air lock and the gowning room of the plenum have a volume of  $\sim 4.5 \text{ m}^3$ , while the pass-through is only  $\sim 200 \text{ l}$ .

All the conditions listed above were required in view of connecting the clean room input to a radon air filter. The filter would supply radon-suppressed make up air. The filter would be effective only if all sources of back-diffusion of radon from outside were very low. Enclosing the air handling equipment minimizes the amount of air to be radon-scrubbed, thus the size (and cost) of the filter. If the room is sufficiently leak tight, a relatively low make up air flow can pressurize it enough to essentially eliminate inward viscous air leaks.

The third condition in the list was put forward foreseeing a radon-free air shower for personnel entering the room. This looked like a potentially big radon contamination path, especially because people would each enter and exit the clean room many times per day.



Figure 3.10: Two views of the Princeton clean room where the Borexino Nylon Vessels have been assembled. The two tables, one per vessel, where the nylon panels of the appropriate size were glued together into spherical “balloons” are shown during the preparation phase (top). The size of the room and that of the tables can be appreciated; the air column height above the tables is approximately 3 meters. A set of Inner Vessel nylon panels laid out for humidification and the completed Outer Vessel envelope (covered, end caps not installed) is shown below (refer to chapter 6 for details).

Other ways radon-rich air could enter the room are by accessing the plenum area and via the pass-through, as shown in fig. 3.9. It was realized later that personnel access to the clean room didn't significantly affect the radon levels (see chapter 5), and so the radon-free shower was never fully implemented. Since it would have been a non-negligible effort to put it in place [107], no radon-free air shower was added. Two views of the clean room are shown in fig. 3.10. Details of the radon filter are discussed in chapters 4 and 5.

### 3.5.1 Clean room specifications

The clean room is certified to class 100 with 4-5 people working in it, and was measured to be around class 10 when unperturbed (the class of a clean room is the number of particles with diameter  $\geq 5 \mu\text{m}$  per cubic foot). This class in a big clean room is achieved by a very high recirculation flow rate ( $\sim 28 \text{ m}^3/\text{s}$ ) and very good laminarity of the air flow. Six blowers push the air through 84 HEPA filters uniformly distributed across the ceiling. The longer sides are built with double walls with 12 grids each that function as the return air path to the blowers. The volume of the clean room is  $\sim 770 \text{ m}^3$  and the turnover time of the air is then about 30 seconds.

The pressure of the clean room as a function of the make up air flow rate is shown in fig. 3.11. The plots suggest that when the recirculation blowers are running, the pressure of the plenum could drop negative with respect to the outside when the make up air flow rate is low. It is important that every part of the clean room be at a higher pressure than the outside to prevent radon backstreaming via viscous inward leaks. During vessel assembly, the make up air flow has constantly been above  $85 \text{ m}^3/\text{h}$  (50 cfm), as discussed in chapter 5.

The temperature and humidity are regulated by an air conditioning unit that treats  $\sim 4.5 \text{ m}^3/\text{s}$  of the recirculated air (approximately 1/6 of the total recirculated air flow). It takes three minutes to process a volume of air equal to the volume of the clean room. During this time, less than  $10 \text{ m}^3$  of fresh make up air have entered the room. The clean room can operate up to 50% RH at room temperature; normally, it runs at  $17 \text{ }^\circ\text{C}$ . The humidity control system first dries the air it processes. The water is filtered and passed under UV light to kill bacteria and reintroduced in the air flow with a vaporizer. Some

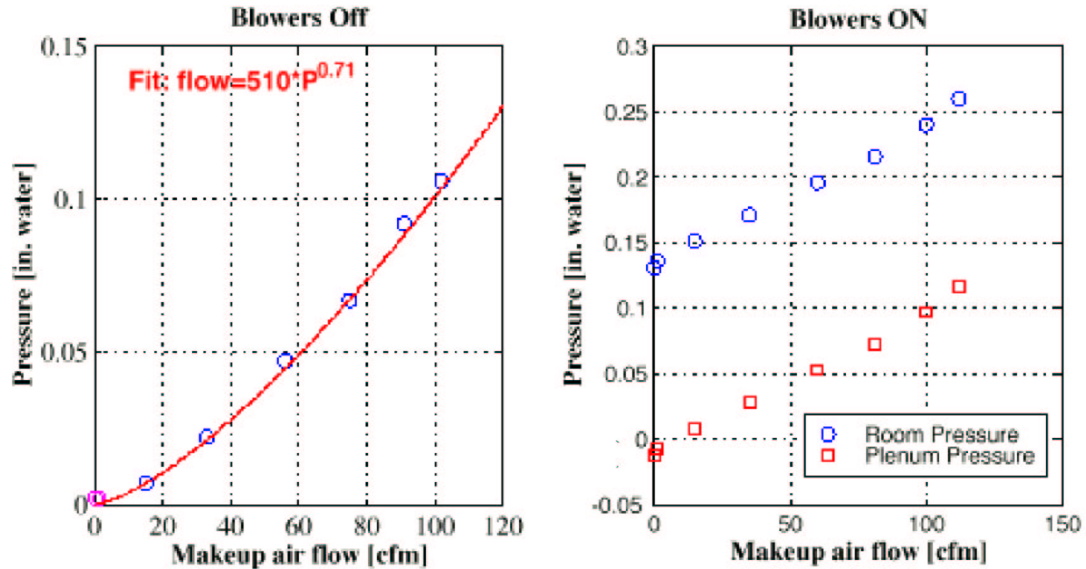


Figure 3.11: The pressure of the clean room for vessel assembly as a function of make up air flow rate. When the recirculation blowers are off, both the main room and the plenum sit at the same pressure; the recirculation blowers set a significant pressure differential between the main room and the plenum. To be safe against viscous inwards leaks it is necessary that the plenum be at a higher pressure than the outside when the clean room is running. As a reminder, 100 cfm equal  $47.2 \ell/\text{s}$  or  $170 \text{ m}^3/\text{h}$ . The plots are taken from [108].

water is lost in the process and has to be replaced. Depending on the humidity of the make up air that supplies the clean room, water is either eliminated or needs to be further added to meet the set value. During vessel assembly the make up air was very dry after passing through the charcoal filter for radon reduction (see chapter 5). In this case, water had to be continuously added, as explained in the next section.

### 3.5.2 The clean room water supply

High relative humidity (50-70%) is required for the air of the clean room in order to safely handle the nylon film during construction of the Borexino scintillator containment vessels (see section 3.2). The water needed to obtain this humidity level has to be added to the make up air, which will be fed to the room essentially dry; all the radon that is present in such water will be directly input into the clean room (this applies to any other contaminant,

such as radium, lead, etc.). It is then important to use low radon water for this purpose. Figure 3.12 schematically shows the water supply system and the air flow patterns of the Princeton clean room.

The temperature in the clean room is  $\sim 17$  °C (62 °F); at this temperature, 50% RH corresponds to 6000 ppm concentration by weight, which translates to  $\sim 1\%$  by volume or  $\sim 7$  g/m<sup>3</sup>. The volume  $V_{\text{cr}}$  of the clean room is approximately 770 m<sup>3</sup>, so that at any given time there are  $\sim 6$  kg of water in its air. For a make up air flow rate of 50  $\ell$ /s (100 cfm), the average time spent in the clean room by every gas molecule is 4-5 hours. Since the mean lifetime of <sup>222</sup>Rn is 5.5 days, the radon activity in the water in the clean room is that of the water as it is supplied (i.e. there is no significant aging of the air inside the clean room). The amount of water  $V_{\text{H}_2\text{O}}$  needed to humidify 50  $\ell$ /s make up air is 0.36 ml/s, or  $\sim 30$   $\ell$ /day (this number scales linearly with relative humidity).

It is useful to estimate the expected radon contribution from the humidification water. Let  $A_{\text{H}_2\text{O}}$  be its radon activity. The total radon activity  $A_{\text{cr, H}_2\text{O}}$  in the clean room air from this source is

$$A_{\text{cr, H}_2\text{O}} = \frac{A_{\text{H}_2\text{O}} V_{\text{H}_2\text{O}}}{V_{\text{cr}}} \quad (3.13)$$

where no significant aging is assumed, as explained above. We do not have a direct measurement of the radon content in the water supplied to the clean room. Information on the average and the seasonal variability of the radon concentration in drinking water released by the local water company is enough to set a very conservative upper limit of  $\sim 1000$  pCi/ $\ell$  (37 Bq/ $\ell$ ) [109]. For air at 50% RH and 17 °C, this would correspond to  $A_{\text{cr, H}_2\text{O}} \sim 0.3$  Bq/m<sup>3</sup>. The water supplied to the system comes from the cooling water loop of the decommissioned Princeton cyclotron; in the loop there is a 1500 gallon (5700  $\ell$ ) tank that actively works as an aging tank for radon. Water sits on the average more than 100 days, or  $\sim 20$  radon mean lives, in the tank. Considering the flow through a big reservoir, this implies that the radon concentration delivered to the clean room is 20 times lower than what initially enters the tank, which yields  $A_{\text{cr, H}_2\text{O}} \sim 15$  mBq/m<sup>3</sup> [110], under our conservative assumptions. This is an acceptable value for the Borexino vessels.

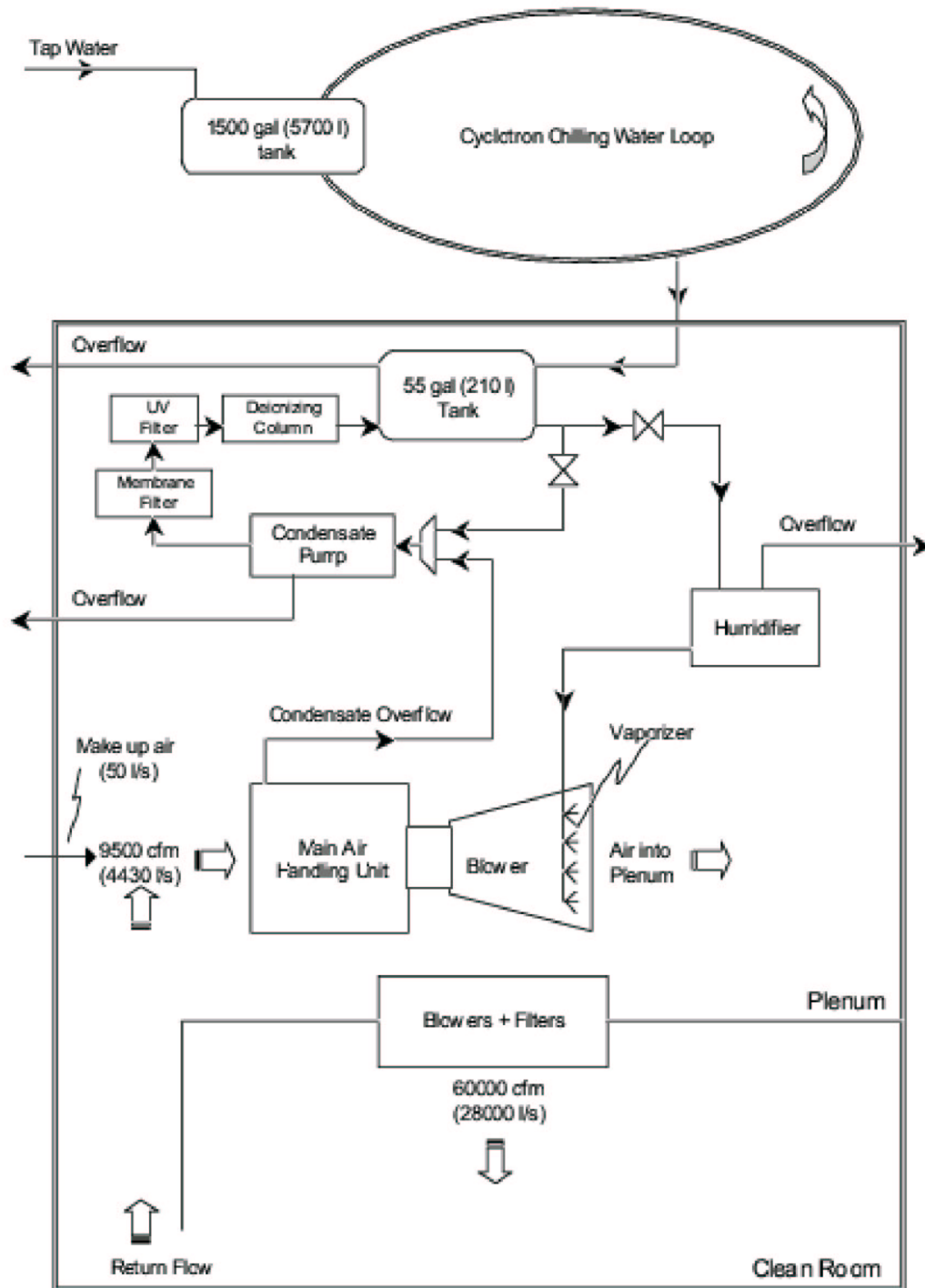


Figure 3.12: The water supply system and the air recirculation pattern of the Princeton clean room used for nylon vessel fabrication.

Details of the operating parameters and radon levels of the clean room during vessel assembly are presented in chapter 5.

---

## A Prototype Radon Filter for Air

A typical, recurring problem in low-background physics is the contamination of sensitive surfaces of experimental apparatus with the radioactive decay products of  $^{222}\text{Rn}$ . What makes radon particularly treacherous is its gaseous nature. Produced in the  $^{238}\text{U}$  natural chain (shown in fig. 3.7) and present in air in variable concentrations [103], it has a long enough lifetime to travel long distances and diffuse into practically any gap before it decays, leaving its long-lived daughters behind. For this reason in such experiments not only must the innermost materials be intrinsically extremely radiopure, but their manufacturing, storage and deployment must be carried out as much as possible in a radon-suppressed atmosphere. For comparison, thoron ( $^{220}\text{Rn}$ ) doesn't pose the same problem since all its daughters are short-lived and decay away in a few days (see the  $^{232}\text{Th}$  radioactive chain in fig. 4.1).

Various techniques are commonly adopted to solve this problem. Highly pure inert gases (e.g. nitrogen or argon) can be used to flush specific volumes of the detectors that must be kept radon-free. When air is specifically required, synthetic air (compressed or liquid) can be used. Each solution is viable, both technically and economically, given particular well-defined experimental conditions. Needless to say, nothing other than air can be used in places where people are supposed to work.

In this chapter the reasons for not adopting such techniques for the assembly of the Borexino Nylon Vessels are summarized, and the basic ideas behind the development of a prototype radon filter specifically designed for the purpose are explained. The features of the

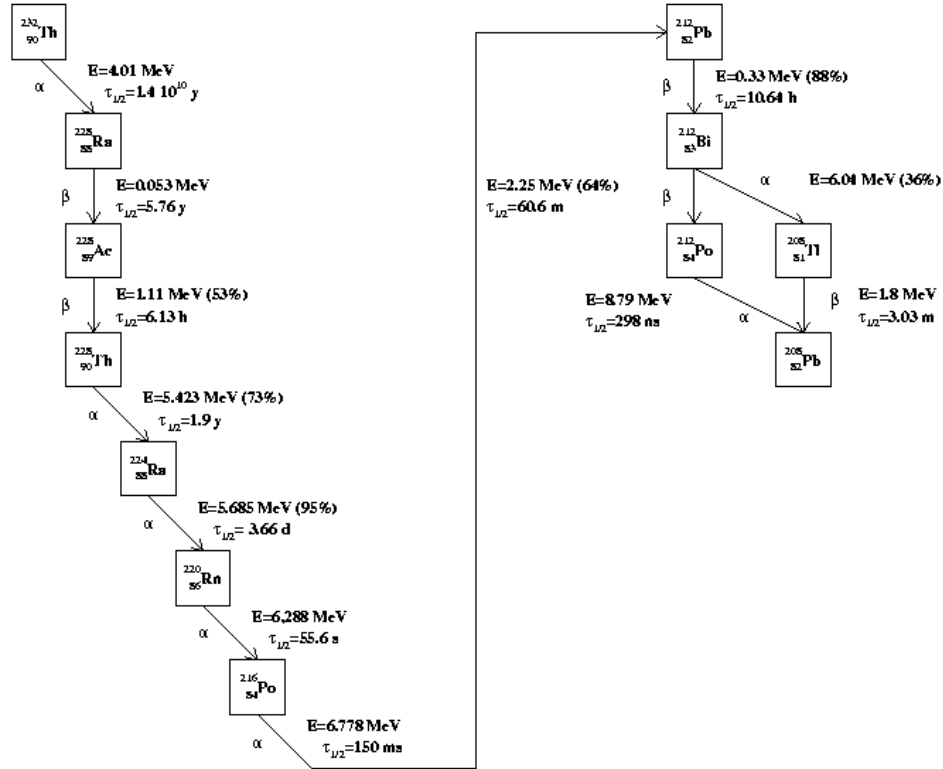


Figure 4.1: The  $^{232}\text{Th}$  natural radioactive chain. Diffusion of thoron ( $^{220}\text{Rn}$ ) and plate out of its daughters doesn't represent a long term problem because  $^{220}\text{Rn}$  has a short half life ( $\sim 1$  minute) and the daughters decay away completely in a couple of days.

radon filter relevant for the design of a scaled up version to meet the flow rate requirements imposed by the Princeton clean room are also illustrated.

### 4.1 Air filtering technique

As described in chapter 3, the Princeton clean room required a flow rate of 85-170  $\text{m}^3/\text{h}$  (50-100 cfm) of fresh radon-"free" make up air, delivered continuously for many months (one year, as it turned out; see chapters 5 and 6).

Possible methods for obtaining low radon make-up air that were initially evaluated for use in the clean room are listed in table 4.1. The use of bottled or liquid synthetic air

technique	requirements	performance
synthetic air (compressed)	250-500 bottles/day or 1 big pressure tank	radon-free (except for emanation)
synthetic air (liquid)	1 truck/week need: cryogenic system evaporator mixer	radon-free (except for emanation)
“Aged” air (buffer tank)	need: compressor big pressure vessel	$\times 100$ reduction ( $10^5$ std $m^3$ tank)
“aged” air (with charcoal, “à la SuperK” [111])	need: compressor big charcoal tank(s) ( $8 m^3$ ) and/or cryogenic system	$\times 10^4$ reduction (15 std $m^3/h$ )
pressure swing (1 atm $\leftrightarrow$ $>$ atm) (on charcoal)	need: compressor two pressure tanks	$\sim \times 100$ reduction (small-scale, inefficient [119])
temperature swing (on charcoal)	need: heater or cryogenic system	unknown

Table 4.1: Possible techniques that have been evaluated to reduce the radon content in the Princeton clean room for use during the assembly of the Borexino nylon vessels.

was immediately discarded because it would have been very impractical and extremely expensive ( $\sim 25,000 m^3$ /week. The cost for bottled synthetic air would, for example, be  $\sim 40k$  \$/week!). With the air flow we needed, a simple “aging” buffer tank was also unfeasible, since an unreasonably large pressure vessel would be needed in order to achieve a sufficient radon reduction. An “aging” system similar to that adopted by the Super-Kamiokande collaboration [111] was interesting (they report a  $10^4$  reduction at  $15 m^3/h$ ). In this setup, the input air flow is passed through a charcoal bed which is big enough to retain the radon front for a time equal to many radon half-lives: the radon decays before it can emerge from the column. Scaling their results up to the flow we needed,  $\sim 80 m^3$  of charcoal at room temperature or several  $m^3$  of charcoal at  $-40$  °C would have been required. Neither of these

options was economically feasible.

A filter large enough to allow radon to decay inside it did not seem like a viable route. Instead, a choice was made to research and develop a charcoal filter with active regeneration that could handle high air flows within a manageable budget. Such a design seemed to offer a filter with a relatively compact size. A regenerating filter is one in which the adsorbing material is periodically “purged” before it reaches saturation of the species to be filtered out. To allow continuous air supply, these filters are typically composed of more than one filtering element (bed), so that one of them can be active along the input flow line at all times. The purging step can be carried out in a variety of ways, depending on the specific process. It is well known that the adsorption properties of an adsorbing bed vary significantly with pressure and temperature; higher pressure and lower temperature result in higher adsorptive capacities of surfaces (i.e. more atoms can be adsorbed per unit surface area). For regeneration filters, the purging step is performed at low pressures or high temperatures.

Our filtering system relies on adsorption of radon molecules on an activated carbon bed. The bed is charcoal, specially treated to produce an extremely porous material with an enormous surface to volume ratio (typical values are  $50 \text{ m}^2/\text{g}$ , but it could be as high as  $1000 \text{ m}^2/\text{g}$  or more [112] with pore diameters of a couple of molecular diameters). As explained below in section 4.1, the charcoal bed preferably adsorbs radon rather than other components of air ( $\text{N}_2$ ,  $\text{O}_2$ , Ar, etc.), separating it, to a certain degree, from the carrier flow. Every filter of finite dimensions eventually saturates if it does not undergo regeneration (consider, for example, home water filters; however, this argument is valid for radioactive species only if their decay mean life is large compared with the filter’s saturation time constant). For this reason, the filtering system will have to undergo a purification (purge) stage, which has to be done using much cleaner air than the input air. This can be achieved using filters based on swing cycles; these devices have two or more filtration units placed in parallel. For a given time cycle, one set of units is used as the actual filter while the other set is purged using purified product from the first filter. At the end of each cycle, the filtration units swap roles. As mentioned above, swing systems exploit the pressure and/or

temperature dependent adsorption properties of activated charcoal.

To avoid the costs and complications associated with a “cold” system we focused our research on pressure swing adsorption at room temperature. Furthermore, as will be detailed in the following section, a pressure swing system on large scales seemed to be a better choice than a temperature swing device. Particularly, the time scales involved in temperature-cycling an appropriate size system would limit its efficiency towards radon removal. Pressure variations can on the other hand be obtained in much shorter times.

#### 4.1.1 Adsorption principles

Adsorption is the phenomenon by which particles in a fluid experience a drop in potential energy associated with their interactions with a solid surface [113]. This allows them to concentrate and “stick” to the surface. Leaving the gas phase, the adsorbed atoms form a new denser phase, called the *adsorbed phase* or *sorbate*. Depending on the chemical and physical structure of the atoms adsorbed and of the adsorbant material, different interactions can take place; adsorption may or may not involve chemical reactions between the sorbate and the surface. When only “weak” forces, such as dispersion (van der Waals) or dipole and quadrupolar electrostatic interactions play a role in the adsorption, the process is called *physical adsorption*. This phenomenon is analogous to the condensation of gases into liquids: a gas tends to be adsorbed on a solid if the temperature is sufficiently low (adsorption is an exothermic process) or the gas’ partial pressure is sufficiently high. The strength of the interaction and the number of active sites (sites where the interaction between the sorbate molecules and the adsorbent can occur) per unit area on the adsorbent surface determine the efficiency with which filtration is carried out.

A general rule of thumb is that polar molecules should be adsorbed using polar adsorbents, and non-polar molecules with non-polar adsorbents. What this means is that in the presence of a dipole-dipole interaction, the van der Waals interaction energy is negligible, even if always present. Contrary, non-polar molecules are adsorbed to surfaces via van der Waals interactions. In the case of radon on activated carbon, the adsorption is driven by residual van der Waals forces, since radon is a non-polar atom and charcoal is a

non-polar surface. Selectivity of radon with respect to the main components of air works as follows:  $\text{N}_2$ ,  $\text{O}_2$  and Ar have similar polarizabilities (ratio of the average induced molecular dipole moment and the applied electric field,  $\alpha \sim 1.6 \text{ \AA}^3$  [114]), so their van der Waals interactions with the charcoal are comparable and very little separation among them by adsorption occurs. On the contrary, radon has a higher polarizability ( $\alpha \sim 5 \text{ \AA}^3$  [114]); its interactions with the charcoal will therefore be stronger and it will more easily be trapped in the micropores of the adsorbent. Activated charcoal has been chosen instead of other materials because of its high porosity, its mechanical properties and its cost-effectiveness. It is extensively used in commercial filters and is optimal for removing trace components from air, for example in gas masks.

#### 4.1.2 Adsorption constant

The adsorption constant is a physical quantity that expresses the capability of a surface to retain particles by adsorption. To illustrate the phenomenon, imagine a container of volume  $V$  filled with gas at temperature  $T$ . The gas will be at pressure  $P = (RT/V)n$  ( $n$  is the number of moles of gas). If a given amount of adsorptive material (e.g. charcoal) is inserted in the container, keeping  $T$  constant, some atoms (molecules) of gas will leave the gas phase to be adsorbed on the adsorber surface. The pressure of the gas will drop since fewer atoms (molecules) are left in the gas phase (assume the intrinsic volume of the adsorber is  $\ll V$  so that it may be neglected). The pressure drop  $\Delta P$  is given by  $\Delta P = (RT/V) \Delta n$ , where  $\Delta n$  is the amount of adsorbed gas. It is found that the amount of gas adsorbed per unit mass of adsorber generally depends on pressure ( $\Delta n = \Delta n(P)$ ) [113].

The functional dependence between the adsorbed amount (number of moles  $n$ ) per unit mass of adsorber  $m$  and the gas pressure  $P$  (at a given temperature and for a specific gas-adsorber system) is called *adsorption isotherm*. The simplest case is a linear dependence,  $n/m_0 = CP$ .  $C$  is called the *adsorption constant*, and it has units of mol/mass/pressure (often in the literature the adsorbed amount is expressed in units of mass and the adsorption constant has units of pressure<sup>-1</sup>). Over small pressure ranges, all isotherms can be considered linear.

For a system of two or more gases, the partial pressure of each species is considered instead of the total pressure of the mixture. In the particular case of a dilute solution of a trace gas in a carrier gas (e.g. radon in nitrogen), the isotherm for the trace species can be thought of as linear. The equilibrium condition between gas and adsorbed phase can be expressed in terms of a partition factor  $K$ ,

$$K = \frac{\text{amount in adsorbed phase}}{\text{amount in gas phase}} \quad (4.1)$$

independent of pressure (this quantity is rigorously defined in eq. (4.8)).

### 4.1.3 Dynamic adsorption

When gas is flowing through an adsorbing bed (column), it is easier to think of adsorption in a formally different way. In our case the goal is to filter out a trace gas (radon) from an carrier gas stream (nitrogen or air) using a charcoal bed. Because charcoal preferentially adsorbes radon than nitrogen (air), the radon-to-nitrogen (air) ratio along the column will depend on time. The trace gas will on the average travel along the bed slower than the carrier gas. The trace gas will define a concentration front that moves along the bed.

For a given mass  $m$  of adsorbent in the bed, the average time  $\tau$  that the concentration front of the species being filtered out takes to emerge from the output is, to first order, proportional to the partition factor  $K$ . This is strictly true when the concentration front inside the column propagates as a step function, that is, neglecting the spreading of the profile as it moves along with the gas flow (see section 4.2 for a rigorous mathematical treatment). An important equation, derived later (eq. (see 4.12)), is:

$$\tau = \frac{k_a m}{\Phi} \quad (4.2)$$

where  $\Phi$  is the volume flow rate.  $k_a$  is called the *dynamic adsorption constant* (the relation between  $K$  and  $k_a$  is shown in eq. (4.10)). The average position of the concentration front thus moves with a velocity  $v_{front}$  defined as

$$v_{front} = \frac{L}{\tau}, \quad (4.3)$$

proportional to  $\Phi$  and inversely proportional to  $k_a$  ( $L$  is the length of the column). If  $v_{gas}$  is the (average) velocity of the gas along the direction of flow in column of cross section  $S$ , then

$$\Phi = v_{gas} S \quad (4.4)$$

and the concentration front's velocity  $v_{front}$  is also on the average proportional to  $v_{gas}$ . So, in principle, neither the pressure nor the mass flow rate  $F$  should affect  $\tau$  (note that for a given  $F$ , since  $F \propto P\Phi$ , if the pressure increases,  $v_{gas}$  decreases).

There are of course other effects that need to be taken into account. If the trace gas to be separated out is mixed with another gas which is also adsorbed on the bed, there will be competition between the different species for the adsorption sites and the effective adsorption constant of each gas will be reduced. For example, if air (or any of its components, each one present in concentrations much higher than that of radon) is significantly adsorbed on charcoal, the quantity of interest is the relative adsorption constant between air and radon. In general, every gas mixture has its own specific behaviour on an adsorbing surface.

The parameter that should more appropriately be used for adsorption (instead of  $v_{gas}$ ) is the *superficial velocity*  $v_s$  of the gas on the adsorbing bed (i.e. the velocity at which the gas "samples" the adsorbing surface). The gas actually flows around the particles in the bed so that

$$v_{gas} = \beta v_s \quad (0 < \beta < 1) \quad (4.5)$$

The superficial velocity  $v_s$  is useful to parametrize (together with  $\tau$ ) the dynamic adsorption along a packed bed. It is worth mentioning at this point that such adsorption processes can be accurately modeled by imagining the column as divided in  $n$  separate equilibrium stages in the direction of the flow, and by assuming adsorption equilibrium in each stage (see section 4.2 for a formal presentation of such model). Each stage will have a certain length (or depth), referred to as height equivalent to a theoretical stage (HETS). The HETS is related to  $v_s$  by the van Deemter equation (see, for example, [113]),

$$\text{HETS} = A + \frac{B}{v_s} + C v_s, \quad (4.6)$$

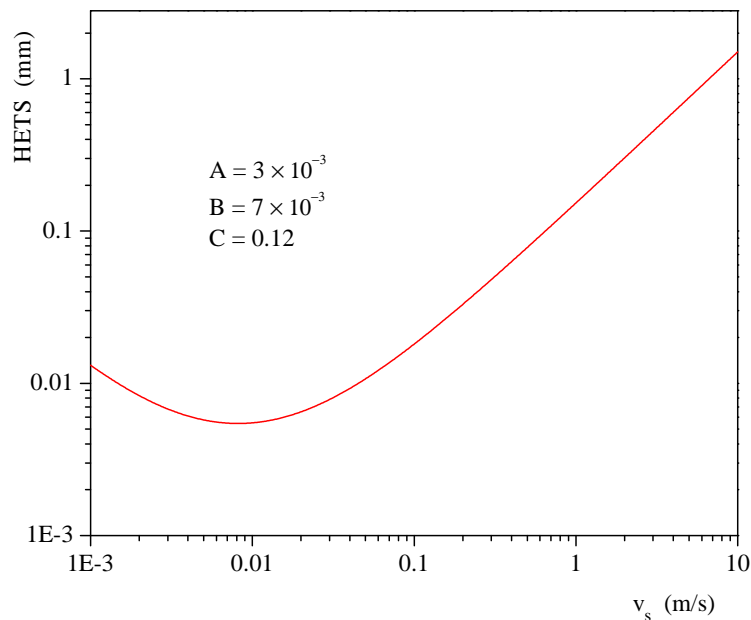


Figure 4.2: HETS as a function of superficial velocity, according to the van Deemter equation (see eq. (4.6)) using the parameters for radon on charcoal reported in [115]. At very low superficial velocities the diffusive spread of the adsorbed species prevails over flow-driven mass transfer.

where  $A$  is a measure of eddy diffusivity of the adsorbed phase (independent of  $v_s$ ),  $B$  of longitudinal diffusivity, and  $C$  of resistance to mass transfer. An example of such curve is shown in fig. 4.2 with an arbitrary choice of parameters. The efficiency (i.e. degree of separation of different species in the gas) of the column increases with the number of stages  $n$  (or with decreasing HETS).

#### 4.1.4 Pressure Swing Adsorption (PSA)

The Pressure Swing Adsorption (PSA) technique relies on the pressure-dependent adsorption properties of the adsorbent, namely its bigger adsorption capacity at higher pressures. This behaviour can be put to use in a two-filter system which undergoes a periodic and symmetric feed/purge cycle (see for example [116] for a detailed analysis of such processes).

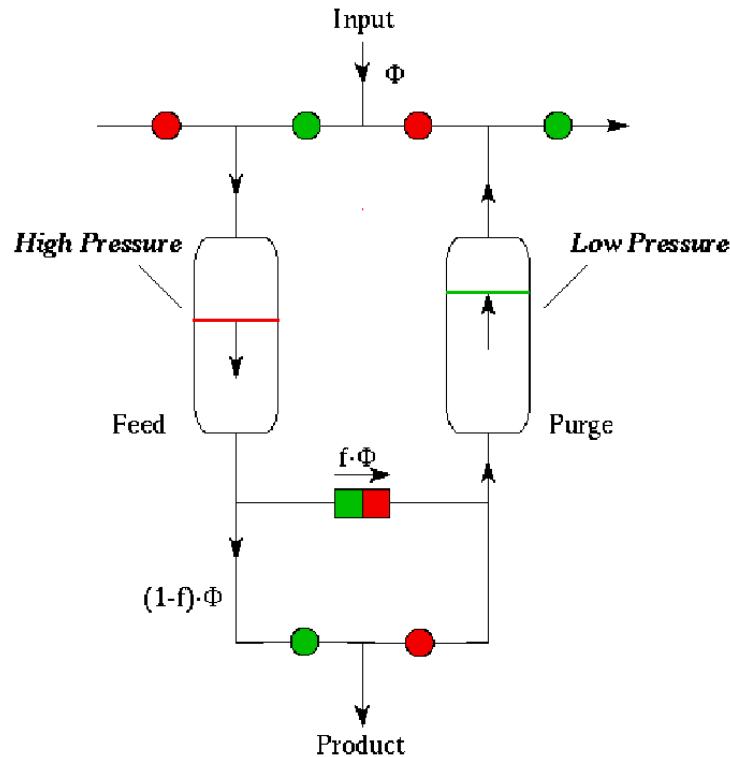


Figure 4.3: Simplified representation of a PSA system, where open (closed) valves are shown in green (red). The feed stage is carried out at higher pressure than that of the purge stage. Thanks to the pressure-dependent adsorption properties of charcoal beds, the latter is performed with just a fraction  $f$  of the total amount of air (mass flow  $\Phi$ ) introduced into the filter. What is left,  $(1-f) \cdot \Phi$ , is clean product. The level of filtration achieved depends on the operating parameters.

A conceptual view of a PSA system is given in fig. 4.3.

During the feed cycle, air is sent into one of the two charcoal-filled columns and emerges, for some time ( $\sim \tau$ ), essentially radon-depleted. The duration of the feed cycle is chosen to be much smaller than the time it takes for the radon to break through from the column output. During this time, a fraction  $f$  of the total flow  $\Phi$  is extracted, expanded to a lower pressure and pushed back into a second column, which had been contaminated during the previous feed cycle. Due to the expansion, the purge air has a lower radon (volume) concentration than the output air from the feed column, by an amount equivalent to the ratio

of the pressures. In addition, part of the radon adsorbed during the feed will be desorbed after the depressurization and will move in the direction of the purge flow, i.e. back toward the column input. In order to be effective in “pushing back” the radon concentration front during the purge step, it is necessary to have a higher superficial velocity than during the feed. This is achieved by an appropriate choice of  $f$  and  $P_{purge}/P_{feed}$  as follows:

$$v_s^{purge} > v_s^{feed} \iff \frac{P_{purge}}{P_{feed}} < f \quad (4.7)$$

If this condition is not satisfied, the front would advance more during the feed than it retreats during the purge. However, this alone is not a sufficient condition for an efficient device. The purge must also be gauged against the complete dynamics of the concentration front. In particular, it must be effective against the spreading of the advancing radon profile.

If the filter is initially radon-free, radon remains confined near the input of both columns (the amount of charcoal, pressure ratio, purge fraction and cycle times being appropriately chosen). If the filter is initially contaminated with high levels of radon, the pressure swing cycle will, after some time, deliver air with very low amounts of radon if the purging capability overpowers the advance of the radon front during the feed cycle. Eventually a steady-state regime is reached, at which point the movement of the radon profiles inside the columns will repeat itself at every cycle (see section 4.2 for a mathematical derivation of the steady state solution within the frame of the plate model).

#### 4.1.5 Early attempts

Swing systems are used extensively in industrial air separation processes. The low radon levels we were pursuing, though, are many orders of magnitude lower than any limit set by health requirements and are of no wide-scale commercial interest. The behaviour of radon on charcoal beds has only sporadically been investigated and reported in literature (see, for example, [115, 117]).

Initial tests at Princeton involving the use of a modified commercial PSA system failed to reduce radon concentrations significantly as expected, so a study of radon suppression by charcoal columns was performed [118]. Notably, the adsorption properties of radon

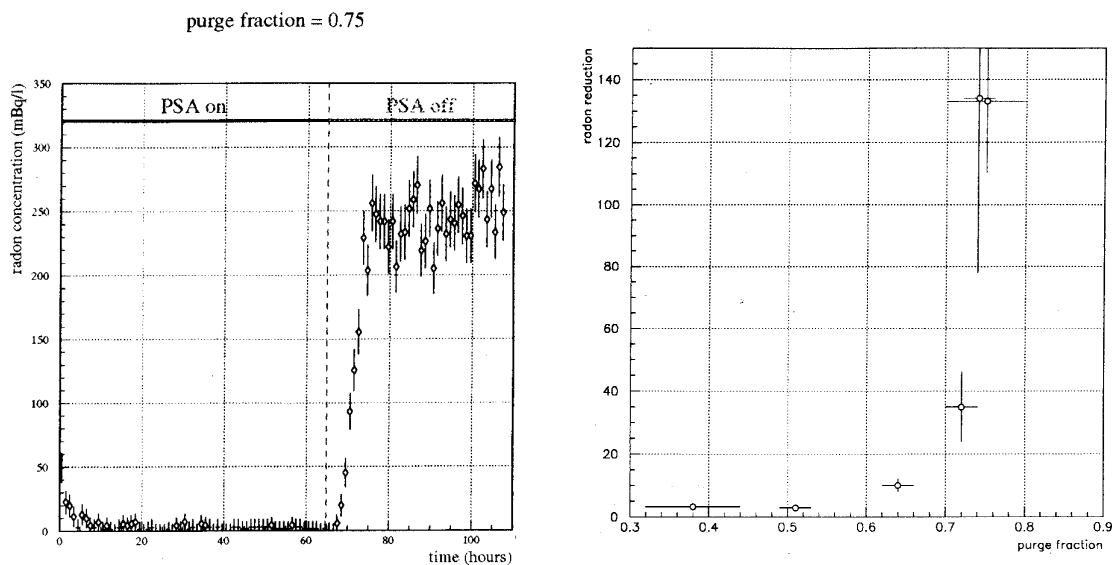


Figure 4.4: Results from early attempts to use a PSA device for radon suppression. The plot on the left shows the data from a run that achieved 100-fold radon reduction with a 75% purge fraction. The radon reduction as a function of purge fraction is shown on the right. The input air flow rate was  $0.3 \text{ m}^3/\text{h}$ . The plots are taken from [119].

in nitrogen carrier gas at high pressures (100 psig) were lower than expected. While no definitive explanation was given, this could have been due to competition between radon and nitrogen for adsorption sites (see section 4.4). This effect succeeds in explaining the observed PSA inefficiency. A second, small-scale ( $\Phi = 0.3 \text{ m}^3/\text{h}$ ) PSA prototype was run and a 100-fold radon reduction was achieved, but only by using  $\sim 75\%$  of the filtered air for the purging step [119] (see fig. 4.4).

#### 4.1.6 Vacuum Swing Adsorption (VSA)

The failure in efficiently operating a PSA device for radon removal was due to the fact that the adsorption constant for radon in nitrogen (and presumably in air) was found to be dependent on pressure (see section 4.3). An elegant way to overcome such a problem was to use sub-atmospheric pressures for the purge phase, in a Vacuum Swing Adsorption (VSA) device.

Conceptually identical to the PSA, the VSA exploits the expansion of gases at low pressures. The rationale behind it is explained as follows. The radon front moves proportionally to the average gas velocity  $v_s$  in the column (see eq. (4.2) and following discussion).  $v_s$  is proportional to the volume flow rate in the column and, consequently, inversely proportional to the pressure (for a given mass flow rate). An efficient filter will need large values of  $v_s^{purge}/v_s^{feed}$ . The pressures and throughputs necessary to have large (10 or more)  $v_s^{purge}/v_s^{feed}$  ratios are readily obtainable with standard vacuum techniques. In the PSA system previously reported, this ratio was only  $\sim 8$ . With the use of vacuum, the feed can be carried out at atmospheric pressure.

Radon adsorption tests under vacuum were performed and are discussed in section 4.3. Section 4.2 focuses on modeling the behaviour of adsorption columns and PSA devices.

## 4.2 The chromatographic plate model

Adsorption columns can be treated mathematically in various ways. One commonly used is the chromatographic plate model. Following a concept used to describe distillation processes, the plate model assumes that the length  $L$  of the column is longitudinally divided into  $n$  equivalent stages (plates), each of finite length  $h = L/n$ , in which equilibrium is reached between the gas and the adsorbed phases. This characteristic length expresses the typical mass-transfer distance along the column for the gas under investigation. It is worth noticing that the condition  $h \ll L$  is not necessarily applicable to all real systems, which prevents from taking the limit  $n \rightarrow \infty$  in the mathematical treatment that follows.

Focusing the analysis on the case of a trace gas (e.g. radon) in a carrier gas (e.g.: air, in which the behaviours of its various components, mainly  $N_2$  and  $O_2$ , are assumed to be the same), the equilibrium condition is expressed by ( $j$  refers to each plate zone):

$$s_j = K \cdot y_j \quad \forall j = 1, \dots, n \quad (4.8)$$

where  $s_j$  and  $y_j$  are the concentrations of the trace gas in the adsorbed phase (number of molecules per unit area) and in the gas phase (number of molecules per unit volume),

respectively; the proportionality constant  $K$  thus has units of length. The trace gas profile evolves in time according to (conservation of mass):

$$\Phi (y_j - y_{j-1}) = -a \dot{s}_j \quad (4.9)$$

where  $a$  is the surface area of the adsorbent in each stage and  $\Phi$  is the volume flow rate in the column (volume/time). Equation (4.9) simply states that the molecules leaving the gas phase moving from one stage to the next have to be adsorbed in the latter stage. For the purpose of the discussion,  $\Phi$  will be considered time-independent (steady flow). It is convenient to define  $\sigma$  as the surface area per unit mass of adsorbent and to introduce a new proportionality constant called *dynamic adsorption constant*:

$$k_a \equiv \sigma K \quad (4.10)$$

with units of volume/mass (inverse density). Substituting eq. (4.8) into eq. (4.9) and using the above definitions gives:

$$\dot{y}_j = -\frac{n}{\tau} (y_j - y_{j-1}) \quad (4.11)$$

where the dot denotes the derivative with respect to  $t$  and

$$\tau \stackrel{\text{def}}{=} \frac{k_a m}{\Phi} \quad (4.12)$$

is the characteristic timescale of the system (compare with eq. (4.2)). As a further step, a dimensionless constant  $\xi = t/\tau$  can be defined and eq. (4.11) turns into:

$$\frac{dy_j}{d\xi} = -n (y_j - y_{j-1}) \quad (4.13)$$

An effective way of solving this set of equations is in Laplace space; with the definition  $\tilde{y} \equiv Lap(y)$ , eqn. (4.13) then becomes:

$$(s + n) \tilde{y}_j - y_j(0) = n \tilde{y}_{j-1} \quad (4.14)$$

The general solution for the concentration in the  $j$ -th stage is readily found to be:

$$\tilde{y}_j = \left(\frac{n}{s+n}\right)^j \tilde{y}_0 + \frac{1}{s+n} \sum_{k=1}^j \left(\frac{n}{s+n}\right)^{j-k} y_k(0) \equiv \tilde{y}_j^{input} + \tilde{y}_j^{ic} \quad (4.15)$$

The initial conditions term can be expressed in time space using  $Lap(\xi^m e^{-a\xi}) = m!/(a + s)^{m+1}$  to give:

$$y_j^{ic}(\xi) = \sum_{k=1}^j \frac{(n\xi)^{j-k}}{(j-k)!} e^{-n\xi} y_k(0) \quad (4.16)$$

The solution of the input term requires the knowledge of the concentration profile entering the column (stage zero); a few important examples are analyzed in the following paragraphs, where use is made of the convolution theorem for Laplace transforms stating that  $Lap^{-1}(\tilde{f}\tilde{g}) = \int_0^\xi dx f(\xi-x)g(x)$ .

#### 4.2.1 Special cases

An analytical solution to the profile of the trace gas concentration that emerges from the output of the column can be obtained when the input profile  $y_0(t)$  is a "spike" ( $\delta$ -function) or a step ( $\Theta$ -function). For both cases the initial concentrations in the  $n$  stages of the column are assumed to be zero:

$$y_j(0) = 0 \quad \forall j = 1, \dots, n \quad (4.17)$$

**"Spike" input** - In this case,  $y_0(\xi) = \alpha\delta(\xi)$  so that  $\tilde{y}_0 = \alpha$  and the general solution is

$$\tilde{y}_j^{delta} = \frac{\alpha n^j}{(s+n)^j} \quad (4.18)$$

which yields

$$y_j^{delta}(\xi) = \frac{\alpha n^j}{(j-1)!} \xi^{j-1} e^{-n\xi} \Theta(\xi) \quad (4.19)$$

called an *elution curve*. It is worthwhile pointing out that for  $n \rightarrow \infty$ , the curve tends to a gaussian peaked at  $\tau$  and with standard deviation  $\sigma = \tau/\sqrt{n}$ . Examples of elution curves are shown in fig. 4.6.

**Step input** - For this second example,  $y_0(\xi) = \alpha\Theta(\xi)$  and  $\tilde{y}_0 = \alpha/s$ ; the general solution becomes

$$\tilde{y}_j^{step} = \frac{\alpha n^j}{s(s+n)^j} \quad (4.20)$$

which in time-space is written as

$$y_j^{step}(\xi) = \alpha \left[ 1 - e^{-n\xi} \sum_{k=1}^j \frac{(n\xi)^{j-k}}{(j-k)!} \right] \quad (4.21)$$

Notice that because of the linearity of eqns. (4.13) and of the Laplace transform operator, the superposition principle applies for the solutions; hence, the step response (4.21) can be obtained by integration of the "spike" response (4.19), since  $\Theta(\xi) = \int_{-\infty}^{+\xi} dx \delta(x)$ .

### 4.2.2 PSA system modeling

Using the results obtained above it is possible, with some assumptions, to give a good description of the PSA system. In the case of a step-profile input, we have:

$$y_j = y_j^{step} + y_j^{ic} = \alpha \left[ 1 - e^{-n\xi} \sum_{k=1}^j c_{jk} \right] + \sum_{k=1}^j c_{jk} y_k(0) \quad (4.22)$$

with the definition  $c_{jk} \equiv \frac{(n\xi)^{j-k}}{(j-k)!}$ . It is useful to express the above equation in matrix form.

For this purpose, define

$$\Theta_{jk} \equiv \begin{cases} 1 & j \geq k \\ 0 & j < k \end{cases}$$

$$M_{jk}(\xi) \equiv e^{-n\xi} c_{jk}(\xi) \Theta_{jk}$$

$$\hat{\mathbf{y}} \equiv (1, \dots, 1)^T$$

and rewrite eq. (4.22) as

$$\mathbf{y}^f = \alpha^f (\mathbf{1} - \mathbf{M}) \hat{\mathbf{y}}^f + \mathbf{M} \mathbf{y}^f(0) \quad (4.23)$$

The above expression holds for the propagation of radon from stage 1 to stage  $n$  (notice the added superscript  $f$  (feed)). In order to describe the purge cycle, a similar expression is needed for the propagation of radon from stage  $n$  to stage 1. This is achieved with the substitution  $k \rightarrow n - j + 1$ . Introducing the matrix  $R_{jk} \equiv \delta_{j, n-k+1}$  it can be seen that

$$\mathbf{y}^{step,p} = \mathbf{R} \mathbf{y}^{step,f}, \quad \mathbf{y}^{ic,p} = \mathbf{R} \mathbf{M} \mathbf{R} \mathbf{y}^p(0) = \mathbf{M}^T \mathbf{y}^p(0) \quad (4.24)$$

Assuming the radon concentration in the purge flow to be constant (which, strictly speaking, is not), we can express the evolution of the profile during the purge as

$$\mathbf{y}^p = \alpha^p \mathbf{R}(\mathbf{1} - \mathbf{M}) \hat{\mathbf{y}}^p + \mathbf{R} \mathbf{M} \mathbf{R} \mathbf{y}^p(0) \quad (4.25)$$

It should be stressed that the number of stages for the feed and purge is generally different. This implies that eqns. (4.23) and (4.25) "live" in  $n^f$ - and  $n^p$ -dimensional spaces respectively. To be able to use this formalism for a complete feed/purge cycle, there has to be a re-binning of the concentration profiles between the feed and purge vector spaces. This is carried out by some  $n^p \times n^f$  matrix  $\mathbf{S}$  (or vice versa). A further simplification is made by assuming that pressurization and depressurization do not move the profile; the change in pressure is taken into account by using the appropriate vapor-adsorbate equilibrium constant (refer to eq. (4.8)). It's convenient to define the quantity  $\kappa \equiv K_f/K_p$ .

Analysis of the cycle may proceed by assuming some concentration  $y_0^f$  at the beginning of a feed cycle. This is essentially the concentration obtained at the end of the previous purge cycle, more precisely,

$$\mathbf{y}_0^f = \kappa \mathbf{S}^T \mathbf{y}^p \quad (4.26)$$

Using eq. (4.25) we have

$$\mathbf{y}^p = \alpha^p \mathbf{R}(\mathbf{1}^p - \mathbf{M}^p) \hat{\mathbf{y}}^p + \mathbf{R} \mathbf{M}^p \mathbf{R} \mathbf{y}_0^p \quad (4.27)$$

with

$$\mathbf{y}_0^p = \kappa^{-1} \mathbf{S} \mathbf{y}_0^f \quad (4.28)$$

Finally, the loop is closed with eq. (4.23) to give

$$\mathbf{y}^f = \alpha^f (\mathbf{1}^f - \mathbf{M}^f) \hat{\mathbf{y}}^f + \mathbf{M}^f (\mathbf{y}_0^f)' \quad (4.29)$$

If the system is operating in a steady-state mode, by definition  $(\mathbf{y}_0^f)' = \mathbf{y}_0^f$ . Concatenating the above equations we obtain

$$\mathbf{y}^{f,ss} = (\mathbf{1}^f - \mathbf{M}^f \mathbf{S}^T \mathbf{R} \mathbf{M}^p \mathbf{R} \mathbf{S})^{-1} [ \alpha^f (\mathbf{1}^f - \mathbf{M}^f) \hat{\mathbf{y}}^f + \kappa \alpha^p \mathbf{M}^f \mathbf{S}^T \mathbf{R} (\mathbf{1}^p - \mathbf{M}^p) \hat{\mathbf{y}}^p ] \quad (4.30)$$

which, even if somewhat cumbersome, is a very quick way to solve the equilibrium operation of the system.

### 4.3 Single column tests

The radon-adsorption properties of charcoal under vacuum had to be explored in order to test the validity of the concept and to obtain data that would allow us to engineer a working device. This was carried out with a single-column setup and a radon source. This apparatus was also useful to test many other aspects of the behaviour of radon on charcoal beds.

#### 4.3.1 Charcoal selection

The activated charcoal selected for the tests is Calgon PCB 4×8LS [120], a coconut-based variety that comes in flakes 3-4 mm in size. According to the limited literature available, coconut-based charcoals seem to have among the best radon adsorption properties [115, 121]. The adsorption constant is not the only parameter to consider. Of equivalent importance are the desorption properties which must allow effective and efficient purging. On the practical side, it is very important that the charcoal be mechanically robust in order to withstand frequent pressure cycling for many months [122]. Also, the charcoal should be low in  $^{226}\text{Ra}$  that emanates  $^{222}\text{Rn}$  (see the results of a radioactivity screening on such charcoal in section 5.6).

#### 4.3.2 Experimental setup

The setup for single-column measurements consists of a stainless-steel cylinder, 4 cm in diameter and 90 cm in length, filled with 500 g of activated charcoal. The charcoal has been initially washed with water to rid it of dust, and then put in an oven to dry. Subsequently, it was put inside the column and flushed with a gentle flow of warm nitrogen for several hours until the dew point of the outcoming gas was  $-40\text{ }^{\circ}\text{C}$ . The column has openings at both ends, and ports at  $1/8$ ,  $1/4$ , and  $1/2$  of its length for measurements with effectively shorter columns. At both ends and at every port felt filters were used to prevent residual dust from clogging downstream valves.

Measurements at above-atmospheric pressures are performed regulating compressed nitrogen down to the desired pressure and sending it into the column. The flow emerges via



the flow through this chamber to collect the radon. Both the radon trap and most of the tubing are made of plastic Polyflo with Swagelok fittings. The flow is then funnelled into a chemical hood approved for the purpose. Operation for subatmospheric pressures is similar, with the addition of two vacuum pumps at the output end of the column. The bigger of the two pumps sets the pressure of the column and removes most of the throughput, while the second, an oil-free diaphragm pump, extracts a small amount to be sent to the radon detector. The fine-tuning of the column pressure is obtained through two needle valves acting as variable impedances, one at each end of the reactor. A schematic view of the experimental setup is shown in fig. 4.5. Both configurations for operation above and below atmospheric pressures are sketched.

### **The radon sources**

The radon sources used are manufactured by Pylon Electronics [125]. They are flow-through, hollow cylinders ( $\sim 100$  cc volume) with fittings at both ends so that they can be inserted in a gas manifold. A  $^{226}\text{Ra}$  salt coats the inside lateral surface of the cylinders and is mechanically kept in place by a radon-permeable membrane. The sources can be evacuated and pressurized up to 3 atmospheres, making them very manageable and easy to use.

### **The radon detector**

The RAD7 detector [123] is a solid-state silicon  $\alpha$  counter placed in a chamber (with a volume of approximately 500 cc) where a several kilovolt electric field is applied so that  $^{218}\text{Po}$  positive nuclides, resulting from  $^{222}\text{Rn}$   $\alpha$  decay, are attracted to its surface with high efficiency. The subsequent decays of the "captured" ions can then be detected (namely the  $\alpha$  decays of  $^{218}\text{Po}$  and  $^{214}\text{Po}$ , see fig 3.7). Using the short-lived  $^{218}\text{Po}$  6.02 MeV  $\alpha$  decay alone decreases the sensitivity of the detector by approximately a factor of two but keeps background levels low even after exposures to high concentrations of radon, allowing repeated and almost continuous use of the apparatus.

### 4.3.3 Measurement procedure

A spike of radon ( $\delta$ -function) is sent into the column at the desired flow and operating pressure and the time profile of the radon concentration is monitored at the output as an elution curve. A few examples are given in figure 4.6, where both the data and the fit with the appropriate analytical function obtained in the frame of the plate model are shown (see section 4.2). The average breakthrough time  $\tau$  and the number of equivalent theoretical stages  $n$  are obtained as fit parameters to the data, according to eq. (4.19):

$$y\left(\frac{t}{\tau}\right) = \frac{\alpha n^n}{(n-1)!} \left(\frac{t}{\tau}\right)^{n-1} e^{-n\frac{t}{\tau}} \quad (4.31)$$

where  $\alpha$  is the amplitude of the input  $\delta$ -function. The maximum of the curve is at

$$t_{max} = \frac{n-1}{n} \tau \quad (4.32)$$

The higher  $n$  is, the more symmetric and narrow the curve becomes (it approaches a gaussian). This condition is met only for low volume flow rates compared to the column size (as is the case, for example, for chromatographic analyses). For the flow rates we are interested in, the elution curves are somewhat asymmetric: this means that the adsorption and desorption edges have different properties which need to be taken into account in the filter design.

Once  $\tau$  is known, the adsorption constant is evaluated from eq. (4.12) as  $k_a = \frac{\Phi}{\bar{m}} \tau$ . The fit parameter  $n$  is used to compute the quantity

$$h = \frac{L}{n}, \quad (4.33)$$

where  $L$  is the length of the column.  $h$  is the height of each equilibrium stage (often referred to as height equivalent of a theoretical stage or HETS) and defines the characteristic size of the equilibrium plates (see sections 4.1.3 and 4.2). The higher the number of theoretical stages (i.e. the smaller the HETS), the more efficient the column is. This description is analogous to that used for distillation columns.

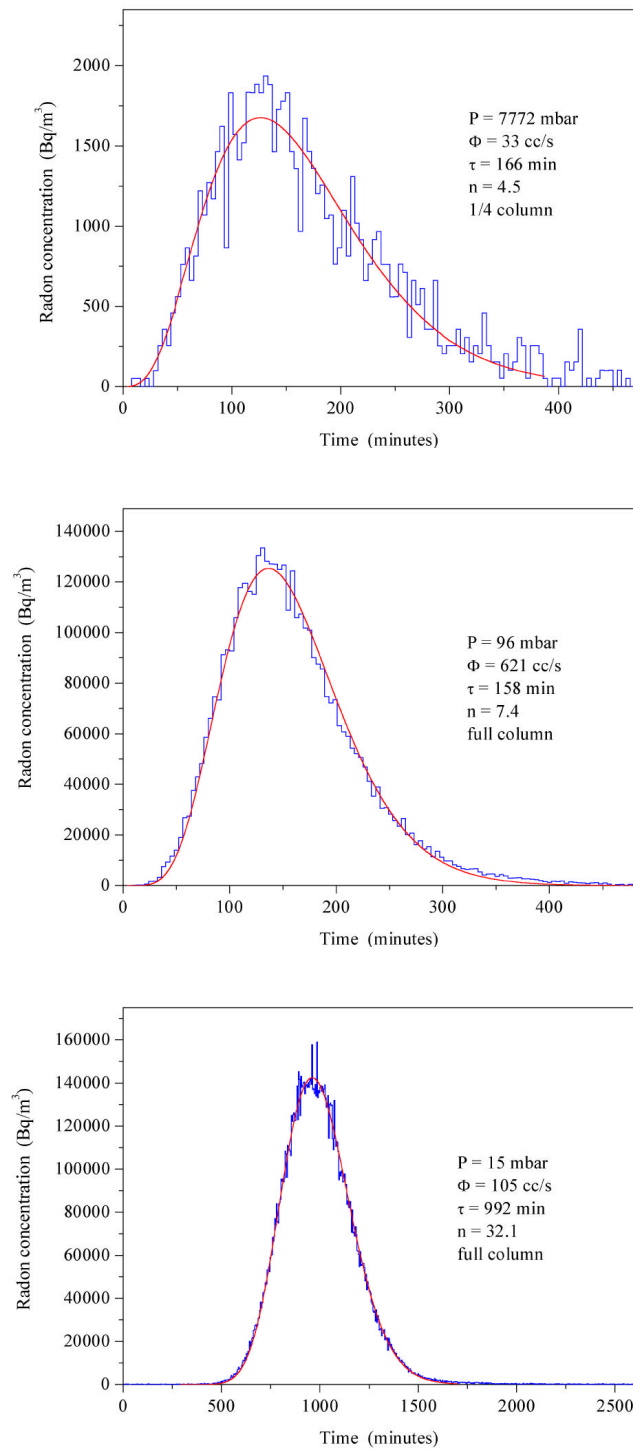


Figure 4.6: Examples of elution curves measured at various pressures and flow rates. The radon concentration of the output is plotted against time. The average time for the radon concentration to emerge from the column depends on the actual superficial velocity  $v_s$  of the air in the column (recall that  $v_s \propto \Phi$ , eqns. (4.4) and (4.5)). This would be strictly true for runs performed at different pressures only if  $k_a$  were pressure-independent.

#### 4.3.4 Measurements and results

Elution curves have been measured over a wide range of pressures and flow rates. Pressures spanned between 15 and 8000 mbar, volume flow rates from 30 to 625 cc/s. The corresponding mass flow rates were between 2 and 260 scc/s. The radon sampling was performed at one of the three ports along the column or from the output end.

Adsorption constants for all the runs are shown in fig. 4.7, and the pressure dependency can be appreciated. An important point to remember is that while the adsorption “constant” in the plot drops with pressure, it does not mean that less radon is adsorbed at higher pressures. If such were the case, it would make no sense to have PSA devices with the feed at higher pressure than the purge. The adsorption constant  $k_a$  is calculated using the *volume flow rate*, not the *mass flow rate*. The actual amount of radon adsorbed on the charcoal *per unit mass of nitrogen (air)* at high pressures is larger than at low pressures (to understand the effect of pressure, recall the similarity between adsorption and condensation suggested in section 4.1). Note that the radon adsorption capacity of the column does not have a linear behaviour with pressure, but shows a saturation effect. Specifically, the radon capacity at 8 bar is just  $\sim 3$  times that at 1 bar (see fig. 4.11). If such capacity increased linearly with pressure, its value at 8 atm would be 8 times that at 1 atm (the effective radon capacity at 8 atm is less than half of what expected). These values are in very good agreement with the tests mentioned in section 4.1.5, performed with a different type of charcoal [118]. The adsorption of air as a function of pressure showing saturation at high pressures is reported in [126], and is most likely due to overall adsorptive capacity for *any* gas, not just air in particular. We have experimentally measured the adsorption of  $N_2$  as a function of pressure, and the results are reported in section 4.4.

To investigate possible differences in using air instead of nitrogen as carrier gas (due, for example, to the presence of  $CO_2$ ), two runs were performed at 1 and 4 bar using bottled synthetic air. Some air components have been could compete with radon for adsorption sites on the carbon [124]. No significant difference in radon adsorption properties was observed at 1 bar, while a possible 10-15% decrease in adsorption capabilities at 4 bar could be

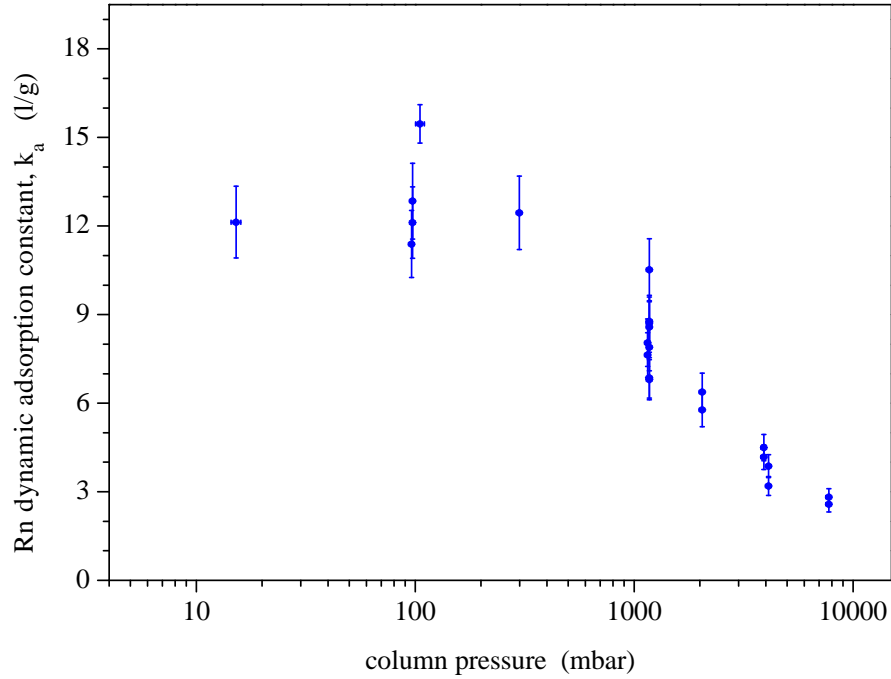


Figure 4.7: The value of the adsorption constant  $k_a = \frac{\Phi}{\bar{m}} \tau$  (in  $\ell/g$ ) for radon in nitrogen carrier gas. The saturation effect observed at high pressures seems to fade away at sub-atmospheric pressures (see text).

suggested by the (limited) data. This study was not pursued further, since it didn't offer any new particular insight.

The increase of  $k_a$  with decreasing pressures appears to plateau approximately below 300 mbar. A wide spread in the results for the data around 100 mbar was recorded (some runs yielded values of  $k_a$  as large as 23  $\ell/g$ , affected by big error bars). This was due to many factors, among which are:

- ports are only nominally at definite fractions of the column length and are orthogonal to the air flow direction in the column. Radon could possibly “overshoot” the port and remain in the column for a longer time, apparently increasing the value of the adsorption constant;

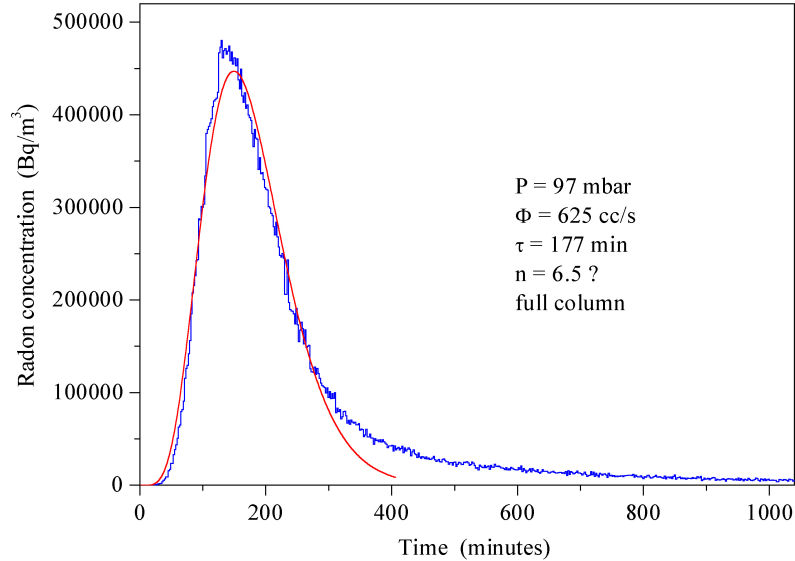


Figure 4.8: An elution curve at sub-atmospheric pressure that shows an extremely long “tail” caused by radon trapped in dead ends in the tubing. The fit with eq. (4.31) is not good. The value of  $\tau$  is not strongly affected by such effect.  $n$ , however is completely unreliable since it strongly depends on the shape of the elution profile.

- handling of radon injection for runs at low pressures presented at first some experimental difficulties connected to dead ends in the plumbing where radon would tend to be trapped for long times, thus shifting the elution curve. In fact, for certain runs, very long “tails” have been observed (see the example in fig. 4.8);
- the measurement of the flow rate was initially affected by large uncertainties because the pressure at which the flowmeters were operating was not carefully set.

The last three runs performed at  $\sim 100$  mbar using the full column, with the radon injection step well controlled, and the flowmeters carefully kept at atmospheric pressure yielded values for  $k_a$  between 11.8 and 13.3  $\ell/g$ , which thus are the most reliable ones (the values obtained in the initial runs at 100 mbar are not shown in fig. 4.7). It looks then as if  $k_a$  actually is a constant below  $\sim 300$  mbar, where the saturation effect disappears. Otherwise stated, the

dynamic adsorptive capacity  $k_a P$  of the charcoal increases linearly with pressure. Using vacuum not only allows very high volume flow ratios between purge and feed with a modest use of purge gas, but also seems to remove the saturation effect!

The results obtained with the single column setup show that the original idea of a VSA filter for radon separation from air via adsorption on activated carbon is well founded and preferable over a PSA system given the behaviour of the dynamic adsorption constant  $k_a$ . The measured radon adsorption constant at 1 bar (feed pressure for a VSA) is approximately 8  $\ell/g$  (see fig. 4.7), which is in good agreement with values reported in literature for the chosen charcoal [115, 121].

#### 4.4 Nitrogen adsorption

A test was performed to measure the adsorption of pure nitrogen on Calgon PCB 4 $\times$ 8LS activated carbon. This test involved the use of two identical steel cylindrical containers of volume  $V \sim 3.5 \ell$ , as shown in fig. 4.9 (the same two columns used for our prototype VSA filter described in section 4.5.1). One column was filled with nitrogen at pressure  $P_1$ , while the other was filled with charcoal ( $\sim 1.35$  kg) and evacuated ( $P_2 < 1$  mbar). A valve connecting the two volumes is then opened and the equilibrium pressure  $P_{eq}$  observed. Sufficient time is allowed for equilibrium to be reached to account for temperature changes induced by the exothermal adsorption process. In the absence of charcoal, the pressure would reach the value  $\frac{P_1}{2}$  (we can assume  $P_2 \simeq 0$ ). If the specific volume  $\alpha V$  occupied by the charcoal and inaccessible to the nitrogen is taken into account, the equilibrium pressure in the absence of adsorption would be

$$P_0 = \frac{P_1}{2 - \alpha} \stackrel{\text{small } \alpha}{\simeq} \frac{P_1}{2} \left(1 + \frac{\alpha}{2}\right), \quad (4.34)$$

where the small  $\alpha$  is justified by the extremely high porosity of activated carbon. Since a significant amount of the nitrogen is adsorbed on the charcoal surface, the equilibrium pressure  $P_{eq}$  is lower than  $P_0$ . The amount of adsorbed nitrogen is proportional to the

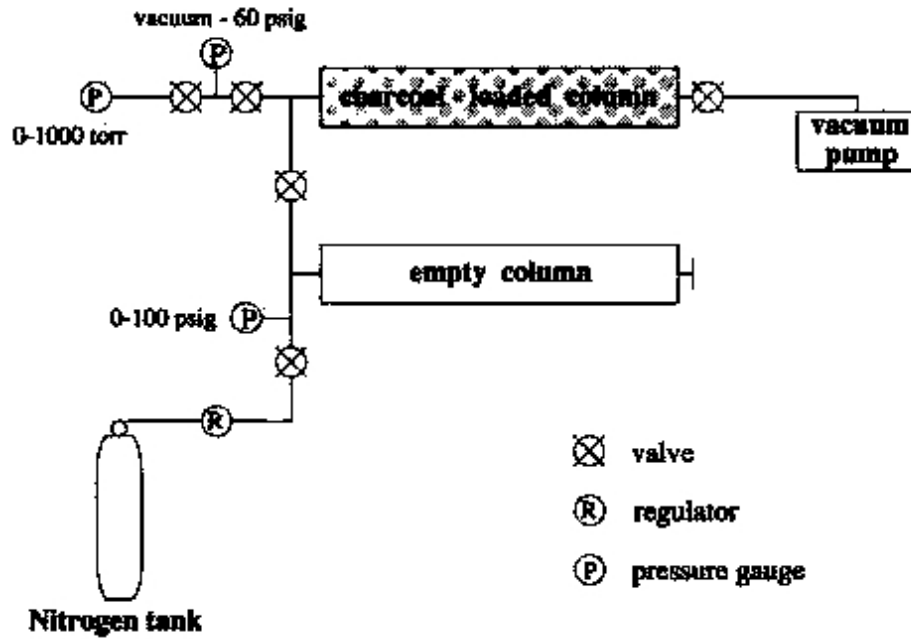


Figure 4.9: The setup for measuring static nitrogen adsorption on activated charcoal.

“missing” pressure, namely

$$\text{adsorbed N}_2 \propto P_{ads} = P_0 - P_{eq}. \quad (4.35)$$

The behaviour of  $P_{ads}$  as a function of adsorption pressure  $P_{eq}$  is shown in figure 4.10 using assumed values for  $\alpha$  of 0 and 0.2. Although the absolute estimation of the charcoal volume might be inaccurate, the saturation trend of pure nitrogen adsorption at high pressures is evident. Fitting with a growing exponential  $P_{ads}(P) = a(1 - \exp(-kP_{eq}))$ , we get (with  $P_{eq}$  expressed in mbar)

$$P_{ads} = 3342 \left(1 - e^{-6.9 \cdot 10^{-4} P_{eq}}\right) \text{ mbar} \quad (\alpha = 0) \quad (4.36)$$

$$P_{ads} = 4022 \left(1 - e^{-6.6 \cdot 10^{-4} P_{eq}}\right) \text{ mbar} \quad (\alpha = 0.2) \quad (4.37)$$

In these two cases, the nitrogen adsorptive capacity of charcoal at 8 bar deduced from the fits is, respectively, 2 and 2.1 times that at 1 bar (this ratio expresses the degree of saturation).

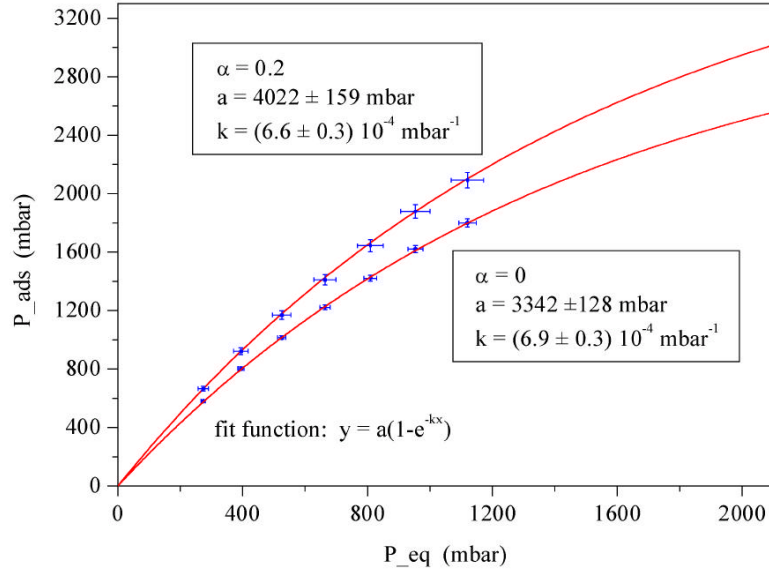


Figure 4.10: Adsorption of pure nitrogen on Calgon PCB 4×8LS activated carbon. The two curves are obtained from the same data assuming charcoal volume fractions  $\alpha = 0, 0.2$  respectively.  $P_{eq}$  is the pressure of the gas phase after adsorption, while  $P_{ads}$  is the pressure drop due to adsorption (see eq. (4.35)) and is therefore a measure of the amount of adsorbed gas.

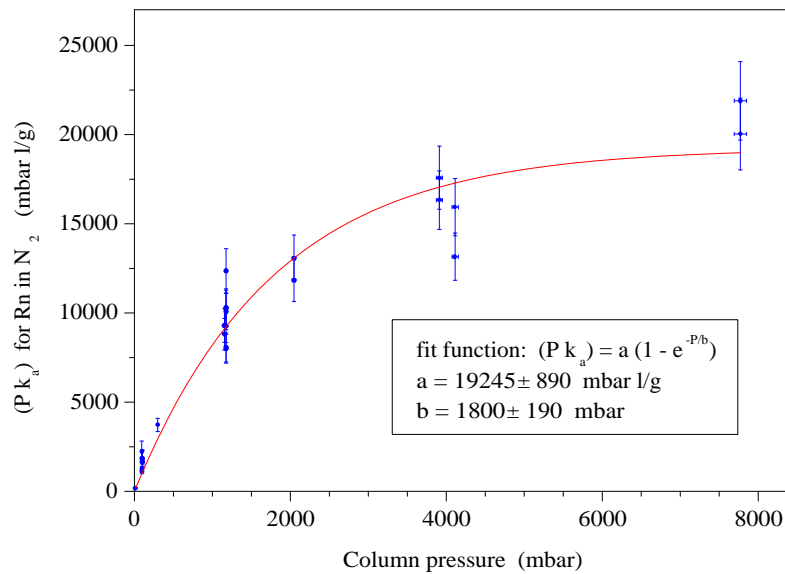


Figure 4.11: Radon adsorption capacity in nitrogen carrier gas on activated charcoal. The quantity plotted is the adsorption constant  $k_a$  of fig. 4.7 multiplied by the pressure. The saturation effect is clearly visible and it can be qualitatively attributed to the saturation of the nitrogen adsorption capacity of the charcoal, as shown in fig. 4.10.

The radon adsorption capacity in nitrogen carrier gas is shown in figure 4.11 in units of  $\text{mbar} \times \ell / \text{g}$  to better highlight the saturation effect; the plot uses the same data used in the plot in fig. 4.7, where  $P \times k_a$  instead of  $k_a$  is plotted versus pressure. The data points are fitted with a growing exponential  $y(P) = a(1 - \exp(-P/b))$  and the best fit is:

$$P \times k_a = 19245 \left(1 - e^{-\frac{P}{1800}}\right) \frac{\text{mbar } \ell}{\text{g}}, \quad (4.38)$$

where  $P$  is expressed in mbar. The ratio of the radon adsorption capacity of charcoal between 8 and 1 bar deduced from the fit is 2.3. The degree of saturation observed for radon is very similar to that observed in static adsorption of pure nitrogen. The loss of adsorption for radon in nitrogen at high pressures is thus completely compatible, within experimental errors, with the saturation of the overall nitrogen capacity of the charcoal. In other words, although the adsorption constant for radon is much higher than that of nitrogen at these pressures and temperatures, the overwhelmingly dominant nitrogen carrier gas occupies and saturates the available adsorption sites. This behaviour is dictated by the ultimate nitrogen adsorptive capacity of the charcoal being used. We could expect a very different result if radon were a considerable fraction of the gas mixture being adsorbed.

For completeness, it is interesting to compare the saturation of nitrogen adsorption with results of a calculation presented by Underhill et al. [126] for static adsorption of air on activated charcoal. In this calculation  $\alpha \sim 0.15$  and the ratio between the air adsorbed at 8 atm and 1 atm is  $\sim 5.2$ , and the saturation effect results only half as pronounced as what shown in eq. (4.37). Radon adsorption using air or nitrogen was proven quantitatively very similar by the elution tests (see section 4.3.4). The discrepancy on the degree of adsorption might then be attributed by different properties (adsorption capacity) of the charcoal. This argument is strengthened by noticing how the overall air capacity (at 1 atm) computed in [126] is more than twice that measured above.

The next step was then to build a small-scale VSA device to directly apply what was learned with the single column setup.

## 4.5 The VSA prototype

The knowledge of radon adsorption properties on activated carbon presented in the previous sections was used for the realization of a charcoal-based Vacuum Swing Adsorption filter. The system was sized to provide approximately one hundredth of the flow rate of the one needed for the nylon vessel assembly clean room; the feed flow was set to be around 1.5 m<sup>3</sup>/h. A significant step towards the final system was to use air instead of bottled nitrogen.

### 4.5.1 Experimental setup

The VSA prototype system is shown in figures 4.12 and 4.13. It consists of two identical stainless steel cylinders, 85 cm in length and 8 cm in diameter. Each contains 1.35 kg of activated charcoal, the same type as that used in the single-column system (Calgon PCB 4×8LS [120]); for the final run, the amount of charcoal was increased to 1.52 kg. Assuming  $k_a \sim 8$  g/l at 1 atmosphere as measured with the single-column setup, each column of the prototype VSA has a breakthrough time of approximately 6 hours at the design flow of 1.5 m<sup>3</sup>/h. The same washing and drying procedure for the charcoal was adopted. Again, felt filters were added to prevent dust from going into the tubing and valves, and a system of plates and springs was inserted at both ends to improve the column packing and to prevent the charcoal from being crushed during the pressure swings.

Compressed air was dried with a membrane dryer [127], regulated to just-above atmospheric pressure and sent into the system. The air was taken from the department's compressed air supply. For this test setup, the air was not required to be breathable-grade; no particular filtration for oil (from compressors) or particulate was provided. Most of the tubing is high density polyethylene flexible Polyflo with Swagelock fittings. Eight solenoid valves of the normally closed type driven by three timers (Omron H3CR-F) divert the flows according to the cycle's feed/purge pattern; six of them are 1/8" in diameter, enough not to cause significant pressure drops in the system. The two through which the columns are evacuated (numbers 3 and 4 in fig. 4.12) are 1", for a smaller opening would have been an intolerable impedance along the crucial low pressure side of the device and would have

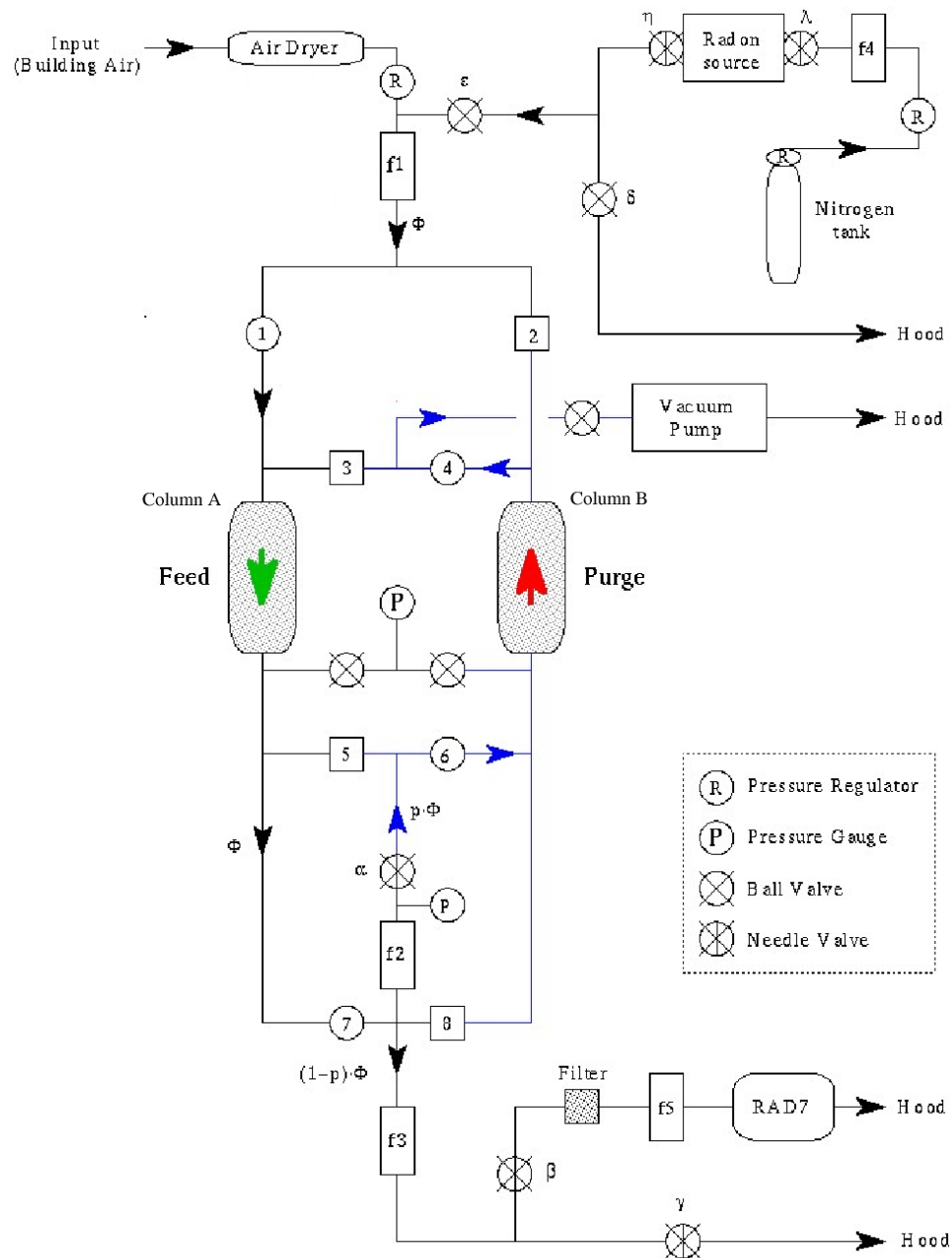


Figure 4.12: Schematic representation of the small-scale prototype VSA system used for testing. The valve configuration shown is that needed to feed the column A while purging column B (circle = open valve, square = closed valve). The details of radon insertion from the source and of radon measurement at the output with a solid state  $\alpha$  detector are also shown.

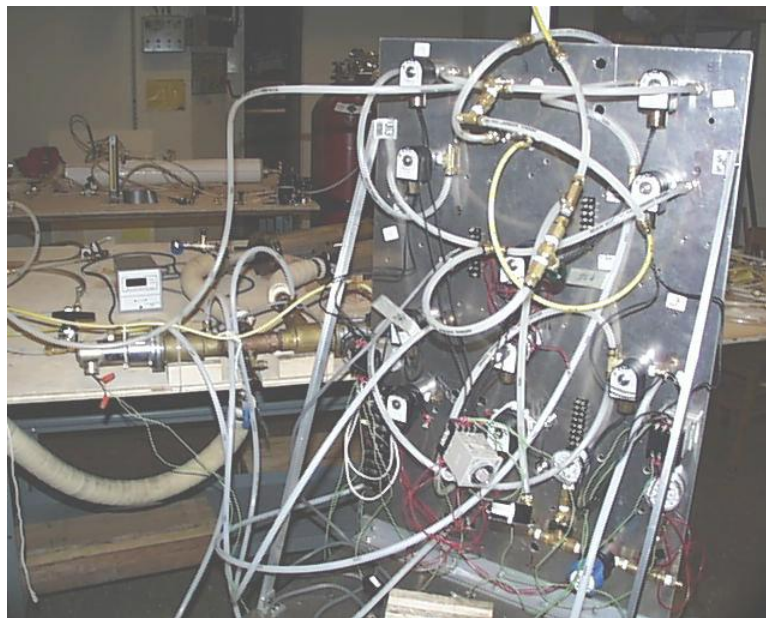


Figure 4.13: The prototype VSA columns (top) and valves (bottom). Other elements such as flowmeters, pressure gauges and the 1" valves and hose of the vacuum line can be seen.

limited the pump speed at the columns. Likewise, a 1" rubber hose has been chosen for the connections between the pump and the columns so as to not defeat the device's purging efficiency. This keeps the pressure drop to a small fraction of a mbar and the flow through it is laminar (see [128] and [129] for flow classification and the calculation of the conductance of a length of pipe). The vacuum pump is a Welch Duo-Seal model 1397B. A needle valve is used to control the amount of air used in the purge phase. A 2 MBq source connected to a nitrogen bottle supplies a constant radon concentration at the input, well above ambient values [125](see section 4.3.2).

#### 4.5.2 The VSA cycle

Particular care has been taken in calibrating the cycle phase time. The simplest configuration is to have a two-step pattern in which half of the solenoid valves open at any given time, and then periodically switch their roles in a symmetric fashion, allowing the two columns to exchange their feed/purge condition. This would work well if the pressurization and depressurization steps were instantaneous, but this is not the case. What really happens when the valves are interchanged is that the low pressure column fills with air coming from both the input and the output of the system. This backflush causes an unacceptable interruption of the air supply for approximately 20 seconds, which could be dangerous when used for air delivery to a clean room. The solution to this problem was to divide the cycle into 4 parts consisting of two, two-step symmetric subcycles. Every feed cycle ( $\sim 10$  minutes, much less than the characteristic radon breakthrough time  $\tau$  of each column of approximately 6 hours at  $1.7 \text{ m}^3/\text{h}$  feed flow rate) is followed by a short re-pressurization step during which the input air enters both columns in parallel. When both columns are at "high" pressure, the next feed cycle can start. This particular opening sequence of the valves ensures a continuous, positive air delivery and is schematically shown in figure 4.14.

A drop of the output flow rate was noticed during the re-pressurization stages. This is because some of the input air would be diverted into the other column at lower pressure. The flow drop was about 30% for several seconds. While acceptable for the prototype device, this problem must clearly be addressed for a filter connected to the clean room (see

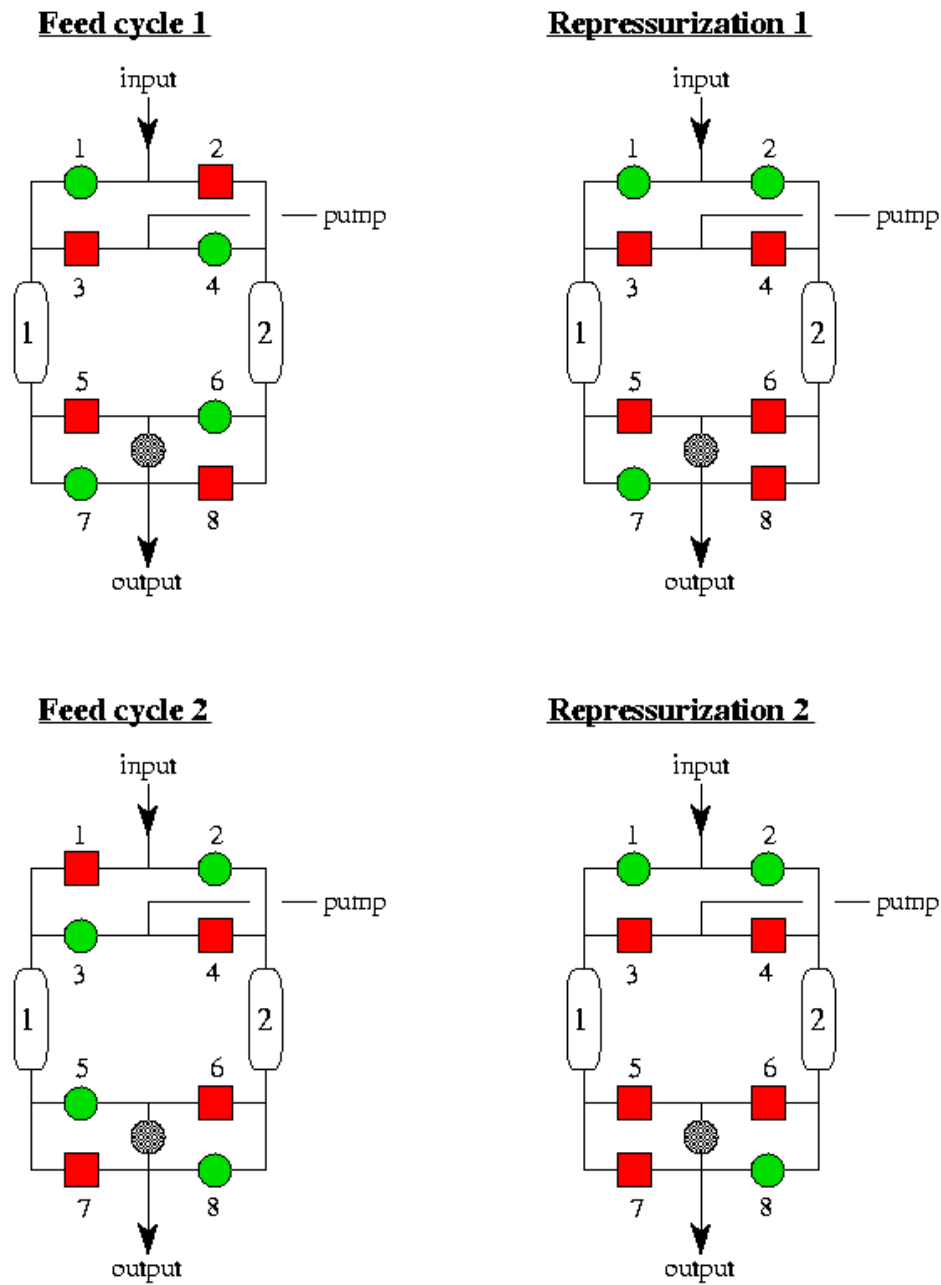


Figure 4.14: Opening sequence of the valves in the VSA prototype system. Red squares indicate a closed valve, green circles an open one. Every column is fed for ~10 minutes, while a re-pressurization time (about half a minute) is allowed for re-pressurizing the evacuated column before switching the cycle.

section 5.3.2).

### 4.5.3 Measurements and results

The runs were performed flowing radon-enriched air through the system until a stable, constant radon concentration at the output was achieved; this was set as the reference starting point, after which the swing system was turned on and the output radon concentration time evolution was recorded until the steady-state level was reached. Examples of typical runs are shown in fig. 4.15; the initial radon plateau and the time when the swing system is turned on are easily identifiable.

The input flow rate for all runs  $F_{feed}$  was between 1.6 and 1.85 standard  $\text{m}^3/\text{h}$  ( $\sim 0.5$  std  $\ell/\text{s}$  or 1 std cfm) and the feed pressure  $P_{feed}$  was between 1280 and 1720 mbar (1.3 - 1.7 atm). Other quantities need to be defined before discussing the results. The low pressure (purged) column is identified by the purge flow rate,  $F_{purge}$ , and by the purge pressure,  $P_{purge}$ . Because of pressure drops, the pressures at the two ends of the evacuated column are different. It is useful to measure the pressure at both ends. The pressure at the column end closest to the vacuum pump will be identified with  $P_1$ ; the one at the other end with  $P_2$ . The relation  $P_1 \leq P_{purge} \leq P_2$  always applies. The volume flow rate  $\Phi$  (at any given pressure  $P$ ) is defined as

$$\Phi_i \equiv \frac{P_0}{P_i} F_i \quad (i = feed, purge, 1, 2), \quad (4.39)$$

where  $P_0$  indicates atmospheric pressure. Another important quantity is the ratio  $G$  between the purge and feed volume flow rates (referred to as volume flow rate gain in the following). Explicitly, such gain at the two ends of the low pressure column is given by

$$G_{1,2} \equiv \frac{\Phi_{1,2}}{\Phi_{feed}} = \frac{P_{feed}}{P_{1,2}} \frac{F_{1,2}}{F_{feed}}. \quad (4.40)$$

The average volume flow rate gain  $G$  can then be defined as

$$G \equiv \frac{G_1 + G_2}{2} = \frac{\Phi_1 + \Phi_2}{2\Phi_{feed}} = \frac{P_{feed}}{2F_{feed}} \left( \frac{F_1}{P_1} + \frac{F_2}{P_2} \right) \quad (4.41)$$

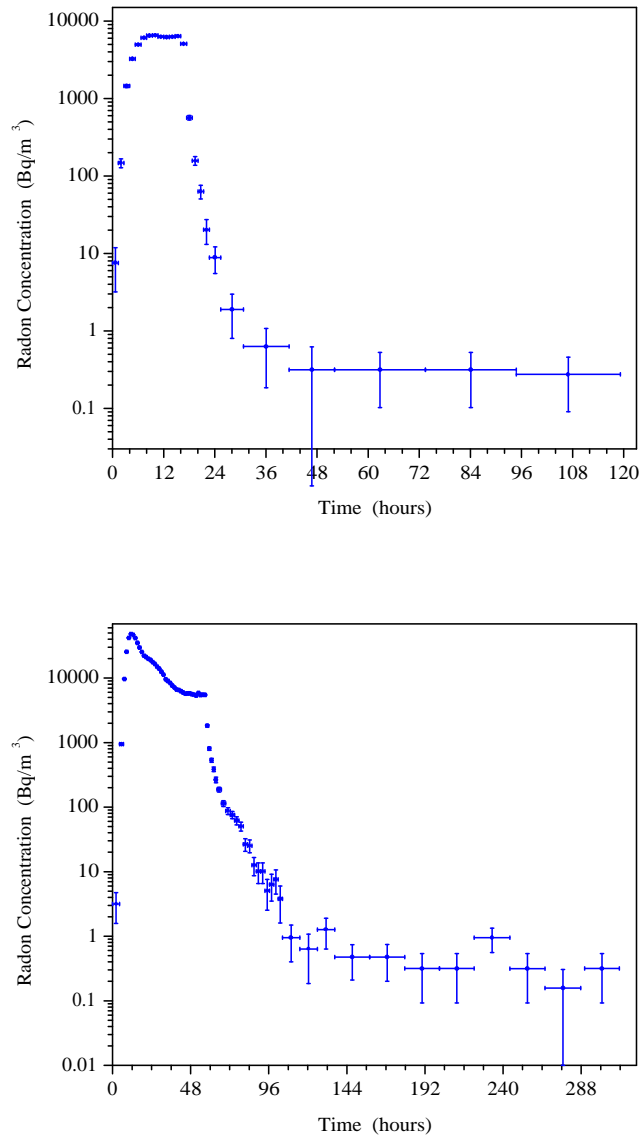


Figure 4.15: First results obtained with the small-scale VSA system. The two runs (300 and 303 in table 4.2) differ by having just one of the columns (top) or both (bottom) contaminated with radon before starting the swing system, while the running conditions are essentially the same. The final radon reduction achieved is the same, within experimental errors. These runs show that whatever the initial condition, a unique steady state operation is reached for a given set of operating parameters. The continuous radon level delivered by the source is represented by the plateau around  $6000 \text{ Bq/m}^3$  in both plots, and sets the initial reference level with which to compare the concentrations achieved after the filter is turned on.

The two successful runs shown in fig. 4.15 (runs 300 and 303 in table 4.2) were performed using the full speed of the vacuum pump and a purge fraction of  $\sim 10\%$ , i.e.  $\sim 0.17$  std  $\text{m}^3/\text{h}$ . A radon reduction of  $2 \times 10^4$  was observed for both. The feed flow was  $F_{feed} = 1.7$  standard  $\text{m}^3/\text{h}$  and the feed pressure  $P_{feed} = 1280$  mbar, corresponding to a feed volume flow rate  $\Phi_{feed} = 1.35$   $\text{m}^3/\text{h}$ . The pressure at the end of the purged column close to the pump was  $P_1 = 20 \div 25$  mbar and the pressure drop across the columns  $\Delta P = P_2 - P_1 \leq 10$  mbar (this pressure was measured only occasionally during these initial runs, so that a more precise value cannot be stated). A pressure range is given for  $P_2$  because its value actually slowly decreases during the purge cycle. The purge volume flow rates at the two ends of the column were thus  $\Phi_1 \sim 8$   $\text{m}^3/\text{h}$  and  $\Phi_2 \geq 5$   $\text{m}^3/\text{h}$  respectively. The corresponding volume flow rate gains were  $G_1 \sim 6$  and  $G_2 \geq 4$ . The average volume flow rate gain is  $G \geq 5$  (the values of these quantities reported in table 4.2 are the best estimates obtainable by careful evaluation of all information available for these initial runs).

The two runs mainly differed for their initial condition: in one case, the VSA was turned on after only one column had been contaminated with radon, while in the second, both columns were saturated before starting the filter. Important considerations can be drawn from the data. First of all, the radon reduction achieved, in excess of  $10^4$  in both cases, supplies experimental confirmation that the principle on which the filter rests is conceptually valid and applicable (compare this reduction factor with the 100-fold reduction obtained with a comparable PSA filter using a 75% purge fraction, see section 4.1.5). Secondly, the theoretically expected result that the steady-state behaviour of such devices only depends on the operating parameters and not on the initial conditions at which the system is started is demonstrated by the fact that the final radon concentration is the same for the two runs, within experimental errors. The only difference is the time it takes for the columns to "clean up"; in other words, the nature of the initial conditions determines the time it takes for the device to converge to its final state (see section 4.2.2).

The radon reduction mentioned previously is given considering every radon event recorded in the RAD7 detector as due to radon emerging from the filter, and does not include an estimate of the detector's background. In fact, the RAD7 background was measured by

flowing bottled nitrogen through the detector and recording the radon activity. No radon concentration below  $A_{RAD7} \sim 0.1$  Bq/m<sup>3</sup> has been observed during these tests. This activity corresponds to 0.8 counts/day in the RAD7 detector and should be taken as the detector's intrinsic background activity.

Subsequent tests were made to investigate various combinations of purge fraction and purge pressures. The goal was to determine a region of parameter space that could be realistically scaled up to the size required by the vessel assembly clean room flow rates. In particular, since the cost of the final system is mainly driven by the size of its vacuum pump, effort was put into measuring the smallest volume flow rate gain needed for the purge to achieve a satisfactory radon reduction at the output. Runs were made with reduced purge flow rates and artificially limiting the pumping speed of the pump at the columns by means of a throttle valve inserted between the pump and the columns.

The results of all the runs are summarized in fig. 4.16 and table 4.2. For every run, the radon activity at the output is measured before ( $A_{in}$ ) and after ( $A_{out}$ ) turning the swing filter on. The reduction factor  $R$ , reported in logarithmic scale on the y-axis, is defined as

$$R = \frac{A_{out}}{A_{in}} \quad (4.42)$$

The following operating parameters were carefully recorded: the feed flow rate and pressure,  $F_{feed}$  (std  $\ell$ /min) and  $P_{feed}$  (mbar); the output flow rate  $F_{out}$  (std  $\ell$ /min); the purge flow rate  $F_{purge}$ ; the purge pressure at both ends of the evacuated column,  $P_1$  and  $P_2$  (mbar). Care was put into keeping the flowmeters close to atmospheric pressure to minimize calibration errors. Consistency checks were performed to confirm that the relation

$$F_{feed} = F_{out} + F_{purge} \quad (4.43)$$

was maintained and a direct calibration of the flowmeters was performed with a soap bubble meter.

The volume flow rates  $\Phi_{feed}$ ,  $\Phi_1$ , and  $\Phi_2$  were computed using eq. (4.39). The volume flow rate gains  $G_1$  and  $G_2$  at the two ends of the column undergoing the purge were also computed via eq. (4.40). Finally the average volume flow rate gain  $G$  was calculated using eq. (4.41).

run	input Rn conc. (Bq/m <sup>3</sup> )	input pressure (mbar)	input flow rate (std $\ell$ /min)	output Rn conc. (Bq/m <sup>3</sup> )	purge flow rate (std $\ell$ /min)	P <sub>1</sub> (mbar)	P <sub>2</sub> (mbar)	average gain (G)	normalized output Rn conc. ( $\times 10^{-5}$ )
501.1	4055 $\pm$ 455	1720 $\pm$ 20	31.1 $\pm$ 0.4	0.4 $\pm$ 0.4	2.65 $\pm$ 0.03	8.4 $\pm$ 0.1	23.4 $\pm$ 0.7	11.9	< 9.9
501.2	"	"	"	24 $\pm$ 2.2	"	38.7 $\pm$ 0.1	44.3 $\pm$ 0.4	3.6	580 $\pm$ 85
501.3	"	"	"	0.2 $\pm$ 0.1	"	23.3 $\pm$ 0.1	31.9 $\pm$ 0.5	5.4	4.4 $\pm$ 2.8
501.4	"	"	29.7 $\pm$ 0.9	< 0.23	1.04 $\pm$ 0.03	4.0 $\pm$ 0.1	13 $\pm$ 0.4	9.8	< 5.7
501.5	"	"	30.0 $\pm$ 0.9	0.1 $\pm$ 0.1	"	6.9 $\pm$ 0.1	14 $\pm$ 0.4	6.4	< 2.2
501.6	"	"	"	2.2 $\pm$ 0.4	"	11 $\pm$ 0.4	17 $\pm$ 0.5	4.4	55 $\pm$ 11
501.8	"	"	"	30 $\pm$ 0.8	"	11 $\pm$ 0.1	17 $\pm$ 0.3	4.4	740 $\pm$ 86
501.9	"	"	28.5 $\pm$ 0.7	37 $\pm$ 3.0	0.14 $\pm$ 0.03	1.7 $\pm$ 0.2	5.2 $\pm$ 0.9	3.2	910 $\pm$ 130
501.10	"	"	28.3 $\pm$ 2.0	3.0 $\pm$ 0.4	0.66 $\pm$ 0.03	7.8 $\pm$ 0.3	13 $\pm$ 0.1	4.2	74 $\pm$ 13
305.1	5980 $\pm$ 50	1280 $\pm$ 107	26.5 $\pm$ 2.7	14 $\pm$ 1.5	0.95 $\pm$ 0.09	9.1 $\pm$ 0.7	18 $\pm$ 1	3.8	230 $\pm$ 25
305.2	"	"	"	30 $\pm$ 2.5	"	9.8 $\pm$ 0.7	18 $\pm$ 1.3	3.6	490 $\pm$ 42
305.3	"	"	26.0 $\pm$ 2.8	0.5 $\pm$ 0.2	0.50 $\pm$ 0.05	3.6 $\pm$ 0.3	12 $\pm$ 0.7	4.4	8.4 $\pm$ 3.3
305.4	"	"	26.5 $\pm$ 2.7	7.0 $\pm$ 0.7	0.95 $\pm$ 0.09	8.5 $\pm$ 0.7	18 $\pm$ 0.7	4.0	120 $\pm$ 12
305.5	"	"	26.7 $\pm$ 3.0	2.9 $\pm$ 0.8	1.15 $\pm$ 0.12	8.4 $\pm$ 0.7	20 $\pm$ 0.7	4.7	48 $\pm$ 13
304.1	6410 $\pm$ 40	1280 $\pm$ 107	28.8 $\pm$ 2.1	2.4 $\pm$ 0.3	3.3 $\pm$ 0.2	38 $\pm$ 2	55 $\pm$ 2	3.2	37 $\pm$ 5
304.2	"	"	"	170 $\pm$ 3	"	55 $\pm$ 2	70 $\pm$ 2	2.3	2700 $\pm$ 50
303	5520 $\pm$ 50	1280 $\pm$ 107	28.8 $\pm$ 2.1	0.4 $\pm$ 0.1	"	26 $\pm$ 2	42 $\pm$ 2	4.5	7.2 $\pm$ 1.6
301	6290 $\pm$ 100	"	27.3 $\pm$ 3.2	0.2 $\pm$ 0.2	1.8 $\pm$ 0.2	8 $\pm$ 1.3	25 $\pm$ 2	7.0	< 2.5
300	6360 $\pm$ 60	"	28.8 $\pm$ 2.1	0.3 $\pm$ 0.1	3.3 $\pm$ 0.2	19 $\pm$ 1.3	37 $\pm$ 2	6.0	4.7 $\pm$ 1.7

Table 4.2: Results from the VSA prototype radon filter. Runs 300, 301, and 303 are affected by some uncertainty in the measurement of  $G$  (see text).

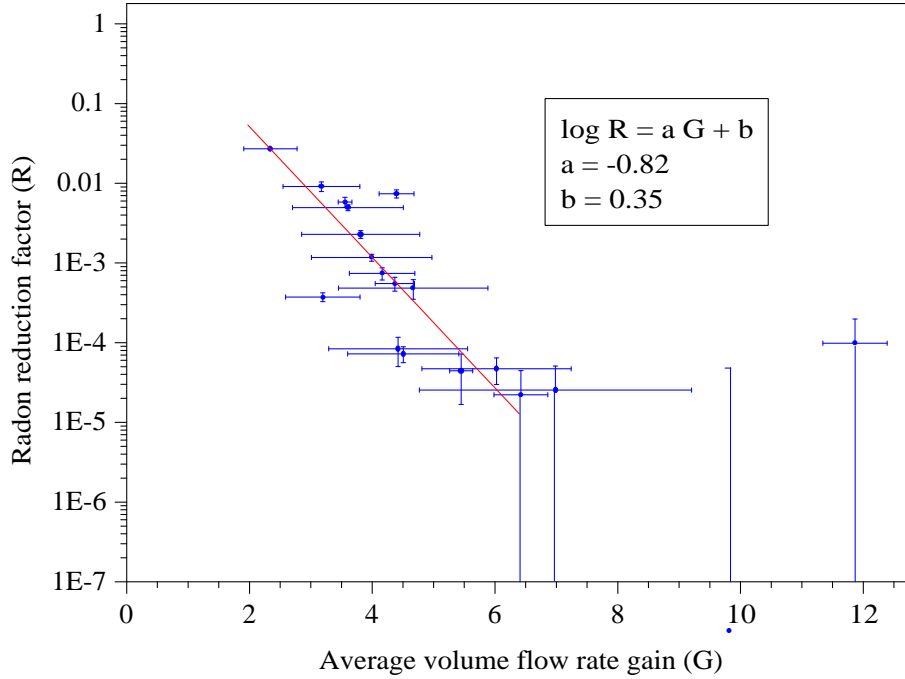


Figure 4.16: Summary of the results from the prototype VSA radon filter. The volume flow rate gain  $G$  is defined in equations (4.40) and (4.41). The data are summarized in table 4.2, where  $R$  is referred to as the normalized output Rn concentration.

Even if with considerable experimental uncertainty, the plot shows that *the radon-filtering properties of the device improve exponentially with the average volume flow rate gain  $G$  between the purge and the feed*. In particular, a fit to the data yields

$$\log_{10} R = -0.82 G + 0.35 \implies R = 2.24 e^{-1.89 G} \quad (4.44)$$

The fit does not include the 4 points with the highest volume flow rate gain since the radon concentration recorded for these runs was very low and deduced with just a few events. One of the points is actually just an upper limit since no counts were seen during the observation time. In addition, the data point with  $G \sim 4$  and  $R \sim 0.01$  should be considered more appropriately as an upper limit, given that a quick look at the radon profile of the corresponding run reveals that the ultimate, steady-state radon level had not

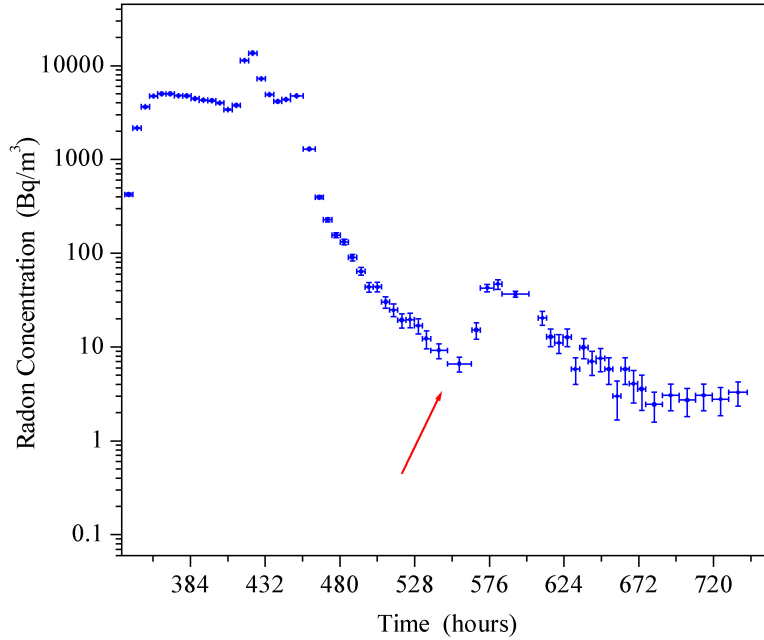


Figure 4.17: Radon profile for run 501. The arrow shows the point of the curve for which a clear plateau was not reached. The radon concentration for such data point can safely be considered as an upper limit.

been reached (see fig. 4.17). The data points for which the error on the gain is bigger reflect the uncertainty in the value of the purge flow rate before a thorough calibration of the flowmeters was performed.

The error bars on the radon reduction factor  $R$  are purely statistical and do not include a background evaluation of the RAD7 radon detector. As mentioned earlier, all recorded counts are thus recorded as radon signal from the output of the filter. Since the ultimate radon sensitivity  $A_{RAD7}$  of the RAD7 was measured at  $\sim 0.1 \text{ Bq/m}^3$ , this has undoubtedly very little effect for runs where the ultimate radon concentration is above  $\sim 1 \text{ Bq/m}^3$ . It does affect the runs in which the output radon concentration satisfies is comparable to  $A_{RAD7}$ .

The measured output radon concentration  $A_{out}$  does not account for the radon that decays inside the filter that could artificially increase the filter efficiency; this is a negligible

effect, given that the characteristic time constant of the column is approximately 6 hours while the radon mean life is 5.5 days (only about 4% of the radon decays in 6 hours).

#### 4.5.4 Comments on the prototype VSA results

The results presented in fig. 4.16 and eq. (4.44) summarize the *effective* behaviour of our prototype VSA radon filter. They do not provide a detailed analysis of all the effects that take place in the cyclical adsorptive process.

For example, the same average volume flow rate  $\Phi_{purge}$  in the purge stage can be obtained with infinite different combinations of purge flow rate  $F_{purge}$  and purge pressure  $P_{purge}$  (see eq. (4.39)). A corresponding infinite ways of obtaining the same volume flow rate gain  $G$  follows from eq. (4.40). Each of these combinations will, on the other hand, be characterized by a specific pressure drop  $\Delta P$  across the evacuated column that is fractionally more significant the lower the absolute purge pressure is (formally one can say that  $\Delta P/P_1 \xrightarrow{P_1 \rightarrow 0} \infty$ ). In turn, this will widen the gap between the efficiency of the filtration at the two opposite ends of the column. When the difference in performance widely varies along the column, it is possible that simply taking the average value of  $G$  might not be sufficient to correctly describe the system. The air velocity  $v_s$  of the purge will also significantly vary according to the pressure differential. The height equivalent to a theoretical stage (HETS) would continuously vary along the column, and no single value for this quantity could be used to describe the whole purged charcoal bed. All these effects should be taken into account for an exact modeling of the device, although they seem not to contribute, to first order, in describing the prototype system under study.

The results of the previous section hide the role of the column size in the result. Specifically, with longer columns (more charcoal) and the same operating flow pattern, we would have bigger pressure drops  $\Delta P$  along the purged bed. Since the vacuum pump has a fixed ultimate pumping speed (independent of the size of the columns), with a larger amount of charcoal we would have the same value of  $P_1$ , but a larger  $P_2$  (for a given flow rate  $F_1$ ). This would result in a smaller average volume flow rate gain  $G$  and hence a smaller radon reduction factor. This is clearly in contrast with the intuitive notion that a bigger filter should

be more efficient. The apparent paradox is solved by realizing that eq. (4.44) only applies to this specific filter, with its combination of vacuum pumping speed and charcoal column size. The charcoal mass was chosen so that the breakthrough time at the design flow rate was much bigger than the operating cycle, as mentioned previously. A further complication to the problem arises when the spreading of the radon front is taken into account. As shown with the elution tests (section 4.3), the front is sharper the higher the number of equivalent theoretical plates is. Under given conditions (pumping speed, size of the column, volume flow rate gain), the size of the column (proportional to the number of theoretical plates for a given HETS) is what determines how much of the radon front tails actually manages to escape. Under this point of view, charcoal columns which are deep enough to contain the tail of the radon front are necessary. The charcoal required could in principle be much more than that necessary to contain the average position of the radon front. A quantitative prediction of the behaviour of filters of different sizes is thus a complex problem to solve exactly.

#### 4.5.5 Implications for the full-scale VSA

In determining the scale-up parameters for the VSA radon filter to connect to the clean room the considerations listed in the previous section are taken into account. The final filter will need to supply between 85 and 170 m<sup>3</sup>/h of filtered air to the clean room (50 to 100 times more than the prototype).

The first quantity to consider is the amount of charcoal needed for each column. A 100-fold increase from the amount used in the prototype indicates that at least 135 kg of charcoal per column are required. A considerable safety factor should be included to account for the factors listed below:

1. The feed pressure in the final system will be at atmospheric pressure, instead of  $\sim 1300$  mbar as in the prototype. A 30% increase in the amount of charcoal needed for the feed cycle should be included.
2. The input air in the final system will not be as dry as for the prototype. The first

fraction of the charcoal bed will adsorb the remaining humidity on the feed air stream and will be highly ineffective for radon adsorption. Extra charcoal should be added to the column to counterbalance this effect.

3. Scaling up a system almost always results in some inefficiencies. Some could arise, for example, because of non ideal column packing and channeling inside the packed bed. A safety factor in the amount of charcoal should be included to limit such inefficiencies.

On the other hand, one should try to keep the size of the filter as small as possible for different reasons. In addition to increasing cost, bigger columns imply longer evacuation times and larger pressure drops that can deteriorate the efficiency of the filter (see previous section). The amount of charcoal for the final VSA should be in the 200÷250 kg range.

Once the feed conditions are defined (feed flow rate  $F_{feed}$ , column size, ...), the purge parameters need to be defined according to need. If a 100-fold radon reduction is aimed for, figure 4.16 shows that an average volume flow rate gain  $G \geq 3$  should be adequate. For a maximum design feed flow rate  $F_{feed}^{max} = 170 \text{ m}^3/\text{h}$  of the full-size system, a vacuum pump with a pumping speed  $S_{pump} \geq 500 \text{ m}^3/\text{h}$  is required. The throughput  $Q_{pump}$  the pump needs to handle is also considerable: practical operating purge pressures  $P_{purge}$  are between 5 and 20 mbar, and the corresponding throughput is

$$Q_{pump} \stackrel{def}{=} S_{pump} P_{purge} \geq 10^4 \frac{\text{m}^3 \cdot \text{mbar}}{\text{h}}. \quad (4.45)$$

Efficiency in removing radon is not the sole parameter one must consider when designing a filter for use in connection with a clean room environment. One concern of such a system is potential oxygen depletion in the output air, posing a safety hazard to cleanroom workers [130]. While the partitioning of nitrogen versus oxygen on a charcoal bed optimized for radon removal should not be significant, a measurement was taken as a precaution. A standard oxygen meter [131] was used to monitor both the input and output air of the prototype VSA filter. No measurable variation was observed, even with extremely short cycle times (tens of seconds) for which potential oxygen/nitrogen separation should be greater (this

last statement reflects the fact that the filter works in saturation for oxygen and nitrogen and that for these elements the break through time constant is extremely small).

Particle generation is another concern in the design of such a system. A make-up air supply that is exceedingly high in particle counts could compromise the clean room HEPA units, posing a risk both in terms of cost and contamination. A check was performed on the prototype VSA to understand the basic trends of particulation from a charcoal bed filter. A laser particle counter [132] was used to monitor particle counts from the output air of the filter. Particle levels were highly dependent on whether the charcoal inside the column was well-packed, and how long the system was running in a steady-state mode. Loosely packed columns gave particle counts compatible with worse than Class 10,000 while well-packed columns could be rated better than Class 100 (note that a given Class specifies the number of 0.5 micron and greater particles per cubic foot of air). Starting the system from a full shut-down produced high particle counts initially, but these rapidly fell as a function of running time. Class 100 levels were achieved with well-packed columns after running for at least 2 hours. These levels could be maintained with the addition of simple particle filters on the overall system output. Note that compressed air was the input source for this system and is presumably significantly cleaner than standard room air. These measurements support the idea that this filter is not a particle generator. Typical measured values of room air (which is the source of make-up air for standard clean rooms) are on the order of Class  $10^5 - 10^6$ , so particles generated by the VSA filter are negligible.

# The Full-Scale Radon Filter

The successful radon reduction obtained with the prototype radon filter described in chapter 4 provided the basic experimental information needed to engineer a full-scale system for the vessel construction clean room. A detailed account of the basic principles of operation of vacuum swing adsorption towards radon removal is given in said chapter. The main goals were to engineer a system within a reasonable budget that would give an acceptable radon suppression inside the room. The filter was designed to work without interruptions for the whole period of vessel construction.

## 5.1 Radon mitigation requirements

The basic radioactivity requirements for Borexino were summarized in section 2.3. Among them, the most critical requirement other than the intrinsic purity of the scintillator itself was the cleanliness and radioactivity on the Inner Vessel. The requirements and various aspects of vessel radioactivity contamination were addressed in sections 3.2 and 3.4. In the latter, the contamination of the nylon surfaces following radon exposure was analysed in detail. It was estimated (eq. (3.11)) that  $\sim 6500pw$   $^{210}\text{Bi}$  and  $^{210}\text{Po}$  decays/day would be generated inside the Borexino scintillator (because of radon exposure) for every hour of exposure of the entire IV surface to average air (30 Bq/m<sup>3</sup> radon activity). The coefficients  $p$  and  $w$  are the plate out and wash off fraction and in general range from 0 to 1. One third ( $\sim 2200pw$ ) of such decays would be in the fiducial volume.

As explained in chapter 6, many precautions were taken to minimize the exposure time of the nylon film during vessel assembly, and an average of one hours seems realistic. Assuming such exposure time, a reduction factor

$$R = 2200pw \quad (5.1)$$

is required from the full-scale VSA radon filter to meet the requirements ( $< 1$  event/day in the fiducila volume). Using the plate out and wash off values ( $p \sim w \sim 0.01$ , measured after the prototype VSA radon filter was operated successfully) discussed in chapter 3, no radon suppression in the clean room air would be needed. On the other hand, long term wash off effects could result in a greater scintillator contamination than these numbers suggest. Also, a longer than expected exposure time of the vessels during construction is always possible and being able to supply ample safety margins is ausplicable.

## 5.2 Scale-up parameters and requirements

The difficulties met while scaling up the prototype radon filter were of both technical and non-technical nature. The choice of most components, such as the quality of the charcoal-packed tanks, the valves, and the tubing has been dictated by the need to optimize performance within a limited budget. On the other hand, choosing the most adequate vacuum pump system posed technical problems as well.

Ideally, one would want a vacuum pump with the highest possible pumping speed to obtain the best gain factor  $G$  during the purging stage (see section 4.5.3 for a definition of  $G$ ). As explained in chapter 4, the ratio between the purge and feed flows is what basically determines the radon filtering efficiency of the filter. Based on what was learnt with the prototype, the pump has to handle a very high throughput at a relatively moderate vacuum ( $\sim 15$  mbar) in steady-state conditions. The radon filter is designed to supply up to 170  $\text{m}^3/\text{h}$  (100 cfm) of filtered air to the clean room (100 times more than the prototype). Based on the results of the prototype filter, an average volume flow rate gain  $G \geq 3$  is needed for a 100-fold radon reduction or better (see fig. 4.16) ( $G \geq 4$  is required to obtain

a 1000-fold reduction). Since for the Borexino vessel a radon suppression by a factor of 100 is recommended, a pumping speed  $S \geq 500 \text{ m}^3/\text{h}$  is required for the vacuum pump if the filter is operated at the maximum design flow rate.

The amount of charcoal used per column is  $\sim 250 \text{ kg}$ . We do not have a more accurate measurement of the weight of the charcoal since the it was put in the columns still wet after it was washed; it was dried after loading inside the tanks with a flow of dry air. The prototype used 1.35 kg of charcoal per column: it was decided to multiply this value by more than 100 to account for inefficiencies (see section 4.5.5). Four main factors were considered. The feed pressure for the final filter is just  $\sim 10 \text{ mbar}$  above 1 atm. The feed pressure in the prototype was 1.25 atm or above (see table 4.2). 25% more charcoal is thus needed for the full-scale device. secondly, the air entering the final filter would not be as dry as the one fed to the prototype, so that effectively some fraction of the charcoal would separate out the water from the air stream and become very inefficient for radon adsorption. Also, it is not a trivial task to have uniform, well-distributed flow patterns inside big packed beds. Scaling up the small-scale prototype most likely means having some “dead” charcoal volumes, especially close to the input and output of the columns. Finally, a deeper bed allows for longer cycle times; this is crucial for minimizing the frequency at which the columns are evacuated and re-pressurized, period during which the filter is in a transient, inefficient condition.

The shape of the columns was changed from that of the prototype. A shorter and wider geometry was chosen over a long, thin column to reduce the pressure drops across the charcoal bed and have a corresponding uniformity of radon adsorption capability throughout the filter. It also made it possible to limit the overall physical size of the device.

A problem that had to be specifically addressed was how to dry the input air. Ambient relative humidities in Princeton can be very high, especially during the summer. As described in the next section, a compromise had to be reached in order to keep expenses low. The air fed to the final radon filter was kept below  $\sim 10\% \text{ RH}$ . A further difference was that we needed a blower to push air through the filter. The prototype was run with compressed air regulated down to almost atmospheric pressure. The use of a blower at essentially full

speed meant that there was no flow capacity margin during the re-pressurization step of the VSA cycle (see below).

### Leak tightness requirements of the system

An important consideration for the design of the radon filter is leak tightness. In other words, what is the maximum leak one can tolerate given the radon levels one plans to achieve? The answer to this question determines the specifications required for the components (tanks, valves, fittings, ...) and possibly help limit the cost of the system.

Leaks can occur at any point along the lines, and have two main effects on the system. Because of leaks, the purified air stream emerging from the filter could be contaminated. This is true only if the leak occurs at the output; if there's a leak before the charcoal bed, it will mix with the input air and be radon-filtered as well. In addition, leaks can add an unnecessary load to the vacuum pump and limit the purging efficiency of the filter by reducing the gain factor  $G$  (see chapter 4). The latter is a problem only if the leak is very significant. For example, a 1 std cc/s leak corresponds to 50 cc/s (180 ℓ/h) at a purge pressure of 20 mbar, which is just a small fraction of the expected purge volume flow rate ( $> 400 \text{ m}^3/\text{h}$ ). The acceptable contamination coming from leaks into the purified air stream depends on the radon concentration one expects to emerge from the filter. The rule of thumb is that radon from leaks should contribute a radon concentration smaller than that delivered by the filter. For a quantitative estimate suppose a leak rate  $Q_{\text{leak}}$  mixes with the output flow  $Q_{\text{feed}}$ . The radon concentration of the air leaking in is  $A_{\text{air}}$  and, for simplicity, let the output flow be perfectly radon-free (conservative assumption). If the requirement is to deliver air where radon is suppressed by a factor  $f$  or more, the following trivial relation has to be satisfied:

$$\frac{Q_{\text{leak}}}{Q_{\text{feed}}} < \frac{1}{f} \quad (5.2)$$

For  $Q_{\text{feed}} = 85 \text{ m}^3/\text{h}$  (minimum design specification), a leak rate of 20 cc/s would still give a 1000-fold radon reduction, thus meeting the requirements for vessel construction. These specifications can easily be met using components not meant for high vacuum applications.

### 5.3 Experimental setup

The full-scale radon VSA filter was assembled in Princeton in the Summer of 2001. It came on-line before vessel (IV and OV) panels were glued together and any IV nylon film panels for the Borexino vessels were exposed to the clean room air.

The conceptual design of the device is very similar to the prototype, described in detail in chapter 4. Minor improvements in the layout and a slight change in the VSA cycle sequence during the re-pressurization phase had to be implemented. A schematic drawing of the filter is shown in fig. 5.1.

The charcoal is held in two carbon steel tanks ( $\sim 0.9 \text{ m}^3$  in volume) [133]. The body of each tank is 91 cm in diameter, 140 cm tall, and is self-standing. The tanks have lids that can be lifted to insert the charcoal supporting frame and to load the charcoal. The seal between the lid and the tank is done with a 1/4"-thick neoprene gasket. There is one 4" and one 3" opening for air input and output: the bigger is also used for connecting the vacuum pump. They are equipped with slip-on flanges. Two smaller 1" flanged ports are provided for monitoring of the gas parameters (pressure, temperature, humidity) at both ends of the charcoal bed. All counter flanges are of aluminum, custom made with grooves for viton o-rings. Each tank also has a drain plug at the bottom. Inside each tank is a cast iron support structure for holding the activated carbon in place during the pressure swings. A drawing of a tank is shown in fig. 5.2.

The charcoal is coconut-based Calgon PCB4 $\times$ 8LS [120], the same as that employed in the small-scale prototype VSA device. As with the prototype filter, the charcoal was washed with water to eliminate most of the dust. The rinsing proceeded until the drain water was visibly clear (see fig. 5.3). Before being loaded with the charcoal, the inner surfaces of each tank were thoroughly cleaned and coated with an acrylic paint to prevent rusting. The loading of the charcoal proceeded as follows: a bottom iron grid with a metal mesh finer than the charcoal flake size was put in place for the charcoal to rest on. The charcoal was subsequently loaded wet into the tanks, where it was dried for a few days with a continuous flow of dry air. The charcoal bed was covered by an iron grid with metal sheet mesh.

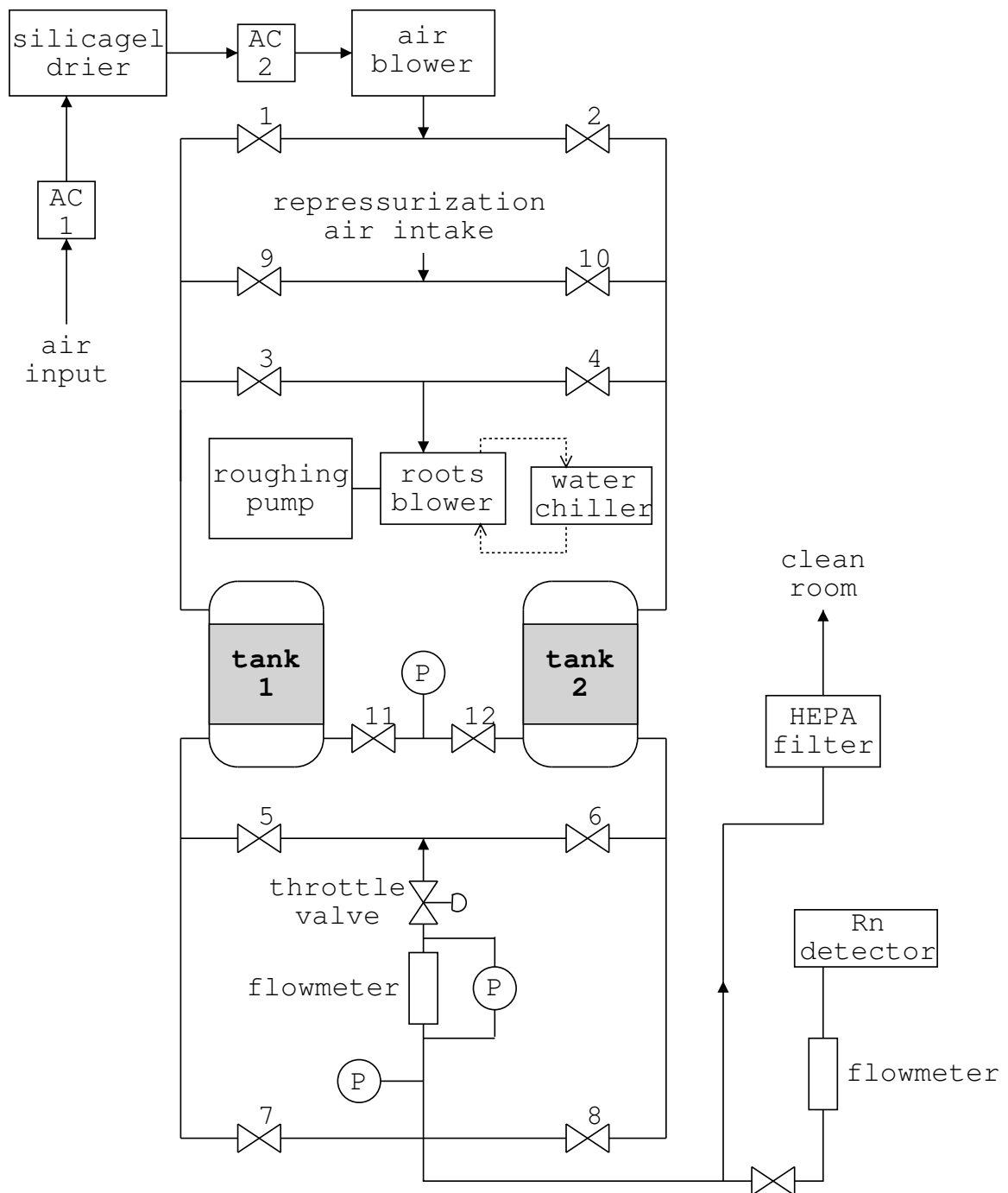


Figure 5.1: Diagram of the full-scale VSA radon filter. Valves 9 and 10 were added from the layout of the small-scale prototype (fig. 4.12) to allow for a quicker re-pressurization of the evacuated charcoal columns and guarantee a smooth, constant output air flow. Along the air input line, “AC” stands for air conditioner.

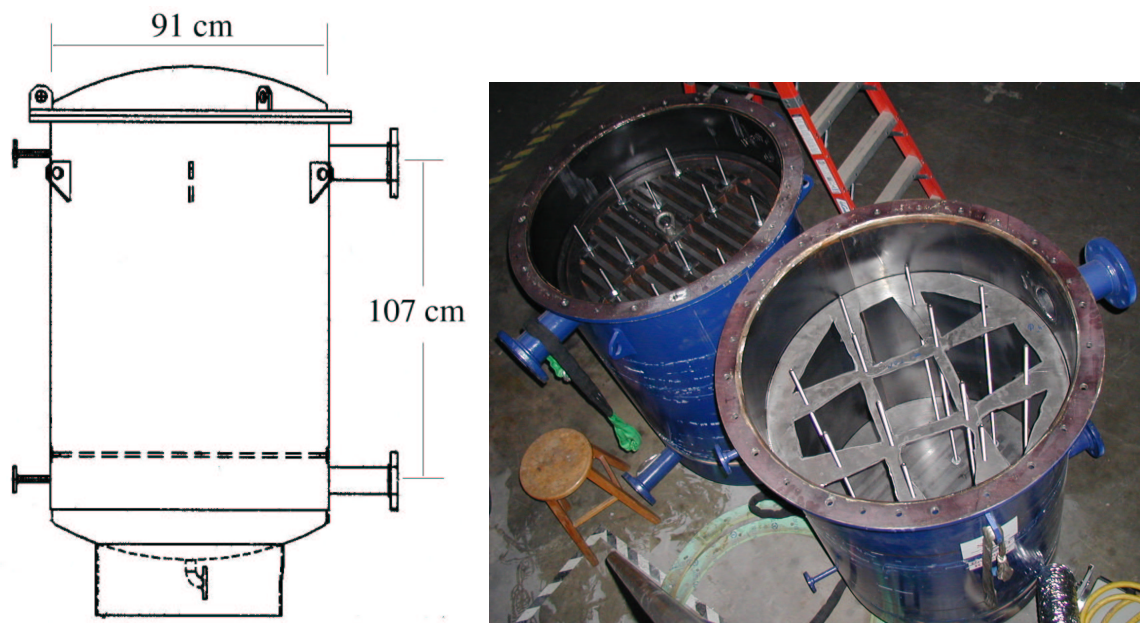


Figure 5.2: A schematic drawing of a radon filter tank (left [133]); an internal lip is provided to hold the internal charcoal support structure. Details of the support structure inserted in the tank are shown on the right. The tank shown in the foreground doesn't have the top grid, visible in the one in the background. The actual charcoal volume is  $\sim 500$  liters.

Threaded rods were inserted through the bed to clamp the two iron grid plates together, keeping the bed compact. Stiff metal springs were also inserted to keep the charcoal bed tightly clamped during the pressure swings.

After considering various vacuum pumping systems (among which are water-ring pumps and steam ejectors), a conventional roughing pump + roots blower combination was chosen. The roots blower is an Edwards EH1200 [134], while the roughing pump is a Becker U4.400F [135]. The latter is specifically manufactured for moderate vacuum, high throughput industrial applications. Such a sturdy pump was required by the significant amount of gas to be evacuated, by the frequency of evacuation and by the presence of water vapour in the evacuated air stream. In addition, the system had to rely on just minimal maintenance for the whole nylon vessel construction period (interruptions in the filter operation would lead to higher radon exposure of the nylon surfaces). A water chiller was also required for



Figure 5.3: Washing the activated charcoal for the radon filter (left). The rinse water was monitored until the visible level of dust was negligible (right).

cooling the roots blower. The nominal pumping speed for such a combination is  $\sim 650 \text{ m}^3/\text{h}$  at the inlet. The installed vacuum pump system is shown in fig. 5.4.

The air feed to the input of the system was required to have low humidity. The residual water would be adsorbed in the first fraction of charcoal, reducing the volume useful for radon removal. A commercial silica gel air drier was chosen to handle the entire input air flow [136]. For an enhanced drying efficiency and for reducing the temperature of the air sent to the VSA filter, two air conditioning units were placed before and after the drier (5000 and 15000 BTU/h respectively), as shown in the sketch in fig. 5.1. The input air was at  $21 \text{ }^\circ\text{C}$  and 5-10% RH. Air was pushed into the system and through the charcoal columns by a 5 HP pressure blower [137]. The silica gel drier and the pressure blower can be seen in the bottom left corner of fig. 5.5. The connections between the drying units and the air blower were made with flexible 6" and 8" plastic hose.

Pneumatically controlled solenoid angle valves with aluminum body were chosen as process control valves for most of the system [138]. Six (valves 1, 2, 5, 6, 7, and 8 in fig. 5.1) are 2" diameter with KF fittings (NW 50); two (valves 3 and 4 in fig. 5.1) are 3" diameter with LF fittings (NW 75). Throughout the system (except where specifically mentioned), wire reinforced PVC vacuum tubing is employed. The connection to the valves



Figure 5.4: Side view of the radon filter. The vacuum pump is visible in the foreground with the 3" PVC inlet connection. The roots blower ("a") is placed on top of the more massive roughing pump ("b"). The two blue charcoal tanks are visible in the background (tank 2 is labelled "c"). Between the tanks and the pump is the frame housing, all the pneumatic valves, and the output HEPA filter ("d"). The orange 10" hose ("e") at the output of the HEPA filter housing on the left connects the VSA to the input of the clean room. The other hose visible on the top right corner of the picture ("f") is the "muffled" inlet for the air used for re-pressurizing the columns at the end of a purge stage.



Figure 5.5: Top view of the charcoal-based VSA radon filter for the Borexino vessel construction clean room. On the left, from the bottom, are the silica gel drier, the input air blower, the control computer, and the chiller for the roots blower. The big hose at the top of the picture serves as a muffler for the re-pressurization air intake, otherwise very noisy. The connection to the clean room is via the hose on the right.

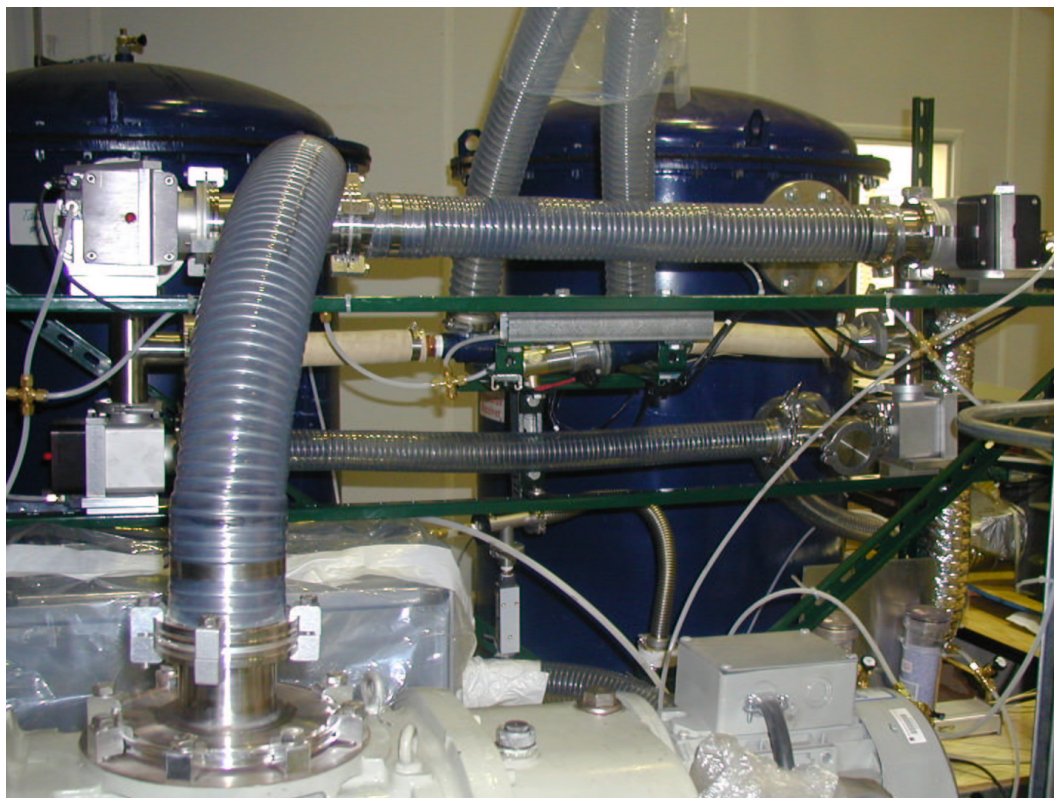


Figure 5.6: Closeup of the VSA system. From the top left corner, valves 3, 4, 9, 10, 1, and 2 can be seen. The 3" line to the vacuum pump can be seen in the front. Most fittings are KF 2" and LF 3".

is performed with KF and LF half-nipples and fittings; the connection to the tanks is made with custom-made half nipple aluminum flanges. The PVC tubing is hose-clamped onto the half-nipple stubs. All atmospheric pressure lines are 2" diameter, while the low pressure ones are 3" diameter. A closeup of valves and lines is shown in fig. 5.6. The sizing of these lines followed a specific study of flows through the system and was designed to optimize performance by maximizing conductances while maintaining the system within a manageable budget. In particular, the tubing was sized to achieve laminar flow through it in the low pressure (purge) lines, where pressure drops would limit the pumping speed of the system deteriorating the filter's efficiency [129]. The two valves for re-pressurization air intake (9 and 10 in fig. 5.1) were not foreseen in the original design and were added at a



Figure 5.7: Closeup of the purge regulating line.

second stage of assembly. They are 1" pneumatically controlled valves, previously employed in the low-pressure lines of the prototype VSA radon filter (valves 3 and 4 in fig. 4.12). The need for these valves is explained in section 5.3.2. Two 1/8" solenoid valves (11 and 12 in fig. 5.1) separate the tanks from a pressure gauge. The line for regulating the amount of purge gas is made with a manual butterfly valve and a visual rotameter. The pressure at the input of the rotameter and the pressure drop across it are measured with Magnehelic gauges. The purge flow is an important parameter of the system and its accurate reading relies on it being operated at atmospheric pressure. A detail of this part of the system is shown in fig. 5.7.

Although the tests performed on the prototype VSA had shown a particulate level at its output lower than that of standard indoor air (see section 4.5.4), a particle filter was placed at the output of the full-scale system. This consists of a layer of coarse prefiltering

material followed by a clean room grade HEPA unit [139]. The particle filter was placed in a stand-alone housing, as shown in fig. 5.4. The addition of the HEPA filter to the radon filter followed the general philosophy to build different plants of a system so that they are, if possible, completely independent, without having to rely on the optimal performance of other plants they are connected to.

The opening and closing sequence of the valves (1 to 12 in fig. 5.1) is automated by a LabVIEW program that controls 12 relay switches along the power supply lines of the solenoid of the valves [140]. A graphical interface to easily set opening and closing patterns for all valves independently, as well as setting feed and purge times, was programmed. A view of this interface is shown in fig. 5.8.

### 5.3.1 Cost of the VSA filter

The cost of full-scale VSA radon filter was approximately 50k US\$. A break down of the cost for the main components is presented in table 5.1. Approximately half of the expense was for the vacuum pump (22k US\$,  $\sim$  16k US\$ for the roughing pump). The tanks, the charcoal, and the solenoid valves also significantly contribute to the total cost of the device.

### 5.3.2 The filter cycle

The basic VSA cycle for the full-scale system is very similar to that used in the prototype setup (see section 4.5.2). The only addition is the additional air intake path for re-pressurizing the columns at the end of the purge cycle. In detail, the cycle is divided in six stages as follows (see fig 5.8):

#### 1. feed through column 1, purge column 2

Valves 1, 4, 6, 7, and 12 are open. The air travels through valve 1, column 1, and valve 7 to the output. A fraction of it is sent back through valve 6 to column 2, which is being evacuated through valve 4. This stage lasts for a time ranging from 10 to 30 minutes. Valve 12 connects column 2 to a pressure gauge to monitor the purge

item	cost (US\$)
tanks	8k
charcoal (0.5 t)	6k
vacuum pumps	22k
valves	4k
dryer	3.5k
blower	1.5k
HEPA filter + housing	1.5k
computer and valve control boards	1.5k
other (fittings, tubing, ...)	5k
total	53k

Table 5.1: Cost of the main components of the VSA radon filter for the Princeton clean room. The main fraction ( $\sim 70\%$ ) of the vacuum pump cost was that for the roughing pump; the roots blower was a refurbished one.

pressure.

**2. feed through column 1, re-pressurize column 2**

Valves 1, 7, 10, and 12 are open. The feed path through column 1 is unchanged. The purge is interrupted by closing valve 6. The evacuation of column 2 is interrupted by closing valve 4. Air is let into column 2 through valve 10 to re-pressurize it. This stage lasts for approximately one minute.

**3. feed through column 1, bring column 2 to the feed pressure**

Valves 1, 2, and 7 are open. The feed path through column 1 is unchanged. Valve 10 is closed, while valve 2 is opened. This allows a small fraction of the incoming air to equilibrate the pressure of column 2 to that of the input. This stage lasts for a few seconds only.

**4. feed through column 2, purge column 1**

Symmetric to stage 1. Valves 2, 3, 5, 8, and 11 are open. The air travels through valve 2, column 2, and valve 8 to the output. A fraction of it is sent back through valve 5 to column 1, which is being evacuated through valve 3. This stage lasts for a

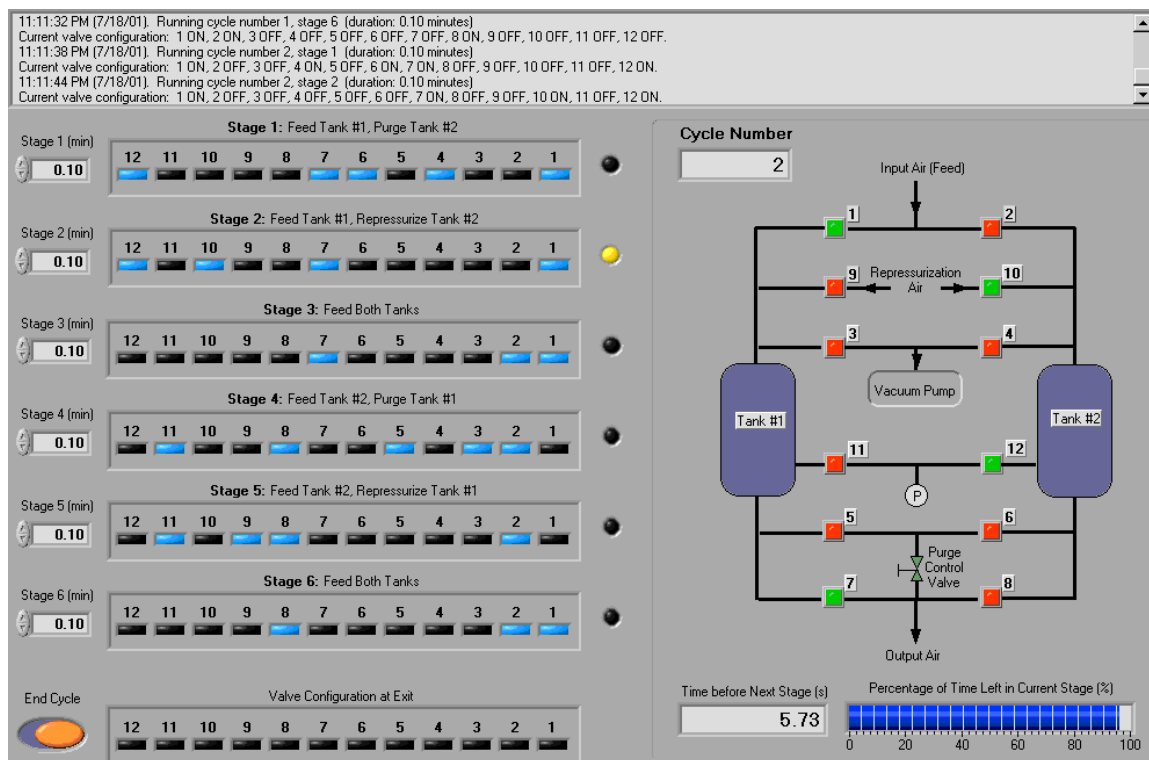


Figure 5.8: Screen shot of the control system for the VSA radon filter. By clicking on the corresponding box, a valve can be opened or closed. The time of each cycle phase is set by typing in the value in the boxes on the left. The status of each valve at any time is given by its colour on the display on the right (red=closed, green=open). The view is taken during re-pressurization of column 2; the times shown are for a test run of the system.

time ranging from 10 to 30 minutes. Valve 11 connects column 1 to a pressure gauge to monitor the purge pressure.

##### 5. feed through column 2, re-pressurize column 1

Symmetric to stage 2. Valves 2, 8, 9, and 11 are open. The purge is interrupted by closing valve 5. The evacuation of column 1 is interrupted by closing valve 3. Air is let into column 1 through valve 9 to re-pressurize it. This stage lasts for approximately one minute.

##### 6. feed through column 2, bring column 1 to the feed pressure

Symmetric to stage 3. Valves 1, 2, and 8 are open. Valve 9 is closed, while valve 1 is

opened. This allows a small fraction of the incoming air to equilibrate the pressure of column 1 to that of the input. This stage lasts for a few seconds only.

## 5.4 Preliminary tests

Preliminary tests were performed to measure the leak rate of the two charcoal tanks, the speed of the pumping system, and the purge pressures achievable as a function of purge flow.

### Leak tightness

The leak tightness of the tanks was tested by pumping them down to vacuum and observing the rate of the pressure rise. During the test all ports were sealed with blank caps with viton o-rings and leak tested using snoop after slightly pressurizing the tanks. A flat neoprene 1/4" thick gasket was used on the big 1-meter lid flange. For both tanks, the measured pressure increase rate was  $\sim 5 - 7 \times 10^{-3}$  mbar/s. For an assumed tank volume of  $1 \text{ m}^3$ , the corresponding leak rate is 5-7 cc/s. The leak is then  $< 0.05\%$  of the output flow rate of the filter (25-50 l/s or 85-170  $\text{m}^3/\text{h}$ ). If the entire leak mixes with the "radon-free" output, it would limit the possible efficiency of the device to a maximum 5000-fold radon reduction. After a leak check using snoop, the leak was determined to be at the 1-meter neoprene gasket; in this case the air leaking in mixes with the input flow and is radon-filtered by the charcoal bed. Thus the measured leak rate does not represent a problem for the device's performance.

### Evacuation time and pumping speed

The evacuation speed of the pump was measured next. The pump system was connected to the 4" port of one of the tanks with a 5-meter 3" PVC reinforced tube. An 3", angle solenoid valve was inserted in the line to simulate the final operating conditions. Tests were performed with both empty and charcoal-packed columns. The results are shown in fig. 5.9, where the pressure time profiles during evacuation are plotted. The pumping speed  $S$  at

column/pump configuration	$\tau$ (s)	$P_{min}$ (mbar)	$S$ (m <sup>3</sup> /h)
empty tank, backing pump only	$14.3 \pm 0.4$	$\sim 4$	252
empty tank, backing pump and roots blower	$6.7 \pm 0.1$	$\sim 0.4$	537
charcoal-packed tank, backing pump and roots blower	$19.0 \pm 0.3$	$\sim 1.5$	-

Table 5.2: Evacuation time  $\tau$  and corresponding pumping speed  $S$  for various pump/tank combinations. The pumping speed is calculated using  $S = V/\tau$  and assuming  $V = 1 \text{ m}^3$ . No value for  $S$  is given in the presence of charcoal since the volume  $V$  in this case is unknown (certainly significantly larger than  $V$ ).

the tank is extracted by fitting the exponentially decaying part of the curve with

$$P = P_0 e^{-t/\tau}, \quad \tau = V/S \quad (5.3)$$

where  $V$  is the volume of the tank and  $P_0$  is the initial pressure (1 atm in this case). This formula is valid in the regions where  $S$  is constant as a function of pressure [128].  $S$  and the pumping speed at the pump  $S_p$  are related by  $1/S = 1/S_p + 1/C$ , where  $C$  is the conductance of the line that connects the pump and the tank. Regardless of  $S_p$ , what determines the radon filtering efficiency of the VSA is  $S$ .

The fits to the pumpdown data yield the characteristic evacuation times for different configurations and are summarized in table 5.2. The ultimate pressures  $P_{min}$  are also reported and can be read from the plots in fig. 5.9. The pumping speed at the tank with the backing pump + roots blower combination is 537 m<sup>3</sup>/h (150  $\ell$ /s). This value needs to be compared with the maximum required input flowrate to the filter,  $\Phi_{max} \simeq 180 \text{ m}^3/\text{h}$ . The maximum achievable volume flowrate gain  $G_{max}$  (see chapter 4) is given by

$$G_{max} = \frac{S}{\Phi_{max}} \simeq 3 \quad (5.4)$$

A value for the pumping speed for the charcoal-packed column cannot be stated in the absence of an accurate estimate of its effective volume and in the presence of adsorptive processes. A look at fig. 5.9 suggests that the effect of adsorption is non-negligible below 10

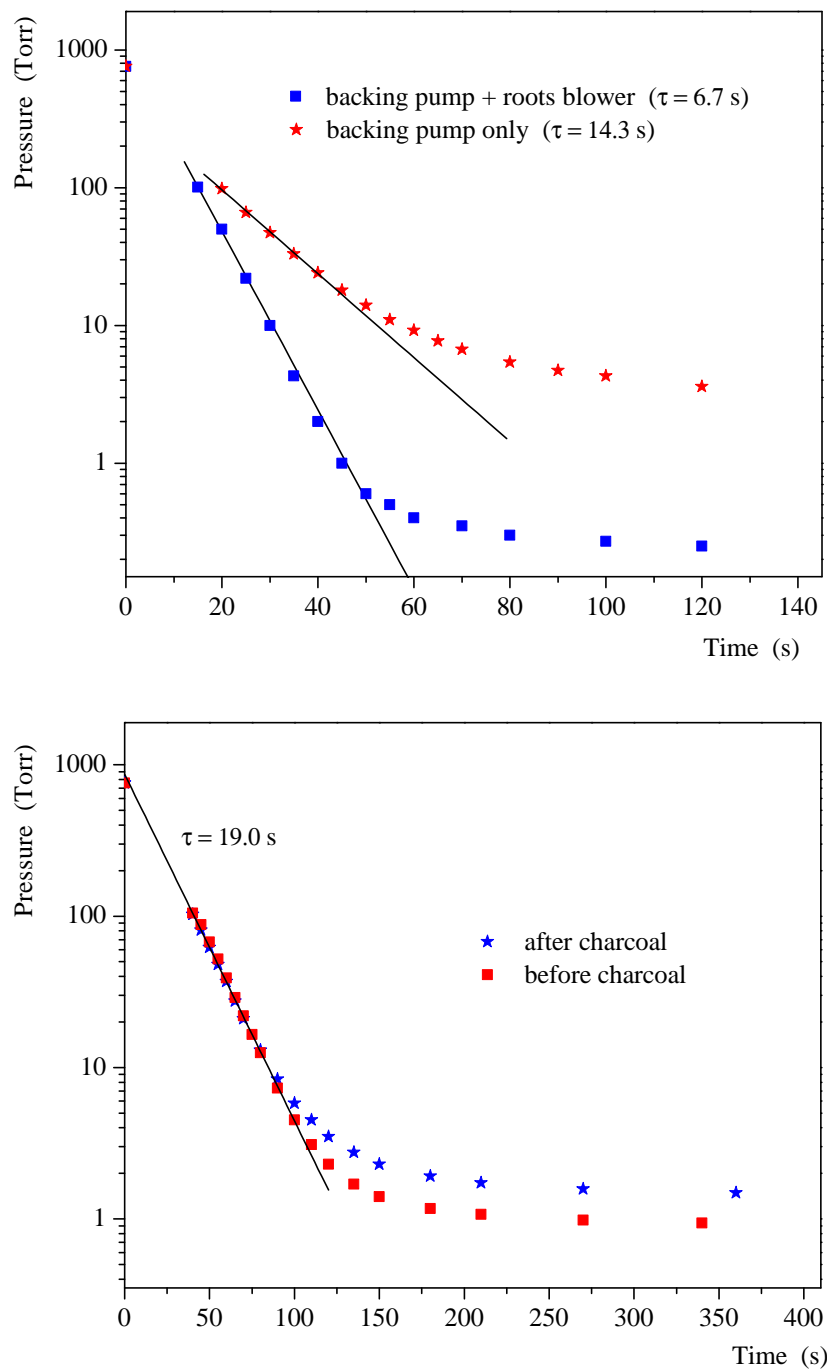


Figure 5.9: Pumpdown time for the columns of the VSA system with the final vacuum pump. The top plot refers to the evacuation of an empty column. The pumpdown time significantly increases in the presence of the charcoal bed (bottom). Refer to the text for the details of the fits and the extrapolated pumping speeds.

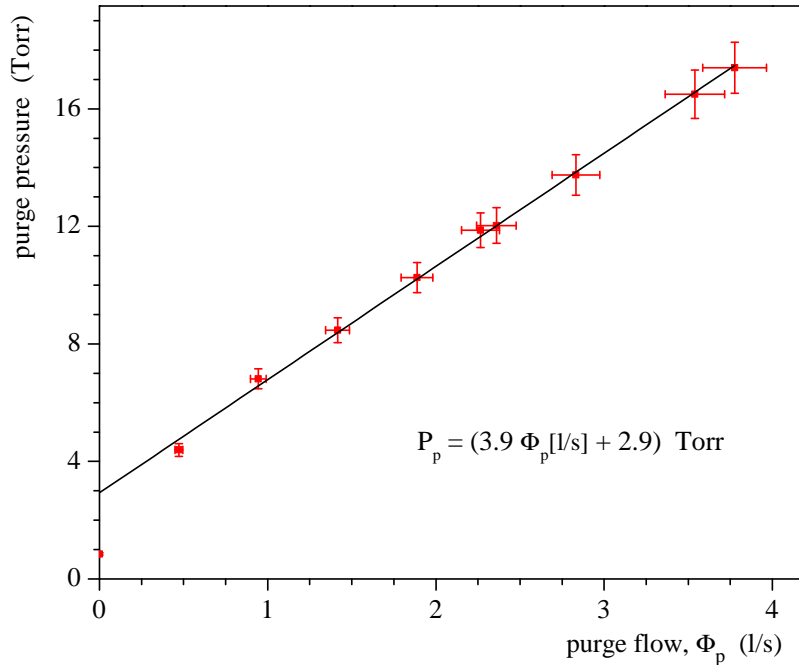


Figure 5.10: Pressure in the charcoal column (tank 1) as a function of purge flow ( $P_p^{far}$  in the text). The pressure was measured at the end opposite to that the vacuum pump.  $\Phi_p$  is expressed in standard  $\ell/s$ . The result is reported in mbar in eq. 5.5

Torr (15 mbar), where the pressure profile of the charcoal-loaded columns during evacuation deviates from an exponential decay and levels out.

### Purge pressure vs purge flow

The pressure of the charcoal column as a function of the purge flow rate  $\Phi_p$  was also measured in the final configuration. A feed cycle was set up through tank 2, with valves 2, 8 open and valves 1, 4, 6, 7, 9, 10 closed (refer to fig. 5.1). Tank 1 was evacuated and the purge flow was bled through it, with valves 3, 5 open. The throttle valve was used to regulate  $\Phi_p$ , which was read on the rotameter, kept at atmospheric pressure. The pressure  $P_1$  of tank 1 was recorded (valve 11 open). The pressure as a function of purge flow is shown in fig. 5.10. Above  $\sim 4$  Torr (6 mbar and  $\Phi_p \sim 0.5 \ell/s$ ) the behaviour is linear, and

a fit to the data yields:

$$P_p^{far} = A\Phi_p + B = (5.2 \pm 0.1)\Phi_p + (3.9 \pm 0.2) \text{ mbar}, \quad (5.5)$$

where  $\Phi_p$  is expressed in  $\ell/s$  in the last equality. From eq. (5.5) one can deduce the *effective* pumping speed  $S_p^{far}$  at the end of the charcoal column away from the vacuum pump via the relation

$$S_p^{far} = \frac{P_0}{P_p^{far}} \Phi_p = \frac{P_0}{A + B/\Phi_p} \xrightarrow{\text{large } \Phi_p} \frac{P_0}{A}, \quad (5.6)$$

where  $P_0$  is atmospheric pressure and eq. (5.5) has been used. The data in fig. 5.10 show that larger purge pumping speeds (i.e. larger volume flow rate gains) are achieved at larger purge flow rates. The pumping speed  $S_p^{near}$  at the end of the charcoal column closest to the pump is larger because of the pressure drop  $\Delta P$  across the charcoal, and is given by

$$S_p^{near} = \frac{P_0}{P_p^{near}} \Phi_p = \frac{P_0}{(A - \Delta P/C_c) + B/\Phi_p} \xrightarrow{\text{large } \Phi_p} \frac{P_0}{A - \Delta P/C_c}, \quad (5.7)$$

where the assumption is made that  $\Delta P = \Phi_p/C_c$ , with  $C_c$  being the conductance of the charcoal bed.  $\Delta P$  was measured to be extremely small ( $\sim 1$  mbar) during these and the evacuation tests discussed in the previous paragraph. The pumping speed is thus essentially constant along the charcoal bed.

As reported in section 5.7, the VSA was run with  $\Phi_p \sim 3.5 \ell/s$  for most of its operation during vessel assembly. From eq. (5.6) and table 5.3, this value yields  $S_p^{far} \sim 150 \ell/s \sim 510 \text{ m}^3/\text{h}$ . This value almost coincides with the pumping speed measured during the evacuation of the empty tanks (see table 5.2) and confirms that  $\Delta P$  across the charcoal bed is small. For the maximum design feed flow rate  $F_{feed} = 170 \text{ m}^3/\text{h}$ , this value of  $S_p^{far}$  gives a gain factor  $G \sim 3$  which, according to eq. (4.44) and fig. 4.16, should give a reduction factor  $R$  of the filter  $R \sim 150$ . For the minimum design flow rate  $F_{feed} = 85 \text{ m}^3/\text{h}$ ,  $G \sim 6$  and  $R$  could be as high as 20000, according to the results obtained with the prototype. The results from the VSA are reported in section 5.7.

feed cycle time (min)	$\Phi_{out}$ (std $\ell/s$ )	$\Phi_p$ (std $\ell/s$ )	$P_p^{far}$ (mbar)	$A_{out}$ (Bq/m <sup>3</sup> )	test duration (h)
15	31	1.2	$12 \pm 1$	$\sim 1$	38
15	31	2.0	$14 \pm 1$	$\sim 1$	13
15	31	2.5	$17 \pm 1.5$	$\sim 1$	9
10	31	3.5	22.5 – 26	$\sim 1$	34
20	31	3.4	22 – 25	$0.5 \pm 0.3$	70
20	25	3.4	22 – 25	$0.15 \pm 0.15$	24

Table 5.3: Initial tests of radon reduction with the VSA filter. The re-pressurization time was set at 30 seconds for all runs. The total input air flow being filtered is  $\Phi_p + \Phi_{out}$ . The uncertainty on  $P_p^{far}$  is due to the fact that the pressure in the evacuated tank slowly decreases during the cycle.

## 5.5 Stand-alone radon tests

Radon reduction tests were performed before connecting the VSA to the clean room. The re-pressurization time was set at 30 seconds. The feed cycle was varied between 10 and 20 minutes and the purge flow rate between 1.2 and 3.5  $\ell/s$ . The results are summarized in table 5.3. The radon concentration at the input averaged  $\sim 15$  Bq/m<sup>3</sup> during the tests.

The data are not systematic enough to give an exact, quantitative description of the radon reduction properties of the device. Nonetheless, they give indications on how to preferably operate the VSA. Cycle times should not be too short, possibly 20 minutes or maybe even longer. At shorter cycle times, the transient time for re-pressurization is a bigger fraction of cycle: the filter’s efficiency is thus reduced. The radon concentration decrease observed between the last two data points could just be a low-count fluctuation and a longer measurement time in order to be confirmed.

The tests were unexpectedly interrupted because of a manufacturing defect of the backing pump. As soon as the pump came back after repair, vessel construction had begun and the VSA was connected to the clean room. The discussion of these results and of those achieved during this second, operational phase are discussed together in section 5.7.

measurement technique	$^{40}\text{K}$	$^{137}\text{Cs}$	$^{228}\text{Th}$	$^{226}\text{Ra}$	$^{222}\text{Rn}$ (150 °C)	$^{222}\text{Rn}$ (20 °C)
Ge $\gamma$ spectroscopy (Bq/kg)	$402 \pm 12$	$0.56 \pm 0.06$	$1.2 \pm 0.1$	$1.8 \pm 0.2$		
Rn emanation (mBq/kg)					$170 \pm 90$	$9.4 \pm 0.7$

Table 5.4: Intrinsic radioactivity and radon emanation rate for the Calgon PCB 4×8LS charcoal used in the VSA system. The measurement was performed by our collaborators in Heidelberg.

## 5.6 Charcoal radioactivity and radon emanation

The radioactivity content of Calgon PCB 4×8LS charcoal used in the VSA was measured by our Heidelberg collaborators. The charcoal was measured before being washed with water to remove dust (evidence has been seen that washing charcoal with water significantly reduces the  $^{40}\text{K}$  contamination [141]). The results are summarized in table 5.4. It is interesting to notice how only  $\sim 10\%$  and  $\sim 0.5\%$  of the radon is extracted at 150 °C and 20 °C, respectively. An interesting quantity to know is how much of the radon emanated by the charcoal escapes the charcoal itself and contaminates the output air stream. Implications of these results are discussed in section 5.8.

## 5.7 Performance and results

The VSA radon filter was connected to the clean room on August 23, 2001. For a year, during nylon vessel construction, it filtered all the make up air fed to the clean room. The filter was shut down only once, for an hour, to perform an oil change in the vacuum pumps.

Initially, the feed cycle time was set at 22 minutes (increased to 25 minutes after 1.5 months of running); the re-pressurization (stages 2, 5, refer to section 5.3.2) was set at 1 minute and the pressure equalization step lasted 6 seconds (stages 3, 6). The output flow rate was initially set at  $F_{out} \sim 70$  std  $\text{m}^3/\text{h}$  ( $\sim 20$  std  $\ell/\text{s}$ ), and was measured with the make

up air flowmeter of the clean room. The flow was changed a few times during the following year. A time profile of the make up air flow to the clean room is shown in fig. 5.13. The feed pressure  $P_{feed}$  was approximately 10 mbar throughout the run. The purge flow rate was initially set at  $F_{purge} = 2.5$  std  $\ell/s$ , with  $P_{purge} \sim 9$  mbar. After 3 weeks it was raised to  $F_{purge} = 3.9$  std  $\ell/s$  (with  $P_{purge} = 23 \div 25$  mbar) and finally stabilized at  $F_{purge} = 3.5$  std  $\ell/s$  after 1.5 months from the beginning of the run. The corresponding purge pressure was  $P_{purge} = 21 \div 23$  mbar. The purge fraction  $f$  (ratio of purge to feed flow rates) was kept between 8% and 14%. The observed purge flows vs purge pressures agree well with what was measured before connecting the VSA to the clean room (see fig. 5.10).

Radon reduction was immediately observed in the clean room air. The radon concentration profile during the first days of operation of the filter is shown in fig. 5.11. The initial exponential decay of radon is clearly noticeable. After 2-3 days, the radon concentration reaches a plateau. The data are fit with a decaying exponential plus a constant term,  $A_{cr} = A_0 + A_1 \exp(-t/\tau)$ . The best fit values are

$$\tau = (18.2 \pm 1.0) \text{ hours}, \quad A_0 = (1.7 \pm 0.2) \text{ Bq/m}^3. \quad (5.8)$$

The plot demonstrates that the clean room is supplied with significantly radon-reduced air (radon decreases), but it also shows that the radon concentration stabilizes at a value higher than what expected to be delivered by the filter. The VSA was run with operating parameters similar to those used in the last preliminary test, so radon activities on the order of 0.5 Bq/m<sup>3</sup> or less were expected in the clean room (see table 5.3).  $A_0$  is 3-10 times higher than the radon concentration measured at the output of the VSA during the preliminary test. As explained above, during the following several weeks the purge flow was varied between 2.5 and 3.9  $\ell/s$ , but no significant change in the radon concentration was observed. The profile was essentially stable at  $\sim 1.5$  Bq/m<sup>3</sup>.

The radon concentration profile during the year the VSA filter was running is shown in fig. 5.12. The plot also shows the radon concentration of the air at the output of the filter (in boxes). The radon concentrations inside the clean room and directly at the output of the VSA could not be measured simultaneously since only one radon detector was available.

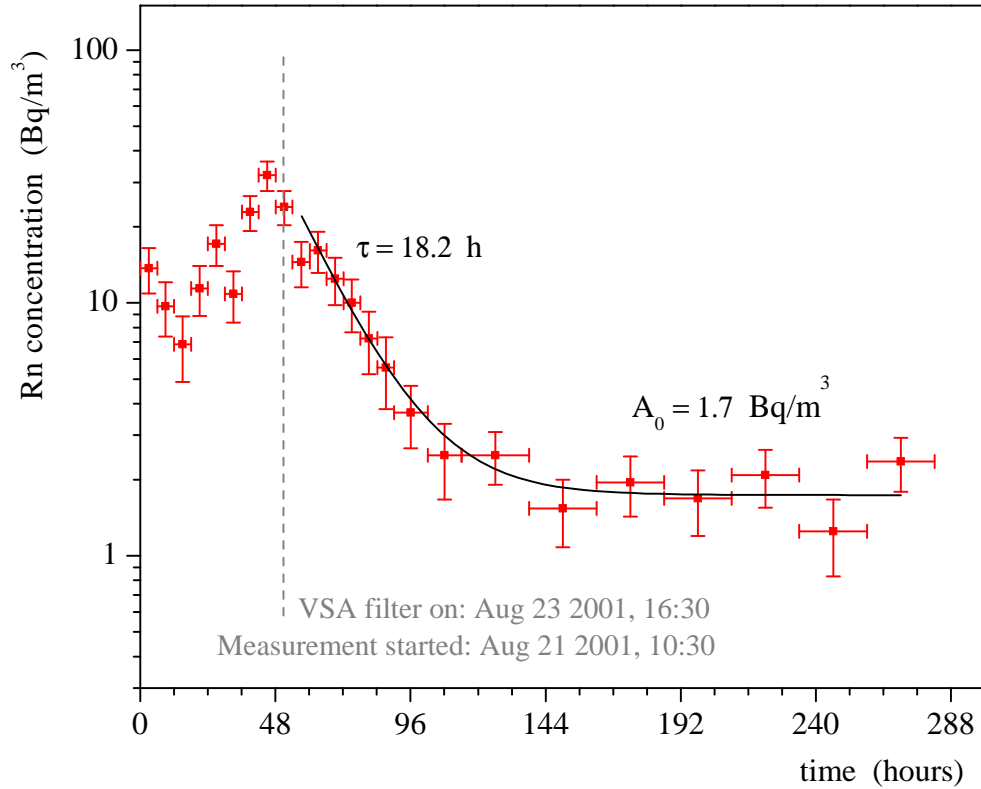


Figure 5.11: Radon concentration profile inside the clean room during the first days of operation of the VSA filter. The radon concentration in the clean room before the filter was connected varied between 7 and 30 Bq/m<sup>3</sup> (average over two days  $\sim 15$  Bq/m<sup>3</sup>).

The make up air flow rate  $\Phi_{cr}$  of the clean room (i.e. the output flow rate of the filter,  $\Phi_{out}$ ) during the same period is shown in fig. 5.13 (top plot). The pressure of the clean room with respect to the outside, the humidity of the air, and its temperature are also shown in figure 5.13.

It is immediately clear from fig. 5.12 that the radon concentration emerging from the VSA is lower (by a factor of 4 to 10) than that measured in the clean room. The radon activity  $A_{cr}$  inside the clean room is (data points outside the boxes in fig 5.12)

$$A_{cr} \sim 1.5 - 2 \text{ Bq/m}^3, \quad (5.9)$$

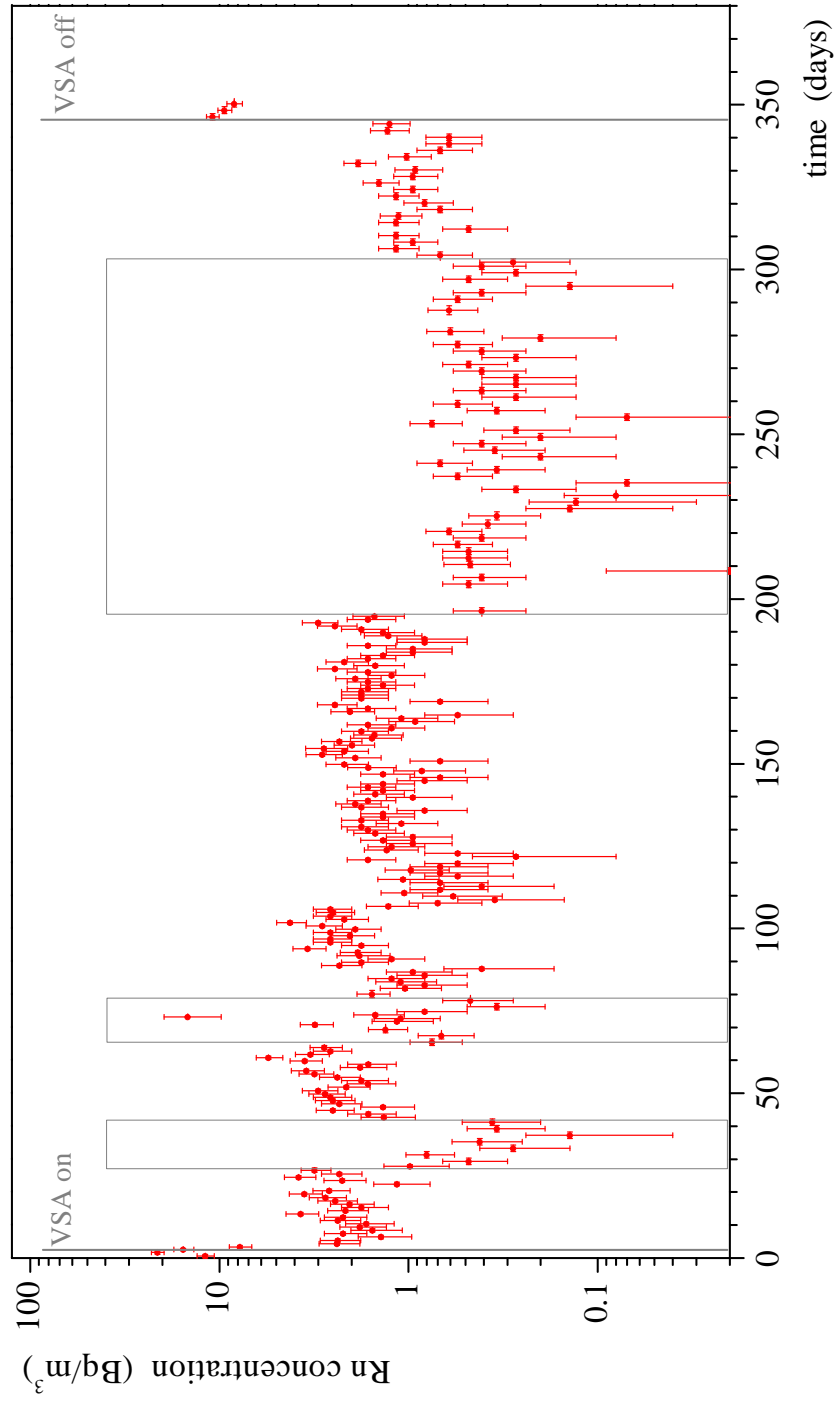


Figure 5.12: The radon concentration profile in the Princeton clean room during the construction of the nylon vessels for Borexino.

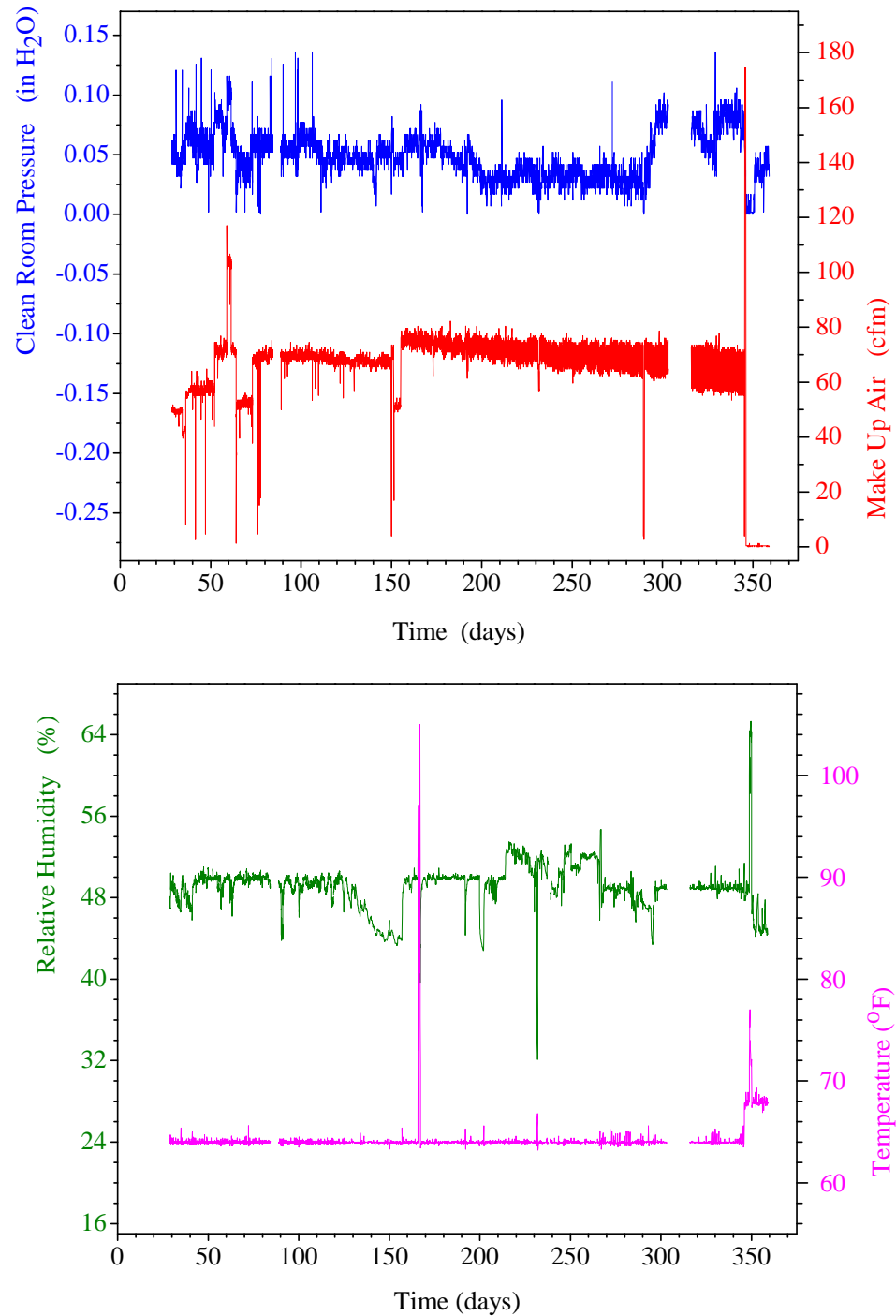


Figure 5.13: Clean room parameters during vessel construction. The time axis starts on August 21, 2001 when the radon concentration began being measured (see fig. 5.11 and 5.12). For reference, 1 cfm  $\sim$  0.5  $\ell$ /s  $\sim$  1.7  $\text{m}^3$ /h. The data are recorded by the clean room control system [106]. The temperature rose sharply around day 167 because of a failure of the air conditioning system, readily fixed. The clean room was opened at day 345 to ship the vessel.

while that of the air delivered by the VSA filter ( $A_{out}$ ) is (data points inside the boxes in fig 5.12)

$$A_{out} \sim 0.3 - 0.4 \text{ Bq/m}^3. \quad (5.10)$$

The reason for this is not completely understood. Some hypotheses are brought forward in section 5.8.

Further details of the data shown in fig. 5.12 are worth discussing. For example, the very noticeable step-like decrease in radon activity just after day 100 is in fact fictitious, and has an explanation. Until that time, a column of dessicant was placed at the input of the radon detector to dry the sampled air. Suspecting that the dessicant could be a source of radon itself and explain the apparently high radon concentration in the clean room, it was taken out of the sampling line. Since then the radon detector sampled humid clean room air. The efficiency of the detector with humid air is reduced. The exact efficiency drop has not been measured, but it should be approximately a factor of two [142].

The filter's performance needs to be compared against the predictions obtained from the prototype (section 4.5.3) and the preliminary testing reported at the end section 5.4. Assuming an ambient radon concentration  $A_{air} = 30 \text{ Bq/m}^3$  at the input of the filter, eq. (5.10) yields an observed reduction factor  $R \sim 100$ . For most of its operation (from day 70 onwards, fig 5.13) the make up flow rate  $\Phi_{cr}$  was between  $90 \text{ m}^3/\text{h}$  and  $130 \text{ m}^3/\text{h}$  (at 1atm). The purge flow rate was  $F_{purge} = 3.5 \text{ l/s}$  ( $12 \text{ m}^3/\text{h}$ ). The feed flow rate of the filter was then  $F_{feed} = 112 \div 142 \text{ m}^3/\text{h}$ . The purge volume flow rate (with  $P_{purge} \sim 23 \text{ mbar}$ ) was  $\Phi \sim 510 \text{ m}^3/\text{h}$  (this value is more precisely an average value, since the purge pressure would range between a maximum and a minimum value, slowly decreasing during each purge cycle because of slow residual desorption from the charcoal). The volume flow rate gain is thus  $G \sim 3.6 \div 4.6$ ; note that  $\Phi_{feed} = F_{feed}$ , since feed occurs at atmospheric pressure. A comparison with eq. (4.44) and fig. 4.16 suggests that the observed reduction  $R$  factor should be between 400 and 2900, corresponding to a radon activity  $A_{out} \sim 10 \div 75 \text{ mBq}$ . The observed radon concentration emerging from the VSA is radon-reduced by a factor of

100 yielding  $A_{out} \sim 0.3 \text{ Bq/m}^3$  (see eq. (5.10)). This value runs somewhat short from the expectations. A discussion is provided in section 5.9.

## 5.8 Comments on the radon levels achieved in the clean room

Various hypothesis have been considered to explain the discrepancy between the radon concentration in the clean room and that delivered by the VSA filter (see equations (5.9) and (5.10)). The average radon concentration difference  $\Delta A \equiv A_{cr} - A_{out}$  is approximately  $1 \text{ Bq/m}^3$ . An analysis of some possible scenarios follows:

1. Radon emanation from the dessicant at the input of the radon detector: ruled out by removing it and not observing a significant radon decrease, as explained above.
2. Radon in the water used for humidifying the clean room air: as shown in section 3.5, a  $1 \text{ Bq/m}^3$  radon concentration would require an activity in the supply water of  $120 \text{ Bq/l}$ , which seems unrealistically high. If the aging of such water is taken into account, this value must be 20 times higher.
3. Inward leaks into the clean room: let  $A_{air}$  be the radon concentration of the leak and  $\Phi_{cr}$  the make up air flow rate of the clean room. Then the leak required to explain the phenomenon is

$$\Phi_{leak} = \frac{\Delta A}{A_{air}} \Phi_{cr}. \quad (5.11)$$

For  $A_{air} = 30 \text{ Bq/m}^3$  and  $\Phi_{cr} = 30 \text{ l/s}$ ,  $\Phi_{leak} = 1 \text{ l/s}$ . This source cannot be completely ruled out, especially if some areas of the plenum volume of the clean room are not at above-atmospheric pressure when the clean room blowers are running.

4. Radon emanation from clean room surfaces: this seems to be a realistic source. The clean room, its HEPA filters in particular, have a very large surface area. It is likely that the emanation rate is humidity-dependent. Values for Rn emanation from the filtering material in use in the clean room nor from the dirt accumulated in the filters are currently not available.

It is interesting to estimate what the emanation rate  $E$  from the clean room surfaces would have to be to completely account for the constant “excess” radon activity in the clean room  $\Delta A$ . For a given make up air flow rate  $\Phi_{cr}$ , the emanation rate is (ingoing activity must be equal to the outgoing activity)

$$E = \Phi_{cr} \Delta A \quad (5.12)$$

If the make up air flow rate is  $\Phi_{cr} = 85 \text{ m}^3/\text{h}$  ( $\Delta A = 1 \text{ Bq}/\text{m}^3$ ),

$$E = 50 \text{ Bq}/\text{h} \sim 14 \text{ } \mu\text{Bq}/\text{s} \quad ({}^{222}\text{Rn activity}). \quad (5.13)$$

The emanation rate quoted in eq. (5.13) corresponds to a  ${}^{226}\text{Ra}$  activity of  $\sim 7 \text{ Bq}$ . Assuming secular equilibrium in the uranium chain, the amount of typical “dirt” (e.g. trapped in the HEPA filters) with 1 ppm  ${}^{238}\text{U}$  content needed to account for such emanation rate is about 0.5 kg, yielding an expected emanation of 2 mBq/g from this source.

### 5.8.1 Implications for vessels exposure

The clean room air was kept at an average radon concentration of  $A_{cr} \sim 1.5 \div 2 \text{ Bq}/\text{m}^3$  throughout vessel construction. This value is 15-20 times smaller than the radon concentration considered in section 3.4. From eq. 3.11, one obtains ( $A_{air} \rightarrow A_{cr}$ )

$$\sim 400 \text{ } w p t \quad {}^{210}\text{Bi}, {}^{210}\text{Po} \text{ decays}/\text{day}, \quad (5.14)$$

where  $t$  is expressed in hours. Approximately 130  $pw$  of these events are in the fiducial volume.

For  $p \sim w \sim 0.01$  (see section 3.4), the radon reduction achieved with the VSA filter gives an ample margin on the allowed exposure time of the nylon film of the IV (up to 75 hours to meet the specification of 1 event/day in the fiducial volume). On the other hand, setting a more realistic value of  $t = 1$  hour, the product  $pw$  needs to be  $\sim 8 \times 10^{-3}$  in order to meet the Borexino specification.

In conclusion, the radon reduction in the clean room air supplied by the VSA filter contributed a significant safety factor to meet the radon contamination requirements for the Borexino inner vessel.

## 5.9 Comments on the VSA filter performance

The radon reduction observed at the VSA output is  $\sim 100$ , while estimates based on the gain factor  $G$  suggested a reduction  $\geq 400$ . Many possible explanations can be provided and it is not possible at this time to give a definitive explanation.

The radon concentrations observed at the output are not significantly above the sensitivity of the RAD7 detector used to measure them. The radon reduction of 100 should be taken assuming this figure has a non-negligible error since it is based on an event rate of a few counts/day. Also, 100 is an average reduction factor. The data in fig. 5.12 show that the radon activity  $A_{out}$  varies by approximately  $\pm 0.3$  Bq/m<sup>3</sup>. This can be due to variations in ambient radon concentration, varying efficiency of the VSA (due, for example, to varying humidity levels in the input air), or just to statistical fluctuations of the recorded radon activity. What is worth of notice is that  $\sim 0.3$  Bq/m<sup>3</sup> is the lower radon activity observed with both the prototype and full-scale VSA systems (compare fig. 5.12, fig. 4.15, table 5.3 and table 4.2). This suggests the important possibility that this represents the true ultimate sensitivity of the RAD7 (the value of 0.1 Bq/m<sup>3</sup> for the RAD7 sensitivity was obtained with measurements that lasted a few days at most, see section 4.5.3).

Another possible explanation could be radon emanation from the charcoal (this would justify the same lower radon activity achieved with the two VSA devices, since they employed the same charcoal). The radon emanation value at room temperature reported in section 5.6 is  $\sim 10$  mBq/kg. An upper limit to the activity that such radon emanation can contribute in the output air stream from the VSA filter can be estimated as follows. The mass of charcoal in each column is 250 kg, which gives a total radon emanation rate of each charcoal of 2.5 Bq. The feed flowrate during operation was about 100 m<sup>3</sup>/h. There will be at most (i.e. neglecting adsorption dynamics inside the column)  $90$  <sup>222</sup>Rn atoms/m<sup>3</sup> in the output air. This gives a radon activity of  $\sin 2 \times 10^{-4}$  Bq/m<sup>3</sup>, and is thus too small to account for the observed inefficiency of the full-scale VSA.

## 5.10 Ideas for VSA improvement

The experience gathered with developing and running VSA radon filters for breathable air allows some conclusions on such devices to be drawn and ideas for improvement to be put forward.

The original use of a vacuum swing process on activated charcoal for radon removal proved feasible and, on the long run, inexpensive. Most of the cost is for building the device, not for operating it. The charcoal-based VSA filters have proven to be mechanically very reliable. During one whole year of operation, for example, the backing pump of the full-scale filter required one oil replacement only, although significant quantities of dust and humidity were pumped through it. The oil was changed in a few hours, while air, at reduced flow, was still being pushed through the filter and used to feed the clean room (obviously the swing system was interrupted). The resulting air contamination was minor (see the radon data point at approximately day 75 in fig. 5.12).

The level of charcoal crushing observed after such a long period of uninterrupted operation was also very limited. The charcoal presented no problem with dust that could not be easily handled with standard HEPA filtering units and proved completely compatible with the use in connection to a clean room.

The radon suppression achieved in the clean room air thanks to the VSA filter reduced the radon contamination of the Borexino inner vessel by at least one order of magnitude. However, the reduction was less than expected and lower than what supplied by the VSA filter itself. If the reason is radon emanation from the clean room surfaces, the solution would be to supply a larger, radon-filtered make-up air flow (see section 5.8). The practicality and feasibility of an even bigger VSA filter is questionable, given the size of the vacuum pump that would be needed. Nonetheless, the Borexino clean room is large, and VSA filters like ours could be used more effectively in smaller environments.

The importance of radon suppression in clean rooms or other environments where breathable air cannot be substituted with other, cleaner gases goes beyond the need for

Borexino. As stated at the beginning of chapter 4, radon contamination of detector surfaces is a widespread problem of most low background experiments. It is worth then listing ideas for potential improvements of the current VSA design for future applications. The following items are listed without any particular order and are meant as starting points for discussion and, possibly, development.

1. Before designing a radon reduction device for clean room air, it would be advisable to estimate or, better, measure the radon emanation from the constituent materials, with particular emphasis on the filtering material of the HEPA units. The ducts that carry the air to the clean room should be cleaned and the feed air pre-filtered, especially when the clean room is first operated, to minimize the amount of dust trapped in the filters. Such dust could emanate radon at the level of  $\sim 2$  Bq/g (assuming 1 ppm uranium content for dust).
2. Should radon emanation from the charcoal become a problem for certain applications, very low radon-emanating synthetic charcoal is available. Due to its high cost ( $\sim 1000$  US\$/kg [143]), it is conceivable to use it only for the final bed thickness at the output of each column.
3. The pressure drops across the feed column for the full-scale VSA were small. A design with thinner and longer columns, as conventionally done for many applications, might improve the flow pattern in side each bed, minimizing “dead” charcoal volumes and channeling phenomena.
4. A very interesting possibility is to design a VSA device with chilled columns. If liquid nitrogen temperature might not be appropriate for air filtering, since it could enhance oxygen and nitrogen separation, liquid methanol or dry ice could be valid alternatives. The adsorption properties of a material exponentially increase with decreasing temperature. The adsorption constant  $k_{ads}$  depends on the temperature  $T$  according to [113]:

$$k_{ads} \propto e^{-\frac{E_{ads}}{kT}}, \quad (5.15)$$

where  $k$  is Boltzmann's constant and  $E_{ads}$  the adsorption binding energy. Small temperature changes greatly affect the adsorption process. A colder filter could have significantly smaller columns for a given design flow rate. This reduces the cost of the columns and the charcoal. It also reduces the transient times between feed and pressure stages (evacuation and re-pressurization). Such a design would require some development, but it could, in principle, be very promising.

5. Since the VSA worked as a radon filter, it should also work as a radon concentrator at the opposite end (output of the pump) [144]. A VSA system could be used, together with standard radon counters, as a radon concentrator for low-level radon sampling.

# Aspects of Vessel Assembly

The assembly of the Borexino nylon vessels took place in Princeton between July 2001 and August 2002. The nylon vessel package comprises of the two nested “balloons” with all the connecting hardware for their fluid filling and operation, mechanical robustness and connection to the surrounding structures and plants of Borexino. It also includes monitoring instrumentation. In detail, it consists of:

- a. nylon film spherical envelopes for Inner Vessel (IV) and Outer Vessel (OV)
- b. bulk nylon “end cap” rings and pipe sections at both poles of each vessel
- c. 6 copper struts at each IV polar region
- d. 8 stainless steel struts at each OV polar region
- e. stainless steel coaxial pipe sections for IV and OV fluids
- f. double set of ropes for each vessel to hold them in place against positive and negative buoyancy; they are connected in groups of 6 (IV) and 5 (OV) to load cells for buoyancy measurement
- g. load cells: 8 at each IV pole (6 connected to the ropes and 2 in parallel with the stainless steel pipe), 10 at each OV pole (8 for the ropes and 2 on the pipe)
- h. flexible nylon sampling and pressure measurement lines for each vessels

- i. light sources at specific locations on each vessels to be connected to lasers and LEDs via optical fibers for monitoring scintillator stability, vessel shape, and position (see chapter 7)
- j. 8 temperature sensors: 2 at each pole in IB and 2 at each pole in OB
- k. break-out connections for routing electrical signals from instrumentation

The OV struts, the electrical break out hardware and the OV load cells were prepared in Princeton but will be mounted on the vessel at LNGS. The assembled vessels were shipped from Princeton on August 6 and arrived at LNGS on August 14, 2002.

## 6.1 Preliminary operations

Numerous preconditions had to be satisfied before actual vessel assembly could begin. These are in addition to all the R&D carried out to characterize the nylon film, measure residual radiopurity of the materials and test the basic joint making technique.

All of the nylon film was precision cleaned by CleanFilm [145] to Level 25 Mil. Std. 1246C [91] using a non-contact ultrasonic technique (fig. 6.1). Cleaning the bulk nylon pieces for the end caps and pipes was a joint effort by technicians at Princeton and AstroPak [92]; these parts were also precision cleaned to Level 25.

Several clean room operations took place prior to envelope construction. Two tables of the appropriate length for IV and OV and racks for nylon acclimatization were built (see fig. 3.10). The radon “scrubber” (see chapter 5) was completed and functional before any nylon film for the vessels was handled. Inside the clean room, the ropes were pre-tensioned (500 N for 30 minutes, fig. 6.2) to eliminate their inter-thread slack, carefully cleaned with alcohol using clean room wipes, precision cut, and labelled. Loops were made at the ends of each rope to allow connection to the load cells. This operation was delicate, since the final ropes needed to be equal in length to within 1 cm. The light sources were individually assembled, their optical fibers were cleaned with alcohol (as were the ropes), spooled, and labelled (this system is described in chapter 7).

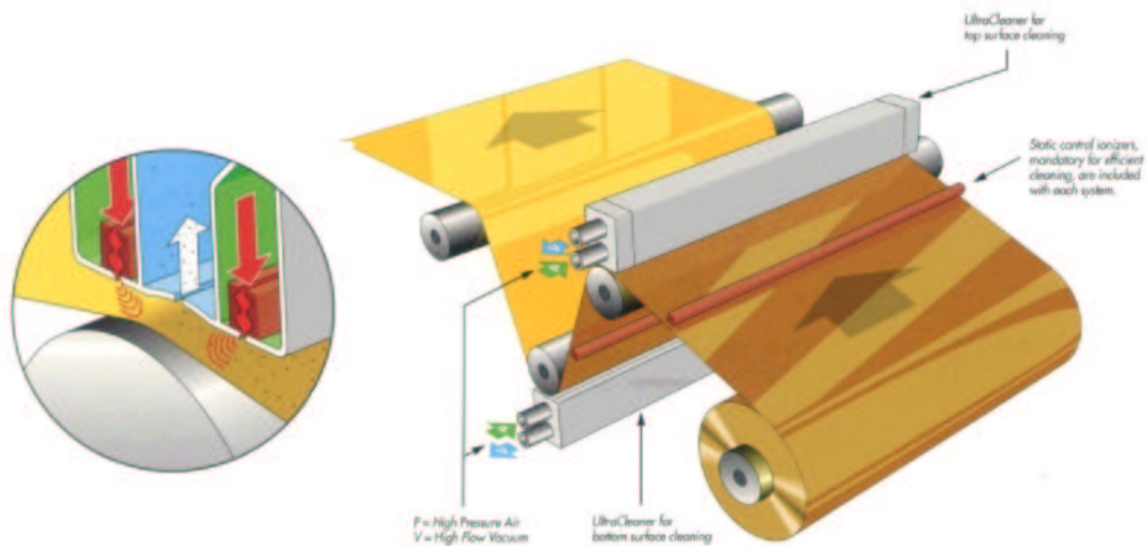


Figure 6.1: “Web cleaning” apparatus similar to the one used to precision clean the nylon film for the Borexino vessels [146]. Particulate is ultrasonically removed from the film and vacuumed away. Deionizing bars placed in close proximity to the ultrasonic heads enhance particulate removal by reducing static charge adhesion forces.

## 6.2 Chronology and details of vessel construction

The first step in vessel construction was preparing the film for assembly of the OV and IV. As the cleanliness and leak tightness requirements of the OV were less stringent, this envelope was constructed first. There were two film candidates for the envelopes, referred to as Capron and Sniamid. These films were selected based on their mechanical strength, optical clarity, and radiopurity. Capron, extruded in Pennsylvania, USA, by Allied-Signal/Honeywell using Capron B732P pellets [147, 148] was selected as the prime candidate based on its superior mechanical properties [76, 86]. Sniamid (a mixture of Sniamid ADS40T and Bayer PA6 pellets), extruded in Germany, had mechanical and optical characteristics well within the vessel design specifications and was chosen as the “backup” film. Prior to construction the only means of predicting film radiopurity was through measurements of the pellets before extrusion. From this point of view, both film candidates

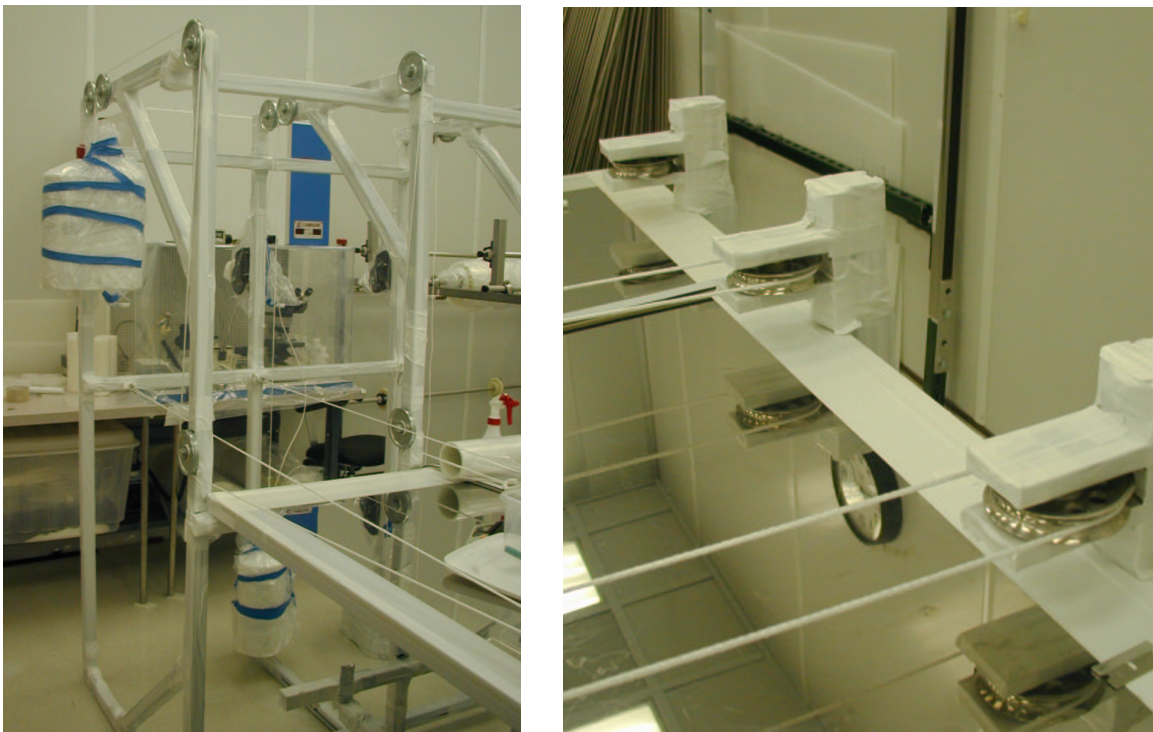


Figure 6.2: The apparatus used to stretch the ropes for the hold-down system of the Borexino nylon vessels.

were acceptable. By the time construction was ready to proceed, a break-through method for measuring the radon emanation rate of the final film product had been developed by our Heidelberg colleagues. The prime film candidate (Capron) was measured and radon emanation levels were higher than expected (two batches yielded 18 and 45 ppt Ra equivalent [150]); this is almost one order of magnitude higher than the original pellets [76, 149]. Counting the film is a time-consuming process, and to keep on schedule preparations were made to construct the envelope using Capron, and in the meantime perform a measurement of the Sniamid film. In the end, the Sniamid presented an extremely low radon emanation rate ( $1.3 \pm 0.4$  ppt Ra equivalent [150]) and the decision was taken to use it for the IV. Since the OV was already constructed out of Capron (which met the OV specifications), no actions were taken to redo it. Thus the final set of vessels has a Capron OV and a Sniamid IV.

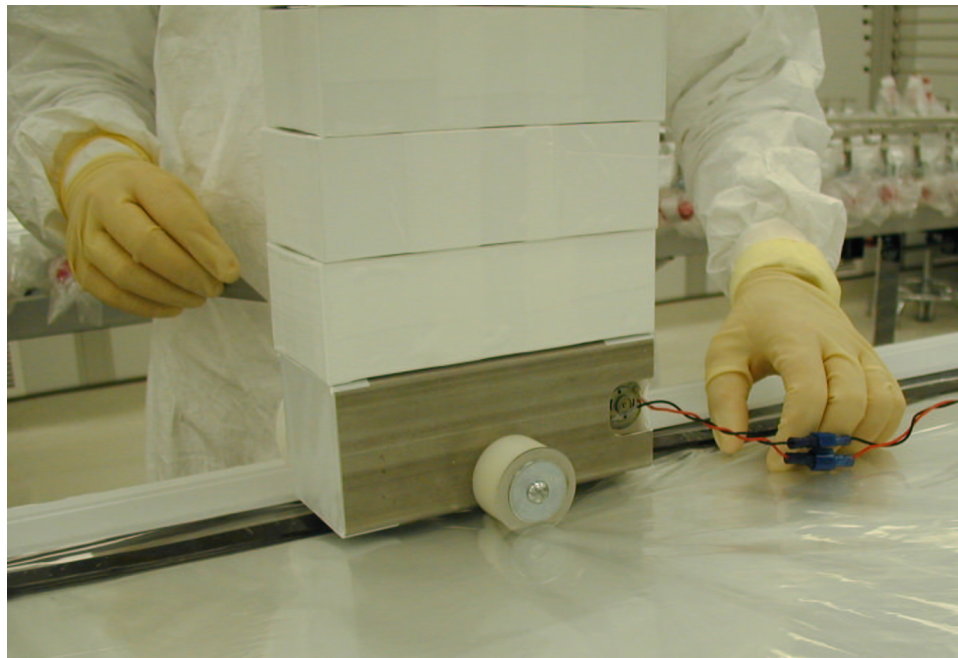


Figure 6.3: Cutting the panels for the Borexino nylon vessels into the right shape [153]. The remotely-controlled cart on magnetic tracks guides the circular blade along the edge of the panel, delivering a clean, smooth cut.

The nylon film first had to be equilibrated with the clean room humidity, set to  $\sim 50$  %. Nylon is extremely dry as initially extruded, and it stays dry for a very long time when tightly spooled and packaged. The moisture intake causes it to expand by a few percent [151], much larger than the tolerable error on the shape and dimension of every single panel. The problem with exposing the nylon film to the clean room air to reach humidity equilibrium is radon and particulate contamination. The humidification of the nylon film was carried out by sandwiching the nylon film between two thinner layers of commercially available nylon film ( $25 \mu\text{m}$  thick) certified at Level 25 surface cleanliness [145]. The covered nylon panels were placed on racks (see fig. 3.10) for at least 3 days, time that tests had shown to be appropriate for complete humidity equilibration with the clean room air, even in the presence of such cover film [152]. Several deionising bars were used while unspooling the film to minimize static charge build up that acts as a particle magnet.

Once humidified, each panel was cut to its final, almond-like shape. A circular blade

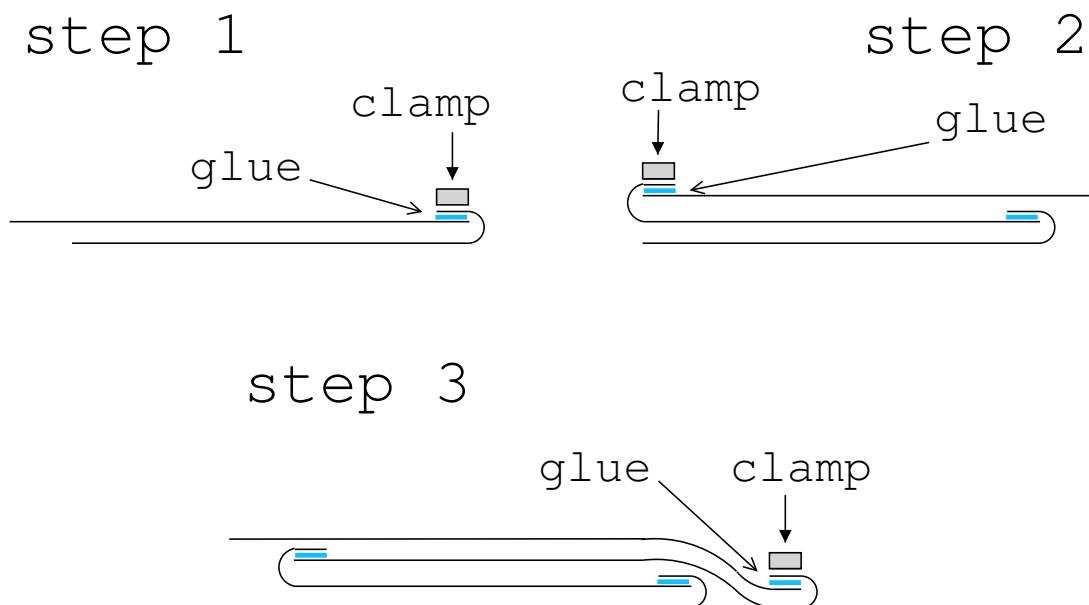


Figure 6.4: The accordion-style stack technique used for constructing the nylon vessels envelopes. The process continues until all panels of each vessel are in the stack. The last glue joint is conceptually identical but requires unfolding some panels in the stack to align the top and bottom panels for gluing.

mounted on a remote-controlled cart follows a template laid on the table (fig. 6.3). Magnets serve as tracks for the cart and hold the nylon film on the table. This operation is performed with the cover film in place to minimize any vessel membrane exposure. The positions of the light sources were then marked with tape, and nylon hoops (“tabs”) for routing the ropes were glued at predefined locations on each panel. Such tabs were specifically designed to have a lower yield point than the vessel membrane so that the unnatural pull from a potentially misguided rope would not compromise vessel integrity.

The panels were then glued along one edge into an accordion-style stack that would define a sphere once inflated [154]. The technique is schematically sketched in fig. 6.4. The glue for joining the panels is a Resorcinol-based solution [155] (in water and ethanol, with the addition of sodium meta bisulphite [156]). Plenty of experience in gluing panels was accumulated within the group during the construction of the CTF and the Borexino prototype vessels. The glue amount, tacking time and spray mist characteristics were

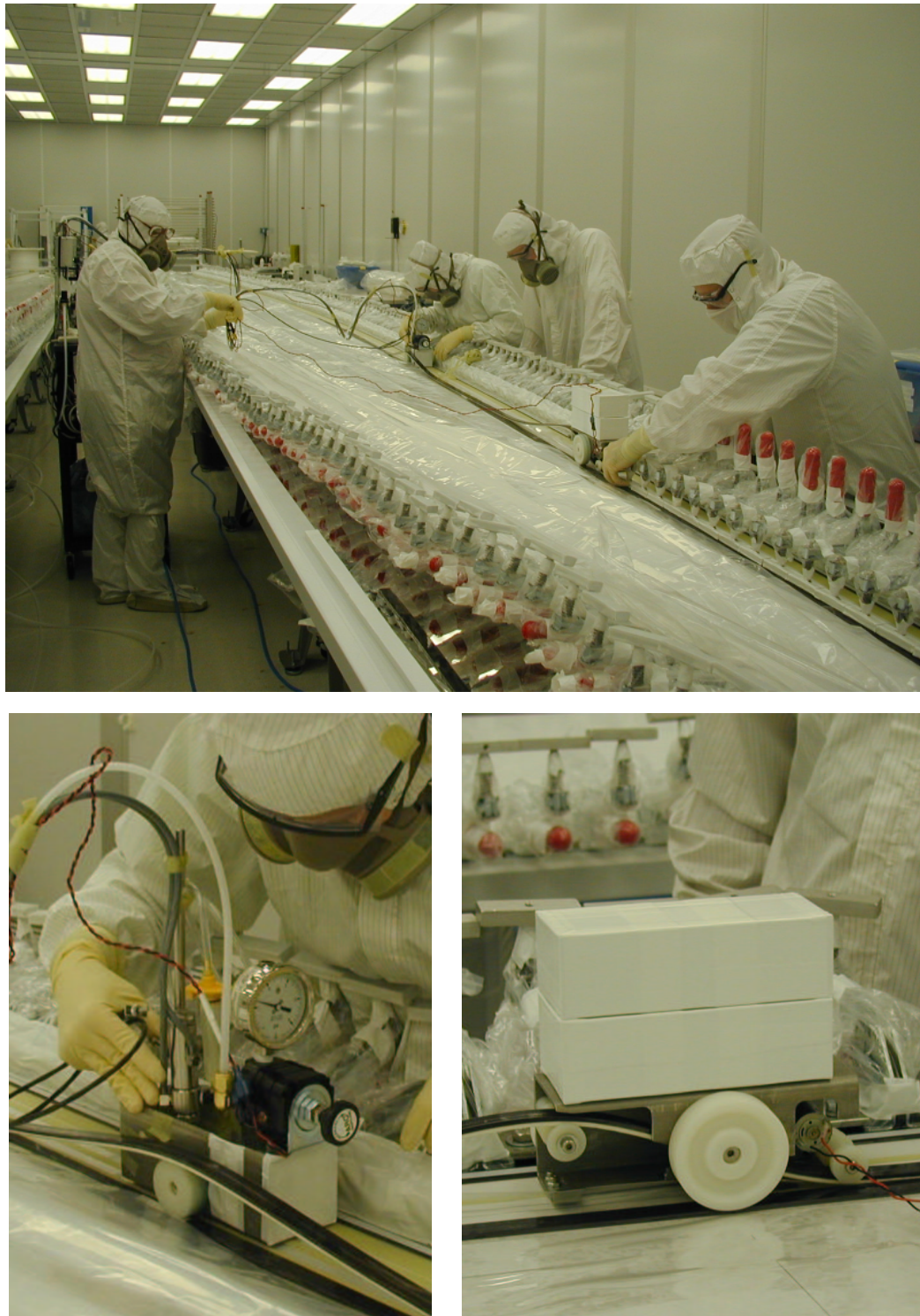


Figure 6.5: Making a glue joint for the Borexino IV. A first cart carries the spray gun with which the resorcinol solution is applied and a second cart follows folding the edge of the panel beneath onto the one above. The clamps are then closed to apply the necessary pressure (top). Close ups of the spray and folding carts are shown too (bottom) [153].



Figure 6.6: Closing the clamps on a vessel glue joint for mechanical strength and leak tightness of the seal.

optimized to obtain reliable, long-lasting joints [156]. For every joint, a region of two edges (one per panel) to be glued together were masked with low-residue clean room tape. A spray gun mounted on a remote-controlled cart sprays glue on the exposed surface. A second remote-controlled cart follows (one minute behind or so to allow for the right tack time) and fold the lip of one panel onto the one above, both glue-covered, and make the joint. The curvature of such fold was kept big enough to avoid creasing the nylon film. Before the passage of the folding cart, the masking tape would be removed. The making of a joint and close ups of the carts are shown in fig. 6.5. The joint would be tightly clamped for 12-24 (fig 6.6) hours to assure mechanical strength and avoid leaky “channels” through the glue. The glue for the tabs used to route the ropes and the light sources was hand-sprayed using a hand-held masking frame.

Precautions were taken to minimize film exposure to ambient air. The cover film was

lifted to uncover just the very edge of the panels being glued together. The stack geometry also self-covers the underlying layers very effectively (see fig. 6.4). The whole stack was always covered overnight with a couple of layers of clean nylon film and one layer of metalized film (that also prevented discoloration of the glue-joint areas). The OV was assembled first, leaving the last seam open to allow the nesting of the IV inside. Once each envelope was completed, it was moistened with generous amounts of deionized water and covered with clean, thick polyethylene film to hold the moisture and provide an extra barrier for radon.

The OV was assembled first with the last seam left unglued to allow the subsequent nesting of the IV. The IV envelope was constructed and completed with all polar region hardware in place. This part of the vessel makes the transition between the nylon film and the piping that carries fluids (fig. 6.7) in the different volumes inside the SSS. It also provides the mechanical structure that supports the vessel in place, as described in chapter 3. A description of the gluing technique and the R&D for this delicate step is presented in section 6.3.

The assembly of the end region proceeds as follows (a sketch of the completed assembly is shown in fig. 6.13): a bulk nylon 60 cm diameter ring is glued as a collar on the inside of the vessel (fig. 6.7, top). As explained in the following, this is a Resorcinol glue joint. The central nylon pipe assembly with the “bridge” nylon film and two flexible nylon sampling tubes, prepared and leak checked separately (see section 6.3), is then added (fig. 6.7, bottom). Finally, a second bulk nylon ring, the so-called “L-ring” from its cross-sectional shape, is placed onto the “collar” ring, clamping both the nylon vessel and the bridge film membranes between them. This last step only adds mechanical strength to the structure. The leak tightness relies upon the previous two glue joints.

Next, the ropes are threaded through the tabs along the corresponding panels and across the end cap. A given rope is attached at both ends to one pole, with the rope following a great circle through the opposite end cap, which has holes in the “L-ring” to accommodate the passing of ropes. The ropes anchored to the south pole oppose upward buoyancy movements of the vessel, while those anchored to the north oppose downward movement. The load cells

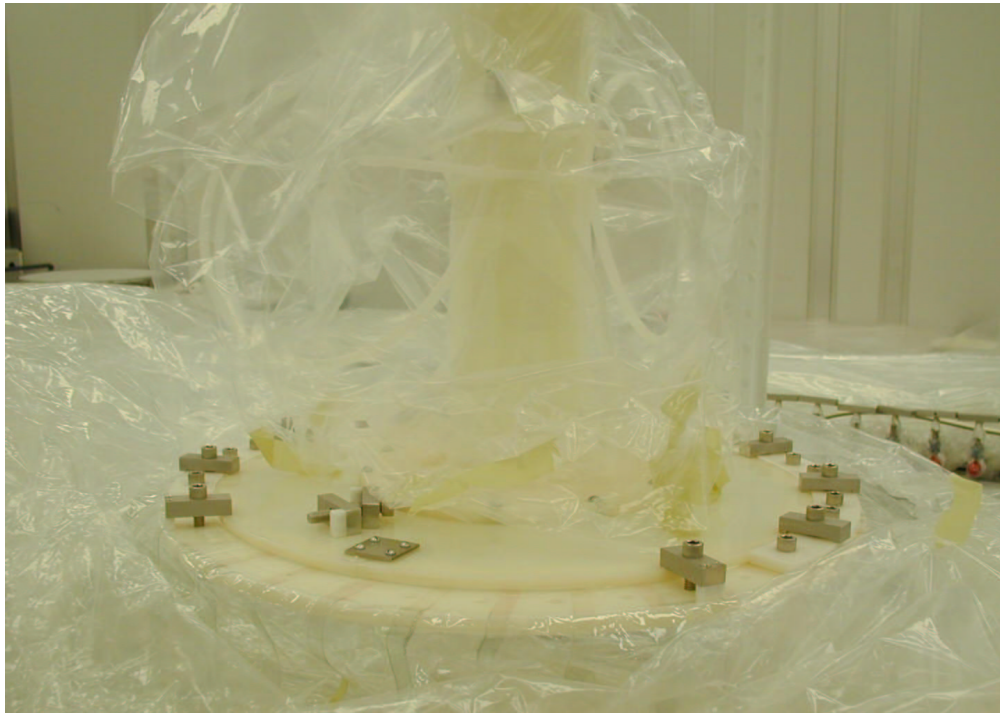


Figure 6.7: Gluing the “collar” nylon ring (top) and the “bridge” film + nylon pipe assembly (bottom) on the south pole of the Borexino IV.

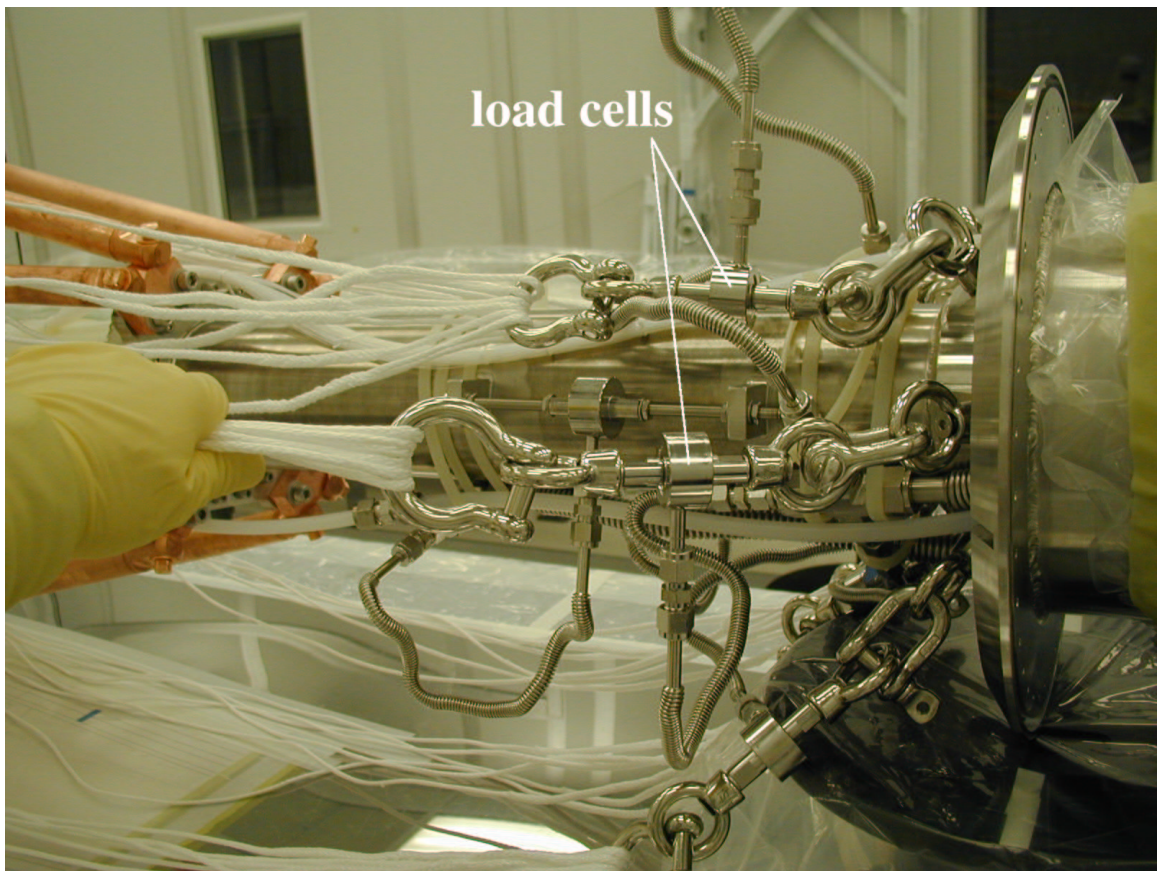


Figure 6.8: IV load cell assemblies. One of the load cells for measuring the stresses on the stainless steel pipe is also shown.

are mounted on a stainless steel pipe section connected to the centermost nylon section. The transition to stainless steel for the pipe guarantees mechanical strength for the assembly; the choice of nylon for the pipe section closest to the IV aims at minimizing radioactivity near the center of the detector. To further strengthen the end regions of the IV, eight copper struts are inserted between the “L-ring” and the steel pipe section. Finally, the IV surface light sources are positioned and glued onto the vessel and their optical fibers routed along the panels through the tabs and bundled at the north pole (see fig. 7.8).

A load cell assembly is shown in fig. 6.8. There are six such assemblies at each pole of the IV, and 8 per pole on the OV. Each IV (OV) load cell reads the tension of 6 (5) ropes,

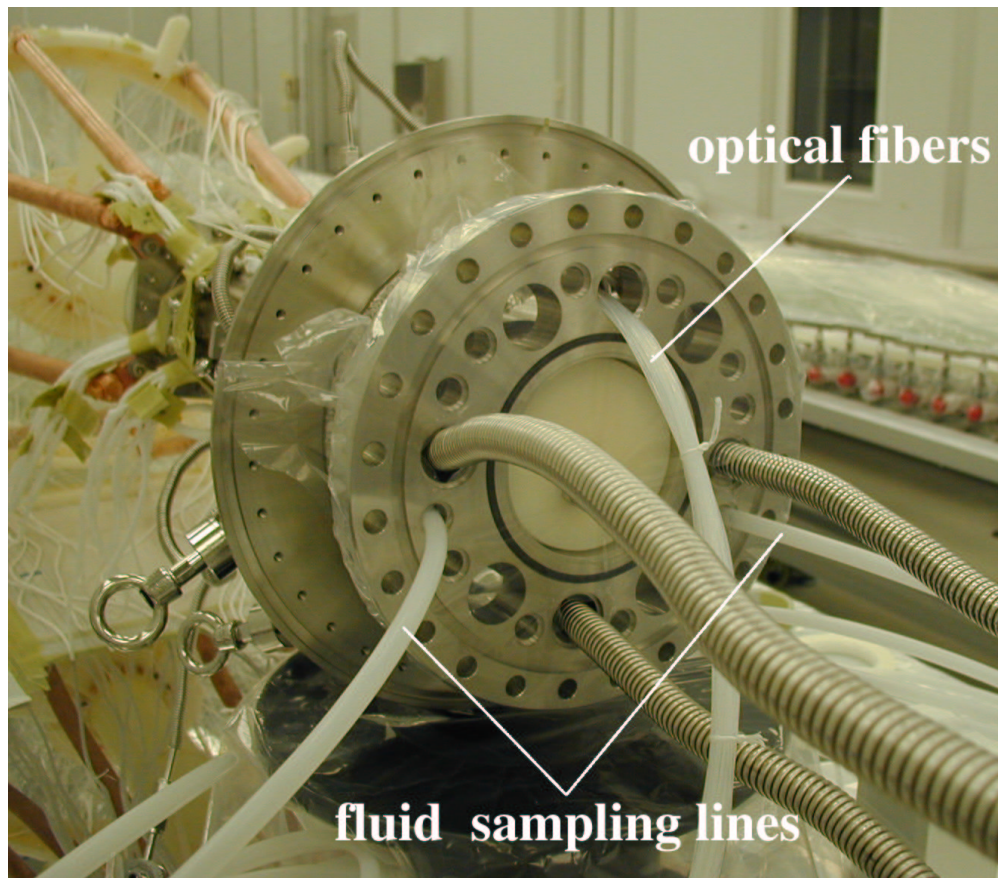


Figure 6.9: The optical fibers, the two fluid nylon sampling lines and the bellows conduits containing the electrical wires for the load cells and the temperature sensors for the IV are routed through the north polar flange. They will be routed through several meters of conduit out of the SSS and WT during the vessel installation operations.

as mentioned in section 3.2. The sum of the tension of each rope, corrected by the cosine of the angle of incidence with the support pipe, gives the total buoyancy force on the vessel. An additional four load cells are mounted along the stainless steel pipe at each pole (two in the IB and two in the OB) to measure its elongation and stress (fig. 6.8).

The light sources were subsequently put on both vessels and their optical fibers routed along the panels, conveniently bundled, and routed through appropriate conduits in the polar stainless steel pipes. These, along with the leak tight bellows that contain the electrical readouts for the load cells and the temperature sensors, will be routed out of the SSS and

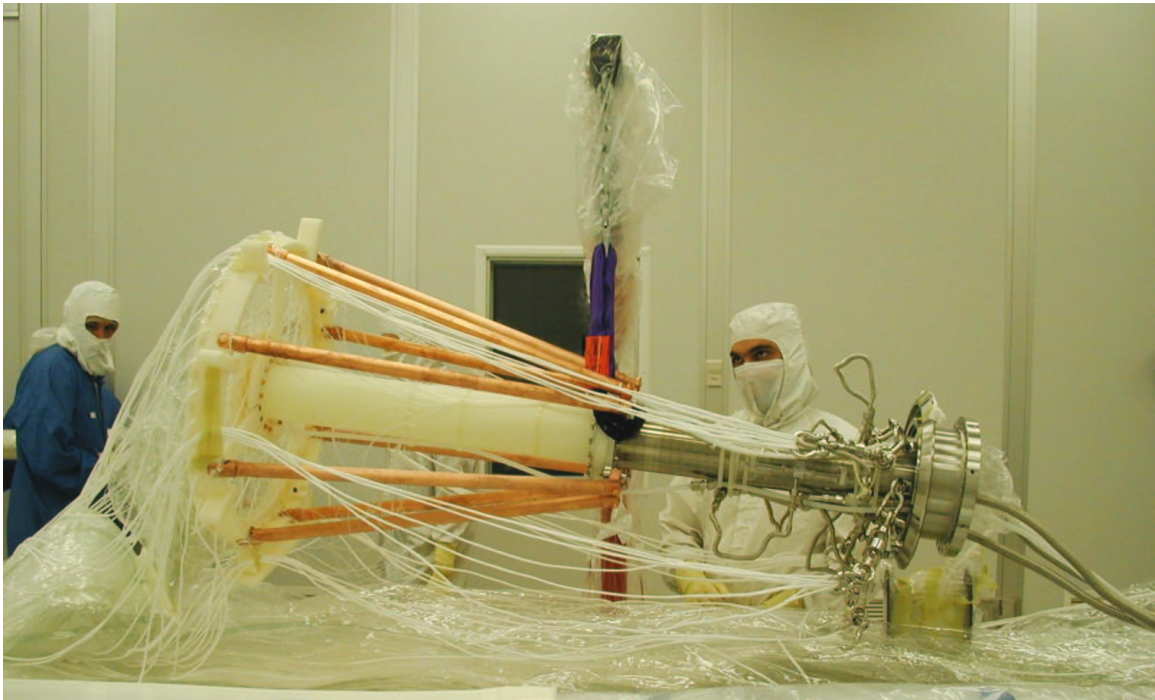


Figure 6.10: A complete IV end region assembly during nesting operations into the OV. The copper struts, nylon and stainless steel pipe sections, the ropes attached to the load cells and the end ring and nylon bridge film are visible. The bellows coming out of the flange on the right are the leak tight conduits for the electrical connections of the load cells.

WT as part of the vessel installation operations. The optical fibers, bellows and nylon fluid sampling lines routed out of the IV north polar flange are shown in fig 6.9.

The complete IV was then ready for leak checking (see section 6.4) and subsequent nesting inside the OV. A completed IV end region assembly is shown in figure 6.10.

The OV was also prepared for nesting. Its last seam was only partially glued, a two meter section at each end, in order to allow the end cap hardware to be put in place. This is similar to the IV one, but simpler. The OV end caps have no nylon bridge film because optical coverage and radioactivity requirements are not as stringent as they are at the IV radius. The OV envelope is clamped between a specifically prepared (see section 6.3) bulk nylon clamp ring, similar to the IV one, and an L-shaped ring. A bulk nylon plate extends inwards from the L-ring and connects it to the stainless steel section of the pipe mounted on

the IV. The connection is via an o-ringed flange and is performed during the vessel nesting step (fig. 6.11). A collection of pictures of all the phases of vessel construction can be found in [157].

The next step was to complete the final OV glue joint, thus definitively sealing off the IV. The ropes and the light sources were then put on the OV; the optical fibers were neatly spooled for transportation. The connection of the OV ropes to their load cells is part of the installation inside the SSS at LNGS, since their attachment point is not part of the vessel assembly shipped to Italy from Princeton. The nested vessels were capped off, abundantly moistened with deionized water and wrapped. Two layers of half millimeter thick, precision cleaned polyethylene film and one of aluminized nylon film were applied and heat sealed to prevent humidity loss and radon contamination. The vessels were then folded into a frame (see fig. 6.12) and shipped to LNGS. A collection of pictures of all the phases of vessel construction can be found in [157].

### 6.3 End region design

A very significant effort has been put into designing the end regions of the nylon vessels, shown in fig. 6.13. The parts include the end rings (collar and L-rings), the bridge film, the nylon pipe, and the flexible nylon sampling lines. The main technical difficulty is how to transition from nylon film to bulk nylon. Initially, attempts were made to use a paste produced by dissolving nylon pellets in pure formic acid. Mechanically strong structures were produced with this technique, but the paste would stiffen the film on the edge of the application area producing small cracks that could potentially leak [158].

The final design is shown in fig. 6.13. The assembly proceeded as follows: a layer of thick (0.5 mm) nylon film (C38F, the same film used for the CTF inner vessel) is glued onto the bulk nylon surface using pure formic acid. Such thickness of the film is required to avoid ripples and brittleness when treated with formic acid. For this step, the bulk nylon surface would first be pre-treated with pure formic acid to enhance the level of “fusion” between film and bulk. The joint would also be secured by applying pressure. Thin nylon film



Figure 6.11: Nesting the IV inside the OV. The north pole IV assembly is bolted to the OV end region. The load cell bellow conduits and the two spools for the IV and OV optical fibers can be seen in the foreground (bottom).

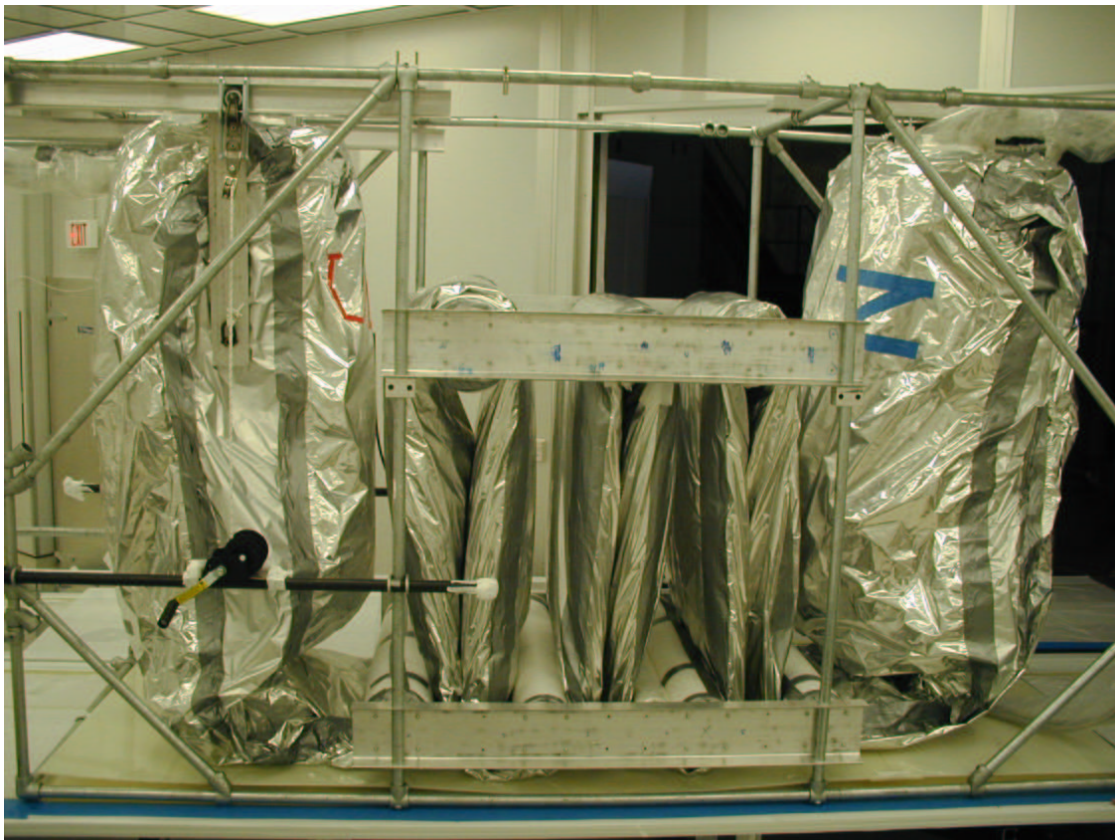


Figure 6.12: The packaged Borexino nylon vessels in their shipping frame.

could then be resorcinol bonded, with a “standard” film-to-film glue joint [159] (fig. 6.14 shows the gluing technique for the IV membrane and bridge film assembly). After the vessel membrane was glued onto the collar ring, the surface of the glue joint was cured with small amounts of raw formic acid that fuses the film together eliminating leaks, but preserving their flexibility at the same time. This step is particularly important because the vessels’ surface is by construction not smooth, having glue joints that come in orthogonally to the collar ring. These joints are natural channels for leaks, as shown in fig. 6.15. The formic acid treatment fuses the nylon film and plugs the open paths.

The design philosophy of the end regions is such that under stress nothing fails before the film itself. Assuming 30-50 MPa yield point for the vessel nylon film (which corresponds to a 5 °C temperature difference between the scintillator and the buffer region) and neglecting

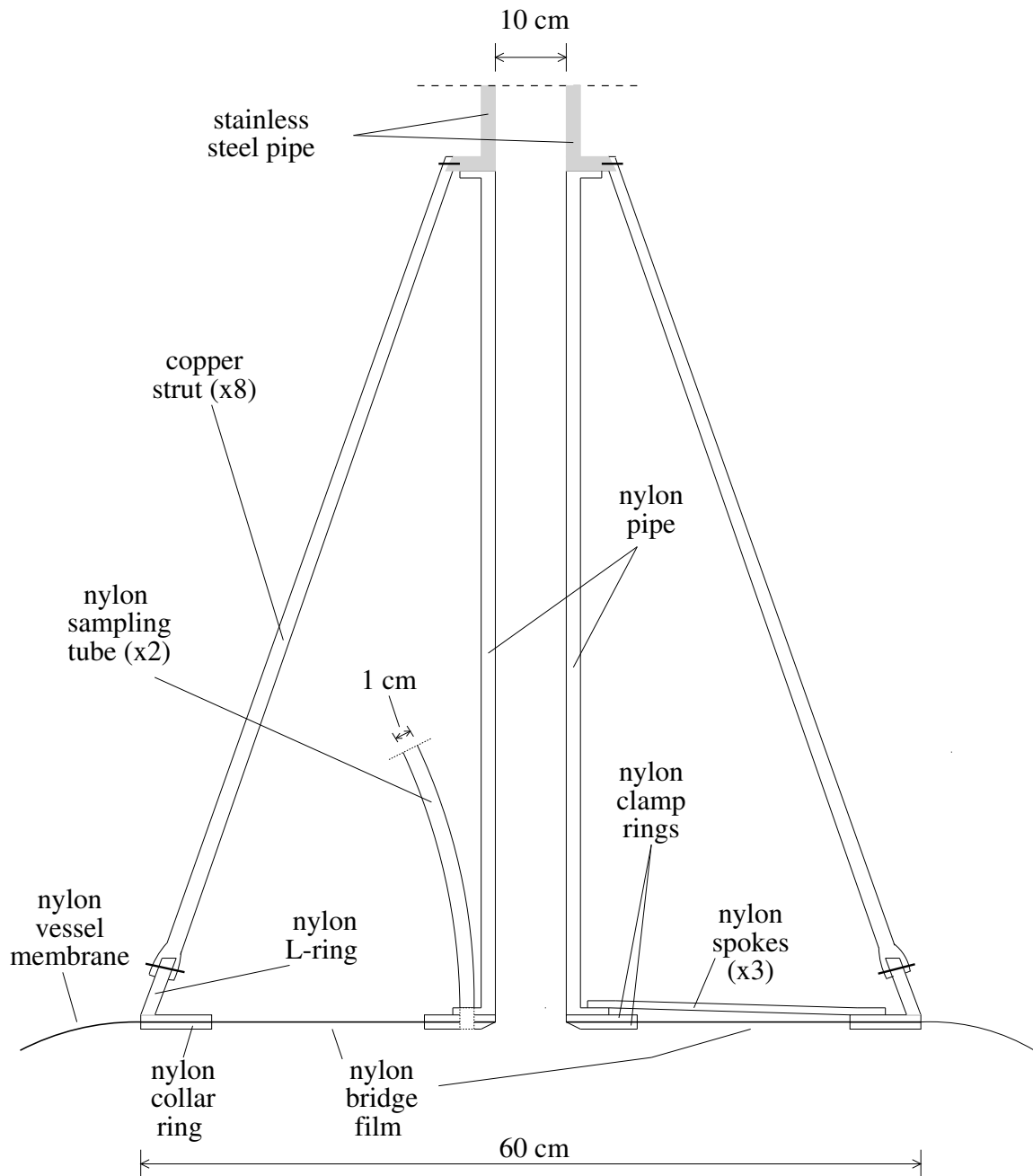


Figure 6.13: Sketch of the IV end region (i.e. polar) assembly in cross-section. The gluing technique for transitioning from nylon film to bulk nylon is shown in fig. 6.14. A photograph of an assembled end region is shown in fig. 6.10.

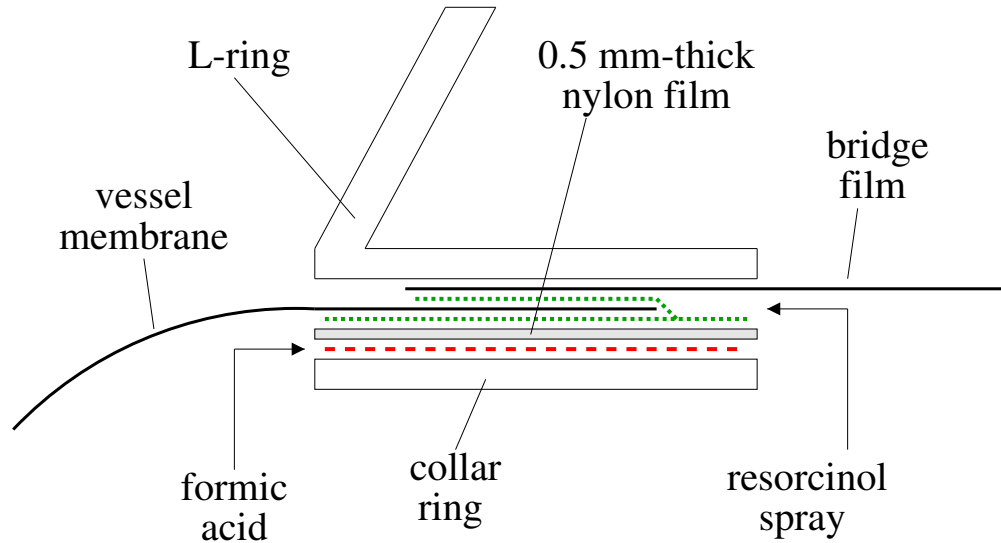


Figure 6.14: Gluing scheme for the end region transition between the vessel nylon membrane and the polar assemblies. A layer of half millimeter-thick nylon film is placed on the bulk nylon surfaces with pure formic acid. The vessel membrane can then be glued to the assembly relying only on well-tested resorcinol bonding. The drawing refers to the IV collar ring region, but this technique is applied to all the film-to-bulk nylon transitions. The L-ring is simply bolted in place (nylon bolts not shown for simplicity).

creep of the film, the end region has to withstand a 3000 N load; a value 3 to 10 times smaller should be expected if creep is considered [88]. The overall leak tightness specification for the IV is 1 cc/s in the gas phase at 1 mbar pressure differential (see section 6.4). Mechanical and leak checking tests were performed on prototype end region assemblies under stress (fig. 6.16). The measured leak rate at full load, scaled to  $\Delta P = 1$  mbar, was:

$$\text{test IV end region gas leak rate} = 1.5 \times 10^{-6} \text{ cc/s} \quad (6.1)$$

Such leak rate is many orders of magnitude better than the specifications.

Construction of the nylon pipe + bridge film assembly also employed the above mentioned technique to bond nylon bulk and film. Bulk pieces constituting the nylon pipe section of the assembly were glued together with nylon + formic acid paste, preceded by formic acid treatment of the surfaces. The two 3/8" flexible nylon lines at each pole for

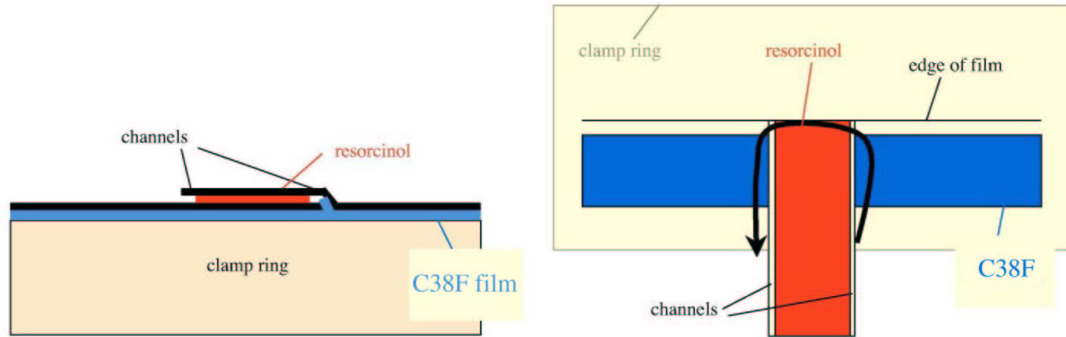


Figure 6.15: The channels along the glue joints are natural leak paths on the vessel (as shown by the arrow in the picture on the right). Pure formic acid treatment following the vessel gluing onto the collar ring slightly fuses the film together plugging the gaps.

fluid sampling and pressure measurement were connected via a nylon Swagelok fitting after attempts to glue them failed. Each end pipe was leak checked several times during assembly (fig. 6.17) using  $\text{SF}_6$  gas to pressurize the assembly, while the outside was sampled in sniff mode with a mass spectrometer [160]. No signal was observed from either of the two end pipes.

## 6.4 Vessel leak checking

The leak tightness specification for the IV is set by the following argument. A limit of 10 ppm PPO ( $10^{-5}$  g/g for PPO in PC) is allowed before scintillation in the quenched buffer region would give an intolerable trigger rate in Borexino (see section 3.2 and [67]). Assuming no fluid purification over ten years, this limit corresponds to transferring  $2.1 \text{ m}^3$  of IV scintillator solution (1.5 g/l PPO in PC) into the inner buffer volume ( $284 \text{ m}^3$ ). The equivalent leak rate is then [96].

$$\text{IV tolerable leak rate} = 10^{-2} \text{ cc/s (PC)}. \quad (6.2)$$

One can assume that leaks are characterized by viscous behaviour through small apertures, where the throughput for a fluid is obtained from that of another by multiplying by the ratio of their viscosities (throughput is inversely proportional to the viscosity for viscous

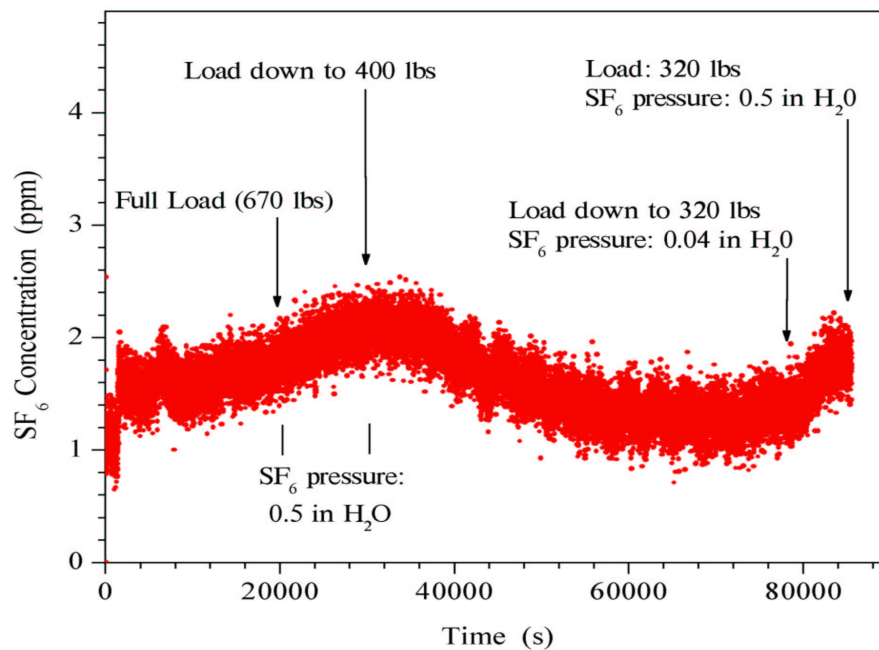


Figure 6.16: Leak checking and mechanical testing of a prototype IV end region assembly. The region below the bridge film was filled with pure SF<sub>6</sub> and kept at a slight overpressure (few inches of water). The bag around the assembly is an accumulation volume for SF<sub>6</sub> tracer gas sampling. A fan is also used to mix the gas and prevent the denser SF<sub>6</sub> component from stagnating (top). The results of the measurement at full load are shown, and the leak rate,  $1.5 \times 10^{-6}$  cc/s, is given by the slope of the curve between 20000 and 30000 seconds (i.e. the change in SF<sub>6</sub> concentration as a function of time).



Figure 6.17: One IV nylon pipe + bridge film assembly assembled and prepared before being glued into the vessel. The assembly is mounted on a device that allows leak checking with  $\text{SF}_6$  gas. The two  $3/8$ " flexible nylon sampling lines are also mounted at this stage. The capillary tube from the mass spectrometer used to sniff for  $\text{SF}_6$  is also visible.

flow according to Poiseuille's equation). The ratio of viscosity coefficients  $\eta$  between PC and air is

$$\frac{\eta_{\text{PC}}}{\eta_{\text{air}}} = \frac{1.5 \text{ cp}}{0.018 \text{ cp}} \sim 100, \quad (6.3)$$

giving

$$\text{IV tolerable leak rate} \simeq 1 \text{ cc/s (air)}. \quad (6.4)$$

Since it is impractical to leak check the vessels with liquids,  $\text{SF}_6$  gas is used as a tracer in air. For small setups, such as that for the nylon pipe assemblies (fig. 6.17), pure  $\text{SF}_6$  can be used to enhance sensitivity. The operating overpressure foreseen for the IV is 1 mbar; the leak rate specifications have to be met at this pressure differential.



Figure 6.18: The sealed Borexino IV is filled with  $\text{SF}_6$  for leak checking. A bag is placed around it to collect  $\text{SF}_6$  leaking out. After an adequate accumulation time is allowed to pass, the accumulation bag is opened up and the  $\text{SF}_6$  concentration inside the clean room is measured, giving the integrated leak rate.

#### 6.4.1 Leak checking procedure

Once the IV was sealed (with both polar end regions glued into the envelope, but prior to nesting) it was prepared for leak checking (fig. 6.18). The vessel was completely covered with clean polyethylene film and the cover film was meticulously taped to the table, serving as an accumulation bag for  $\text{SF}_6$ .

The vessel was filled with 500 liters of pure  $\text{SF}_6$ , humidified by allowing bubbling through deionized water. Enough gas was inserted to “puff up” the vessel to fill every fold, yet maintaining it in a neat, folded stack. A few layers of thick polyethylene film were added as weight to increase the pressure of the gas inside the IV and improve the sensitivity of the measurement. After a certain build up time, the cover layer was lifted, every fold

of the vessel opened up to allow even the deepest folds to be flushed, and the step-like increase in SF<sub>6</sub> concentration inside the clean room (of known volume) recorded with a mass spectrometer [160], giving the total amount of SF<sub>6</sub> released from the vessel. Knowing the accumulation time and the gas pressure, this number is converted into a leak rate.

An important reason for using the clean room as accumulation volume is that the mixing of its air is essentially instantaneous. The smaller bag that wraps the vessel during accumulation would ideally give a higher sensitivity because of its significantly smaller volume; on the other hand, it is very hard to achieve a good SF<sub>6</sub> mixing, especially given the folded stack geometry of the vessel. It is also hard to determine the volume of such bag accurately.

The SF<sub>6</sub> mixing was directly tested. An SF<sub>6</sub> spike was released in the clean room and the tracer concentration monitored as a function of time. The concentration profile is reported in fig. 6.19. The plot proves that SF<sub>6</sub> mixing occurs in a short time compared to the decay time of the SF<sub>6</sub> concentration due to leakage of air from the room and dilution with “fresh” make up air. The exact amount of SF<sub>6</sub> introduced in the clean room was estimated to be approximately 15 liters. For an approximate clean room volume  $V_{cr} \sim 750 \text{ m}^3$  [161], the peak should be at around 20 ppm, confirmed by the data. The measured time constant  $\tau$  of the clean room (i.e. one  $e$ -folding of its air) is 9.4 hours, corresponding to a make up air flow rate of  $\sim 80 \text{ m}^3/\text{h}$  (recall that  $V_{cr} \sim 750 \text{ m}^3$ ). Opening up every fold of the IV to release the SF<sub>6</sub> into the clean room takes only about half an hour (the operation needs to be carried out carefully to avoid damaging the vessel; in particular, the nylon membrane needs to be constantly kept very moist by spraying deionized water on it). This procedure is thus reliable and the total amount of accumulated SF<sub>6</sub> can then be observed as a step in the SF<sub>6</sub> concentration in the clean room air.

Figure 6.19 shows that the SF<sub>6</sub> concentration at any given time is known up to about  $\pm 0.5$  ppm (width of the data band). Assuming this to be the size of the lowest detectable concentration step  $\Delta\rho_{\min}$ , and knowing the total enclosed volume of the clean room, the minimum detectable leak rate  $R_{\min}$  is:

$$R_{\min} = \frac{V_{cr} \Delta\rho_{\min}}{t} \sim \frac{375}{t} \text{ cc/s (air)}, \quad (6.5)$$

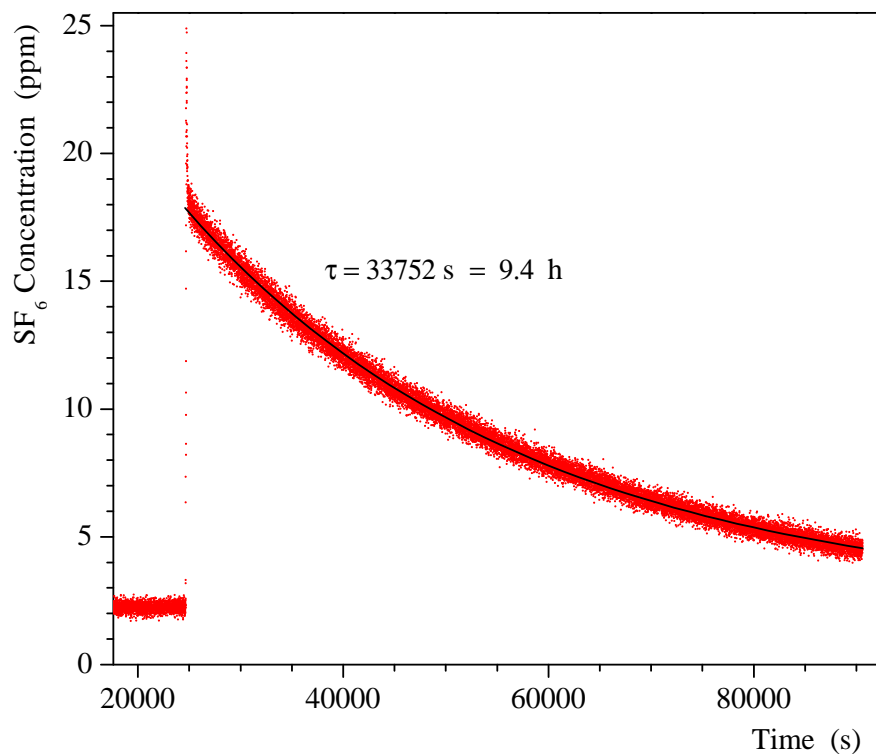


Figure 6.19: SF<sub>6</sub> concentration profile inside the Princeton clean room after a 15 liter spike of the tracer were released. The plot shows that full gas mixing is achieved in a much smaller time scale than that needed for the SF<sub>6</sub> to decay away by dilution with “fresh” make up air. The initial concentration peak above the exponential decay curve is due to local fluctuations in the SF<sub>6</sub> amount in proximity of the mass spectrometer during the vessel uncovering and handling.

where  $t$  is the SF<sub>6</sub> accumulation time for the measurement. An accumulation time of less than 10 minutes is enough to reach the needed sensitivity for testing the IV leak tightness specifications. In other words, the achievable sensitivity is  $5 \times 10^{-2}$  (cc/s)/(day of accumulation) at 1 mbar.

A subtle issue related to the accuracy of this leak checking procedure is related to the uncertainty in the knowledge of the pressure of the SF<sub>6</sub> inside the vessel. SF<sub>6</sub> is very dense, so that a 0.5 cm column corresponds to approximately 0.1 mbar. The IV stack is about 10 cm high, and the bottom panels are under higher pressure. Also, the deeper layer would

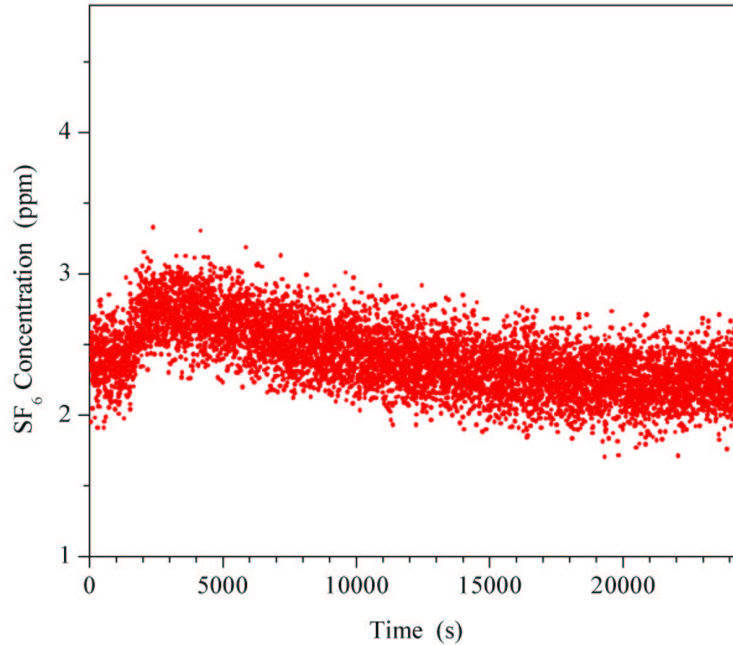


Figure 6.20: SF<sub>6</sub> profile during the leak checking test of the IV. The concentration step corresponds to an IV total leak rate of  $\sim 0.1$  cc/s (air) at 1 mbar, an order of magnitude better than required by the design specifications. This measurement represents an upper limit due to some systematic uncertainties on the pressure of the SF<sub>6</sub> and because of the assumption of purely viscous, pressure-dependent leaks (see text).

feel the weight of the nylon panels above them. The weight applied on top of the stack was gauged to compress the gas at the top of the stack to about 0.1 mbar. The bottom feels a pressure up to two or three times as high. The results that follow are reported under the conservative assumption of 0.1 mbar pressure differential and scaled to an equivalent leak rate at 1 mbar assuming viscous leaks varying linearly as a function of pressure differential.

#### 6.4.2 Leak checking results

Figure 6.20 shows the results of a leak test of the IV. The accumulation time was  $\sim 10$  hours. The observed step is  $\sim 0.5$  ppm, which translates into a leak rate of 0.01 cc/s, at the actual pressure. Scaling the result to 1 mbar gives

$$R_{IV} \simeq 0.1 \text{ cc/s (1 mbar)}, \quad (6.6)$$

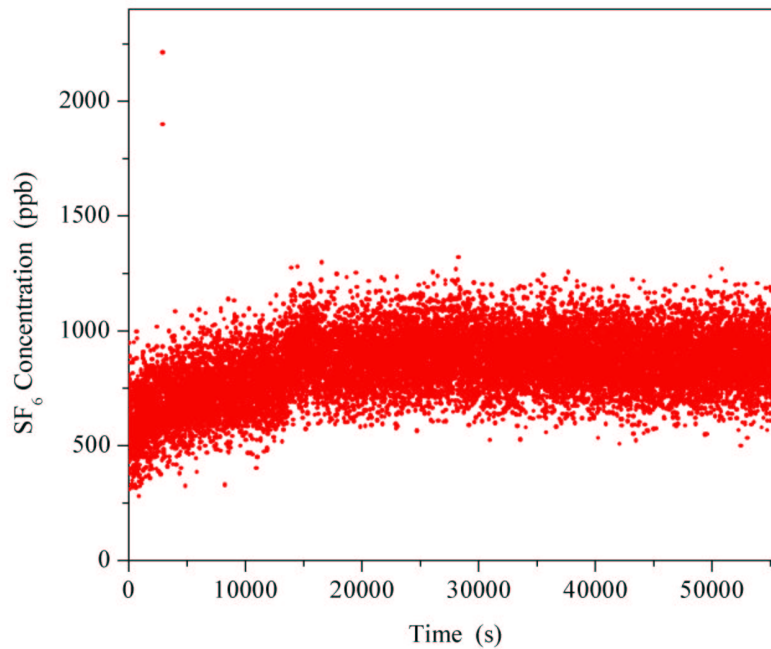


Figure 6.21: Results from the second IV leak rate measurement. The observed leak rate is 50 times smaller than that seen in the previous test (fig 6.20). The SF<sub>6</sub> concentration step (when the bag around the vessel is opened up) is after 15000 seconds. The slow rise before then could be a leak out of the accumulation bag or a big pressure change of the clean room (unlikely). It is unclear whether there was a leak in the accumulation bag for the previous test or if the first one was contaminated.

which is 10 times better than the specifications require.

This value represents an upper limit in that a lower limit on the SF<sub>6</sub> pressure inside the IV is assumed (the result could be better by a factor of two or three, as explained above). An assumption is also made on the viscous nature of the leaks (as opposed to molecular flow). In the case of viscous leaks, the leak rate (the throughput in Poiseuille's equation) varies linearly with the pressure differential that drives it. Should some of the signal be caused by leaks that do not depend on pressure, the total leak rate would be a factor of ten smaller (a specific measurement of the diffusivity of SF<sub>6</sub> through thin nylon membranes is not available).

A second test was performed allowing SF<sub>6</sub> to build up for two weeks. The configuration of the cover layers had been left untouched. A much smaller signal was seen, as shown in

fig. 6.21, leading to a significantly reduced measurement of the IV total leak rate ( $\sim 50$  times smaller). It is unclear whether the accumulation bag was leaky, or if the first measurement was somehow contaminated. In either event the IV was considered to have met the leak rate specification.

## 6.5 Inner Vessel contamination from air exposure and handling

A general expression was given in chapter 3 for radon contamination of the IV surface (eq. (3.11)):

$$215 (w p A_{\text{air}} t) \quad {}^{210}\text{Bi}, {}^{210}\text{Po} \text{ decays/day}$$

where  $p$  and  $w$  are the plate out and wash off fractions, respectively, and  $t$  is expressed in hours. The equation assumes a uniform contamination of the entire surface of the IV. This is clearly not true, given the precautions in covering the nylon film during all construction stages. The exposed surface during glue joint making is  $\sim 3\%$  of the total IV surface. Such surface is exposed for one day at most. Assuming  $t = 1$  hour is thus realistic. From section 5.8.1, during fabrication  $A_{\text{air}} \sim 2 \text{ Bq/m}^3$ . Finally, assuming  $p \sim w \sim 0.01$  as measured in laboratory tests (see section 3.4), yields

$$4 \times 10^{-2} \quad {}^{210}\text{Bi}, {}^{210}\text{Po} \text{ decays/day} \quad ({}^{222}\text{Rn} \text{ exposure to clean room air}), \quad (6.7)$$

in the Borexino fiducial volume from radon contamination of the IV during vessel construction. This figure is well within the original design specification. Some caution should be put in analysing this number. Recoil of nuclides away from the nylon surface and into the scintillator during radioactive decays could significantly increase  $w$ , as explained at the end of section 3.4.

Another potential radon contamination source is the  $\text{SF}_6$  used for leak checking. 500  $\ell$  were used (see section 6.4.1) and an upper limit of  $\sim 0.2 \text{ Bq/m}^3$  radon activity was measured using the RAD7 detector [123]. Assuming that all the  ${}^{222}\text{Rn}$  in the  $\text{SF}_6$  plates out on the

vessel's surface (realistic because it was never flushed), but assuming  $w \sim 0.01$  as before, yields

$$\leq 4 \times 10^{-2} \quad {}^{210}\text{Bi}, {}^{210}\text{Po} \text{ decays/day} \quad ({}^{222}\text{Rn} \text{ exposure to SF}_6), \quad (6.8)$$

which meets the Borexino requirements as well.

Summarizing, it must be noticed how radon-filtering the clean room air and covering the nylon panels during vessel construction were necessary for Borexino. Without these precautions, the value stated in eq. (6.7) would presumably be at least 1000 times higher:

$$\geq 40 \quad {}^{210}\text{Bi}, {}^{210}\text{Po} \text{ decays/day} \quad (\text{no panel covering, no clean room air filtering}), \quad (6.9)$$

which would seriously endanger the success, or even be fatal, for the experiment. For comparison, the KamLAND collaboration has recently reported [162] a  ${}^{210}\text{Pb}$  activity in their scintillator of  $100 \text{ mBq/m}^3$ . This corresponds to  $\sim 10$  events/s in 100 tons of scintillator, many orders of magnitude higher than what we expect in Borexino from radon contamination of the vessel. No particularly stringent precautions were taken to minimize the  ${}^{222}\text{Rn}$  exposure of the surface of their vessel, although it is not clear that the measured contamination is entirely due to such exposure.

Finally, the particulate contamination could not be tested after assembly, and is assumed to meet Level 25 Mil. Std. 1246C, which corresponds to  $\sim 3$  mg of particulate mass. This meets the Borexino requirements of  $\leq 1$  count/day in the 100-ton fiducial volume.

# Light Sources on the Nylon Vessels' Surfaces

The nylon vessels are justifiably the most delicate component of the Borexino detector. Handling them properly during installation and fluid filling of the SSS as well as maintaining them in a safe condition during steady-state operations is extremely important. During operations, both vessels will be subject to significant mechanical stress and it is highly advantageous to monitor their deformations in real time, to correct for possible problems. This is not an easy task in a dark environment (the SSS) and given the limitations on the materials that can be used.

Apart from the need to preserve the mechanical integrity of the vessels, their actual shape and exact position inside the detector are extremely important. The IV defines the boundary of the active region of the detector since it contains the liquid scintillator solution. Its shape and position therefore define the background-suppressed central spherical fiducial volume Borexino relies upon to look for solar neutrino events (see chapter 2). Distortions or displacements of the IV could affect the physics of the experiment and complicate data analysis. The shape of the OV is also important. Pronounced deformations that locally reduce the buffer thickness between the vessels could enhance  $\gamma$ -ray background in the corresponding region inside the IV.

A set of light diffusers has been placed on pre-defined points of both vessels. These are attached to the tip of an optical fiber that carries light from a source outside the WT (LED

or laser). The illuminated spots can be seen by inward-looking digital cameras placed on the surface of the SSS, much like the PMTs, and their position reconstructed with good accuracy. The position of one or more light points together with the knowledge of their position on the vessel (carefully logged!) gives important information about the vessels. The specific features looked for are the overall position of the vessels, their sphericity (which is lost whenever they are in an under-inflated state, for example) and, possibly, local folds of the vessels' envelopes.

A second set of light sources is present on the IV. Eight optical fibers which are not terminated with the light diffusers have their tips carefully cleaved and glued onto a mechanical support that holds them at an angle (approximately  $45^\circ$ ) with respect to the surface of the IV. This allows the light emerging from the fiber's end to penetrate through the vessel membrane into the scintillator volume. A laser of a specific wavelength (355 nm) is used to directly excite the PPO molecule in the scintillator and emulate particle interactions in the scintillator [163]. The attenuation length of this light in the scintillator solution is of the order of a couple of centimeters [164], smaller than the expected resolution of the detector. The light from such spots of PPO scintillation light is then detected with the PMTs and spatially reconstructed. This provides a means for monitoring the stability of the scintillator's response close to the IV's surface, a possible calibration tool for the reconstruction code complementary to the use of radioactive or laser sources and, possibly, a way to monitor the position of the IV's surface using the PMTs instead of the cameras.

## 7.1 The Borexino CCD cameras

Borexino has 7 CCD cameras that look inside of the SSS. They are reasonable quality commercial-grade digital cameras [165] mounted with a fish-eye lens and placed inside a leak tight can with a transparent dome for underwater photography. The resolution in air has been proven to be 1.36 cm [166] with red LEDs. Six cameras are positioned in three diametrically opposite pairs at the intersection of the SSS with three mutually orthogonal diameters tilted by  $45^\circ$  with respect to the north-south axis of the sphere. The seventh

camera is placed in proximity of the SSS's north pole and has the primary function of monitoring the north pole region of the vessels, particularly critical during liquid filling of the detector.

## 7.2 The light diffusers

The original idea for having light points on the vessel involved putting LEDs directly on the nylon surface [167]. This design required having electric cables routed inside the SSS and finding an effective gluing technique to adhere the LEDs to the nylon membrane. The main difficulties with this method dealt with overall compatibility of materials with PC and the material budget for acceptable radioactivity load on the vessel system.

A design that solves both these problems is using optical fibers to carry light into the SSS from outside the WT. The overall mass added to the vessel can be kept low, and the fiber (both its quartz core and Teflon jacket) is PC-compatible. The difficult part is to find a way to diffuse almost isotropically the well-collimated light emerging from the fiber. The optical fibers adopted are the same as those used throughout the Borexino calibration system (timing fibers for the PMTs and fibers for laser calibration of the detector, an extensive description of which is found in [164]). They are multimode, 110  $\mu\text{m}$  diameter fibers. The quartz core (100/  $\mu\text{m}$  diameter) is covered by a 10  $\mu\text{m}$  thick quartz clad, a 15  $\mu\text{m}$  polyamide jacket and a Tefzel jacket for mechanical robustness [168, 169]. The total diameter with the jacket is 1mm. For most of the preliminary tests fibers with a thinner Tefzel jacket (500  $\mu\text{m}$  total diameter), otherwise identical to the final ones, were used instead. The results presented in the following do not depend in any significant way on this small difference.

Initially, Capron or Sniamid pellets from the very same nylon used to produce the OV and IV nylon film were suggested as possible diffusers (since they had the advantage of being already screened for radioactivity with good results) [170]; these were glued onto the fiber tip and their ability to scatter light away from the forward direction was tested. The diffusive properties of these cylindrical nylon pellets were investigated and the result was unsatisfactory: most of the light would not be scattered away from the forward direction.



Figure 7.1: Optical fiber tip etched in hydrofluoric acid in ambient light (left) and illuminated with a green laser light (right). Significant amounts of light could be scattered away from the forward direction by removing the polyamide coating wrapping around the quartz core. Because of the low reproducibility of the results, fragility of such fibers and the complications related to using aggressive chemicals in the clean room environment, the design was abandoned.

An attempt was then made to eliminate the polyamide jacket to allow the light channeled in the fiber to escape from its sides (without being totally internally reflected). The fiber tip was dipped in hydrofluoric acid to dissolve the jacket. The acid also attacked the quartz surface creating irregularities that would scatter light away from the forward direction. An example of an etched fiber tip illuminated with a green laser is shown in figure 7.1 [171]. This technique gave interesting results. Forward scattering was still non-negligible, but it could be reduced by carefully trimming the tip into a “conical” shape, using, for example, very fine sand paper (this was a very delicate step requiring a trained hand to be done properly!). Nonetheless, the technique was abandoned because it involved the use of aggressive acids that were difficult to work with in a clean room environment in proximity of the nylon vessels. In addition, it would be hard to reproduce the same result numerous times with tolerable precision. The etching is strongly time-dependent and fibers would often break during manufacturing and handling because of the fragile unjacketed extremity. Also, the amount of diffused light would be dependent on the index of refraction of the medium that surrounds the fiber and the results would be different in water, PC, and air. Finally, the

integrity of the nylon film could be put at risk in presence of sharp fiber tips.

### **7.2.1 The Teflon diffusers**

A material with excellent diffusive properties is Teflon. An example of such use is reported in [172]. Teflon spheres of different diameters (1/16", 3/32", and 1/8") were therefore placed at the tips of optical fibers and tested for light diffusion. The best results were obtained with the 3/32"-diameter beads. They had a good total light output (limited absorption in the Teflon) and a small forward scattering component (the 1/16"-diameter beads had very pronounced forward scattering).

#### **Gluing technique**

Gluing the Teflon balls to the fiber was a challenging task. Teflon is chemically very inert and the standard gluing techniques developed by the group for joining nylon parts alone were not sufficient. A specific gluing procedure was developed and successfully tested. The steps of such procedure, shown in fig. 7.2, can be outlined as follows:

1. The Teflon ball is punctured approximately one third of the way along its diameter with a thin needle to accommodate the quartz core of the fiber. Such a pinhole should not be too shallow or the light emerging from the fiber would be mainly absorbed and confined to just a fraction of the ball. If the pinhole is too deep there could mostly forward light transmittance and limited diffusion.
2. One end of the optical fiber is stripped of its protective Tefzel jacket a little more (approximately 0.5-1 mm) than the depth of the hole in the Teflon ball. It is then carefully cleaved. Good cleaving is important because it determines the amount of light that emerges from the fiber, but polishing the tip after the cut is not required since the ultimate goal is to diffuse light. All the diffusers built for testing, as well as the final ones, were cut with a standard manual cleaving tool.
3. The cleaved fiber tip is wetted with nylon + formic acid paste (8.5% solution) and inserted into the hole in the Teflon ball. The paste guarantees a modest adhesion

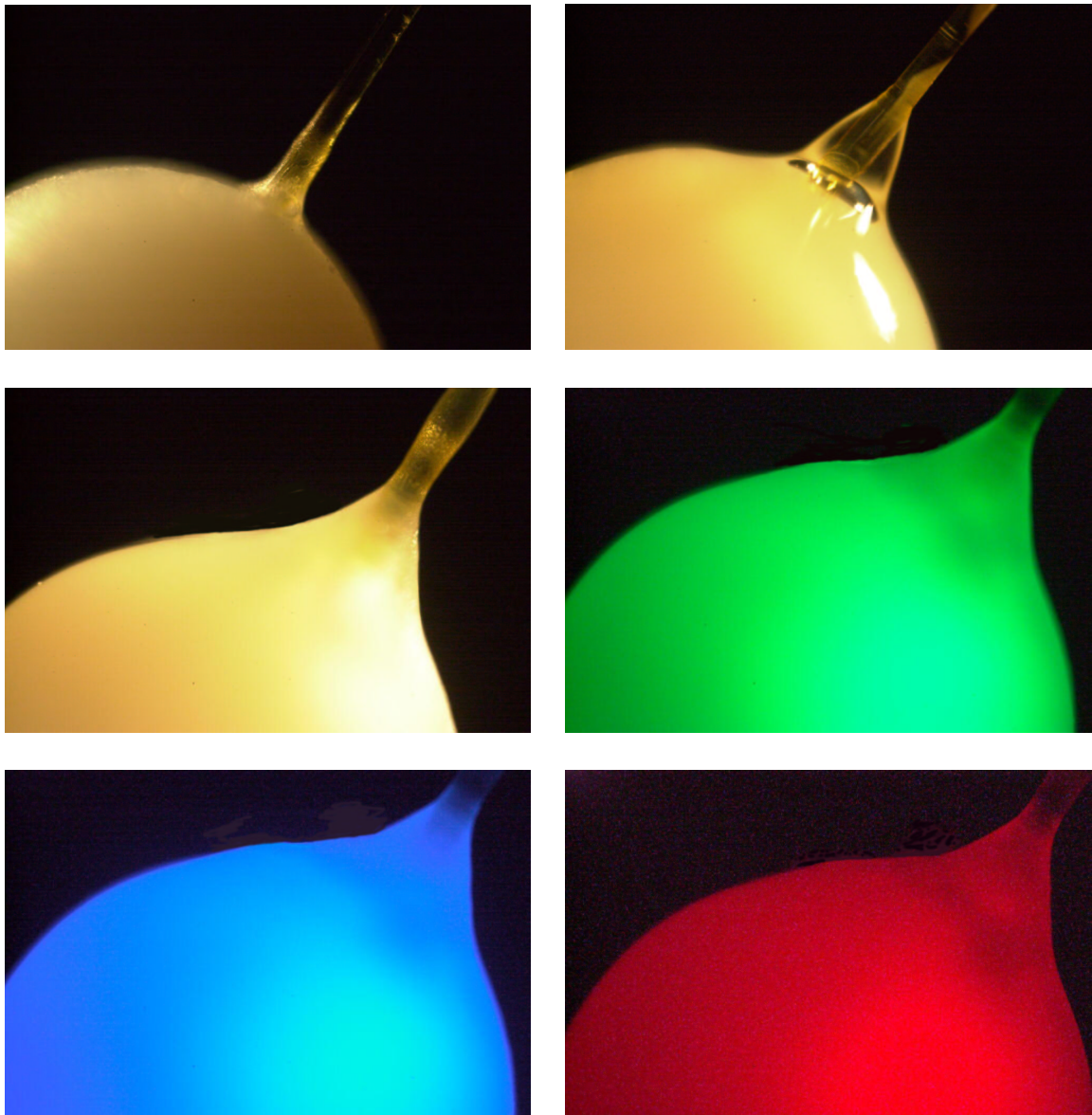


Figure 7.2: Gluing sequence for the diffuser assembly and test with lasers and LEDs of different colours. The stripped and cleaved fiber ( $110\ \mu\text{m}$ , multimode) is inserted into the Teflon ball ( $3/32''$  diameter) and weakly secured in place with a drop of nylon + formic acid paste. A first coating of Nafion polymer is applied on the surface of the ball and of the terminal section of the optical fiber (top left). A thicker Nafion coating mechanically couples the diffuser and the fiber, creating a smooth transition (top right). The end product is obtained dipping the assembly in nylon + formic acid paste that leaves a nylon coating upon drying (center left). This layer gives good mechanical robustness to the device. The diffuser performance is demonstrated with laser or LEDs of different colours: green, blue, and red (center right, bottom left and right respectively).

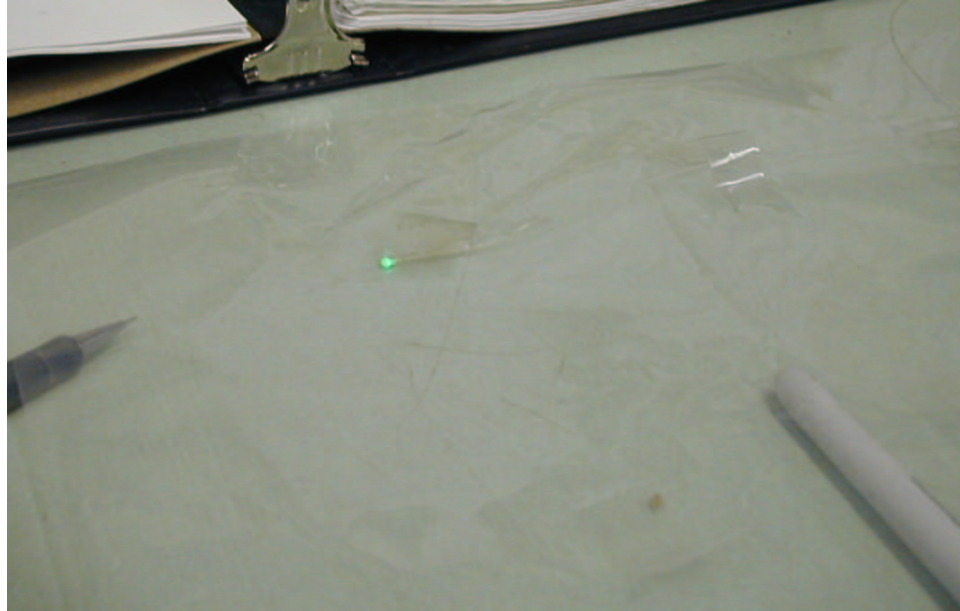


Figure 7.3: Tests of Teflon diffusers. A single prototype is glued onto a nylon sheet the same way all the diffusers have been placed onto the vessels (see fig 7.4). It is then lit up using green laser light: the diffuser is easily visible even when the lights are kept on in the room (top). Ten diffusers are glued onto a nylon sheet and fed with a red laser light: the pattern is easily visible (bottom). Both pictures were taken with a commercial-style digital camera, similar to those installed in Borexino.

that allows the assembly to stay together during the following steps (gentle handling is still required!).

4. The assembly is coated with several layers of polymeric Nafion solution (in water and alcohol) [173] that has the ability to adhere to Teflon, Tefzel, and nylon [174]. If properly performed, allowing the coating to dry thoroughly after every immersion in the solution (i.e. keeping the diffuser vertical and upwards, see fig. 7.6), the Nafion provides a good mechanical connection between the Teflon diffuser and the fiber (fig. 7.2).
5. The final step is to dip the assembly in nylon + formic acid paste (8.5 % solution) several times. This provides a nylon coating that gives mechanical strength to the device. As with the Nafion, every layer has to dry keeping the assembly vertical with the diffuser on top, so that a smooth and gradual adherence at the junction between the Teflon ball and the fiber is assured (fig. 7.2).

A sense of the realistic performance of prototype diffusers for Borexino and a demonstration of the patterns in which they can be arranged is shown in fig. 7.3.

### **Anchoring technique to the nylon film**

A safe way to attach the diffuser tips to the nylon vessels' surface has also been developed. The fiber is "sandwiched" between two rectangular nylon tabs (approximately  $2.5 \times 5$  cm) to form a "winglet" which can then be glued onto the vessel surface (fig. 7.4). The gluing technique is Resorcinol-based like that developed for the rope tabs (see chapter 6). Two of these "winglets" are used for each fiber: one is placed in close proximity of the diffusing tip, the other is kept 10-20 cm behind. This design prevents the rotation of the tip which would tend to tear the tab apart and, more importantly, it prevents the fiber from sliding out of place breaking the diffuser. The corners of the winglets are trimmed so as to avoid sharp, rigid edges on the nylon vessels that could initiate a dangerous crease. The remaining part of the fiber, each many meters long, is routed through the same tabs used for the ropes.

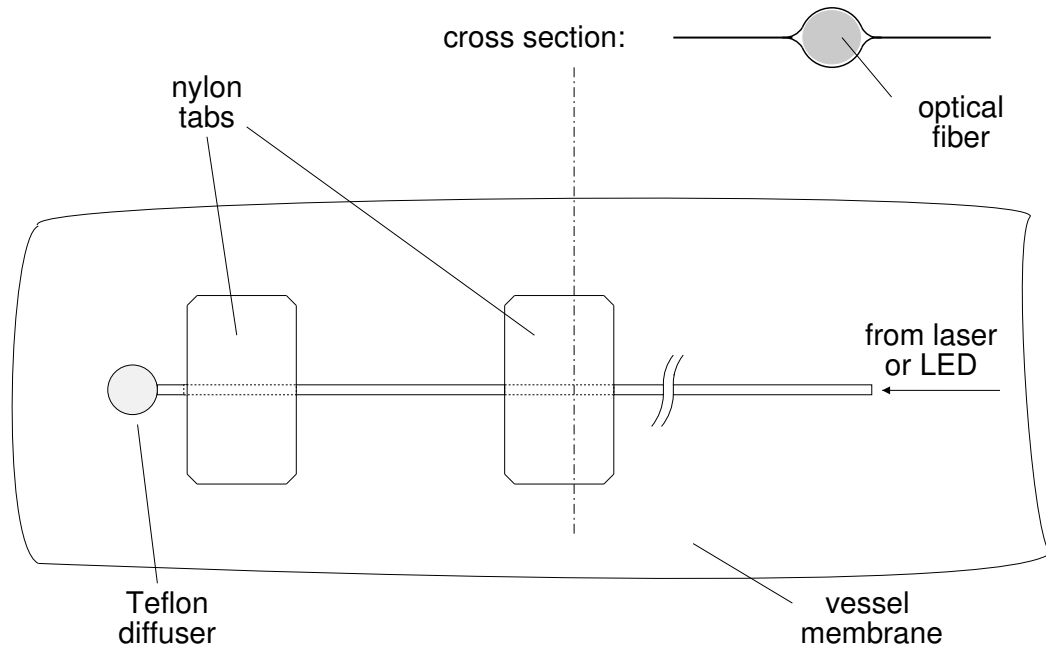


Figure 7.4: A schematic view of the light diffusers and their anchoring technique to the nylon vessels' envelope. The optical fiber is first “sandwiched” between two nylon tabs, as shown in the cross section at the top. The resulting “winglets” are then glued onto the vessels at predefined positions using the same technique adopted for the nylon tabs used to route the ropes (described in chapter 6). The fibers are secured in two points to prevent them from sliding causing the diffusive tip to come apart.

### 7.3 Light sources for scintillator stability monitoring

As mentioned previously, there is a second type of light source on the surface of the IV. Optical fibers carrying light from a laser source outside the WT are mounted on the vessel's surface so that the tip points into the scintillator region. The angle of incidence is approximately  $45^\circ$ . Photons from a 355 nm wavelength laser light are barely energetic enough to excite PC (see fig. 2.7), but can directly excite the PPO molecule. Although the decay time of this excitation is slightly faster ( $\sim 2$  ns [163]) than for the PC+PPO scintillator solution, it provides a useful calibration and monitoring tools for the scintillator close to the IV. Stability monitoring of the scintillator response over time is one of the goals at which

these light sources aim.

The attenuation length of such light in the scintillator is 1.5 cm [164]. A short pulse of light emerging from the fiber will generate a scintillation spot just inside the IV, a couple of centimeters across, that will be detected by the PMTs and spatially reconstructed. The length of the pulses emitted by the laser is  $< 1$  ns, shorter than the jitter time of the PMTs. Since the light points are at fixed positions on the IV surface, they could be used, like the diffusers, to detect movements of the nylon membrane. Alternatively, if their position is assumed stable, they could be used to test the accuracy of the Borexino detector's spatial reconstruction algorithm. The sensitivity of this method depends on the actual physical size of the scintillation spot. Important information on the behaviour of events very close to the IV's surface can also be extracted via these light sources. In particular, it could be possible to study light trapping by total internal reflection. When this occurs, events of a given energy are reconstructed as having a lower energy because of photon loss. This effect is not expected to be very significant in Borexino where nylon and PC have almost matching indices of refraction. The phenomenon is enhanced in the presence of local deformations and asymmetries of the vessel (scallop from the ropes, bubbles from air entrapment and fluid degassing, ...).

### **Fiber tip holding structure**

The main problems in designing a support to hold the optical fiber at a fixed angle with respect to the vessel's surface include mechanical robustness to protect the fiber against breaking, minimization of the mass (and therefore of radioactive background), and developing a reliable gluing technique onto the nylon membrane. The natural candidate material was nylon, for which the expertise gained during vessel R&D and fabrication could be used.

A sketch of the assembly is shown in fig. 7.5. A 5 mm thick nylon "button" is cut from a rod of extruded nylon (1 cm diameter) and a groove is cut out along a diameter on one side. Extruded rather than cast nylon stock is used since it has been found to have significantly lower radioactive contaminants due to a different fabrication process. The groove is a couple of millimeters wide and deep. The upper edge of the button that is in direct contact with

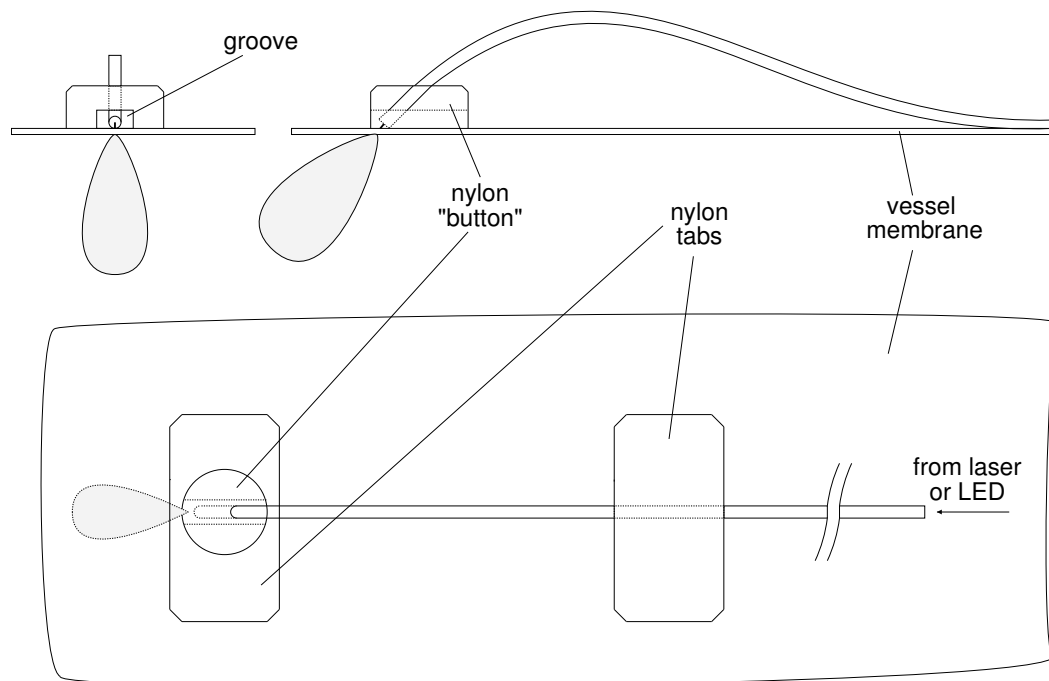


Figure 7.5: A schematic view of the light sources placed on the surface of the IV for scintillator calibration. The front, side and top views are shown. A hole is drilled in the bulk nylon “button” that holds the tip of the optical fiber at the desired angle. The fiber is purposely not orthogonal to the vessel’s surface. Firstly a shallower angle forces a smaller bend on the fiber and is mechanically more stable. Secondly the fiber’s inclination prevents the light spot produced in the scintillator (shaded in the figure) from being directly under the opaque nylon button and hence more visible by the PMTs.

the adjacent panel of the IV during shipment and installation is smoothed. A diagonal hole, just wide enough for the jacketed fiber to be inserted in it is drilled at a 45° angle. The hole is drilled so that the fiber’s tip is fully contained within the button. The button is then glued onto a rectangular nylon tab that will in turn be glued to the vessel. The tip is carefully cleaved before it is threaded through the button. Once inserted, the fiber should have a snug fit inside the button for mechanical strength.

In addition to the nylon tab under the button, the assembly is attached to the vessel's surface with a nylon "winglet" identical to those used for the light diffusers (see section 7.2.1). This holds the fiber in place avoiding stress at the fiber-button interface that could break the fiber. It also sets a gentle curvature to the section of the fiber that is raised from the nylon surface.

An earlier design had no groove carved in the nylon button. Only later it was noticed that in air, light would be partially reflected off the nylon film tab and be diffused by the bulk nylon button. The groove ensures that the fiber tip is immersed in PC (these light sources are not used with air or water). The almost perfect matching of the index of refraction of nylon and PC is thus exploited to minimize any backscattering of light off the vessel's surface.

## 7.4 Placing the light sources on the vessels

The entire assembly process of the light points (diffusers and calibration sources) and their placement on the vessel took place in the clean room. The chemicals employed were exposed to the clean room environment only.

The fibers were first cut to length according to their position on the vessels. All fibers are routed along the vessels to the north pole of the SSS and out of the WT. An extra 6 meters outside of the WT were allowed for each fiber to comfortably connect them to the LEDs and laser systems. Each fiber was cleaned by hand with alcohol-soaked fresh clean room wipes. They were then individually spooled and one tip of each fiber was assembled into either a diffuser or calibration light source (fig. 7.6). The positions of each light source are summarized in table 7.1.

Once the vessels were complete (but before nesting), the light sources were glued on and the optical fibers were routed through the nylon rope tabs placed on each panel. The loose ends of the fibers of each vessel were individually labeled and spooled together. Figures 7.6 and 7.7 show some phases of the production and deployment of the light sources in the clean room. Figure 7.8 shows the collection of optical fibers at the north end cap of the IV.

light source type	co-latitude ( $\theta$ )	longitude ( $\phi$ )	panel number
calibration	45°, 135°	30°, 120°, 210°, 300°	IV-4, IV-13, IV-22, IV-31
IV diffuser	30°, 90°, 150°	20°, 50°, 60°, 110°, 140°, 220°, 260°, 300°, 340°	IV-3, IV-6, IV-7, IV-11, IV-15, IV-23, IV-27, IV-31, IV-35
IV diffuser	15°, 30°, 45° 60°, 75°, 90° 105°, 120°, 135° 150°, 165°	180°	IV-19
OV diffuser	30°, 90°	54°	OV-6
OV diffuser	30°, 60°, 90°	18°, 54°, 90°, 126°, 162°, 198°, 270°, 306°, 342°	OV-3, OV-7, OV-11, OV-15, OV-19, OV-23, OV-31, OV-35, OV-39
OV diffuser	15°, 30°, 45° 60°, 75°, 90° 105°, 120°, 135° 150°, 165°	234°	OV-27

Table 7.1: The position of the light sources on the Borexino vessels. Both vessels have diffusers to monitor their shape and position using the CCD cameras. There are also 8 light sources on the IV used to monitor the scintillator by exciting its molecules with laser light. The co-latitude angle  $\theta$  goes from 0° (north pole) to 180°. The origin of the longitude angle  $\phi$  is arbitrarily set at the center of panel number 1 for each vessel. A single panel corresponds to 10° longitude for the IV and 9° for the OV.

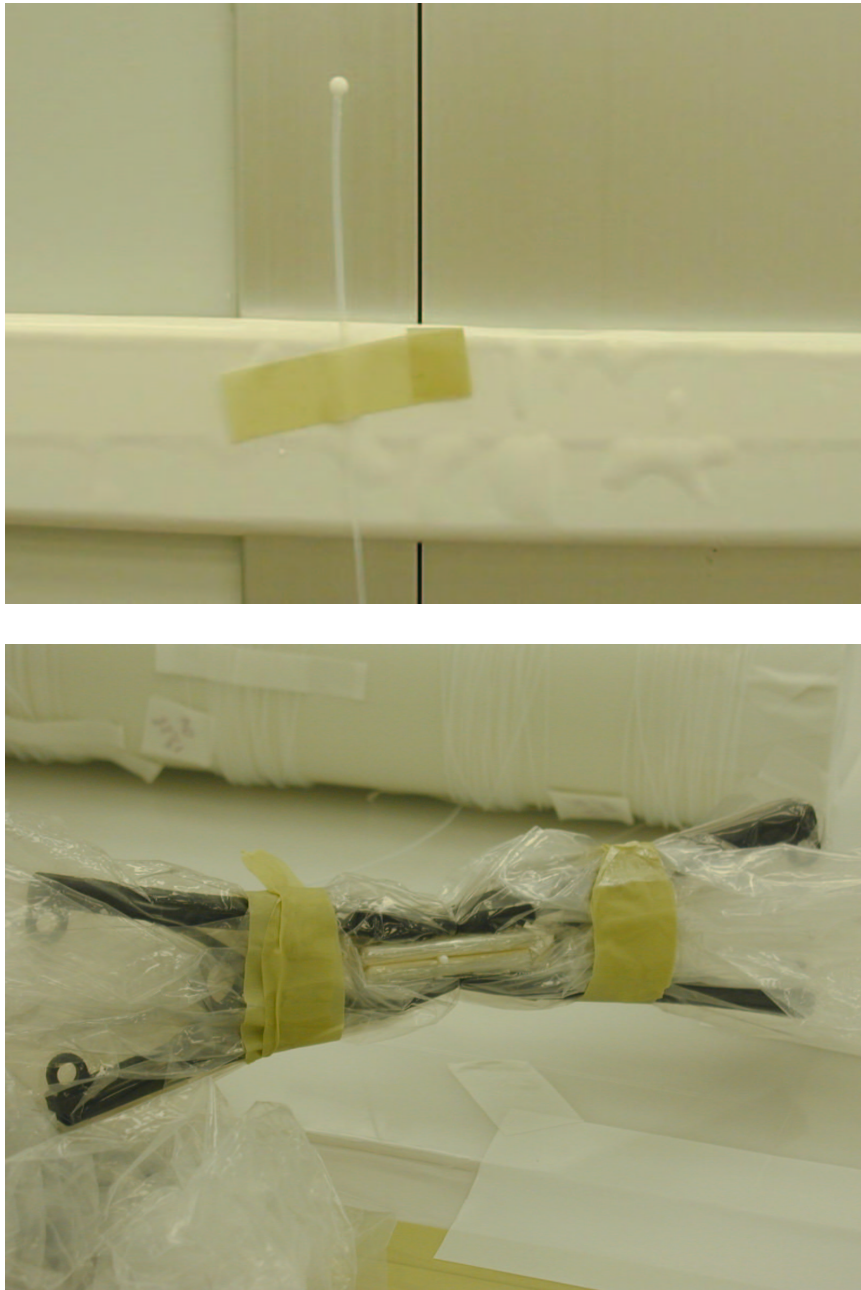


Figure 7.6: Two details of the light diffuser assembly for the Borexino vessels. The  $3/32$ "-diameter Teflon diffuser is placed on a cleaved optical fiber tip ( $100\ \mu\text{m}$  core, 1 mm Teflon jacket), coated with several layer of Nafion polymeric solution and a few layers of nylon + formic acid paste. For each coat, the assembly is dipped in the solution and allowed to dry diffuser-up to allow a smooth, mechanically strong transition between the diffuser and the fiber (top). The fiber is sandwiched between two nylon film tabs in a “winglet” for adhering to the vessel’s surface via Resorcinol gluing and clamping (bottom).

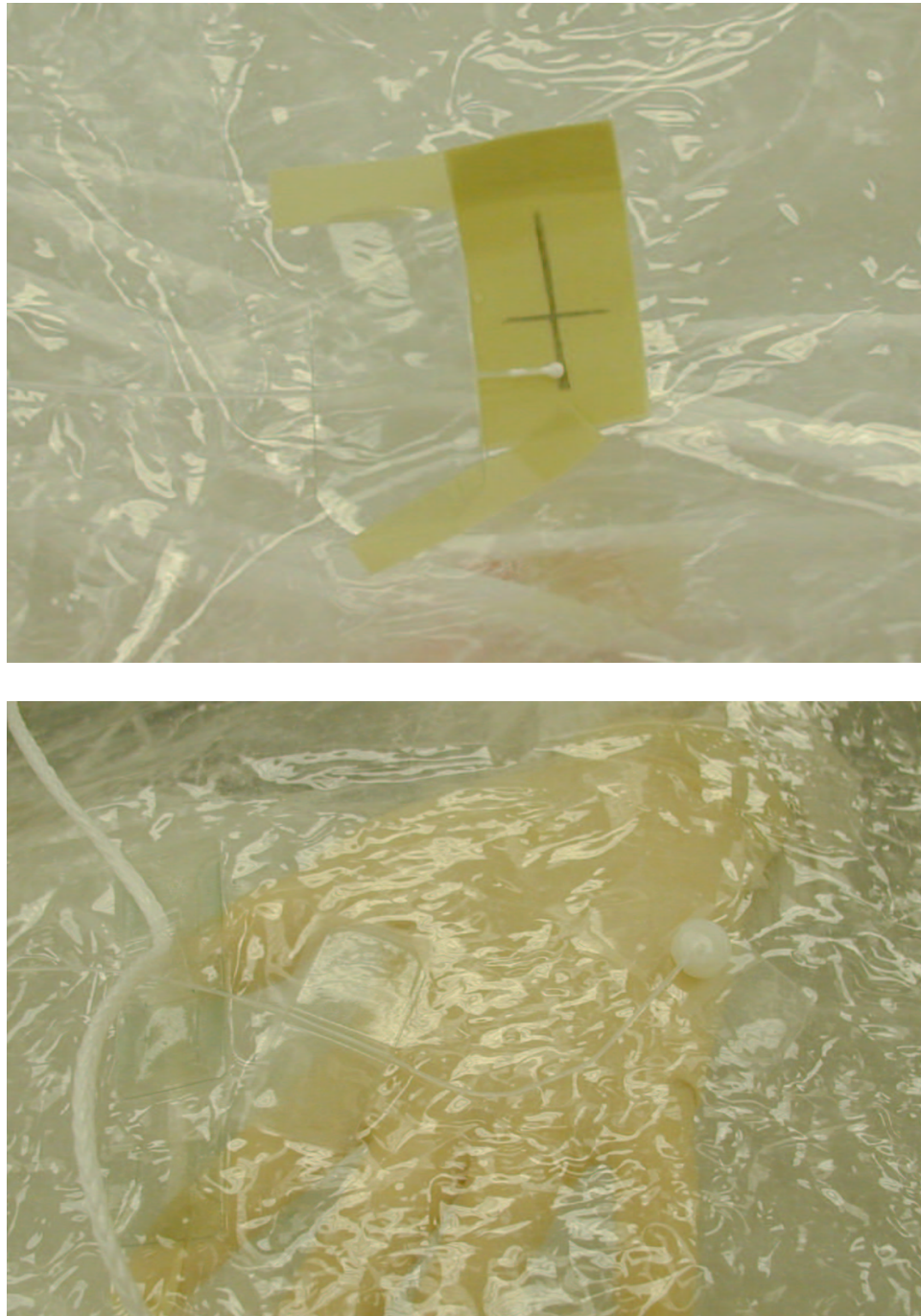


Figure 7.7: A diffuser before being glued on the OV (top) and a calibration light source placed onto the IV (bottom). Reflections of the clean room lights on the nylon surfaces make the pictures hard to decipher. A bend was introduced to the section of fiber between the two attachment points of the latter: such configuration offers protection from compression from the panels above it in the vessel stack.

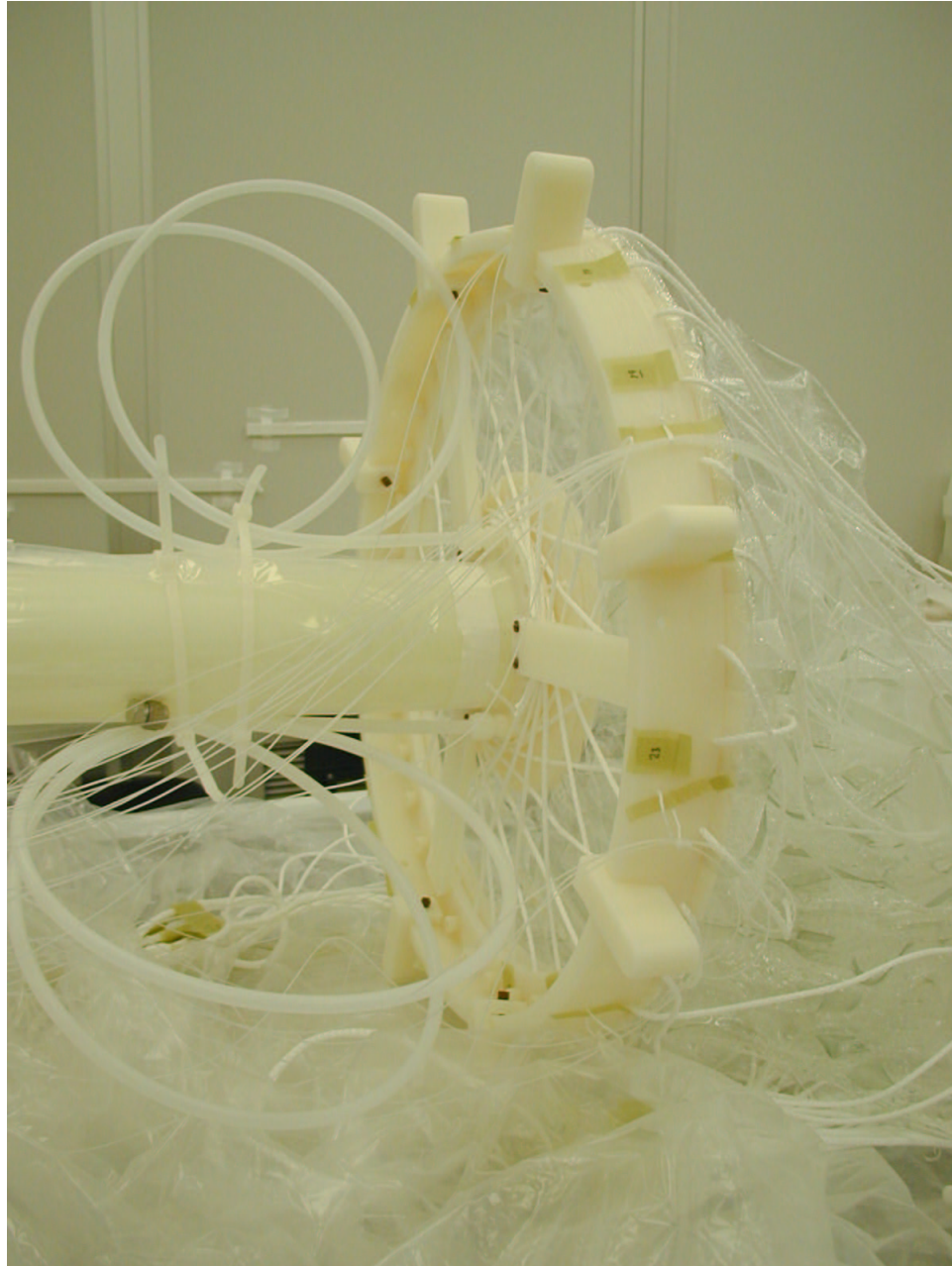


Figure 7.8: Optical fibers routed past the IV north endcap. The 3/8" flexible nylon sampling ports, the tensylon ropes, the nylon "bridge" film, and the nylon "bumpers" that sustain the nylon L-shaped nylon ring are also visible.

component	mass (g)	$^{238}\text{U}$ (ppt)	$^{232}\text{Th}$ (ppt)	$\text{K}_{nat}$ (ppb)	fraction of contribution from the PMTs (in IV) <sup>1</sup>
Resorcinol	< 1	26	100	51	$< 2 \times 10^{-4}$
formic acid	< 1	< 2	< 2	14	$< 10^{-7}$
Nafion-coated Teflon beads	1	18	29	13000	$1.2 \times 10^{-2}$
optical fiber <sup>2</sup>	$\sim 500$	< 50	< 30	135	0.18
nylon film <sup>3</sup>	0.6	1.1	1.6	1.6	$3 \times 10^{-9}$

<sup>1</sup> The values in this column refer to the  $\gamma$  activity inside the entire IV (300 tons), for events above 250 keV. The activity is significantly lower ( $\sim 3000$  times) in the central 100 tons fiducial volume. The simulated values are taken from [76].

<sup>2</sup> Fiber from a different batch than the one used on the vessel, with a 0.5 mm instead of a 1 mm jacket, was measured. The numbers refer to the whole fiber (i.e. quartz core + jacket): they are scaled to the mass of the thicker fiber. This is a conservative approach, since it is likely that the potassium comes mainly from the quartz core, identical for both batches, rather than from the jacket.

<sup>3</sup> The values for the nylon are taken from measurements on the pellets used to extrude the Sniamid film for the IV [76].

Table 7.2:  $^{238}\text{U}$ ,  $^{232}\text{Th}$ , and  $^{40}\text{K}$  radioactivity present in the materials used for the light sources on the Borexino nylon vessels. The isotopic abundance of  $^{40}\text{K}$  in  $\text{K}_{nat}$  assumed in this estimate is  $10^{-4}$  [175]. The measurements were performed by ChemTrace [176]. The data for the PMTs radioactivity are taken from [76].

The number of diffusers was dictated by two factors. First, some degree of redundancy is desired since it is possible that the fibers can break during vessel shipping and installation which involves aggressive film handling. Second, a particular geometry needed to be respected to define certain patterns on the vessels' surfaces in mind. The equator and other parallel circles are highlighted as well as a complete meridian so as to allow monitoring of the sphericity of the vessels.

## 7.5 Radiopurity screening

The components and materials employed for the fabrication of the vessel light sources have been measured for residual radioactivity. The requirement for  $^{238}\text{U}$ ,  $^{232}\text{Th}$  and  $^{40}\text{K}$  is that of adding a negligible amount of radioactivity to the vessel system. Table 7.2 summarizes the radioactivity budget. It shows that the main contribution is from  $\gamma$ 's from  $^{40}\text{K}$ , likely coming from the quartz of the optical fibers and the Nafion solution. The contribution of the light source system is approximately 1/5 of that from the PMTs in the whole scintillator volume for events above 250 keV, but it drops to about  $10^{-4}$  of it in the 100-ton expected fiducial volume. The radioactivity of the system is thus acceptable.

## 7.6 External connection to LEDs and lasers

The IV and OV fibers are routed as two separate bundles from the vessels out the north pole of the SSS and the WT into a small class 10 clean room where most of the calibration equipment is installed. The design of the leak tight break out for the optical fibers is under way [177] at LNGS.

The optical fibers were not terminated at the time the vessel was shipped to Italy. An SMA connector will be mounted on each one; this is the same type of connector used for the optical fibers of the Borexino calibration system. The inward-pointing fibers for scintillator calibration will be connected to a 355 nm laser.

The original idea for the light diffusers was to connect them to LEDs. Laboratory tests have shown that light from standard, commercial red LEDs is safe to shine even if the PMTs are on [178]. If confirmed it would be possible to check the position of the vessels relatively often while the detector (i.e. the PMTs) is running. Such a system would be completely manual as far as controlling which diffusers to light up and in what sequence. The operation would require a two-man crew in CR4 connecting the fibers to the LED and taking pictures.

An alternative and possibly more powerful way of using the light diffusers is to connect them to the fast, low emission LED system used for calibrating the outer muon Čerenkov

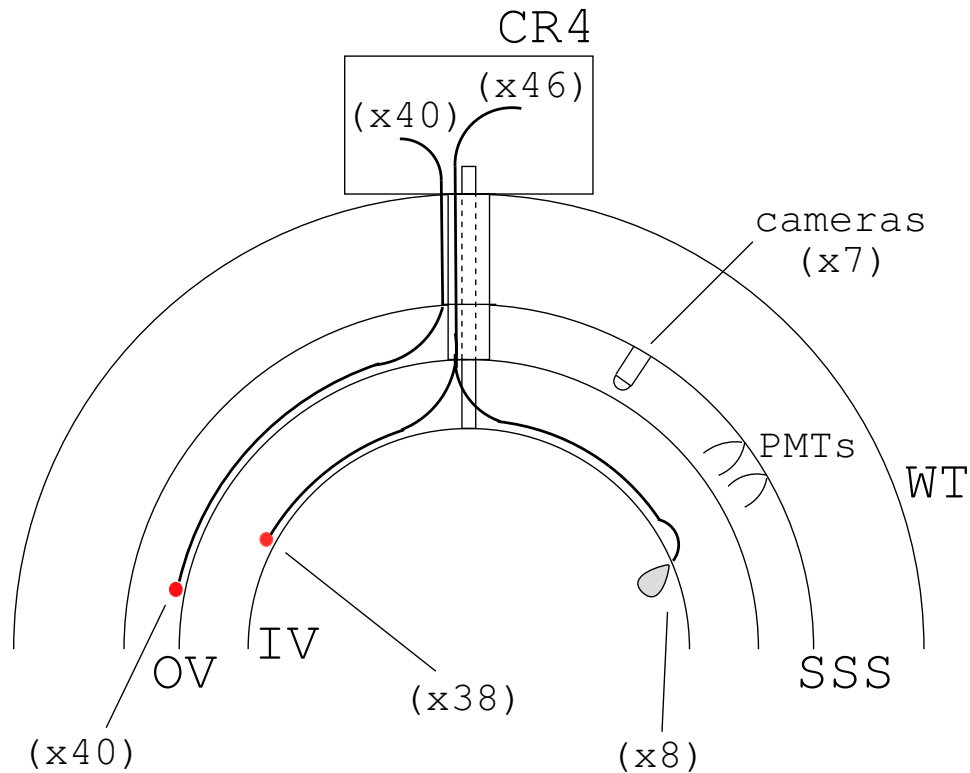


Figure 7.9: Sketch of how the light sources are deployed on the Borexino vessels and routed out the north pole of the SSS and WT into the CR4 class 10 clean room where the calibration lasers are installed. The optical fibers and the light diffusers are not to scale.

detector [179]. The light output of these LEDs is set by a VME-based system and can be controlled to very low levels. The wavelength of the light from such LEDs is one to which the PMTs are sensitive. The position of the light diffusers could then be reconstructed using the PMTs and the standard reconstruction algorithm. The light diffusers therefore provide a way to cross-check the position reconstruction technique for events at the surface of the vessels. In this configuration, it is conceivable to shine particular sequences of diffusers in a completely automatic way [180]. It would also be possible to have a set of diffusers lit at the beginning of every run and their position recorded. This would locate the IV at every run, potentially helping to identify instabilities in the definition of the fiducial volume where neutrino events will be looked for. The outer muon detector calibration system (electronics,

LEDs and optical fibers) is currently installed at LNGS, and some ten spare LEDs would be available. To use this system, the optical fibers must first be extended from CR4 down to the control room where the electronics for Borexino are placed.

---

## Results from CTF3

The Counting Test Facility (CTF) started its third data-taking phase in May 2001. The detector, a prototype of Borexino, is described in chapter 2 together with a summary of the results from past CTF runs. The current CTF3 campaign has the following main goals:

- 1) test the  $^{14}\text{C}$  content of the Borexino scintillator delivery
- 2) test the initial contamination of the scintillator from trace radioactive isotopes, such as  $^{238}\text{U}$ ,  $^{232}\text{Th}$ ,  $^{40}\text{K}$ ,  $^{85}\text{Kr}$ , etc.
- 3) test the performance of the scintillator purification techniques and plants for Borexino

### 8.1 CTF3 operations

The CTF3 nylon vessel was installed in February 2001; the detector was water-filled that May (see fig. 2.12). Its electronics calibration took place in the following months, until the first pseudocumene batch for the Borexino scintillator was delivered. CTF3 was filled with scintillator at the end of November. For the following seven months, tests proceeded steadily.  $^{14}\text{C}$  from all the pseudocumene deliveries was measured (see section 8.2) and scintillator purification tests using the Borexino plants were carried out. These included counter current water extraction, nitrogen stripping and impurity removal on a silicagel adsorption bed. Table 8.1 summarizes the main CTF3 operations and tests in chronological order.

date	operation	run(s)	comments
Feb. 2001	nylon vessel installed		
May 2001	water filling		
July 21 2001	beginning of data taking	2000	water runs
Nov. 22-28 2001	scintillator loading	2042-2047	
Jan. 10-11 2002	$^{14}\text{C}$ test	2074-2075	
Feb. 6-11 2002	silicagel colulmn test	2094-2103	continuous loop mode
March 20-28 2002	water extraction test	2123-2130	continuous loop mode
April 26 2002	$^{14}\text{C}$ test	2153	
May 9-23 2002	water extraction test	2162-2173	stop-and-go mode, acidic water
June 3 2002	$^{14}\text{C}$ test	2180	
June 9-20 2002	silicagel column test	2184-2188	batch mode
June 21 2002 - date	data taking	2189-date	

Table 8.1: Chronology of operations and tests carried out with the CTF3 detector. Minor operations, such as nitrogen stripping of the water, shroud refillings and closed loop scintillator recirculation without any purification, are not listed.

A complete analysis of the results of such tests is beyond the scope of this work. The measurement of the  $^{85}\text{Kr}$  contamination of the scintillator and of the efficiency of its removal by nitrogen stripping is found in section 8.5. A sudden and unexpected shutdown of all operations involving pseudocumene came in August 2002. Since then, the detector has been essentially unperturbed, although still taking data.

## 8.2 $^{14}\text{C}$ contamination of the scintillator

$^{14}\text{C}$  is a long-lived radioactive isotope of carbon. It  $\beta$ -decays ( $Q = 156$  keV) with a mean life of more than 5000 years, as shown in fig. 8.1. Since it is present in the pseudocumene molecule, it is impossible to eliminate with any purification technique. The lower energy

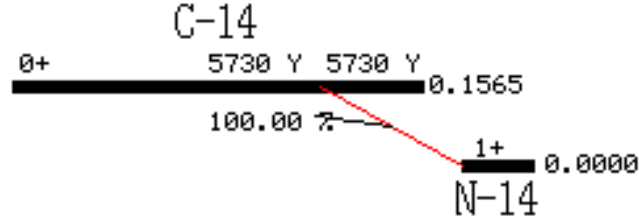


Figure 8.1: The  $^{14}\text{C} \rightarrow ^{14}\text{N}$   $\beta$  decay scheme [182]. The  $\log ft$  value for the decay is 9.04 [175]

threshold as well as the overall event rate of Borexino depend on the  $^{14}\text{C}$  abundance inside the scintillator. It is essential then that its amount be as low as possible.

The  $^{14}\text{C}$  amount in several samples taken during the scintillator delivery campaign has been measured with CTF3. The first batch used to initially fill the CTF3 vessel was measured in December 2001. For the subsequent three pseudocumene deliveries (January, April, and June 2002),  $\sim 500 \ell$  of scintillator were displaced with the introduction of an equivalent amount of new PC. The  $^{14}\text{C}$  content is computed keeping the relative amounts of old and new PC in the vessel into account.

The  $^{14}\text{C}$  activity  $A_{C14}$  (total number of events divided by the data-taking time) is measured by fitting the energy spectrum with a simulated one where the amplitude is used as the fit parameter [181]. Let  $N_{C14}$  and  $\tau_{C14}$  be the total number of  $^{14}\text{C}$  atoms in the CTF3 scintillator and its lifetime respectively. The  $^{14}\text{C}$ -to- $^{12}\text{C}$  mass ratio  $R$  is given by

$$R \left( \frac{^{14}\text{C}}{^{12}\text{C}} \right) \equiv \frac{N_{C14}}{N_{C12}} = \frac{A_{C14} \tau_{C14}}{N_{C12}} = \frac{40}{3} \left( \frac{\tau_{C14}}{m_{IV} N_A} \right) A_{C14} \quad (8.1)$$

where  $N_A$  is Avogadro's number and  $m_{IV}$  is the mass of PC in the CTF3 inner vessel. The measurements and results are summarized in table 8.2, and the  $^{14}\text{C}$  content for the various pseudocumene batches are reported in fig. 8.2 together with the average of the whole PC delivery.

From the amounts of PC delivered with each batch and using the measured values of  $R(^{14}\text{C}/^{12}\text{C})$  from each, the average  $^{14}\text{C}$  content in the scintillator for Borexino is

$$R \left( \frac{^{14}\text{C}}{^{12}\text{C}} \right)_{\text{Borexino}} = 5.0 \pm 2.0 \times 10^{-18}. \quad (8.2)$$

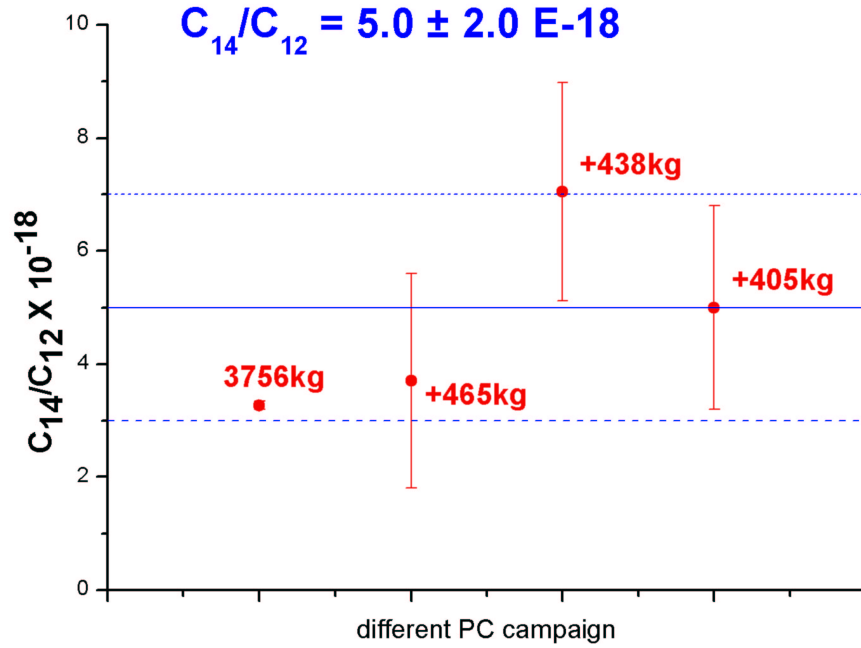


Figure 8.2:  $^{14}\text{C}$  content in the pseudocumene for the Borexino scintillator, as summarized in table 8.2. The average value for the mass ratio  $R(^{14}\text{C}/^{12}\text{C})$  is  $5.0 \pm 2.0 \times 10^{-18}$  [183].

date	amount delivered (kg)	operation	$R(^{14}\text{C}/^{12}\text{C})$ ( $10^{-18}$ )
4 Dec 2001	17560	Fill IV with 3.76 t (initial batch)	$3.27 \pm 0.06$
10 Jan 2002	18440	+0.47 t (new) -0.39 t (old)	$3.7 \pm 1.9$
26 Apr 2002	18500	+0.44 t (new) -0.32 t (old)	$7.1 \pm 1.9$
3 Jun 2002	217340	+0.41 t (new) -0.35 t (old)	$5.0 \pm 1.8$

Table 8.2: Chronology of  $^{14}\text{C}$  tests in CTF3. The  $^{14}\text{C}$  content is computed using eq. 8.2, where  $R$  is the mass ratio between the mass of  $^{14}\text{C}$  and the mass of scintillator in the IV. The rate  $R$  in the column to the right gives the  $^{14}\text{C}$  contamination of the “new” (added) PC.

Thus the  $^{14}\text{C}$  amount in the scintillator for Borexino is  $\sim 2.5$  times higher than what was measured with CTF1, where  $(1.94 \pm 0.09) \times 10^{-18}$  was measured [75]). The achieved result is still within the Borexino specifications.

### 8.3 Detector monitoring using radon

Radon ( $^{222}\text{Rn}$ ) from the  $^{238}\text{U}$  natural radioactive chain is a difficult source of background to eliminate, that leaves the long-lived  $^{210}\text{Pb}$  isotope behind (see fig. 3.7). Radon can enter the detector through many paths. Air leaks may be present in the containers and pipes carrying the scintillator. Radon is also emanated by  $^{226}\text{Ra}$  in the walls of the pipes and tanks and in the nylon vessel. Finally, radon present in the water in which the inner vessel is immersed can permeate through the nylon membrane and end up inside the scintillator.

Although one would ultimately make all possible efforts to eliminate it, radon also represents a very powerful monitoring tool. Its presence can be easily tagged by looking for the mass 214 ( $^{214}\text{Bi}$ - $^{214}\text{Po}$ ) delayed coincidence decays (“BiPo-214” coincidences in the following). This event sequence effectively selects radon events because all isotopes in the  $^{238}\text{U}$  chain between  $^{222}\text{Rn}$  and  $^{214}\text{Bi}$  have a mean life of less than half an hour. Practically, if the time profile of such coincidence events follows the  $^{222}\text{Rn}$  mean life (5.518 days), their origin can unmistakably be attributed to radon out of equilibrium with isotopes higher in the  $^{238}\text{U}$  chain (this is a very common scenario, since radon can travel far from its production site during its lifetime). If on the other hand the BiPo-214 coincidence rate is constant in time (or, more precisely, roughly constant during a time window which is long compared to the radon lifetime), and all possible radon leaks are eliminated, it has to originate from the presence of  $^{226}\text{Ra}$  (2340 years mean life) from which it emanates; in this case, measuring the number of BiPo-214 coincidence events actually represents a direct measurement of the  $^{226}\text{Ra}$  contamination. If one further assumes secular equilibrium in the higher part of the decay chain, the  $^{238}\text{U}$  contamination can be deduced.

A spike of radon inside the CTF scintillator is a very effective way of calibrating the detector. It represents a completely internal contamination, that can in principle be used to

understand how to discriminate between intrinsic contamination of the scintillator and that coming from the nylon vessel and the surrounding water. On the other hand, as long as artificially introduced radon is present, the  $^{226}\text{Ra}$  (and, consequently,  $^{238}\text{U}$ ) contamination of the detector cannot be measured. Furthermore, the presence of radon (i.e. of the BiPo-214 coincidence events) significantly interferes with the search for BiPo-212 coincidences; this sequence is found in the  $^{232}\text{Th}$  natural radioactive chain. The time and energy cuts that can be applied to isolate the BiPo-212 coincidences can't completely prevent the leakage into the data set of BiPo-214 events, particularly when large amounts of radon are present.

Even without being deliberately introduced, radon enters the detector after practically any fluid operation. This can be due to some air contamination during major fluid transferring, such as during the initial loading of the detector, or because of emanation from the walls of the storage tanks and of the lines used to transfer it. Figure 8.3 shows the radon profile in CTF3 since the initial loading with scintillator. The major operations are also shown.

The plot in fig. 8.3 clearly shows how radon rises, in variable amounts, after every major scintillator handling. Large radon activity was present after the initial scintillator loading of the detector, after every  $^{14}\text{C}$  test, and following each scintillator purification test. It is present in “new” pseudocumene or collected through tiny leaks in the system. The radon emanated from the walls of the transfer and purification plants lines is also collected when recirculating the scintillator. There is one instance in which a very significant increase in the radon counts (thousands of counts per day) was not related to fluid operations. It is the peak after almost 60 days of data taking (labelled “1” on the plot). It turned out that it was due to a valve that developed a leak towards the outside along one of the pseudocumene lines. The problem was readily fixed and the radon counts decreased according to its lifetime, as expected.

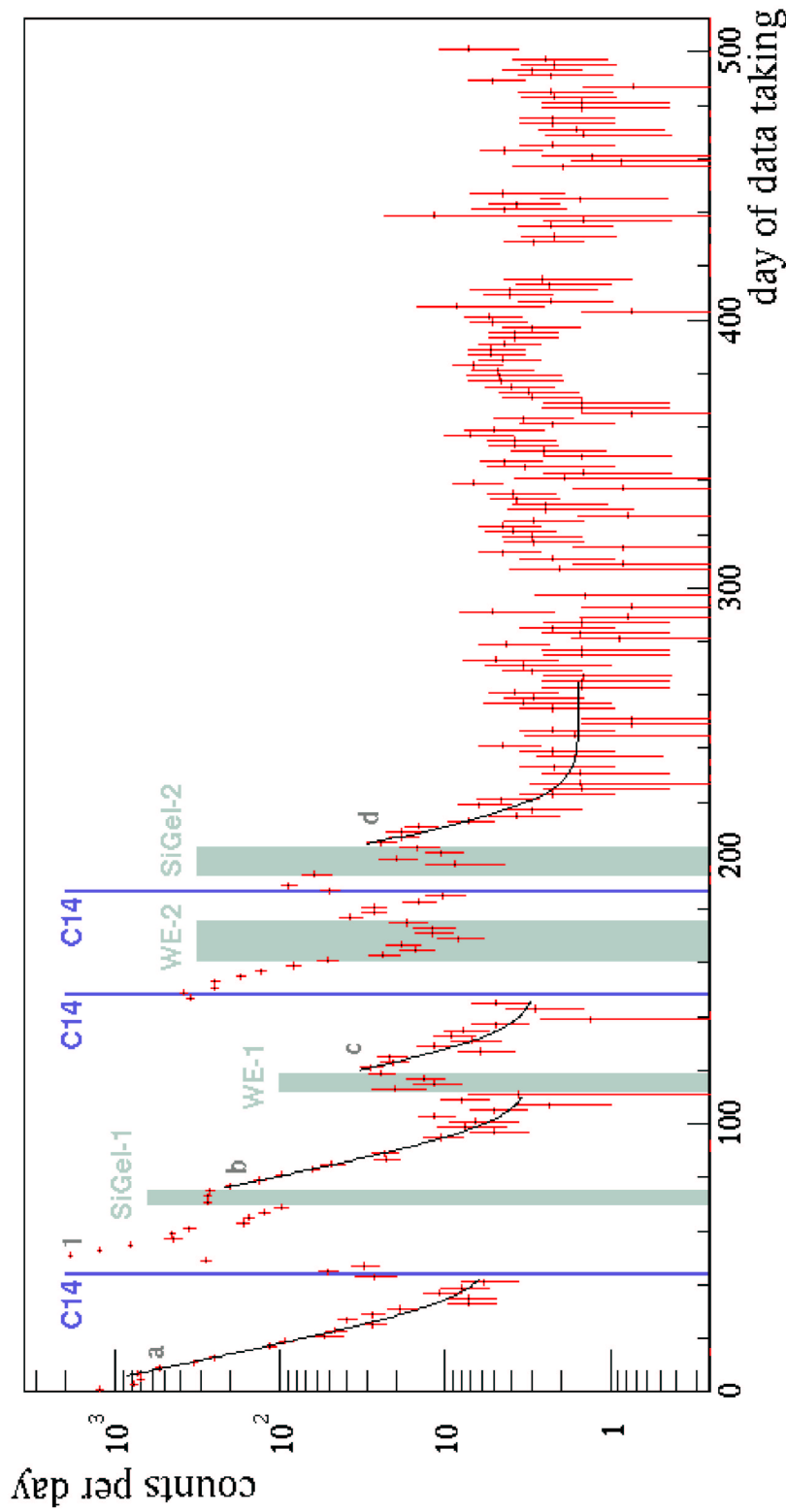
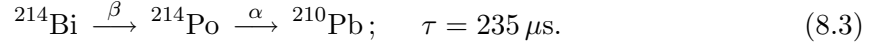


Figure 8.3: The radon contamination profile in CTF3. The data are shown between November 27, 2001, and April 17, 2003 (runs 2047-2300). The events are identified via the  $^{214}\text{Bi}$ - $^{214}\text{Po}$  delayed coincidence  $\beta$ - $\alpha$  sequence. The event selection cuts are those summarized in sections 8.3.1 and 8.3.2; no radial cut is applied. The purification cycles and the insertions of “new” PC for  $^{14}\text{C}$  screening are indicated. The fits are performed with a decaying exponential with the radon mean life (5.5 d) plus a constant, and their results presented in section 8.4

### 8.3.1 $^{214}\text{Bi}$ - $^{214}\text{Po}$ coincidence sequence

The mass 214 Bi-Po delayed coincidence sequence used to tag radon is:



The  $Q$ -value of the  $^{214}\text{Bi}$   $\beta$  decay is 3.27 MeV; the energy of the  $\alpha$  particle is 7.69 MeV.

### 8.3.2 $^{214}\text{Bi}$ - $^{214}\text{Po}$ event selection

The cuts used to select the BiPo-214 delayed coincidence events and the corresponding efficiencies  $\epsilon_i$  are:

1. energy of the first event ( $\beta$ ):  $300 \text{ keV} < E_1 < 4 \text{ MeV}$  ( $\epsilon_1 = 97\%$ )
2. energy of the second event ( $\alpha$ ):  $500 \text{ keV} < E_2 < 900 \text{ keV}$  ( $\epsilon_2 \simeq 100\%$ )
3. delay time:  $20 \mu\text{s} < t < 500 \mu\text{s}$  ( $\epsilon_3 = 80\%$ )
4. muon flag off

The total efficiency  $\epsilon = \epsilon_1 \epsilon_2 \epsilon_3$  of the cuts is 78%.

The definition of the cut on the energy of the second event (cut #2) requires the knowledge of the quenching factor for 7.7 MeV  $\alpha$  particles in CTF3 (it was 10.2 in CTF1, in which the gaussian peak from these  $\alpha$  decays was observed at 751 keV [79]). In the absence of a direct measurement of this quantity, the following method was followed to optimize such cut. A preliminary, first guess for cut #2 was made to identify runs with large amounts of radon ( $600 \text{ keV} < E_2 < 900 \text{ keV}$ ), imposing the other cuts as listed above. The  $\alpha$  peak was then identified, its position located precisely, and the cut fine tuned.

The efficiency  $\epsilon_1$  of the first energy cut (cut #1) is based on a simulated spectrum of  $^{214}\text{Bi}$  decay. Figure 8.4 shows the energy histograms of the first and second event of BiPo-214 coincidences during the initial phase of CTF3 (runs 2056-2093).

The lower cut on the delay time is imposed in order to discard potential contamination of the data by faster delayed coincidences, such as the  $^{212}\text{Bi}$ - $^{212}\text{Po}$   $\beta - \alpha$  sequence in the

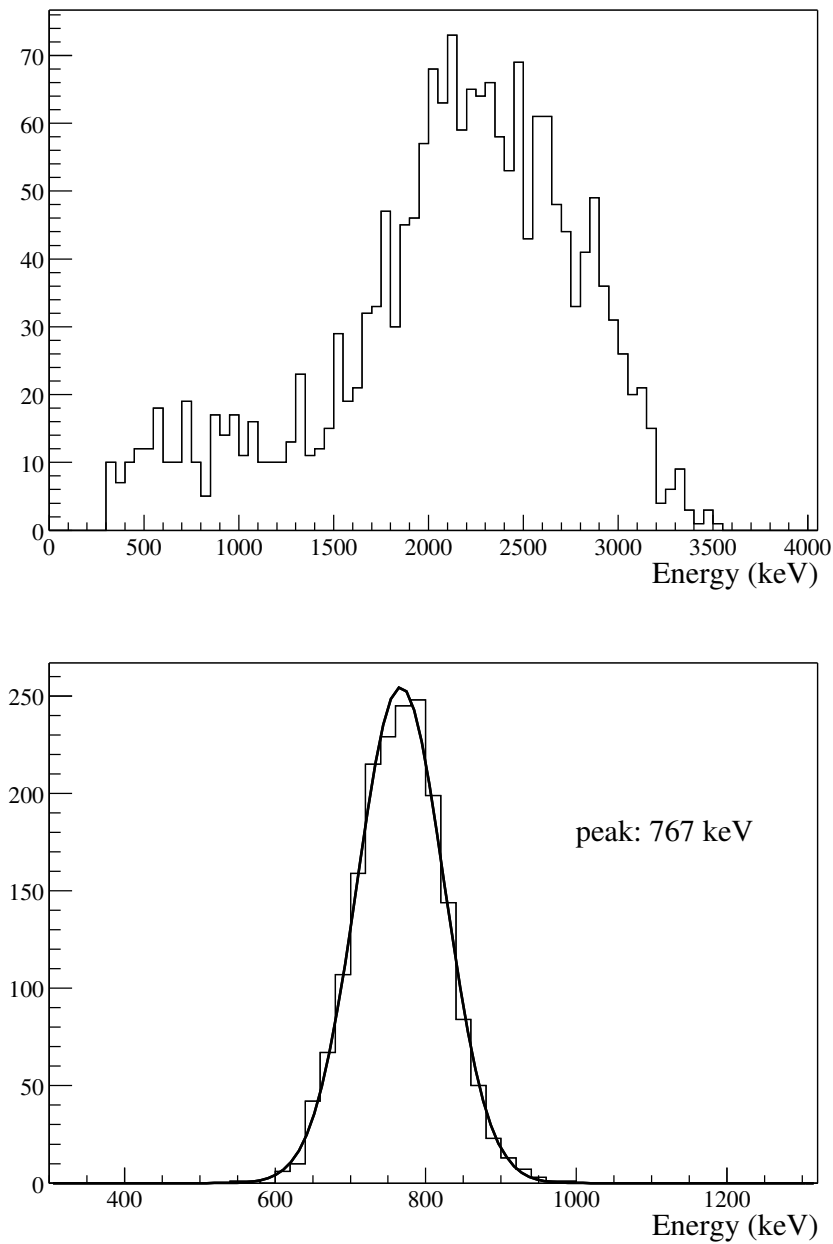


Figure 8.4: Energy spectra of the  $\beta$  (top) and  $\alpha$  (bottom) BiPo-214 delayed coincidence events for the first, unpurified scintillator batch (runs 2056-2093). The cuts applied are those listed in the text. The shape of the  $^{214}\text{Bi}$   $\beta$  decay spectrum (top) displays the de-excitation  $\gamma$  peak characteristic of the decay. The gaussian peak from the 7.69 MeV  $\alpha$  decay of  $^{214}\text{Po}$  (bottom) is observed at  $767 \pm 58$  keV (quenching factor: 10). A 60 cm radial cut was applied for selecting the  $^{214}\text{Po}$   $\alpha$  events.

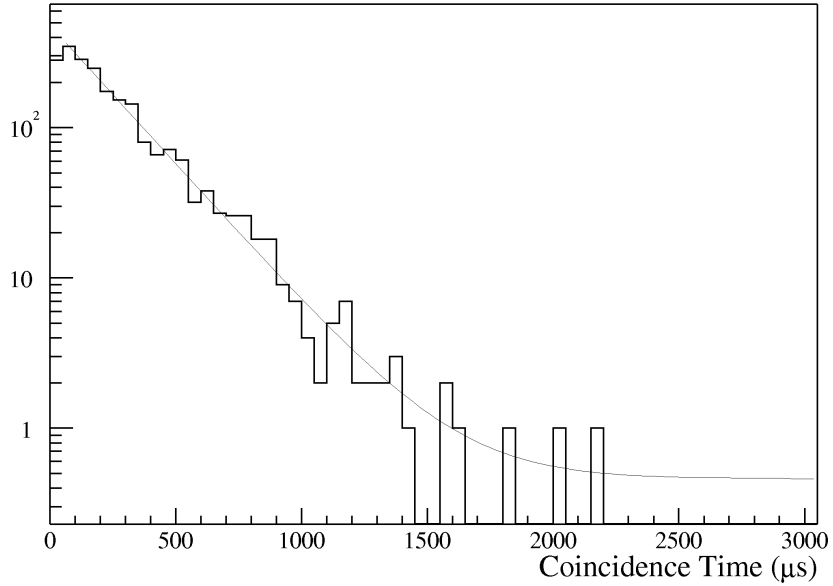


Figure 8.5: Coincidence time profile for  $^{214}\text{Po}$   $\alpha$  decays for the first, unpurified scintillator batch (runs 2056-2093). The two energy cuts and the muon flag cut are imposed; the coincidence time is only required to be larger than  $20 \mu\text{s}$ . A 60 cm radial cut was applied for selecting the  $^{214}\text{Po}$   $\alpha$  events. The data fit a decaying exponential with the expected  $235 \mu\text{s}$  lifetime. The fit value of the constant background from random coincidences that pass the energy cuts is  $(9.2 \pm 6.5) \times 10^{-2} \text{ ev}/\mu\text{s}$ .

$^{232}\text{Th}$  radioactive decay chain. Fig. 8.5 shows the profile of the coincidence time when only cuts #1, #2, and #4 are imposed. The data are fit (between  $50 \mu\text{s}$  and  $5 \text{ ms}$ ) with the sum of a constant and a decaying exponential,

$$N(t) = N_0 e^{-t/\tau} + N_1, \quad \tau = 235 \mu\text{s} \quad (8.4)$$

where  $N_0$  and  $N_1$  are the number of counts in the first bin, and the constant background (counts/bin), respectively; the bin size is  $50 \mu\text{s}$ . It can be seen that the profile fits very well with a decaying exponential with the  $^{214}\text{Po}$  mean life ( $\tau = 235 \mu\text{s}$ ). When  $\tau$  is left as a free parameter of the fit, one obtains  $\tau = 229 \pm 6 \mu\text{s}$ , fully compatible with the  $^{214}\text{Po}$  mean life. The value of the constant term, which indicates the number of random coincidences that pass the energy cuts, is  $N_1 = 0.46 \pm 0.32 \text{ ev/bin}$ ; scaling this number by the size of the bin ( $50 \mu\text{s}$ ) and the data taking livetime of the sample ( $40.06 \text{ days}$ ) yields  $(2.2 \pm 1.6) \times 10^{-3}$

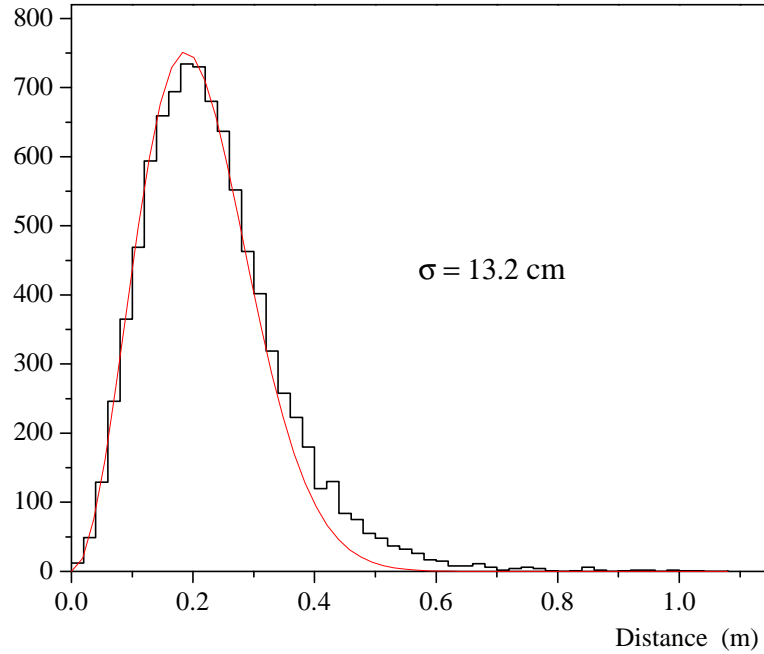


Figure 8.6: Reconstructed distance between the positions of the selected BiPo-214 delayed coincidence events. Data are from runs 2056-2093. Cuts #1–#4 were applied; a 60 cm radial cut was also imposed for the position of the second ( $^{214}\text{Po}$   $\alpha$  decay) event. The data are fit with the function  $d(r) = A r^2 \exp(-r^2/2\sigma^2)$ , obtained by transforming a 3D gaussian distribution in each cartesian coordinate centered in the origin into spherical coordinates and integrating over the solid angle. The fit doesn't account well for the tail at large distances, which appears significantly higher than for a perfectly gaussian distribution.  $\sigma$  is a measure of the resolution of the detector.

ev/ $\mu\text{s}/\text{d}$ . It scales to  $\sim 1$  ev/d in the time window defined by cut #3 and is therefore essentially negligible if the radon levels are high enough. It is significant only when just a few BiPo-214 events/day are selected with the cuts above. An independent measure of the number of random coincidences that contaminate the data sample was also carried out. The events selected with cuts #1, #2, and #4 (energy + muon flag) in the 2-5 ms coincidence time window were counted and scaled to the BiPo-214 time coincidence time window (cut #2). Less than 0.1 ev/day were selected for all runs 2047-2300.

Events associated with the passage of a muon, identifiable by the appropriate muon flag, are discarded. When possible contaminations of the data sample coming from activity on

the surface of the nylon vessel, from the surrounding water or from residual muons that don't trigger the muon flag need to be suppressed, radial cuts to select events in the center for the detector are also implemented. This obviously comes at the cost of shrinking the size of the data sample and its statistical significance.

A further check can be made on the quality of the selected data sample. The two events in the sequence are essentially point-like and occur at the same position inside the detector (the coincidence time is small enough to neglect any diffusive or convective drift of the decaying isotopes). The reconstructed distance between the two events in each BiPo-214 coincidence for runs 2056-2093 is shown in fig. 8.6. The data are fit with with the function

$$d(r) = A r^2 \exp(-r^2/2\sigma^2). \quad (8.5)$$

It represents the 3D distribution, centered on the origin, of events with independent gaussian distribution in each cartesian coordinate, transformed into spherical coordinates and integrated over the solid angle. The fit fails to reproduce the tail at large distances, which appears significantly higher than for a perfectly gaussian distribution.  $\sigma$  is a measure of the resolution of the detector, assumed gaussian and the same along each axis ( $\sigma$  that appears in equation 8.5 is  $\sqrt{2} \times$  the detector resolution,  $\sigma_{det}$ , since it originates from the difference of two independent gaussians with width  $\sigma_{det}$ ). The fact that the spatial resolution of the CTF detector is not perfectly gaussian is not yet completely understood.

## 8.4 Radium (Uranium) contamination

Information on the  $^{226}\text{Ra}$  (and  $^{238}\text{U}$ , if secular equilibrium is assumed) can be obtained from the radon data. Figure 8.3 shows the radon decay profile during most the CTF3 campaign (runs 2047-2300, from November 2001 to April 2003). A fit to the decay of the BiPo-214 count rate  $R$  in four phases of the run is performed with a decaying exponential with the radon mean life (5.52 days) plus a constant:

$$R(t) = R_0 e^{-t/\tau} + R_1, \quad \tau = 5.52 \text{ d}. \quad (8.6)$$

$R_1$  represents the residual BiPo-214 count rate which comes from the decay of radon decaying inside the scintillator at a constant rate. There are three mechanisms by which this can happen:

1.  $^{226}\text{Ra}$  (possibly in secular equilibrium with  $^{238}\text{U}$ ) in the scintillator that decays producing  $^{222}\text{Rn}$ ;
2.  $^{222}\text{Rn}$  produced by  $^{226}\text{Ra}$  (or  $^{238}\text{U}$ ) embedded in the nylon vessel and the other materials in contact with the scintillator;
3.  $^{222}\text{Rn}$  present in the water surrounding the vessel that permeates through the nylon membrane into the scintillator.

The four different radon decay fits to the data shown in fig. 8.3 are listed below. The results of the fit and the equivalent  $^{238}\text{U}$  and  $^{226}\text{Ra}$  contaminations are reported in table 8.3.

**Period a** - Initial scintillator batch before any purification. It includes the first  $^{14}\text{C}$  test (runs 2051-2073, from December 4 2001 to January 9 2002);

**Period b** - After the test of the silica gel column in loop mode (runs 2105-2120, from February 13 to March 17 2002);

**Period c** - After the first water extraction test (runs 2132-2149, from March 29 to April 24 2002);

**Period d** - After the test of the silica gel column in batch mode (runs 2188-2217, from June 20 to August 19 2002).

A first glance at the fits in fig. 8.3 shows that a constant plateau of constant BiPo-214 decays was reached only during period “d”. The constant fit parameter for the other three periods is then presumably affected by a bigger error than the purely statistical one. The factor of two decrease in equivalent  $^{238}\text{U}$  contamination after both silica gel purification tests (see table 8.3) should be taken with caution and might just be an artifact of the fit. The ultimate plateau of 1.5 BiPo-214 events/day in the entire CTF3 inner vessel corresponds

data set (runs)	CTF3 phase	$R_1$ (ev/day/IV)	$^{238}\text{U}$ ( $10^{-16}$ g/g)	$^{226}\text{Ra}$ ( $10^{-22}$ g/g)
a: 2051-2073	initial batch	$5.0 \pm 1.0$	$11.7 \pm 2.3$	$4.3 \pm 0.9$
b: 2105-2120	after silicagel loop test	$3.0 \pm 0.8$	$7.0 \pm 1.9$	$2.6 \pm 0.7$
c: 2132-2149	after first WE test	$2.8 \pm 0.7$	$6.6 \pm 1.6$	$2.4 \pm 0.6$
d: 2188-2217	after silicagel batch test	$1.5 \pm 0.3$	$3.5 \pm 0.7$	$1.3 \pm 0.3$

Table 8.3: The equivalent  $^{238}\text{U}$  and  $^{226}\text{Ra}$  contamination of the CTF3 scintillator deduced from the BiPo-214 delayed coincidences, once radon has decayed away. No radial cuts were applied selecting the events.  $R_1$  is the constant term from eq. 8.6. Secular equilibrium of the BiPo-214 events with  $^{238}\text{U}$  and  $^{226}\text{Ra}$  are assumed in computing the values in the last two columns. The amount of scintillator in the CTF3 inner vessel is 3.75 tons, and its density  $0.88 \text{ g/cm}^3$ . 1 decay/day/ton corresponds to  $8.8 \times 10^{-16} \text{ g}(^{238}\text{U})/\text{g}$  and  $3.2 \times 10^{-22} \text{ g}(^{226}\text{Ra})/\text{g}$  equivalent contamination.

to an equivalent  $^{238}\text{U}$  contamination of  $(3.5 \pm 0.7) \times 10^{-16} \text{ g/g}$ . For reference, the same  $^{238}\text{U}$  contamination would yield  $\sim 120$  counts/day from every isotope in the chain in the Borexino IV.

The increase in BiPo-214 counts observable after almost 400 days (fig. 8.3) is still not completely understood. There is speculation that this could possibly be related to shroud refilling operations using unstripped water taken from the CTF water tank.

It is interesting to recall the CTF1 results regarding radon permeating through the nylon vessel and emanating from the the nylon membrane itself into the scintillator. The estimated uranium equivalent amounts in the CTF scintillator from these sources are [79]:

$$\text{radon permeated (from water)} : \quad ^{238}\text{U}_{\text{perm}} = 3 \times 10^{-17} \text{ g/g}, \quad (8.7)$$

where  $^{238}\text{U}_{\text{perm}}$  is calculated assuming a radon concentration in the CTF3 water of 5 mBq/m<sup>3</sup> [184], and

$$\text{radon emanated (from nylon)} : \quad ^{238}\text{U}_{\text{eman}} = 8 \times 10^{-16} \text{ g/g} \quad (8.8)$$

where the assumed  $^{238}\text{U}$  content in the CTF3 nylon film was assumed to be 2 ppt by weight ( $2 \times 10^{-12}$  g/g).

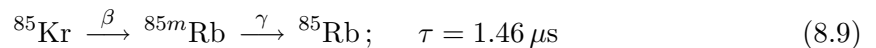
This last estimate assumes secular equilibrium between  $^{238}\text{U}$  and  $^{226}\text{Ra}$ , since it is based on the intrinsic uranium content of the nylon film. The BiPo-214 rate is in fact a measurement of the  $^{226}\text{Ra}$  content of the nylon membrane. A comparison with the CTF3 data (see table 8.3) keeping this in mind shows that radon emanation can completely account for the observed BiPo-214 event rate. Permeation of radon through the film seems to contribute for only a fraction of the signal at most.

## 8.5 Krypton contamination

Krypton is a noble gas and one of its radioactive isotopes,  $^{85}\text{Kr}$ , is present in the atmosphere mainly because of its release from nuclear reactors, nuclear fuel reprocessing plants and nuclear bomb testing. Its concentration has been increasing with time in the past decades and averages now around  $1 \text{ Bq/m}^3$ . Through contact with air, krypton is then present in all fluids used in Borexino, including the scintillator.

### 8.5.1 $^{85}\text{Kr}$ decay channels

$^{85}\text{Kr}$   $\beta$ -decays into  $^{85}\text{Rb}$  with a 99.56% branching ratio; the mean life of the decay is 15.52 years and the  $Q$ -value is 687 keV. Since the energy of the emitted electron is within the Borexino neutrino window (250-800 keV),  $^{85}\text{Kr}$  contamination represents an irreducible background for the experiment (i.e. indistinguishable from  $\nu - e$  scattering events).  $^{85}\text{Kr}$  also decays via the delayed coincidence reaction



with a 0.43% branching ratio. The  $\beta$  decay has a  $Q$ -value of 173 keV. The mean life of the  $^{85m}\text{Rb}$  metastable state is  $1.46 \mu\text{s}$  and the emitted de-excitation  $\gamma$  ray has an energy of 514 keV. By tagging the  $\beta - \gamma$  coincidence with appropriate time and energy cuts, it is possible to measure the  $^{85}\text{Kr}$  contamination of the CTF scintillator. For every identified coincidence

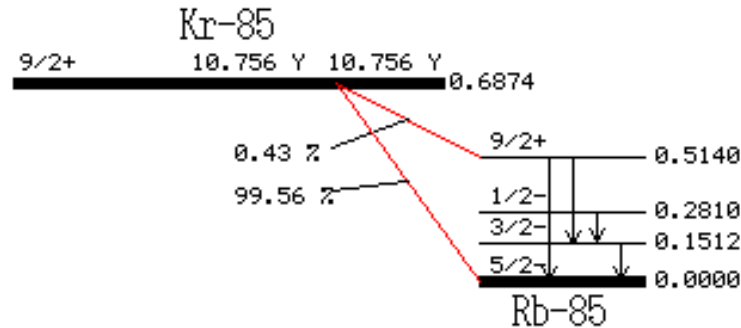


Figure 8.7: The  $^{85}\text{Kr} \rightarrow ^{85}\text{Rb}$  decay. The half-life is 10.76 years. The decay occurs mainly (99.56% branching ratio) via  $\beta$ -decay with a 687 keV  $Q$ -value. A delayed coincidence decay channel occurs with a 0.43% branching ratio and can be readily identified:  $^{85}\text{Kr}$   $\beta$ -decays into  $^{85m}\text{Rb}$  ( $Q$ -value = 173 keV), which de-excites with a 1.46  $\mu\text{s}$  mean life emitting a 514 keV  $\gamma$  ray [182].

event there will be another 231.5 krypton  $\beta$  decay events from the dominant decay channel.

The  $^{85}\text{Kr}$  decay channels are schematically shown in fig. 8.7.

### 8.5.2 $^{85}\text{Kr}$ event selection

The cuts used to select the krypton events and the corresponding efficiencies  $\epsilon_i$  are:

1. energy of the first event ( $\beta$ ):  $E_1 < 241 \text{ keV}$  ( $\epsilon_1 = 61\%$ )
2. energy of the second event ( $\gamma$ ):  $300 \text{ keV} < E_2 < 600 \text{ keV}$  ( $\epsilon_2 = 83\%$ )
3. delay time:  $100 \text{ ns} < t < 6 \mu\text{s}$  ( $\epsilon_3 = 93\%$ )
4. muon flag off

The total efficiency  $\epsilon = \epsilon_1 \epsilon_2 \epsilon_3$  of the cuts is 47%.

The efficiency  $\epsilon_1$  of the first event is limited by the trigger efficiency of the detector. For low energy events, it is possible that the amount of light released is not sufficient to produce a trigger (six simultaneous hit PMTs are needed). The effect of the trigger efficiency is illustrated in fig. 8.8.

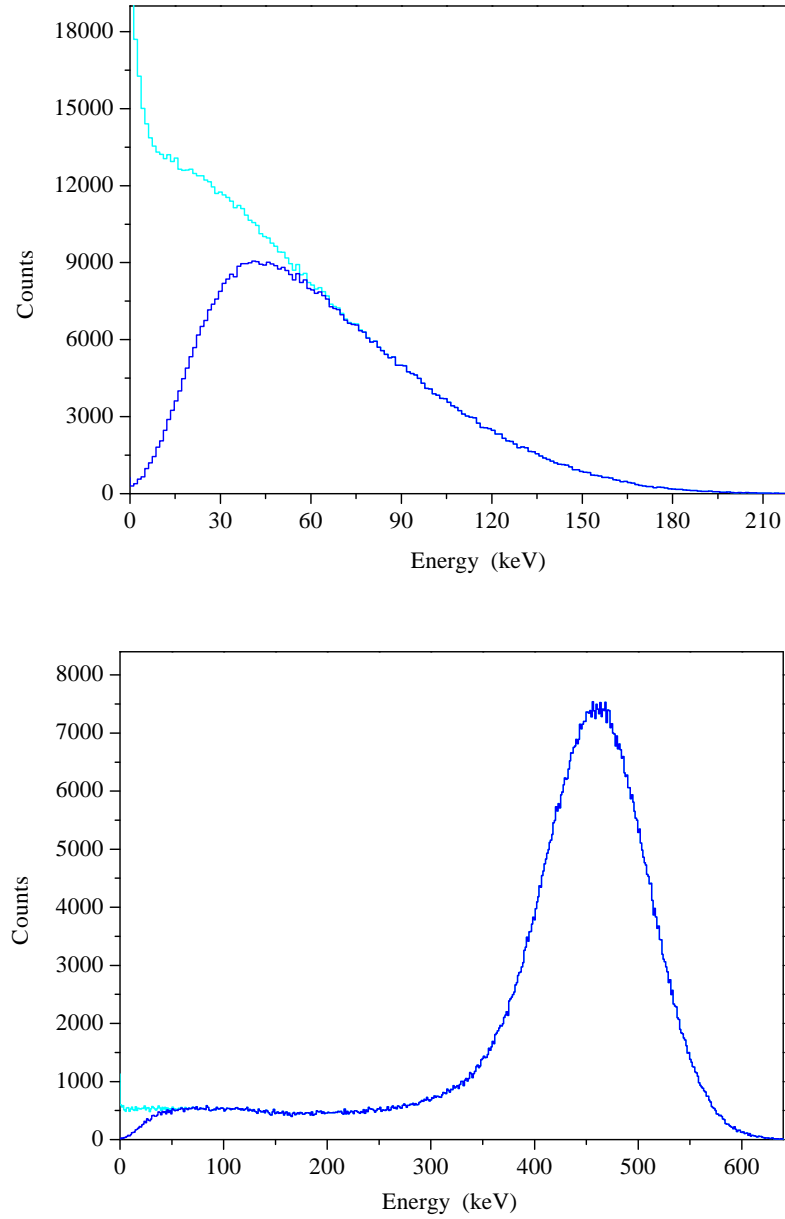


Figure 8.8: Simulated energy spectra of the  $\beta$  (top) and  $\gamma$  (bottom) particles emitted in the  $^{85}\text{Kr} \rightarrow ^{85m}\text{Rb} \rightarrow ^{85}\text{Rb}$  delayed coincidence decay as seen in CTF3 [185]. In each plot, the two lines refer to the reconstructed spectra with and without the trigger efficiency for low energy events taken into account. For the 173 keV  $\beta$  decay the difference is remarkable. The peak of the 514 keV  $\gamma$  ray is set at 459 keV by direct comparison with the data. The  $\sim 50$  keV shift of the  $\gamma$  peak is due to a quenching effect of very low energy (few tens of keV) electrons produced in the shower following  $\gamma$  interactions. Actual data samples of the same spectra are shown in fig. 8.10.

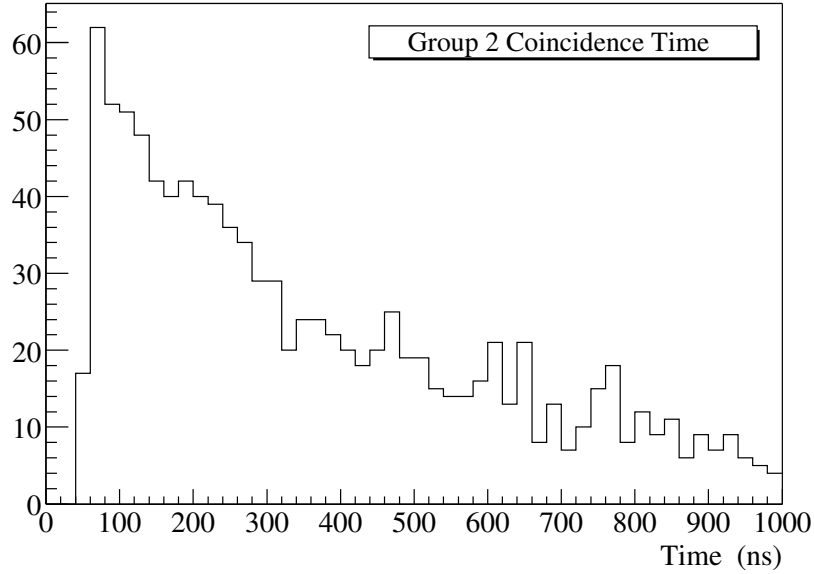


Figure 8.9: The time distribution of the coincidence time for all group 2 events from runs 2125-2300. Events with an associated muon flag were rejected. It can be noticed how the trigger is blind or inefficient below 60 ns, which justifies imposing a lower time cut of the coincidence delay time of 100 ns.

The definition of the cut on the energy of the second event would require the knowledge of the position of the 514 keV  $\gamma$  peak. Such peak is shifted from its nominal energy because of quenching due to very low energy (few tens of keV) electrons produced in the ionization shower following  $\gamma$  interactions. In the absence of a direct measurement of this quantity, the following recipe was followed. The shape of the reconstructed  $\gamma$  events was obtained simulating events using a “guessed” quenching factor. The position of the peak of the  $\gamma$  events was then measured from the data by selecting events with cuts #1 and #3 above, with relaxed constraints on  $E_2$ . The simulated spectrum was then scaled to best fit the position of the peak observed in the data. The data show that the peak shifts by  $\sim 10\%$ . Cut #2, centered on the  $\gamma$  peak, is wide enough to include most of the events while excluding low energy events for which the background from spurious coincidences is higher and the reconstruction of their spatial position loses reliability (see fig. 8.8).

The lower cut on the delay time is needed because of trigger inefficiencies for fast coincidence events. In fact, no coincidence faster than 50 ns is recorded and a loss of efficiency is observed for coincidence times up to approximately 75 ns, as shown in fig. 8.9.

Events associated with the passage of a muon, identifiable by the appropriate muon flag, are discarded. In order to reduce possible contaminations of the data sample coming from activity on the surface of the nylon vessel, from the surrounding water or from residual muons that don't trigger the muon flag, radial cuts are also implemented.

### Contamination of the data sample from radon events

An important quantity to compute is what leakage of BiPo-214 (radon) events to expect in the krypton data sample. Comparing the selection cuts applied for the two decays, one can evaluate their overlap as follows;

- i. approximately 2% of the  $^{214}\text{Bi}$  events are below 241 keV (cut applied for the krypton's first event);
- ii. the upper cut on the energy of the krypton's second event is about 2 standard deviations lower than the peak of the BiPo-214 second event, yielding an overlap of a few percent;
- iii. approximately 2.5% of the BiPo-214 events occur within the delay time window used for selecting krypton events.

The total overlap is on the order of  $10^{-5}$ . It represents a problem only if the radon contamination is very significant.

### 8.5.3 $^{85}\text{Kr}$ analysis method

The krypton contamination in CTF3 was measured in different periods listed in the following paragraph. The analysis method adopted uses a maximum likelihood technique (see the statistics section in [11]) as outlined in reference [186]. For every period the distribution of

the coincidence time  $t$  of the selected events was fitted with the function:

$$f(t; A, B) = \frac{A}{\tau} e^{-t/\tau} + B \quad (8.10)$$

The mean life  $\tau = 1.46 \mu\text{s}$  is that of the  $^{85\text{m}}\text{Rb}$  state,  $A$  is the initial number of  $^{85}\text{Kr}$  atoms that have decayed via the delayed coincidence, and  $B$  is a constant background.

Under the assumption that the entries in each time bin follow a Poisson distribution, the likelihood function to maximize is

$$\mathcal{L}(A, B; n) = \prod_{i=1}^n \frac{f_i^{y_i}}{y_i!} e^{-f_i} \quad (8.11)$$

where  $n$  is the number of bins,  $y_i$  the measured number of entries in the  $i$ -th bin and  $f_i = \int_{t_{i-1}}^{t_i} f dt$  the number of entries in the  $i$ -th bin expected by the fit model. In case of extremely low counting rates, it is possible to find a binning of the events such that the number of entries per bin is either zero or one ( $y_i = 0, 1$ ).

Alternatively, following reference [187], the likelihood function associated with observing  $n$  events at times  $t_i$  ( $i = 1, \dots, n$ ) within an observation time window  $t_a < t < t_b$  is

$$\mathcal{L}(A, B; n) = e^{-\int_{t_a}^{t_b} f dt} \prod_{i=1}^n f(t_i; A, B). \quad (8.12)$$

This approach has the advantage of being independent of binning. Equivalently and more conveniently, one can maximize the logarithm of the likelihood function:

$$\ln \mathcal{L}(A, B; n) = -\int_{t_a}^{t_b} f(t; A, B) dt + \sum_{i=1}^n \ln f(t_i; A, B) \quad (8.13)$$

The equations to solve are then

$$\frac{\partial(\ln \mathcal{L})}{\partial(A, B)} = 0 \quad (8.14)$$

The best fit value for  $A$ , divided by the efficiency of the selection cuts  $\epsilon$  and multiplied by 232.6 gives the number of  $^{85}\text{Kr} \rightarrow ^{85}\text{Rb}$   $\beta$  decays in the selected scintillator volume (defined by the radial selection cut  $r_{\text{cut}}$ ). 99.56% of these come from the dominant channel  $\beta$  decay. Whenever radial cuts were used, the number is scaled up to the whole IV volume to obtain the total krypton activity in the CTF. The best fit value for  $B$  is a measure of

the background events leaking into the krypton data sample (coming, for example, from subsequent single events that are recorded as group 2 events).

The errors and confidence levels for each fit parameter are computed following the standard recipe reported in ref. [11]. To evaluate the uncertainties of a fit parameter, the contour of the maximum of the (log)likelihood function is computed keeping the parameter in question fixed. Different confidence levels are defined around the maximum of such a contour as solutions of the following equation:

$$\ln\mathcal{L} = \ln\mathcal{L}_{max} - \frac{Q}{2} \quad (8.15)$$

where  $\mathcal{L}_{max}$  corresponds to the best fit.  $Q$  depends on the confidence level required and the number of fit parameters of the problem [188]. When a confidence level region falls inside an unphysical region (e.g. a negative background activity), an upper limit is given with a defined confidence level by integrating the (normalized) likelihood function in the physical region of existence.

The Smirnov-Cramèr-von Mises statistic  $nw^2$  goodness-of-fit (g.o.f.) test is finally performed [189]. With the likelihood function used in our analysis (no binning), it reduces to the form

$$nw^2 = \frac{1}{12n} + \sum_{i=1}^n \left[ \frac{1}{n} \int_{t_a}^{t_i} f dt - \frac{2i-1}{2n} \right]^2 \quad (8.16)$$

Appropriate tables [190] convert the value of  $nw^2$  into the corresponding significance of the fit. As for the familiar  $\chi^2$ , smaller values represent better fits.

Another independent method is used to evaluate the background. The number  $N_{\tilde{B}}$  of events selected using the energy cuts #1 and #2 listed in section 8.5.2 within the 6-100  $\mu$ s time window are counted. The number of events per  $\mu$ s  $\tilde{B} = N_{\tilde{B}}/94$  is then computed and compared with  $B$  for a cross check.

#### 8.5.4 Results

The krypton analysis was performed for three periods, corresponding to the following different testing phases, and the results are summarized in table 8.4:

	$t_{live}$ (d)	$r_{cut}$ (m)	$N_{sel}$	$N_{\tilde{B}}$	$A$ (ev)	$B$ (ev/ $\mu$ s)	g.o.f. ( $n\omega^2$ )	$\tilde{B}$ (ev/ $\mu$ s)	$^{85}\text{Kr}$ $\beta$ decays (ev/d/ton)
1	40.06	2	32	11	$30.8^{+7.8}_{-7.1}$	$< 1.38$	0.07	$0.12 \pm 0.04$	$103^{+26}_{-24}$
1	"	0.7	12	3	$11.1^{+5.0}_{-4.5}$	$< 0.94$	0.06	$0.03 \pm 0.02$	$108^{+49}_{-44}$
1	"	0.6	9	3	$6.1^{+4.6}_{-4.0}$	$0.58^{+0.72}_{-0.50}$	0.07	$0.03 \pm 0.02$	$95^{+71}_{-62}$
2	29.03	2	36	11	-	-	-	$0.12 \pm 0.04$	-
2	"	0.7	14	1	-	-	-	$0.01 \pm 0.01$	-
3	259.5	2	65	67	76.5	negative	3.8	$0.71 \pm 0.09$	-
3	"	0.7	6	12	$4.8^{+3.6}_{-3.0}$	$< 0.79$	0.03	$0.13 \pm 0.04$	$7.2^{+5.4}_{-4.5}$
3	"	0.6	5	6	$< 5.4$	$0.41^{+0.62}_{-0.37}$	0.06	$0.07 \pm 0.03$	$< 12.9$

Table 8.4: Krypton contamination in CTF3. All uncertainties are reported at  $1\sigma$  and the upper limits are at 68% C.L. The missing values correspond to data sets for which the fitting routine would not converge or for which the extrapolated values would not be meaningful. Errors have been neglected whenever the quality of the fit was bad. The details of the analysis and the results are discussed in the text.

**Period 1** - Initial scintillator batch before any purification. It includes the first  $^{14}\text{C}$  test (runs 2056-2093, from December 10 2001 to February 6 2002).

**Period 2** - After the test of the silica gel column in loop mode, but before the water extraction test (runs 2094-2122, from February 6 to March 20 2002).

**Period 3** - After the water extraction + nitrogen stripping test (runs 2125-2300, from March 23 2002 to April 17 2003).

The  $^{85}\text{Kr}$  content in the initial scintillator batch (period 1) gives  $\sim 100$   $\beta$  decays per day per ton (equivalent to one  $\beta - \gamma$  coincidence/ton every 2 days); this value, although measured with a non-negligible statistical error, seems independent of the applied radial cut. This activity scaled to the whole CTF inner vessel corresponds to the activity of 5 liters of air ( $\sim 1$  Bq/m<sup>3</sup>). Figure 8.10 shows the energies of the  $\beta$  and  $\gamma$  selected events, with no applied radial cuts. The shapes of these spectra are in good agreement with the simulated ones

(fig. 8.8). Fig. 8.11 shows the coincidence time distribution (simple and cumulative) for the same dataset. The best fit is superimposed to the the cumulative plot.

In the data following the loop purification with the silica gel column (period 2), a reasonable fit with a decaying exponential with the  $^{85}\text{Kr}$  mean life and a constant background is not possible. Applying a radial cut to the data does not improve the fit. A contamination of the data set from mass 212  $\beta - \alpha$  coincidence events in the  $^{232}\text{Th}$  chain explains the phenomenon, as clarified below.

The data from the period after the water extraction + nitrogen stripping purification in loop mode (period 3) show a significant decrease in krypton activity. Most likely, this is due to the nitrogen stripping step. No acceptable fit was obtained when no radial cut was applied. From the best fits obtained when a radial cut ( $r_{cut} = 0.6$  and  $0.7$  m) is imposed it is impossible to discriminate whether there is a non-zero  $^{85}\text{Kr}$  signal or not. It is possible to state that the nitrogen stripping has been very effective in eliminating krypton. What is certain is that nitrogen stripping can eliminate krypton in the scintillator only as much as the purity of the nitrogen used allows. If krypton is present in the nitrogen, it will partition with the fluids with which it interacts, possibly until equilibrium is reached. An estimate of the amount of krypton to be expected in CTF from the krypton contamination of the nitrogen employed in stripping is given in the next section.

### 8.5.5 Possible krypton contamination paths

Krypton can reach the CTF3 scintillator in a variety of ways. On one hand, some was presumably present in the pseudocumene as delivered. On the other hand, krypton could be transferred to the PC from all the fluids it comes in contact with during purification, handling, and inside the CTF. The following paths for krypton are analysed:

- a. krypton present in the nitrogen is transferred to the scintillator during stripping operations;
- b. krypton present in the water of CTF3 diffuses through the nylon vessel membrane into the scintillator;

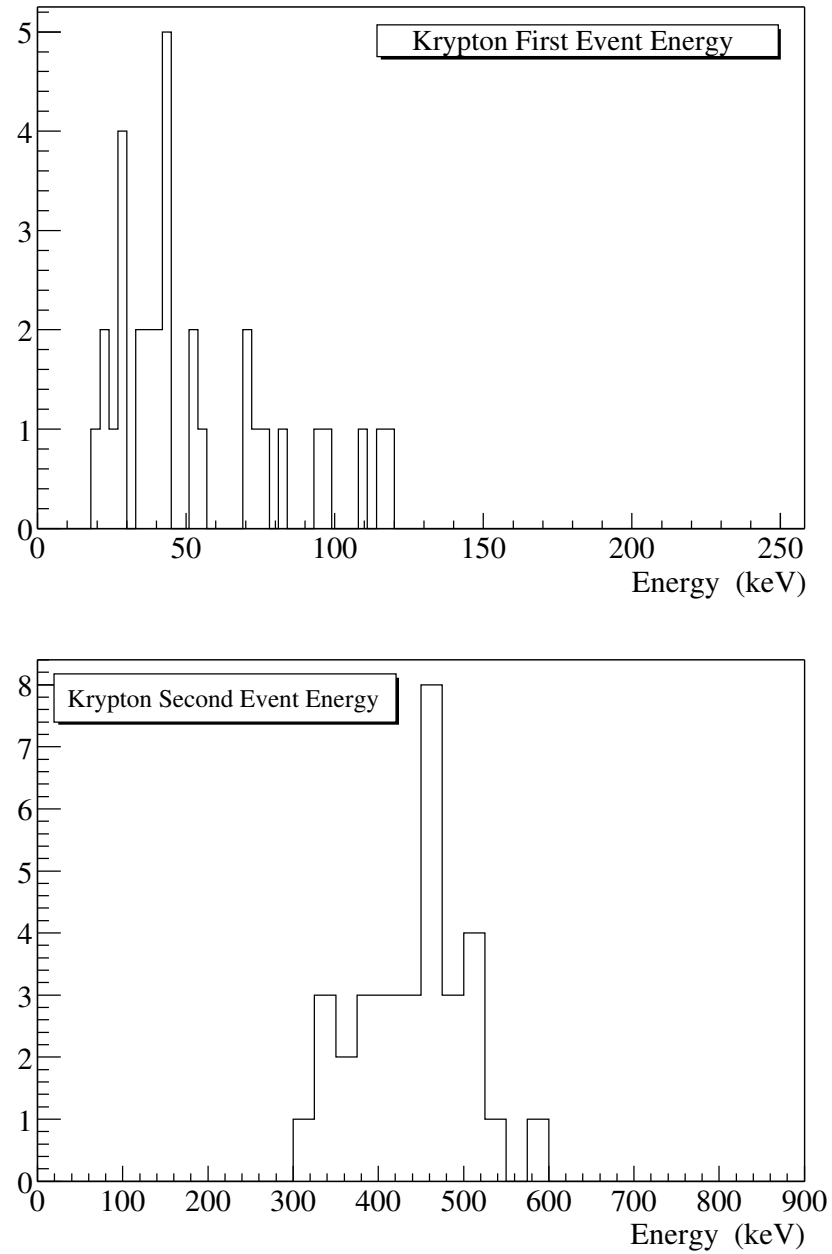


Figure 8.10: Energy spectra of the  $\beta$  (top) and  $\gamma$  (bottom) krypton selected events for the first, unpurified scintillator batch (period 1, runs 2056-2093). Their shape are in good agreement with the simulated ones (fig. 8.8). No radial cut was applied for selecting the events.

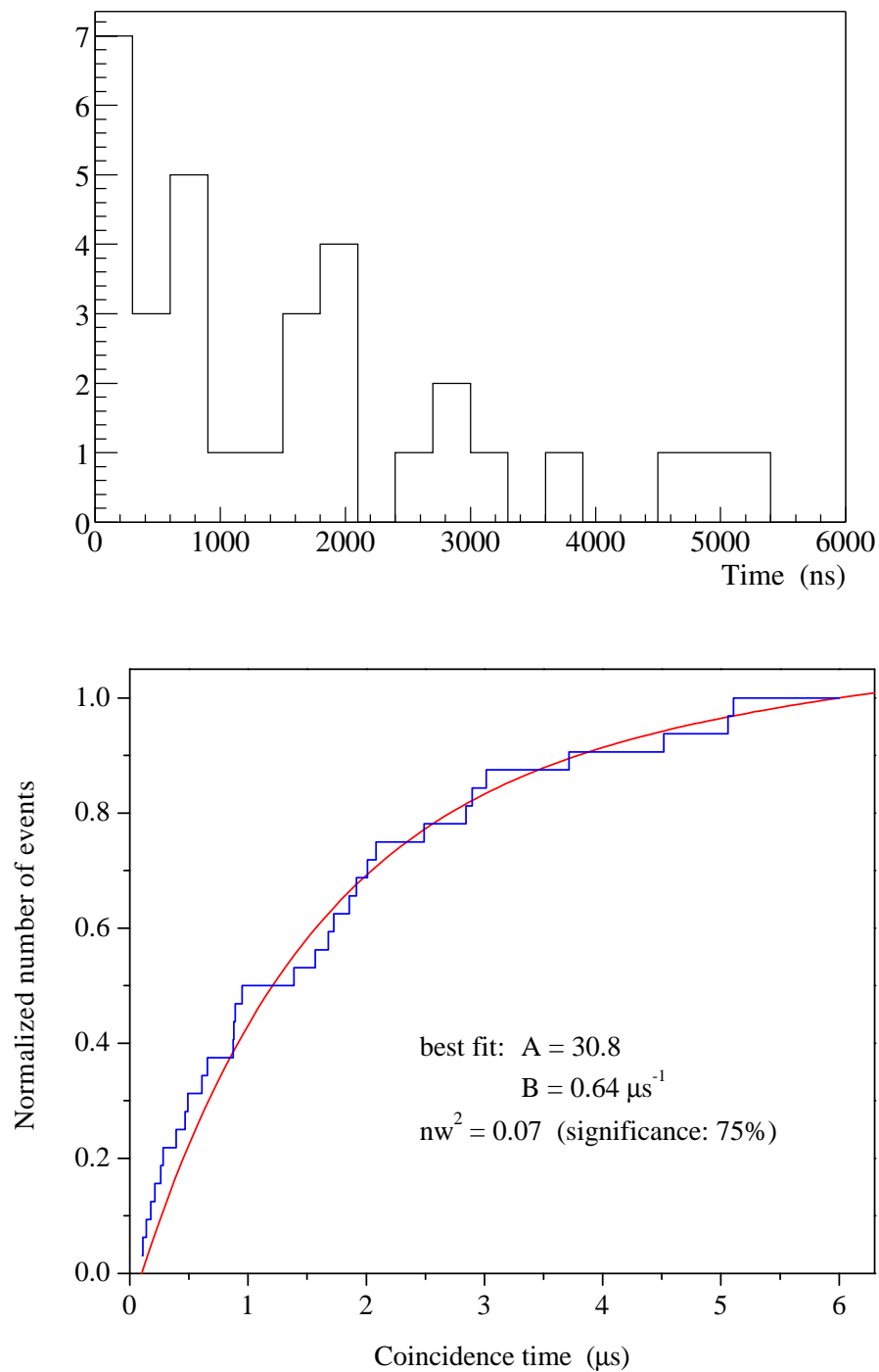


Figure 8.11: The simple (top) and cumulative (bottom) time distribution of the selected krypton events for the first, unpurified scintillator batch (period 1, runs 2056-2093). The best fit curve is superimposed to the cumulative plot, with which it shows very good agreement. No radial cut was applied for selecting the events.

temperature (K)	benzene ( $\times 10^{-4}$ )	toluene ( $\times 10^{-4}$ )	water ( $\times 10^{-5}$ )
273	-	-	4.28 (Ar)
	-	-	8.84 (Kr)
283	8.53 (Ar)	10.85 (Ar)	-
288	28.1 (Kr)	35.0 (Kr)	-
300	8.84 (Ar)	10.98 (Ar)	2.44 (Ar)
	27.2 (Kr)	33.3 (Kr)	4.24 (Kr)
318	9.17 (Ar)	11.26 (Ar)	-
	26.1 (Kr)	-	-
328	-	29.1 (Kr)	-
348	-	-	1.56 (Ar)
353	-	-	2.35 (Kr)

Table 8.5: Values for argon and krypton solubilities in aromatics and water [191]. All units are mol/mol. Note the high solubility of Ar and Kr in aromatics compared to water ( $\sim 100$  times higher).

- c. krypton present in the water at the time of the CTF3 water filling transfers to the scintillator during the volumetric exchange of the fluids.

Values for the solubilities of krypton in PC and water are needed for estimating the krypton partition between gas (nitrogen) and liquid (PC, water) phases. Table 8.5 reports values for krypton solubilities in benzene, toluene and water [191]. No specific data for pseudocumene were found. Note the high solubility of Ar and Kr in aromatics compared to water ( $\sim 100$  times higher).

From the solubility values one can compute the partition fraction of krypton in benzene, toluene and water at atmospheric pressure and 288 K. There are  $4.3 \times 10^{-5}$  mol/ml in an ideal gas at 288 K and 1 atm. The molecular weights of benzene, toluene and water are 78, 92, and 18 and their densities are 0.877, 0.866, and 1 g/ml respectively. Hence there are  $1.1 \times 10^{-2}$  mol/ml in benzene,  $9.4 \times 10^{-3}$  mol/ml in toluene, and  $5.6 \times 10^{-2}$  mol/ml in water

at 288 K. In the (realistic) approximation of an infinitely large gas supply in contact with a finite liquid phase, the liquid-to-gas partition fractions for krypton in benzene, toluene and water at 288 K are then as follows:

$$\begin{aligned} R_{\text{benzene}/\text{N}_2} &= 0.73 \\ R_{\text{toluene}/\text{N}_2} &= 0.77 \\ R_{\text{H}_2\text{O}/\text{N}_2} &= 0.065 \end{aligned} \quad (8.17)$$

The values for benzene and toluene are essentially the same. In the following, their average will be assumed for the pseudocumene/Kr liquid-to-gas partition at 1 atm and 288 K, yielding

$$R_{\text{PC}/\text{N}_2} = 0.75 \quad (8.18)$$

The water/PC partition fraction is

$$R_{\text{H}_2\text{O}/\text{PC}} = \frac{R_{\text{H}_2\text{O}/\text{N}_2}}{R_{\text{PC}/\text{N}_2}} = 0.087 \quad (8.19)$$

#### **Path a: N<sub>2</sub> → PC**

In this case, equilibrium is assumed between the nitrogen and the PC during stripping. This is a good assumption whenever the PC volume of the IV is circulated many times.

The <sup>85</sup>Kr content in the nitrogen used for stripping the CTF3 scintillator is  $A_{\text{N}_2} \sim 40 \mu\text{Bq}/\text{m}^3$  [192]. It is not possible to give a definitive value for the variability of this number for different nitrogen deliveries, although the few measurements performed showed fluctuations on the order of  $10 \mu\text{Bq}/\text{m}^3$ . The <sup>85</sup>Kr content in the CTF3 scintillator is then

$$A_{\text{PC}, \text{a}} = A_{\text{N}_2} R_{\text{PC}/\text{N}_2} \sim 30 \frac{\mu\text{Bq}}{\text{m}^3} = 2.6 \frac{\text{decays}}{\text{m}^3 \text{d}} \sim 11 \frac{\text{decays (IV)}}{\text{d}} \quad (8.20)$$

where the volume of the CTF3 inner vessel (IV) was assumed to be  $4.3 \text{ m}^3$ . This activity is consistent with the <sup>85</sup>Kr activity measured in CTF3 (compare with table 8.4).

#### **Path b: H<sub>2</sub>O → PC (gas, through vessel)**

Another possible contamination path is krypton diffusion from the water to the scintillator

through the nylon vessel film. The  $^{85}\text{Kr}$  activity in the water is that obtained assuming its equilibrium with nitrogen with which it is stripped, namely

$$A_{\text{H}_2\text{O}} = A_{\text{N}_2} R_{\text{H}_2\text{O}/\text{N}_2} \sim 2.6 \frac{\mu\text{Bq}}{\text{m}^3} \quad (8.21)$$

This activity corresponds to a  $^{85}\text{Kr}$  concentration  $\rho_{\text{Kr}85} \sim 1275 \text{ atoms/m}^3$  in the CTF water, where the  $^{85}\text{Kr}$  mean life (15.5 years) has been used (for  $^{85}\text{Kr}$ ,  $1 \text{ Bq} \leftrightarrow 5 \times 10^8 \text{ atoms}$ ). The activity that will enter the CTF scintillator is governed by the diffusion constant  $D_{\text{Kr}}$  for krypton through the nylon membrane. In the absence of a measurement of  $D_{\text{Kr}}$ , a good estimate is obtained by scaling the diffusion constant for radon  $D_{\text{Rn}}$  with the square root of the ratios of the radon and krypton atomic masses,  $(M_{\text{Rn}}/M_{\text{Kr}})^{1/2}$ . The diffusion coefficient for Rn through nylon was measured in CTF1 [79, 76],

$$D_{\text{Rn}} = 6.5 \times 10^{-10} \text{ cm}^2/\text{s}. \quad (8.22)$$

The expected value for krypton in the same condition (i.e. same nylon and humidity conditions) is

$$D_{\text{Kr}} = \left( \frac{M_{\text{Rn}}}{M_{\text{Kr}}} \right)^{1/2} D_{\text{Rn}} \sim 10^{-9} \text{ cm}^2/\text{s}. \quad (8.23)$$

The rate  $\phi_{\text{Kr}85}$  at which krypton atoms diffuse into the CTF scintillator is

$$\phi_{\text{Kr}85} = \frac{S D_{\text{Kr}}}{d} \rho_{\text{Kr}85} \sim 3 \times 10^{-6} \text{ atoms/s} \sim 100 \text{ atoms/y}, \quad (8.24)$$

where  $S$  is the vessel surface ( $12.5 \text{ m}^2$ ) and  $d$  its thickness (0.5 mm). Using the equivalence mentioned above, the rate  $R_{\text{PC}, \text{b}}$  at which the  $^{85}\text{Kr}$  activity increases in the CTF scintillator by diffusion through the vessel is

$$R_{\text{PC}, \text{b}} = 0.2 \frac{\mu\text{Bq}}{\text{y}} \quad (8.25)$$

and the activity accumulated during the CTF3 lifetime is thus negligible compared with  $A_{\text{PC}, \text{a}}$ .

### Path c: $\text{H}_2\text{O} \rightarrow \text{PC}$ (filling)

The amount of krypton transferred from the water to the PC during scintillator filling

of the detectors generally depends on the time during which such operation takes place (transfer time). The most conservative scenario is to assume equilibrium between water and PC. The krypton activity in the PC in this case is:

$$A_{\text{PC,d}} = \frac{A_{\text{H}_2\text{O}}}{R_{\text{H}_2\text{O}/\text{PC}}} = A_{\text{N}_2} R_{\text{PC}/\text{N}_2} \equiv A_{\text{PC,a}} \quad (8.26)$$

where eqns. (8.21) and (8.19) have been used

From eq. 8.20 one would expect  $\sim 3 \frac{\text{decays}}{\text{m}^3 \text{d}} \sim 11 \frac{\text{decays(IV)}}{\text{d}}$  once equilibrium is reached between PC and nitrogen. This number is compatible with the CTF data after nitrogen stripping reported in table 8.4. Since from the data it is impossible to determine with sufficient accuracy whether there is a residual krypton signal or not (after almost one year of data taking), it is clear that CTF is not sensitive enough to measure a potentially cleaner nitrogen used for stripping the scintillator. In particular, CTF will not be able to directly characterize the krypton content in the scintillator at the levels required by Borexino ( $\sim 0.2$  ppt [193]). According to the measurements performed on the nitrogen we currently employ, we need a further reduction of 2 to 3 orders of magnitude for Borexino. Our Heidelberg colleagues are currently trying to address the problem by seeking nitrogen supplies with a lower krypton content and by developing adsorption techniques for reducing the krypton content in nitrogen to the required level.

### 8.5.6 Spurious krypton activity from surface contamination

The cumulative time distribution of the events after nitrogen stripping of the scintillator selected using the krypton cuts (section 8.5.2) with no imposed radial cut is shown in fig. 8.12. The plot highlights how the fit with the  $^{85\text{m}}\text{Rb}$  lifetime is very poor; the events seem to follow a much faster decay time. A fit carried out with the lifetime as a free parameter gives a best fit value of 387 ns ( $nw^2 = 0.05$ , significance = 88%). This observation led to the search for a possible contamination of the krypton data sample by mass 212  $\beta - \alpha$  delayed coincidence events, with a 431 ns lifetime (see the  $^{232}\text{Th}$  radioactive decay chain in fig. 4.1). A first confirmation of this is that a fit performed allowing both krypton and mass 212 delayed coincidences prefers a negative krypton contribution but a statistically

significant positive mass 212 contribution. The significance of the fit to the data with mass 212 coincidence events only (i.e.  $\tau = 431$  ns) is 54% ( $nw^2 = 0.11$ ). The analysis of the coincidence time alone would not be enough to unmistakably prove a  $^{232}\text{Th}$  surface contamination, but it represents a very convincing indication for such possibility.

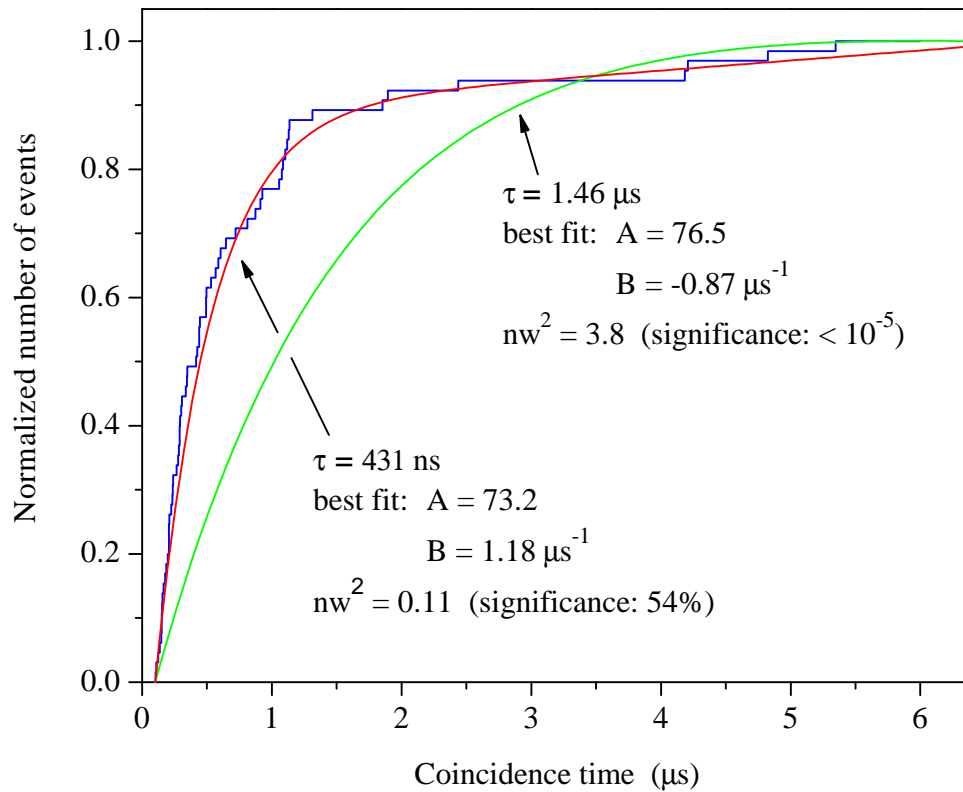


Figure 8.12: Cumulative time distribution of events following nitrogen stripping (runs 2125-2300) selected using the krypton cuts (listed in section 8.5.2) with no radial cut. The dataset clearly does not represent  $^{85}\text{Kr}$  contamination. A fit with mass 212 delayed coincidences ( $\tau = 431 \text{ ns}$ ) fits reasonably well. If the coincidence lifetime is left as a free parameter the fit gives a preferred value of 387 ns.

# Bibliography

- [1] W. Kandinski, “Concerning the Spiritual in Art”, Dover Publications, Inc., New York, translation by M. Sadler, 1977.
- [2] G. Gamow, “Thirty Years that Shook Physics”, Anchor Books Doubleday & Company, Inc., Science Study Series, 1966.
- [3] The Super-Kamiokande Collaboration, Y. Fukuda et al., “Evidence for Oscillation of Atmospheric Neutrinos”, *Phys. Rev. Lett.*, **87**, 1562 (1998).
- [4] The SNO Collaboration, Q. R. Ahmad et al., “Measurement of the Rate of  $\nu_e + d \rightarrow p + p + e^-$  Interactions Produced by  $^8\text{B}$  Solar Neutrinos at the Sudbury Neutrino Observatory”, *Phys. Rev. Lett.*, **87**, 071301 (2001).
- [5] The SNO Collaboration, Q. R. Ahmad et al., “Direct Evidence for Neutrino Flavor Transformation from Neutral-Current Interactions in the Sudbury Neutrino Observatory”, *Phys. Rev. Lett.*, **89**, 011301 (2002).
- [6] W. Pauli, Address to Group on Radioactivity (Tübingen, December 4, 1930) (unpublished).
- [7] J. N. Bahcall, “Solar Neutrinos. I. Theoretical”, *Phys. Rev. Lett.*, **12**, 300 (1964).  
R. Davis Jr., “Solar Neutrinos. II. Experimental”, *Phys. Rev. Lett.*, **12**, 303 (1964).  
R. Davis Jr. et al., “Search for Neutrinos from the Sun”, *Phys. Rev. Lett.*, **20**, 1205 (1968).
- [8] E. Fermi, *Z. Physik*, **88**, 161 (1934).

- [9] F. Reines and C.L. Cowan Jr. “A Proposed Experiment to Detect the Free Neutrino”. *Phys. Rev.*, **90**, 492 (1953).  
C.L. Cowan Jr., F. Reines, F.B. Harrison, H.W. Kruse, and A.D. McGuire. “Detection of the Free Neutrino: A Confirmation”, *Science*, **124**, 103 (1956).
- [10] F. Reines, “The neutrino: from poltergeist to particle”, *Rev. Mod. Phys.*, **68**, 317 (1996).
- [11] K. Hagiwara et al., “Review of Particle Physics”, *Phys. Rev. D* **66**, 010001 (2002).
- [12] B. Pontecorvo, *Sov. Phys. JETP*, **6**, 429 (1958).
- [13] Z. Maki, et al., *Prog. Theor. Phys.*, **28**, 870 (1962).
- [14] B. Pontecorvo, “Neutrino Experiments and the Question of Leptonic-Charge Conservation” *Zh. Eksp. Teor. Fiz.*, **53**, 1717 (1967) [*Sov. Phys. JETP*, **26**, 984 (1968)].
- [15] L. Wolfenstein, “Neutrino Oscillations in Matter”, *Phys. Rev. D* **17**, 2369 (1978).
- [16] S. Mikeyev and A. Smirnov, “Resonance Enhancement of Oscillations in Matter and Solar Neutrino Spectroscopy”, *Sov. J. Nucl. Phys.* **42**, 913 (1985) [*Yad. Fiz.* **42**, 1441 (1985)].
- [17] W. M. Alberico and S. M. Bilenky, “Neutrino Oscillations, Masses and Mixing”, *preprint*, hep-ph/0306239.
- [18] C. Giunti and C. W. Kim, “Quantum Mechanics of Neutrino Oscillations”, *Found. Phys. Lett.* **14**(3), 213 (2001).
- [19] P. Langacker, J. P. Leveille, and J. Sheiman, “On the detection of cosmological neutrinos by coherent scattering”, *Phys. Rev. D*, **27**, 1228 (1983).
- [20] H. A. Bethe, “Energy Production in Stars”, *Phys. Rev.*, **55**, 434 (1939).
- [21] J. N. Bahcall, “How the Sun Shines”, Nobel e-Museum, June 2000, <http://www.nobel.se/physics/articles/>, *preprint*, astro-ph/0009259.

- J. N. Bahcall, “Solar Models: An Historical Overview”, talk given at the Neutrino 2002 conference, München (Germany), May 2002, *preprint*, astro-ph/0209080, to be published in *Nucl. Phys. B (Proc. Suppl.)*.
- [22] J. N. Bahcall, M. H. Pinsonneault, and S. Basu, “Solar Model: Current Epochs and Time Dependencies, Neutrinos, and Helioseismological Properties”, *Astrophys. J.*, **555**, 990 (2001).
- [23] J. N. Bahcall, M. C. Gonzalez-Garcia, and C. Peña-Garay, “Does the Sun Shine by pp or CNO Fusion Reactions?”, *Phys. Rev. Lett.*, **90**, 131301 (2003).
- [24] J. N. Bahcall, S. Basu, and M. H. Pinsonneault, “How uncertain are solar neutrino predictions?”, *Phys. Lett. B*, **433**, 1 (1998).
- [25] B. T. Cleveland et al., “Measurement of the Solar Electron Neutrino Flux with the Homestake Chlorine Experiment”, *Astrophys. J.*, **496**, 505 (1998).
- [26] J. N. Bahcall and H. A. Bethe, “A Solution to the Solar Neutrino Problem”, *Phys. Rev. Lett.*, **65**, 2233 (1990).
- [27] The Kamiokande Collaboration, H. Hirata et al., “Observation of  $^8\text{B}$  Solar Neutrinos in the Kamiokande-II Detector”, *Phys. Rev. Lett.*, **63**, 16 (1989).
- [28] The Kamiokande Collaboration, Y. Fukuda et al., “Solar Neutrino Data Covering Solar Cycle 22”, *Phys. Rev. Lett.*, **77**, 1683 (1996).
- [29] The Super-Kamiokande Collaboration, Y. Fukuda et al., “Solar  $^8\text{B}$  and *hep* Neutrino Measurements from 1258 Days of Super-Kamiokande Data”, *Phys. Rev. Lett.*, **86**, 5651 (2001).
- [30] The GALLEX Collaboration, W. Hampel et al., “GALLEX solar neutrino observations: results from GALLEX IV”, *Phys. Lett. B*, **447**, 127 (1999).
- T. Kirsten, for the GNO collaboration, talk given at the Neutrino 2002 conference, München (Germany) May 2002, to be published on *Nucl. Phys. B (Proc. Suppl.)*.

- [31] The SAGE Collaboration, J. N. Abdurashitov et al., “Measurement of the Solar Neutrino Capture Rate by the Russian-American Solar Neutrino Experiment during One Half of the 22-Year Cycle of Solar Activity”, *J. Exp. Theor. Phys.*, **95**, 181 (2002).
- [32] The CHORUS Collaboration, N. Armenise et al., “A New Search for  $\nu_\mu \rightarrow \nu_\tau$  Oscillations”, CERN-SPSC/90-42 SPSC P254, Dec. 1990.  
The NOMAD Collaboration, P. Astier et al., “Proposal: Search for the Oscillation  $\nu_\mu \rightarrow \nu_\tau$ ”, CERN-SPSC/91-21 SPSC P261, Mar. 1991.
- [33] J. N. Bahcall’s web site, <http://www.sns.ias.edu/~jnb>
- [34] The SNO Collaboration, Q. R. Ahmad et al., “Measurement of Day and Night Neutrino Energy Spectra at SNO and Constraints on Neutrino Mixing Parameters”, *Phys. Rev. Lett.*, **89**, 011302 (2002).
- [35] J. N. Bahcall, M. C. Gonzalez-Garcia, and C. Peña-Garay, “Before and After: How has the SNO neutral current measurement changed things?”, *JHEP*, **07**, 054 (2002).
- [36] G. L. Fogli, E. Lisi, D. Montanino, and A. Palazzo, “Model-dependent and -independent implications of the first Sudbury Neutrino Observatory results”, *Phys. Rev. D*, **64**, 093007 (2001).
- [37] J. N. Bahcall, M. C. Gonzalez-Garcia, and C. Peña-Garay, “Global Analysis of Solar Neutrino Oscillations Including SNO CC Measurement”, *JHEP*, **08**, 014 (2001).
- [38] The KamLAND Collaboration, K. Eguchi et al., “First Results from KamLAND: Evidence for Reactor Antineutrino Disappearance”, *Phys. Rev. Lett.*, **90**, 021802 (2003).
- [39] J. N. Bahcall, D. Barger, and D. Marfatia, “How accurately can one test CPT conservation with reactor and solar neutrino experiments?”, *Phys. Lett. B*, **534**, 120 (2002).

- [40] J. N. Bahcall, M. C. Gonzalez-Garcia, and C. Peña-Garay, “Solar neutrinos before and after KamLAND”, *JHEP*, **02**, 009 (2003).
- [41] The K2K Collaboration, M. H. Ahn et al., “Indications of Neutrino Oscillation in a 250 km Long-Baseline Experiment”, *Phys. Rev. Lett.*, **90**, 041801 (2003).
- [42] G. L. Fogli, E. Lisi, A. Marrone, and D. Montanino, “Status of atmospheric  $\nu_\mu \rightarrow \nu_\tau$  oscillations and decoherence after the first K2K spectral data”, *preprint*, hep-ph/0303064.
- [43] The Super-Kamiokande Collaboration, S. Fukuda et al., “Tau Neutrino Favored over Sterile Neutrinos in Atmospheric Muon Neutrino Oscillations”, *Phys. Rev. Lett.*, **85**, 3999 (2000).
- [44] The LSND Collaboration, L. Athanassopoulos et al., “Evidence for  $\bar{\nu}_\mu \rightarrow \bar{\nu}_e$  Oscillations from the LSND Experiment at the Los Alamos Meson Physics Facility”, *Phys. Rev. Lett.*, **77**, 3082 (1996).
- The LSND Collaboration, A. Aguilar et al., “Evidence for neutrino oscillations from the observation of  $\bar{\nu}_e$  appearance in a  $\bar{\nu}_\mu$  beam”, *Phys. Rev. D*, **64**, 112007 (2001).
- [45] The KARMEN Collaboration, B. Armbruster et al., “Upper limits for neutrino oscillations  $\bar{\nu}_e \rightarrow \bar{\nu}_\mu$  from muon decay at rest”, *Phys. Rev. D*, **65**, 112001 (2002).
- [46] E. D. Zimmerman for the The MiniBooNE Collaboration, “BooNE Has Begun”, *preprint*, hep-ex/0211039.
- [47] F. Boehm and P. Vogel, “Physics of Massive Neutrinos”, Cambridge University Press, 2nd edition, 1992.
- [48] C. L. Bennett et al., “First Year Wilkinson Microwave Anisotropy Probe (WMAP) Observations: Preliminary Maps and Basic Results”, *preprint*, astro-ph/0302207 (Accepted by *Astroph. J.*).

- [49] Ø. Elgarøy et al., “New Upper Limit on the Total Neutrino Mass from the 2 Degree Field Galaxy Redshift Survey”, *Phys. Rev. Lett.*, **89**, 061301 (2002).
- T. J. Pearson et al., “The Anisotropy of the Microwave Background to  $l=3500$ : Mosaic Observations with the Cosmic Background Imager”, *Astrophys. J.*, **591**, 556 (2003).
- C. L. Kuo et al., “High Resolution Observations of the CMB Power Spectrum with ACBAR”, *preprint*, astro-ph/0212289, to appear in *Astrophys. J.*
- [50] G. Bhattacharyya et al., “Particle Physics Implications of the WMAP Neutrino Mass Bound”, *preprint*, hep-ph/0302191.
- [51] S. Bilenky, C. Giunti, J. Grifols, and E. Massó, “Absolute values of neutrino masses: status and prospects”, *Phys. Rep.*, **379**, 69 (2003).
- [52] J. N. Bahcall, “Why do solar neutrino experiments below 1 MeV?”, *Low Energy Solar Neutrino Detection*, Proceedings of the 2nd International Workshop on Low Energy Solar Neutrinos, Y. Suzuki, N. Nakahata and S. Moriyama eds., (World Scientific 2002).
- [53] J. N. Bahcall and C. Peña-Garay, “A road map to solar neutrino fluxes, neutrino oscillation parameters, and tests for new physics”, *preprint*, hep-ph/0305159.
- [54] The Borexino Collaboration, C. Arpesella et al., “Borexino at Gran Sasso: proposal for a real time detector for low energy solar neutrinos”, volumes 1-2, G. Bellini, R. S. Raghavan, et al. editors (INFN Milano), 1991.
- [55] The Borexino Collaboration, G. Alimonti et al., “Science and technology of Borexino: a real-time detector for low energy solar neutrinos”, *Astrop. Phys.*, **16**(3), 205 (2002).
- [56] L. Cadonati, F. P. Calaprice, and M. C. Chen, “Supernova neutrino detection in Borexino”, *Astrop. Phys.*, **16**(4), 361 (2002).
- [57] Rothschild, M. C. Chen, and F. P. Calaprice, “Antineutrino Geophysics with liquid scintillator detector”, *Geophys. Res. Lett.*, **25**(7), 1083 (1998).

- [58] S. Schönert, “Solar- and reactor neutrinos: Upcoming experiments and future projects”, *Nucl. Phys. B - Proc. Suppl.*, **110**, 277 (2002).
- [59] A. Ianni and D. Montanino, “The  $^{51}\text{Cr}$  and  $^{90}\text{Sr}$  sources in BOREXINO as tools for neutrino magnetic moment searches”, *Astrop. Phys.*, **10**(4), 331 (1999).
- [60] L. B. Okun, “Leptons and Quarks”, North Holland, Amsterdam, 1982.
- [61] J. Benziger, F. P. Calaprice et al. editors, “A Proposal for Participation in the Borexino Solar Neutrino Experiment”, Princeton University, 1996.
- [62] M. Aglietta et al., *JETP Lett.*, **63**, 791 (1996).
- [63] M. Fukugita, Y. Kohyama, and K. Kubodera, “Neutrino reaction cross sections on  $^{12}\text{C}$  target”, *Phys. Lett. B*, **212**(2), 139 (1988).
- [64] A. Ianni, “Studio di proprietà non convenzionali per il neutrino mediante sorgenti artificiali di alta intensità in BOREXINO”, Ph.D. Thesis (in Italian), Università degli Studi di L’Aquila, 1998.
- [65] The Borexino Collaboration, G. Alimonti et al., “Light propagation in a large volume liquid scintillator”, *Nucl. Instr. Meth. A*, **440**, 360 (2000).
- [66] Plot generated by Fausto Masetti.
- [67] M. Chen et al., “Quenching of undesired fluorescence in a liquid scintillator particle detector”, *Nucl. Instr. Meth. A*, **420**, 189 (1999).
- [68] T. Hagner et al., “Muon-induced production of radioactive isotopes in scintillation detectors”, *Astrop. Phys.*, **14**(1), 33 (2000).
- [69] K. McCarty et al., “The Borexino Muon Detector and Muon Induced Backgrounds”, *AIP Conf. Proc.*, **610**, 973 (2002).
- [70] R. Dossi, A. Ianni, G. Ranucci, and O. Ju. Smirnov, “Methods for single photoelectron counting with photomultipliers”, *Nucl. Instr. Meth. A*, **451**, 623 (2000).

- [71] V. Lagomarsino and G. Testera, “A gateless charge integrator for Borexino energy measurement”, *Nucl. Instr. Meth. A*, **430**, 435 (1999).
- F. Gatti et al., “The Borexino read out electronics and trigger system”, *Nucl. Instr. Meth. A*, **461**, 474 (2001).
- [72] F. Elisei et al., “Measurements of liquid scintillator properties for the Borexino detector”, *Nucl. Instr. Meth. A*, **400**, 53 (1997).
- [73] G. Ranucci, A. Goretti, and P. Lombardi, “Pulse-shape discrimination of liquid scintillators”, *Nucl. Instr. Meth. A*, **412**, 374 (1998).
- G. Ranucci, “An analytical approach to the evaluation of the pulse shape discrimination properties of scintillators”, *Nucl. Instr. Meth. A*, **354**, 389 (1995).
- G. Ranucci et al., “Scintillation decay time and pulse shape discrimination of binary organic liquid scintillators for the Borexino detector”, *Nucl. Instr. Meth. A*, **350**, 338 (1994).
- [74] M. Balata et al., “The water purification system for the low background counting test facility of the Borexino experiment at Gran Sasso”, *Nucl. Instr. Meth. A*, **370**, 605 (1996).
- [75] The Borexino Collaboration, G. Alimonti et al., “Measurement of the  $^{14}\text{C}$  abundance in a low background liquid scintillator”, *Phys. Lett. B*, **422**, 349 (1998).
- [76] L. Cadonati, “The Borexino Solar Neutrino Experiment and its Scintillator Containment Vessel”, Ph.D. Thesis, Princeton University, Jan. 2001.
- [77] The Borexino Collaboration, C. Arpesella et al., “Measurements of extremely low radioactivity levels in BOREXINO”, *Astrop. Phys.*, **18**(1), 1 (2002).
- [78] G. Alimonti et al., “A large-scale low-background liquid scintillation detector: the counting test facility at Gran Sasso”, *Nucl. Instr. Meth. A*, **406**, 411 (1998).
- G. Alimonti et al., “Ultra-low background measurements in a large volume underground detector”, *Astrop. Phys.*, **8**(3), 141 (1998).

- [79] C. Galbiati, “Data taking and analysis of the Counting Test Facility of Borexino”, Ph.D. Thesis, Università degli Studi di Milano, 1998.
- [80] L. Cadonati, “Potassium Peak in the CTF2 Data”, Princeton University Internal Report, Aug. 2000. (unpublished)
- E. Resconi, “Measurements with the Upgraded Counting test Facility (CTF-2) of the Solar Neutrino Experiment Borexino”, Ph.D. Thesis, Università degli Studi di Genova, 2001.
- M. Göger-Neff, “Development of a Liquid Scintillator and of Data Analysis Methods for BOREXINO”, Ph.D. Thesis, Technischen Universität München, 2001.
- [81] The Borexino Collaboration, H. O. Back et al., “Search for electron decay mode  $e \rightarrow \gamma + \nu$  with prototype of Borexino detector”, *Phys. Lett. B*, **525**(1-2), 29 (2002).
- The Borexino Collaboration, H. O. Back et al., “New limits on nucleon decays into invisible channels with the BOREXINO counting test facility”, *Phys. Lett. B*, **563**(1-2), 23 (2003).
- [82] The Borexino Collaboration, H. O. Back et al., “Study of neutrino electromagnetic properties with the prototype of the Borexino detector”, *Phys. Lett. B*, **563**(1-2), 35 (2003).
- [83] The SNO Collaboration, J. Boger et al., “The Sudbury Neutrino Observatory”, *Nucl. Instr. Meth. A*, **449**, 172 (2000).
- [84] J. Benziger, F. P. Calaprice et al. editors, “NSF Borexino Proposal”, Princeton University, 1993.
- [85] M. I. Kohan editor, “Nylon Plastics Handbook”, Hanser Publishers, 1995.
- [86] C. Galbiati et al. “Glass transition, moisture content and mechanical characteristics of Nylon”, Princeton University Internal Report, March 2001 (unpublished).

- [87] M. Wójcik et al., “Radon diffusion through polymer membranes used in the solar neutrino experiment Borexino”, *Nucl. Instr. Meth. A*, **449**, 158 (2000).
- [88] L. Cadonati and T. Shutt. “FEA Analysis of Filling Scenarios”, Princeton University Internal Report, Jan. 2002 (unpublished).
- [89] F. Rodriguez, “Principles of Polymer Systems”, Francis & Taylor, 1966.
- [90] F. Calaprice, “Particulate contamination in Borexino subsystems” Princeton University Internal Report, Nov. 1999 (unpublished).
- [91] “Military Standard 1246C. Product Cleanliness Levels and Contamination Control Program”, 1994.
- [92] Astro Pak Corporation, <http://www.astropak.com/>
- [93] T. Shutt, “Vessel tie-down ropes for Borexino”, Princeton University Internal Report, Nov. 2000 (unpublished).
- [94] Tensylon is a proprietary product of Synthetic Textiles, Inc., <http://www.synthetictextilesinc.com/>
- [95] L. Cadonati, E. deHaas, and T. Shutt, “Hold-down ropes for the Borexino vessels”, Princeton University Internal Report, Feb. 2002 (unpublished).
- [96] E. Harding and C. Galbiati, “Vessel Integrity: Leak Checking”, Princeton University Internal Report, March 2001 (unpublished).
- [97] Fisher Rosemount, <http://www.rosemount.com/>
- [98] BASF Corporation, <http://www.basf.com/>
- [99] Spectrum Laboratories, Inc., <http://www.speclab.com/>
- [100] C. Galbiati, “Umbilical Measurements for the Borexino Vessels: Measurements of Buoyant Forces and Temperature”, Princeton University Internal Report, August

2000 (unpublished).

A. Pocar, "Coefficient of Thermal Expansion for the Borexino Scintillator Fluids: a Comment", Princeton University Internal Report, March 2001 (unpublished). Original measurement performed by Jay Benziger.

[101] Arizona Instruments Computrac 3000, <http://www.azic.com/>

[102] E. Harding and A. Pocar, "Buoyancy Variations and Leak Rates for the Borexino Inner Vessel", Princeton University Internal Report, March 2001 (unpublished).

[103] W. W. Nazaroff and A. V. Nero Jr., "Radon and its Decay Products in Indoor Air", John Wiley & Sons, New York, 1988.

[104] T. Shutt, "First nylon plateout measurement", Princeton University Internal Report, May 2000 (unpublished).

Tom Shutt, private communication.

[105] Elizabeth Harding, private communication.

[106] "Physics Department Cleanroom Operation & Maintenance Manual for Princeton University, Princeton, NJ". Control Solutions, Inc., 1770 Mason Morrow Road, Lebanon, OH, 45036.

[107] A. Pocar, "The Supply of Radon-Filtered Air to the Connecting Rooms of the Clean Room", Princeton University Internal Report, June 2001 (unpublished).

[108] T. Shutt et al., "Measurement of the tightness of the Princeton University clean room for the Borexino solar neutrino experiment", Princeton University Internal Report, Aug. 1999 (unpublished).

[109] Elizabethtown Water Company, 1999 Water Quality Annual Report, <http://www.etownwater.com/pdfs2/ewc.pdf>

[110] A. Pocar, "Radon Content in the Water Supply to the Clean Room", Princeton University Internal Report, April 2001 (unpublished).

- [111] The Super-Kamiokande Collaboration, S. Fukuda et al., “The Super-Kamiokande Detector”, *Nucl. Instr. Meth. A*, **501**(2-3), 418 (2003).
- [112] R. E. Treybal, “Mass-Transfer Operations”, 3rd ed., McGraw-Hill Book Company, 1987.
- [113] D. M. Ruthven, “Principles of Adsorption and Adsorption Processes”, John Wiley & Sons, New York, 1984.
- [114] “Handbook of Chemistry and Physics”, 70th ed., CRC Press, 1989-1990.
- [115] K. P. Strong and D. M. Levins, “Dynamic Adsorption of Radon on Activated Carbon”, Proceedings of the 15<sup>th</sup> DOE Nuclear Air Cleaning Conference, 1978.
- [116] D. M. Ruthven, S. Farooq, and K. S. Knabel, “Pressure Swing Adsorption”, VCH Publishers, 1994.
- [117] R. Bocanegra and P. K. Hopke, “Theoretical Evaluation of Indoor Radon Control Using a Carbon Adsorption System”, *JAPCA*, **39**, 305 (1989).
- S. C. Scarpitta and N. H. Harley, “Adsorption and Desorption of Noble Gases on Activated Charcoal: II.  $^{222}\text{Rn}$  Studies in a Monolayer and Packed Bed”, *Health Phys.*, **59**(4), 394 (1990).
- [118] N. Darnton, “Adsorption Properties of Activated Charcoal”, Princeton University Internal Report, April 1997. (unpublished)
- N. Darnton, “Charcoal Properties Test Cell”, Princeton University Internal Report and Addendum, Dec. 1996 and Feb. 1997 (unpublished).
- [119] N. Darnton, Princeton University Internal Report, 1997 (unpublished).
- [120] Calgon Carbon Corporation, <http://www.calgoncarbon.com/>
- [121] S. C. Scarpitta, “Optimum  $^{222}\text{Rn}$ -Adsorbing Activated Charcoals”, *Health Phys.*, **62**, 576 (1992).

- [122] T. Shutt, “Choice of charcoal for Rn PSA system”, Princeton University Internal Note, Nov. 1998 (unpublished).
- [123] RAD7 Electronic Radon Monitor, <http://www.durridge.com/rad7.htm>
- [124] R. Bocanegra and P. K. Hopke, “Radon Adsorption on Activated Carbon and the Effect of some Airborne Contaminants”, *Sci. Tot. Env.*, **76**, 193 (1988).
- [125] Model 1025 Flow-Through Radon Gas Sources, Pylon Electronics, <http://www.pylonelectronics.com/nukeinst.html>
- [126] J. W. Ayers, A. S. Goldin, and D. W. Underhill, “Pressure-Swing Sorption Concentration of Krypton-85 for Permanent Storage”, Proceedings of the 13<sup>th</sup> DOE Nuclear Air Cleaning Conference, 1974.
- [127] Matheson Gas Products, <http://www.matheson.com>
- [128] A. Roth, “Vacuum Technology”, 3rd ed., North Holland, Amsterdam, 1990.
- [129] A. Pocar, “Characterization of the Flows and Pressure Drops in the Tubing of the Radon Filter”, Princeton University Internal Note, Sept. 2000 (unpublished).
- [130] Gerd Heusser, private communication.
- [131] Enmet Spectrum Online model 04820-1100.
- [132] MetOne 227A laser particle counter, MetOne Instruments Inc., <http://www.metone.com/>
- [133] Shipco, 1 Schwenk Drive, Shippensburg, Pa 17257-0279.
- [134] BOC Edwards, <http://www.edwards.boc.com/>
- [135] Becker Pumps Corp., 100 East Ascot Lane, Cuyahoga Falls, Ohio 44223-3768, <http://www.beckerpumps.com/>

- [136] Model HC-150 I dryer. Munters Corp., Cargocaire Div., 79 Monroe St., P.O. Box 640, Amesbury, MA 01913-0640.
- [137] PW-II model 5 HP blower. Madison Manufacturing Co., 1 Madison Ave., Hot Springs, NC 28743
- [138] Varian Vacuum, Inc., 121 Hartwell Avenue, Lexington, MA 02421-3133, <http://www.varianinc.com/>
- [139] General Aire, LLC, 21 Brant Avenue, Clark, NJ 07066.
- [140] LabVIEW is a product of National Instruments. The software controlled a NI ER-16 relay board via a PC-DIO-24 PCI-6503 digital input/output board, both produced by National Instruments. <http://www.ni.com/>
- [141] Jose Busto (MuNu collaboration) and Claudine Goldbach (Edelweiss collaboration), private communication.
- [142] Derek Lane-Smith, Durrige Company, 7 Railroad Ave, Suite D, Bedford, MA 01730, private communication.
- [143] Gerd Heusser, private communication.
- [144] This idea was first discussed between Tom Shutt and Andrew Sonnenschein.
- [145] CleanFilm, 95 Hoffman Lane, Str. G, Islandia, NY 11749-5012. Now administered by Texas Technologies, Inc., 17013 FM 1431, Leander, TX 78641, <http://www.texastechnologies.com/>
- [146] Web System, Inc., 1354 Linden Drive, Boulder, CO, 80304.
- [147] Honeywell-BASF Plastics, <http://www.honeywell-plastics.com/>
- [148] E. Harding, "Nylon Film: Extrusion and Cleanliness", Princeton University Internal Note, March 2001 (unpublished).

- [149] L. Cadonati, et al., “Comments on the Nylon Bulk Activity”, Princeton University Internal Note, June 2001 (unpublished).
- L. Cadonati, “Note on Background due to  $^{222}\text{Rn}$  Emanation from the Inner Vessel Nylon Film in Borexino”, Princeton University Internal Note, Sept. 2001 (unpublished).
- [150] M. Wójcik et al., “Ultra-traces of  $^{226}\text{Ra}$  in nylon used in the BOREXINO solar neutrino experiment”, *Nucl. Instr. Meth. A*, **498**, 240 (2003).
- [151] Tom Shutt, private communication.
- [152] Eric Hopkins and Cristiano Galbiati, private communication.
- [153] The track and cart system was designed and built by the Princeton University technician Allan Nelson.
- [154] The accordion-stack design for the nylon vessels was developed by Bruce Vogelaar, Fred Loeser, and Frank Calaprice.
- [155] Resorcinol is made by Acros Organics N.V., Fairlawn, N.J.
- [156] Fred Loeser and Elizabeth Harding, private communication.
- [157] “Borexino Nylon Vessel Construction”, <http://borex.princeton.edu/>
- [158] R. Fernholz, et al., “Mechanical Tests and Leak Checking of the IV End Region Assembly. A Status Report”, Princeton University Internal Note, April 2002 (unpublished).
- [159] R. Fernholz, et al., “Design and Test of the Improved IV End Region Assembly. A Status Report”, Princeton University Internal Note, May 2002 (unpublished).
- [160] OmniStar, Pfeiffer Vacuum Inc., 24 Trafalgar Square, Nashua, NH 03063-1988, <http://www.pfeiffer-vacuum.com/>
- [161] Richard Fernholz, private communication.

- [162] Data presented by K. Inoue, LeptonPhoton03 Conference, Fermilab, Batavia, IL, Aug. 2003, <http://conferences.fnal.gov/lp2003/>
- [163] L. Miramonti, “Tests on PC+PPO 1.5 g/l scintillator excited by a 266 nm and 355 nm laser beam”, Università Statale di Milano Internal Note, Sept. 2000 (unpublished).
- [164] J. Maneira, “Calibration and Monitoring of the Borexino Solar Neutrino Experiment”, Ph.D. Thesis, Universidade de Lisboa, 2001.
- [165] Kodak DC290 digital cameras, <http://www.kodak.com>
- [166] H. O. Back, C. Grieb, and R. B. Vogelaar, “Calibration Source Locating System for the Borexino Solar Neutrino Experiment”, Virginia Tech Draft Note, July 2003 (paper in preparation).
- [167] Bruce Vogelaar, private communication.
- [168] Ceramoptec Corp., <http://www.ceramoptec.com>
- [169] Tefzel is a proprietary product of DuPont, <http://www.dupont.com>. It is in many respects similar to teflon.
- [170] Frank Calaprice, private communication.
- [171] D. Gaiotto, “Light sources inside the Borexino vessels”, Princeton University Internal Note, Oct. 2001 (unpublished).
- [172] I. A. Siddiqi, “Absolute Quantum Efficiency Measurements of a Prototype Ultra-Cold Neutron in Liquid Helium Detection System”, Senior Thesis, Harvard University, 1997.
- [173] Nafion is a proprietary product of DuPont, <http://www.dupont.com>
- [174] Jay Benziger, private communication.
- [175] “The Berkeley Laboratory Isotopes Project”, <http://ie.lbl.gov/education/isotopes.htm>

- [176] ChemTrace, 44050 Fremont Blvd., Fremont, CA, 94538,  
<http://www.chemtrace.com>
- [177] Steve Kidner, private communication.
- [178] Henning Back, private communication.
- [179] Maria Elena Monzani, private communication.
- [180] C. Lendvai, D. D'Angelo, and S. Schönert, "The Outer Detector (OD): progress report", Borexino Progress Report, 2002.
- [181] The fit was performed by Vladislav Kobychiev.
- [182] "Table of nuclides", <http://www.bnl.gov/ton/>
- [183] The plot was generated by Aldo Ianni.
- [184] Hardy Simgen, private communication.
- [185] Plots generated by Oleg Smirnov.
- [186] Aldo Ianni, "Maximum-likelihood analysis and goodness-of-fit estimation in low count-rate experiments:  $^{85}\text{Kr}$   $\beta$  activity in the test facility of the Borexino detector and double beta decay of  $^{76}\text{Ge}$  in the Heidelberg-Moscow experiment", LNGS/EXP-01/03, Feb. 2003. Accepted by *Nucl. Instr. Meth. A*.
- [187] B. T. Cleveland, "The Analysis of Radioactive Decay with a Small Number of Counts by the Method of Maximum Likelihood", *Nucl. Instr. Meth. A*, **214**, 451 (1983).
- [188] C. Cowan, "Statistical data analysis", Oxford Science Publications, 1998.
- [189] B. T. Cleveland, "The goodness of fit of radioactive counting data with application to the data of the chlorine solar neutrino experiment", *Nucl. Instr. Meth. A*, **416**, 405 (1998), and references therein.

- [190] B. P. Roe, “Probability and Statistics in Experimental Physics”, Springer-Verlag, 1992.
- [191] “Solubility Data Series”, edited by the International Union of Pure and Applied Chemistry (IUPAC), Pergamon Press (1979-1997). Published by the *J. Phys. Chem. Ref. Data* since 1997.
- [192] Measurement performed by the Borexino collaborators at the Max Planck Institut für Kernphysik, Heidelberg.
- [193] T. Shutt, “Note of Kr and Ar for filling, along with a comment on Rn and Ra in water for filling”, Princeton University Internal Note, Dec. 2002 (unpublished).

# Afterword

More than a year after their arrival in Hall C at the Gran Sasso laboratories, the Borexino nylon vessels are still packaged awaiting installation inside the stainless steel sphere. This was scheduled to happen in the Fall of 2002, after all pre-requisites had been satisfied. An unexpected, partial shutdown of operations in the underground experimental hall, still effective at the time of writing of this thesis, has prevented vessel installation and hence completion of the detector. While confident that the vessels are constructed and packaged such that they can withstand the current unexpected events, it is difficult to foresee the consequences of such a delayed installation on their overall integrity and cleanliness.

An enormous amount of work has been invested in developing and constructing the vessels along with the rest of the Borexino detector. Every effort is being made to find a timely solution to this problem. I personally want to express the hope that these issues may be resolved soon and that Borexino, with the vessel performing as predicted, will successfully detect solar neutrinos in the near future.